Analysis of the effect of Aβ fibril polymorphism on toxicity, degradation and activation of an inflammatory response

Madeleine Rachel Brown

University of Leeds

School of Molecular and Cellular Biology

Astbury Centre for Structural Molecular Biology

Submitted in accordance with the requirements for the degree of

Doctor of Philosophy

September 2021

Declaration

The candidate confirms that the work submitted is her own and that appropriate credit has been given where reference has been made to the work of others.

Acknowledgements

I would firstly like to thank my supervisors Eric Hewitt and Sheena Radford for their encouragement and guidance throughout my project. Eric, thank you for all of your interesting ideas and help in steering the project, but also for all of the support throughout my PhD and especially through a difficult year of lockdowns and uncertainty. Sheena, thank you for your invaluable direction, insight and enthusiasm throughout the project. Thank you to MRC for funding this project, and the DiMeN DTP for all of the additional training opportunities.

I would like to thank every member of the Hewitt and Radford lab groups for all of your help over the past four years. In particular, I would like to thank Dr Matthew Jackson for imparting your knowledge and wisdom (and sarcasm) when I first joined the lab and Dr Chalmers Chau (4C) for your graphical expertise and great humour. A special thanks goes to Dr Atenas Posada Borbón for teaching me so much, always being so patient with me and for being such a great friend. I would also like to thank Dr Martin Walko for your help with performing and optimising the Aβ purifications; I am very grateful for the time and pain that this saved me. A massive thankyou to Nasir Khan for all of your help, curry and biscuits over the years, without you the lab wouldn't run and nor would the people in it.

To Nicole, Nat and Jess; the only people I was allowed to be within two metres of for the best part of a year, thanks for always staying positive and for the daily lockdown coffee breaks on the front step. I would also like to thank Maia, Baz and Louise, the best PhD girl gang and support team right from the start.

Thankyou to my sister Steph for patiently listening to all of my moaning, for believing so genuinely that I can do it, and for telling me this so often. And of course, thankyou to my parents for all of your love and support.

And lastly I would like to thank Ollie, for being there for me through all of my successes and failures over the last four years, and all the moods that came with them. Thanks for always reminding me what's important and to have fun, for knowing exactly how to cheer me up and most importantly for always keeping the snack cupboard well stocked.

Table of Contents

List of figures

List of tables

List of abbreviations

Aβ	Amyloid-β
$Aβ_{40}$	Amyloid-β residues 1-40
$Aβ_{42}$	Amyloid-β residues 1-42
AD	Alzheimer's disease
APP	Amyloid precursor protein
ARM	Activated response microglia
ASC	Apoptosis-associated speck-like protein containing a CARD
$β_2m$	$β_2$-microglobulin
CAA	Cerebral amyloid angiopathy
CARD	Caspase recruitment domain
COX-2	Cyclooxygenase-2
CSF	Cerebrospinal fluid
DAM	Disease-associated microglia
DAMP	Damage-associated molecular pattern
DLB	Dementia with Lewy bodies
ELISA	Enzyme-linked immunosorbent assay
EM	Electron microscopy
EOAD	Early-onset Alzheimer's disease
ES-MS	Electrospray mass spectrometry
fAβ	Fibrillar Aβ
fAD	Familial Alzheimer's disease
FTD	Frontotemporal dementia
HPLC	High-performance liquid chromatography
IAPP	Islet amyloid polypeptide
IDE	Insulin-degrading enzyme
IEX	Ion exchange
IFN-γ	Interferon-γ
IL	Interleukin
IPTG	Isopropyl β-D-1-thiogalactopyranoside
LAL	Limulus amebocyte lysate
LC-MS	Liquid chromatography-mass spectrometry
LCO	Luminescent conjugated oligothiophenes
LDAM	Lipid-droplet-accumulating microglia
LDH	Lactate dehydrogenase

LOAD	Late-onset Alzheimer’s disease
LPS	Lipopolysaccharide
LRR	Leucine-rich repeats
LTP	Long-term potentiation
MCI	Mild cognitive impairment
MMP	Matrix metalloproteinases
MPL	Mass-per-length
MSA	Multiple system atrophy
MTT	3-(4,5-Dimethylthiazol-2yl)-2,5-diphenyltetrazolium Bromide
NAGA	N-acetylglucosaminidase
NEP	Neprilysin
NFT	Neurofibrillary tangles
NLRP3	NOD-like receptor family, pyrin domain containing 3
NO	Nitric oxide
PAMP	Pathogen-associated molecular pattern
PCA	Posterior cortical atrophy
PD	Parkinson’s disease
PET	Positron emission tomography
PK	Proteinase K
PRR	Pattern recognition receptor
PYD	Pyrin domain
r-AD	Rapidly progressing Alzheimer’s disease
ROS	Reactive oxygen species
SDS-PAGE	Sodium dodecyl sulphate–polyacrylamide gel electrophoresis
SEC	Size exclusion chromatography
ssNMR	Solid-state NMR
t-AD	Typical Alzheimer’s disease
TEM	Transmission electron microscopy
TFA	Trifluoroacetic acid
ThS	Thioflavin S
ThT	Thioflavin T
TLR	Toll-like receptor
TNF-α	Tumour necrosis factor alpha
TPP-1	Tripeptidyl peptidase
TREM2	Triggering receptors expressed on myeloid cells

Abstract

Alzheimer's disease (AD) is the most common form of dementia and has a large social, medical and economic impact. One of the main pathological hallmarks of AD is the presence of extracellular plaques consisting primarily of β-amyloid (Aβ). Aβ fibrils share a characteristic cross-β structure, however structural models for Aβ fibrils have revealed polymorphism at a molecular level *in vitro* and there is also evidence that distinct structural variants could be linked to the presentation of different subtypes of AD.

Working at the interface between structural and cellular biology, this research investigates differences in the cellular responses to different Aβ fibril preparations. Distinct populations of Aβ fibrils were formed from recombinantly purified Aβ monomers, reproducing fibrillation conditions previously used in the production of fibrils from which structures have been published. Namely, 2A, 3Q and *de novo* $A\beta_{40}$ fibril populations were produced, in addition to fibrils formed from a familial mutant form of the peptide, E22Δ $A\beta_{40}$. Further to this, two populations of $A\beta_{42}$ fibrils were compared; one formed at pH 8 and the other formed at pH 2. Fibrils were characterised using transmission electron microscopy (TEM), Thioflavin T (ThT) monitoring, oligothiophene probes and fibril yield analysis.

With neuroinflammation being another major hallmark of AD, this research focuses specifically on the effects of these different Aβ fibril populations on monocytic and microglial cells. A combination of MTT, ATP and LDH viability assays were performed which revealed differences in the toxicity of the different Aβ fibrils towards BV-2 microglial cells, RAW 264.7 macrophage cells and monocytic THP-1 cells. $A\beta_{42}$ fibrils that were formed at pH 8 were found to be significantly more toxic than the population of $A\beta_{42}$ fibrils that were formed at pH 2. E22Δ $A\beta_{40}$ fibrils were also shown to be more toxic towards these cells than the fibril populations that were formed from wild-type $A\beta_{40}$ peptide.

Further to this, differences in the levels of the pro-inflammatory cytokines IL-6, IL-1β and TNF-α released from cells in response to the different fibrils were identified, with the population of $A\beta_{42}$ fibrils produced at pH 8 resulting in the greatest release compared to other fibril populations. These fibrils were also found to associate more with cells, possibly helping to explain this increased toxicity and inflammatory response. Furthermore, differences in the efficiency of clearance by microglial cells of $A\beta_{40}$ fibrils were also identified, with reduced 2A $A\beta_{40}$ fibril clearance compared to other fibril populations. Differences identified between these Aβ fibrils could help to explain the huge amount of variability in symptoms and disease severity that exists between Alzheimer's patients.

1 Introduction

1.1 Alzheimer's disease

Dementia is the leading cause of death in the UK population, accounting for 12.7% of all deaths (Deaths registered in England and Wales - Office for National Statistics). Over 850,000 people in the UK have dementia and this is projected to increase to 1.6 million by 2040 with an estimated annual cost of £26 billion (Wittenberg et al., 2020). Alzheimer's disease (AD) is the most common form of dementia, accounting for 60-80% of dementia and affecting a sixth of the population over 80 (Wittenberg et al., 2020). With such a large medical, social and economic impact, further research is required in order to better elucidate the molecular mechanisms that underly AD, with the goal of developing much-needed treatments.

1.1.1 Clinical features of Alzheimer's disease

AD is a neurodegenerative disease which typically clinically presents as selective amnesia in a temporal gradient, with the most recent memories being affected first (McKhann et al., 2011). In the typical form of AD, impairment in memory and learning is often followed by a progressive global cognitive decline, including deficits in complex attention, executive function, recognition and language functioning (McKhann et al., 2011). AD is now thought to be a continuum, beginning as preclinical AD then advancing to mild cognitive impairment (MCI) before progression to mild, moderate and severe dementia due to AD (Albert et al., 2011; Jack et al., 2011; McKhann et al., 2011; Sperling et al., 2011). This diagnostic system is based on clinical presentation of disease and to what extent symptoms affect day-to-day functioning and independence, in addition to measurement of biomarkers of AD. Increasingly, research is focusing on these preclinical stages of AD, in order to develop a treatment that prevents the progression of disease to dementia.

AD is a very heterogenous disease, with a number of different subtypes and also variability in the age of onset and the range and severity of symptoms presented within disease subtypes (Cummings, 2000; Lam et al., 2013) . The majority of individuals who develop AD are aged 65 or over, known as late-onset AD (LOAD); however, about 5% of cases occur before the age of 65 and are termed early-onset AD (EOAD) (Sims et al., 2020). In addition to the typical form of AD, there are a number of atypical subtypes of AD involving non-memory brain domains, which have different clinical presentations (Lam et al., 2013). Atypical forms of AD include posterior cortical atrophy (PCA), a variant of the disease in which visual processing is disrupted, logopenic aphasia in which

language is affected, and frontal Alzheimer's in which deficits are observed in planning, decision making and social functioning (Lam et al., 2013).

1.1.2 Neuropathology of Alzheimer's disease

The typical form of AD (LOAD) is associated with atrophy of the medial temporal lobe of the brain, where structures important in memory are located, with neurodegeneration later spreading out to wider cortical regions (Jack et al., 1998; Jucker and Walker, 2013). In addition to cortical atrophy, AD is characterised by two main neuropathological hallmarks; intracellular neurofibrillary tangles (NFTs) consisting of hyperphosphorylated tau protein, and extracellular senile plaques formed from β-amyloid (Aβ) (Figure 1.1) (Masters et al., 1985; Braak and Braak, 1991). The mechanisms by which these two pathologies form and deposit, and how they lead to tissue degeneration in the brain is a major focus of research into the disease (Hardy and Selkoe, 2002; Masters et al., 2015; Selkoe and Hardy, 2016). However, in addition to these hallmarks, another important feature of AD is neuroinflammation, in which microglia play a major role (Figure 1.1). Previously thought to be a by-product of disease, evidence has shown that this process is involved in disease progression (McManus and Heneka, 2017).

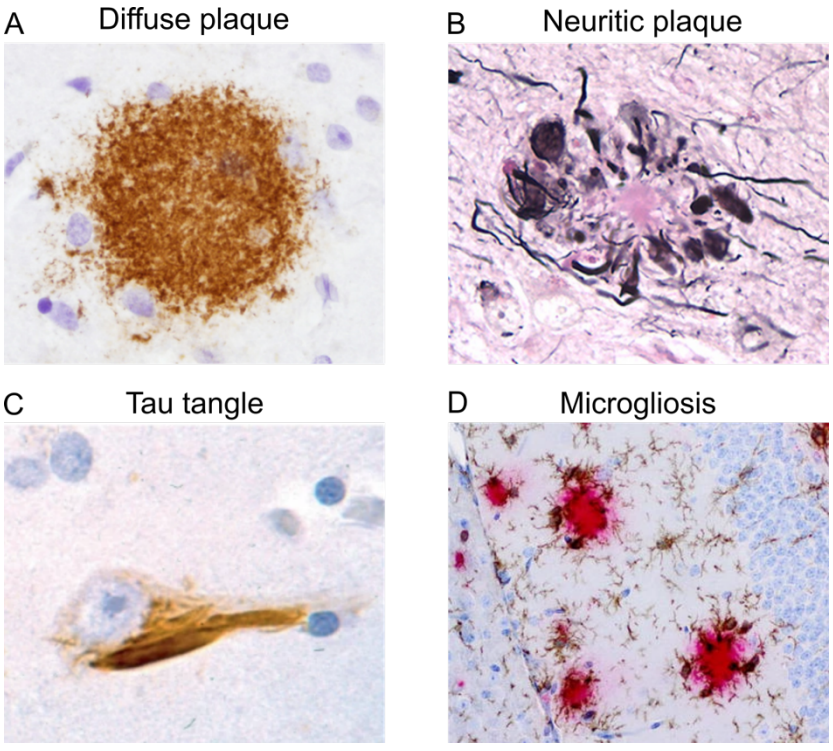

Figure 1.1. Alzheimer's disease histology
(A) Immunohistochemistry of a diffuse Aβ plaque (Agamanolis 2020 - Free neuropathology) (B) Silver staining and counterstain of a neuritic plaque showing an amyloid core in pink and dystrophic neurites surrounding in black (Walker, 2020) (C) Immunohistochemistry of a neurofibrillary tangle in a neuron of an AD patient (Jucker and Walker, 2013) (D) Activated microglia can be seen to closely interact with Aβ plaques in an AD mouse model, Iba1 staining shown in brown, Aβ staining in red (Prokop et al, 2013).

The spread of NFT pathology follows a stereotypic topographic pattern of progression, appearing first in the brainstem and transentorhinal areas, before spreading to the entorhinal cortex, the hippocampus, adjacent temporal cortex then into the surrounding isocortex (Figure 1.2) (Jucker and Walker, 2013; van der Kant et al., 2019). This neuroanatomically connected topology supports a prion-like spread of tau, and is what forms the basis of the Braak staging system of AD patients (Braak and Braak, 1991). However, this pattern of tau spread through the brain does not align with that of Aβ, with the first identified Aβ accumulation occurring in the precuneus and posterior cingulate (Figure 1.2) (Jucker and Walker, 2013; van der Kant et al., 2019). The first stage of Aβ deposition is exclusively in the neocortex, followed by allocortical regions (Thal et al., 2002). As Aβ pathology progresses, the diencephalon and striatum are also affected, followed by deposits in the brainstem and cerebellum in later stages of disease (Figure 1.2) (Thal et al., 2002).

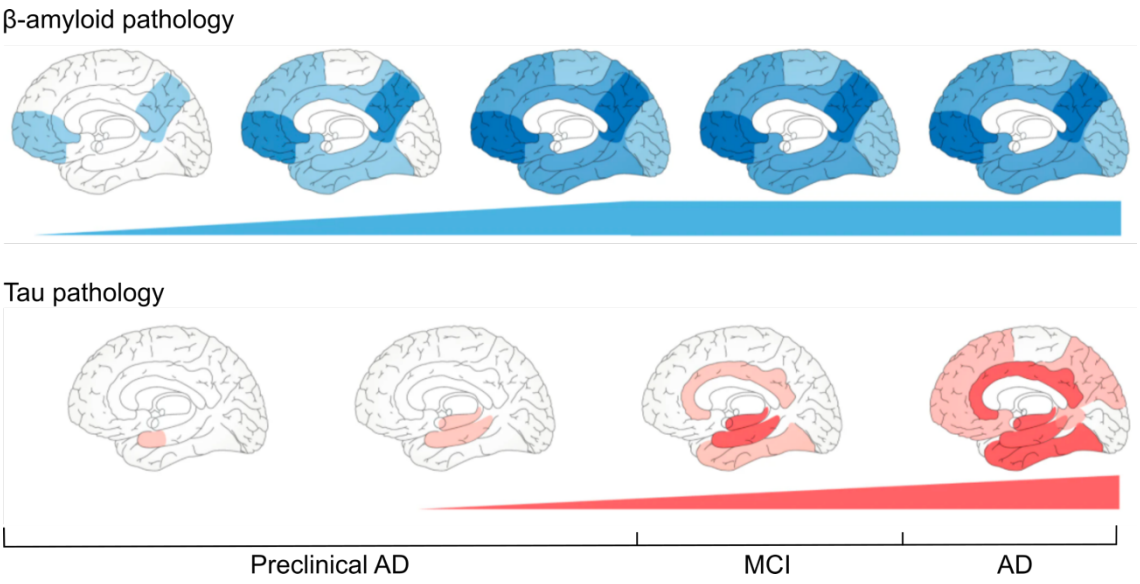

Figure 1.2. Aβ and tau progression in AD
The typical spread of Aβ and tau through preclinical stages of AD, mild cognitive impairment (MCI) and clinical AD are shown. It can be observed that these pathologies do not align, and Aβ pathology is more widespread in earlier stages of disease than tau (Van der Kant et al, 2019).

Aβ deposits in the brain can be classified based on their morphology, and the extent to which they are stained by amyloid dyes such as Thioflavin S, Thioflavin T (ThS/ThT) and Congo red (Serrano-Pozo et al., 2011; Xu et al., 2020). Neuritic plaques are a distinct form of Aβ deposits characterised by the presence of dystrophic neurites and association with reactive astrocytes and microglial cells (Figure 1.1). These plaques are large spherical structures, also referred to as 'dense-core' plaques, as they possess a compact Aβ fibrillar core and are strongly stained by Congo red and ThS. Neuritic plaques are

considered to be a more pathological form of Aβ plaque as they have been associated with cognitive impairment (Serrano-Pozo et al., 2011; Hyman et al., 2012; Xu et al., 2020). Diffuse plaques, conversely, are less compact, more amorphous structures, and are less associated with AD as they are commonly identified in cognitively normal elderly individuals (Figure 1.1) (Knopman et al., 2003).

In addition to the assessment of memory and cognitive impairment, assessment of neuropathology can also be used to aid in AD diagnosis. Aβ and tau levels measured in the cerebral spinal fluid (CSF) are now established biomarkers of AD, recommended for use in the diagnosis of AD, and recent developments have also found that the Aβ status of AD patients can be predicted by measurement of Aβ in the plasma (McKhann et al., 2011; Nakamura et al., 2018; Palmqvist et al., 2019). A decrease in $A\beta_{42}$ in the CSF is indicative of AD, although a ratio of $A\beta_{42}$ against CSF $A\beta_{40}$, total tau or phosphorylated tau (p-tau181) has shown to be more accurate in diagnosis, removing the effects of individual variability in Aβ levels (Hansson et al., 2007, 2018; Wiltfang et al., 2007).

Brain imaging techniques such as positron emission tomography (PET) can also be used to assess the severity of neuropathology in AD (Villemagne et al., 2018). Aβ-PET tracers have been developed; ^{11}C-Pittsburgh compound B being the most widely used in research, and originally demonstrated that Aβ deposition was 2-fold higher in parts of the cortex in AD patients when compared to healthy controls (Klunk et al., 2004). Three Aβ-PET tracers (florbetapir, florbetaben and flutemetamol) have now been FDA approved and are available for use in AD diagnostics (Knopman et al., 2021). The main advantage of these imaging techniques over measurement of Aβ plasma or CSF levels is that the location of Aβ deposition can be identified, and the extent of pathology assessed in different brain regions. This regional information can be key in staging Aβ pathology and AD progression (Figure 1.2).

A recent study found an average of 13.9 years between initial detection of Aβ deposition by Florbetapir Aβ PET, and the onset of MCI (Jagust and Landau, 2021). This suggests that early detection and lowering of Aβ levels within this lag period could be an effective preventative measure in AD. Aβ pathology can be identified in earlier disease stages than tau, suggesting that Aβ deposition precedes and could be driving tau pathology. The injection of $A\beta_{42}$ fibrils into the brains of the P301L AD mouse model, in which human tau with the P301L mutation is expressed, was shown to result in a 5-fold increase in NFTs (Götz et al., 2001). Furthermore, when PET imaging was utilised to assess tau and Aβ pathology in older adults it was found that Aβ accumulation was associated with subsequent tau accumulation, and rate of tau accumulation in the inferior temporal neocortex was associated with the rate of cognitive decline (Hanseeuw et al., 2019).

However, the tau and Aβ pathologies starting in different brain regions creates a 'spatial paradox' which challenges this theory (Figure 1.2) (van der Kant et al., 2019).

1.1.3 Genetics of Alzheimer's disease

The most important risk factor for AD is age; the large majority of AD cases are sporadic and occur over the age of 65. However, approximately 1% of cases can be attributed to dominant familial mutations (fAD), and result in early-onset disease with a more rapid rate of progression (Sims et al., 2020). These dominant mutations occur in the amyloid precursor protein gene (*APP*) and presenilin genes (*PSEN1/PSEN2*) which are involved in the cleavage of APP to form Aβ, directly implicating the amyloid pathway in disease (Rogaev et al., 1995; Sims et al., 2020).

In addition to these dominant mutations in fAD, evidence is mounting that LOAD also has a strong genetic component, with a suggested heritability of 58-79% (Gatz et al., 2006). There are now over 50 loci identified that confer an increased risk of developing AD, and the associated pathways are aiding researchers in developing more of an understanding of complex AD disease mechanisms (Karch et al., 2014; Jansen et al., 2019; Sims et al., 2020). Notably, a large proportion of these identified genes are linked to the immune response (Table 1.5). The strongest risk factor for LOAD is the ε4 allele of the ApoE4 gene (Corder et al., 1993; Sims et al., 2020).

1.1.4 Treatment of Alzheimer's disease

Until 2021, AD treatment has been limited to cholinesterase inhibitors and an NMDA receptor antagonist memantine, both of which target slight and temporary alleviation of symptoms rather than addressing the underlying cause of disease (Doody et al., 2001; Reisberg et al., 2003). Over the past decade a great deal of research has therefore gone into developing an Aβ-targeting AD treatment with the aim of either stimulating Aβ clearance or decreasing Aβ production. A number of such anti-Aβ therapeutics have been developed and tested in clinical trials, without success (Panza et al., 2019). Whilst several of these treatments did show to be effective in reducing Aβ levels, patients did not show clinical improvements in cognition (Panza et al., 2019). Several of these therapies are anti-Aβ antibodies including solanezumab, gantenerumab, and crenezumab (Ostrowitzki et al., 2017; Honig et al., 2018; Salloway et al., 2018). These antibodies were found to be ineffective in patients with moderate to mild AD but are now being tested in patients earlier in disease progression, and those with a high risk of developing AD but currently without symptoms (Huang et al., 2020).

Aducanumab, a monoclonal antibody which targets the protofibrillar form of Aβ, was shown to reduce Aβ brain levels but clinical trials were originally terminated due to lack of efficacy (Sevigny et al., 2016; Haeberlein et al., 2020). However, after additional analysis and review of the data the sponsor claimed that there were clinical benefits to the treatment with evidence for a reduction in clinical decline. This antibody was therefore accepted in 2021 by the FDA under 'Accelerated Approval', as the first approved treatment for AD that targets the underlying neuropathology of disease (Haeberlein et al., 2020).

1.2 Amyloid-β (Aβ)

1.2.1 Aβ production

Aβ, the primary component of senile plaques, is produced by the proteolytic cleavage of amyloid precursor protein (APP), a type I transmembrane spanning glycoprotein with a large extracellular domain (Shoji et al., 1992). APP is expressed in many tissues including the synapses of neurons, and is suggested to be involved in the modulation of synapse formation, iron export and anterograde axonal transport (Priller et al., 2006; Satpute-Krishnan et al., 2006; Duce et al., 2010). The synaptic function of APP is thought to be carried out by the soluble ectodomain fragment sAPPα (Figure 1.3), and it was recently identified that sAPPα binds to GABABR1a, a metabotropic receptor through which the inhibitory neurotransmitter gamma-aminobutyric acid (GABA) exerts its effects at synapses (Rice et al., 2019).

Two pathways of APP processing exist; non-amyloidogenic and amyloidogenic (Shoji et al., 1992). Non-amyloidogenic processing of APP involves cleavage by α-secretase in the ectodomain, followed by cleavage by γ-secretase in the transmembrane domain, whereas amyloidogenic processing consists of initial cleavage in the ectodomain by β-secretase (BACE1) followed by γ-secretase (Figure 1.3A) (Shoji et al., 1992). Both processes generate soluble ectodomains (sAPPα and sAPPβ) and identical intracellular C-terminal fragments (AICD), however cleavage by β-secretase results in the production of Aβ fragments, of varying lengths (Figure 1.3) (Selkoe, 1998).

$Aβ_{40}$, the 40 amino acid form of Aβ, is the most abundant form in the brain (80-90%) followed by the 42 amino acid peptide, $Aβ_{42}$ (Figure 1.3B) (Wang et al., 1996). However, $Aβ_{42}$ is more hydrophobic and prone to aggregation, and is the principal form of the fibrillar Aβ found in neuritic plaques (Jarrett et al., 1993; Iwatsubo et al., 1994). Therefore, $Aβ_{42}$ is often assumed to be more relevant in AD pathogenesis (Murphy et al., 2010). Familial mutations have been identified in APP, PSEN1 and PSEN2, genes encoding presenilin-1/2, critical catalytic components of γ-secretase. These mutations principally

result in the increased ratio of $A\beta_{42}$:$A\beta_{40}$ production (Figure 1.4). Remarkably, a mutation that is protective against AD has also been identified in APP, A673T, which results in reduced Aβ production (Figure 1.4) (Xia et al., 2021).

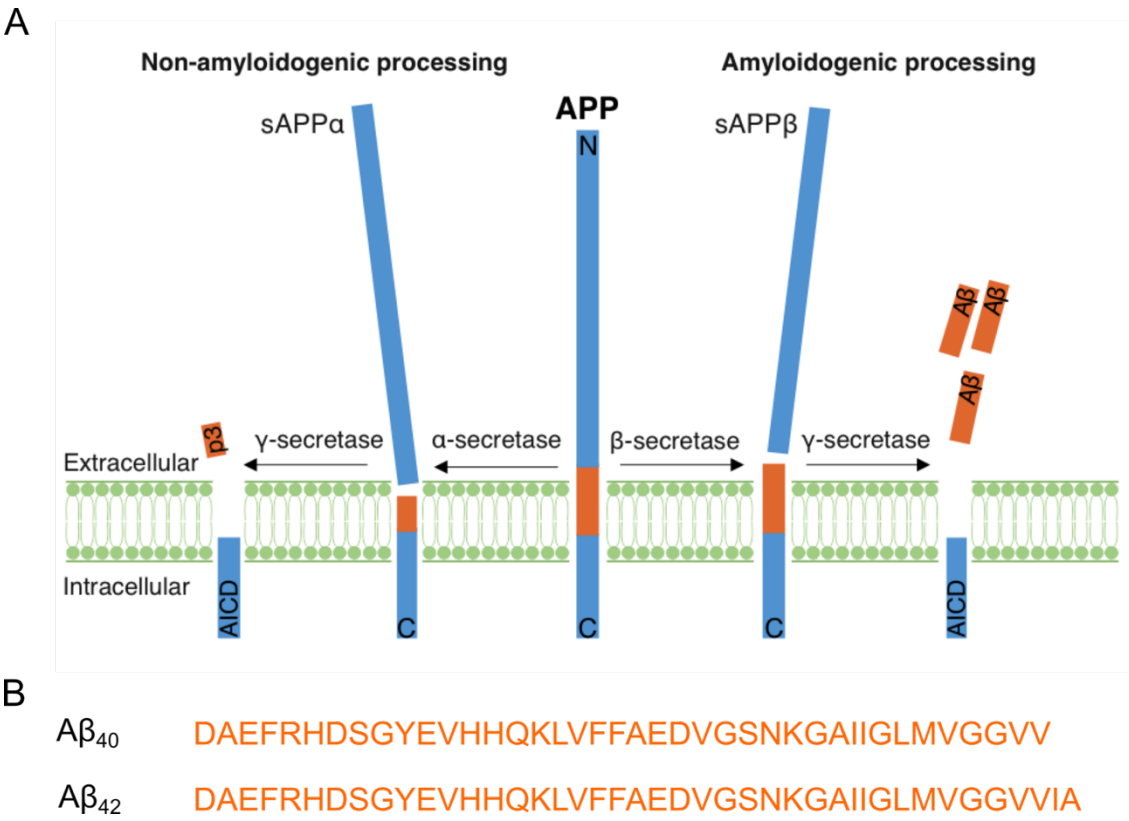

Figure 1.3. Non-amyloidogenic and amyloidogenic pathways of APP processing and Aβ peptide amino acid sequence
(A) Pathways of APP proteolysis are shown; Non-amyloidogenic processing of APP consists of the sequential cleavage of transmembrane protein APP by α-secretase and γ-secretase and results in the formation of an extracellular P3 domain and an APP intracellular domain (AICD). Amyloidogenic processing involves the sequential cleavage of β-secretase followed by γ-secretase and results in the formation of the extracellular Aβ peptide (shown in orange) and APP intracellular domain (AICD). (B) The amino acid sequences of the two most abundant forms of Aβ, $A\beta_{40}$ and $A\beta_{42}$, are shown.

In addition to these two most abundant forms of Aβ, other isoforms exist and have been identified in lower abundance in the brains of AD patients (Portelius et al., 2010; Kakuda et al., 2017). This includes peptides ranging from 38 to 43 residues long ($A\beta_{38}$-$A\beta_{43}$), and N-terminal truncated forms of Aβ such as the 3-pyroglutamate derivate of Aβ3-42 (pGluAβ3-42) (Portelius et al., 2010; Kakuda et al., 2017).

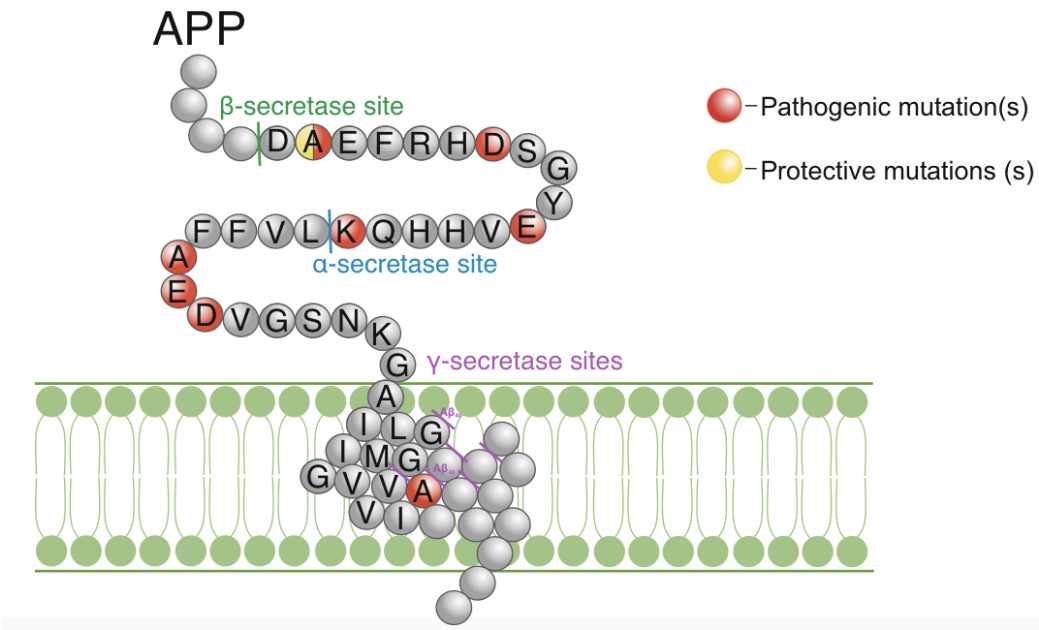

Figure 1.4. APP mutations within the Aβ sequence identified in familial AD
The sequence of Aβ within the APP transmembrane protein is shown, with the location of identified pathogenic and protective mutations within this sequence highlighted in red and yellow respectively. The sites of α, β and γ secretase enzymes are shown. Different cleavages by γ secretase can determine the length of the Aβ peptide that results.

A physiological function for Aβ has been postulated, and evidence suggests that the peptide could have an antimicrobial role (Soscia et al., 2010; Kumar et al., 2016; Brown et al., 2020; Pastore et al., 2020). It has been shown that Aβ can inhibit the growth of eight common microorganisms including both bacterial and fungal species, with a similar effectiveness to LL-37, a well-established antimicrobial peptide (Soscia et al., 2010). Protection against infections has been proposed to result from Aβ binding to microbial cell wall polysaccharides via its heparin-binding domain (VHHQKL) (Kumar et al., 2016). Electron microscopy imaging revealed Aβ fibrillation, with fibrils mediating microbial agglutination (Kumar et al., 2016). Another study found that this microbial agglutination was mediated by $A\beta_{42}$, but not $A\beta_{40}$, suggesting that the more amyloidogenic form of this peptide has greater antimicrobial activity (Spitzer et al., 2016). An antimicrobial function of Aβ suggests an infectious etiology of AD. This is supported by evidence of altered gut microbiota in AD mice models and patients (Cattaneo et al., 2017; Vogt et al., 2017). In addition, a number of studies have suggested a connection between the oral microbiome and AD, with *Porphyromonas gingivalis*, a pathogen in periodontal infections recently identified in AD brains (Poole et al., 2013; Dominy et al., 2019).

1.2.2 Amyloid fibril structure and assembly

As a monomer, Aβ is intrinsically disordered, however it aggregates to form an array of soluble oligomers and ultimately into highly ordered amyloid fibrils with a cross-β structure (Figure 1.5) (Chen et al., 2017; Iadanza et al., 2018). This cross-β structure is characteristic of all amyloid fibrils, consisting of β-sheets in which β-strands are oriented perpendicularly to the fibril axis, as established by x-ray fibre diffraction (Figure 1.5) (Eanes and Glenner, 1968; Sunde et al., 1997). The spacing between the β-strands in a β-sheet is always 4.6-4.7 Å, and the spacing between β-sheets 10 Å (Figure 1.5). Aβ amyloid fibrils are unbranched, typically 5-15 nm in width, can reach up to several microns in length, and can consist of a number of cross-β subunits (Iadanza et al., 2018).

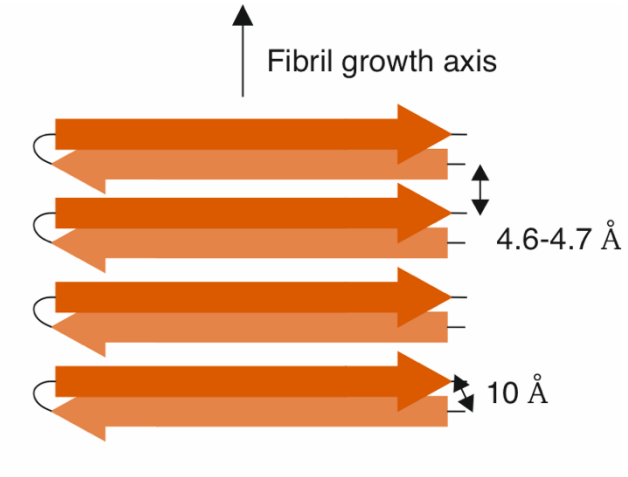

Figure 1.5. Cross-β structure of amyloid fibrils
The cross-β structure of amyloid fibrils describes the arrangement of β-sheets stacked perpendicularly to the fibril growth axis. The distance between β-strands is 4.7-4.8 Å and the distance between β-sheets is around 10 Å within the cross-β structure.

A number of mechanisms are involved in amyloid fibril formation (Figure 1.6). Monomeric Aβ peptide initially forms heterogeneous populations of soluble oligomers. These are largely unstructured (off-pathway) aggregates. However, some oligomers (on-pathway) form more compact and aggregation prone structures with increased β-sheet content, known as a nucleus (Pallitto and Murphy, 2001; Dear et al., 2020). Nucleus formation is a rate limiting step in fibril formation, as the addition of monomer onto the nucleus becomes energetically favourable and fibrils are formed by elongation (Knowles et al., 2014). Secondary mechanisms are also involved in fibril growth kinetics; fragmentation of fibrils can occur, resulting in the presence of a greater number of fibril ends onto which monomer can add (Knowles et al., 2014). In addition, secondary nucleation describes the catalysis of fibril formation by the surfaces of existing fibrils (Tö et al., 2018). Cross-seeding can also occur in which other protein complexes, including fibrils of other amyloidogenic sequences, provide a surface for secondary nucleation to occur (Morales et al., 2013; Ono et al., 2014; Moreno-Gonzalez et al., 2017). Multiple protofilaments can

associate to form a final mature amyloid fibril, and it is these amyloid fibrils that form the cores of amyloid plaques present in the brains of AD patients (Tycko, 2014; Iadanza et al., 2018).

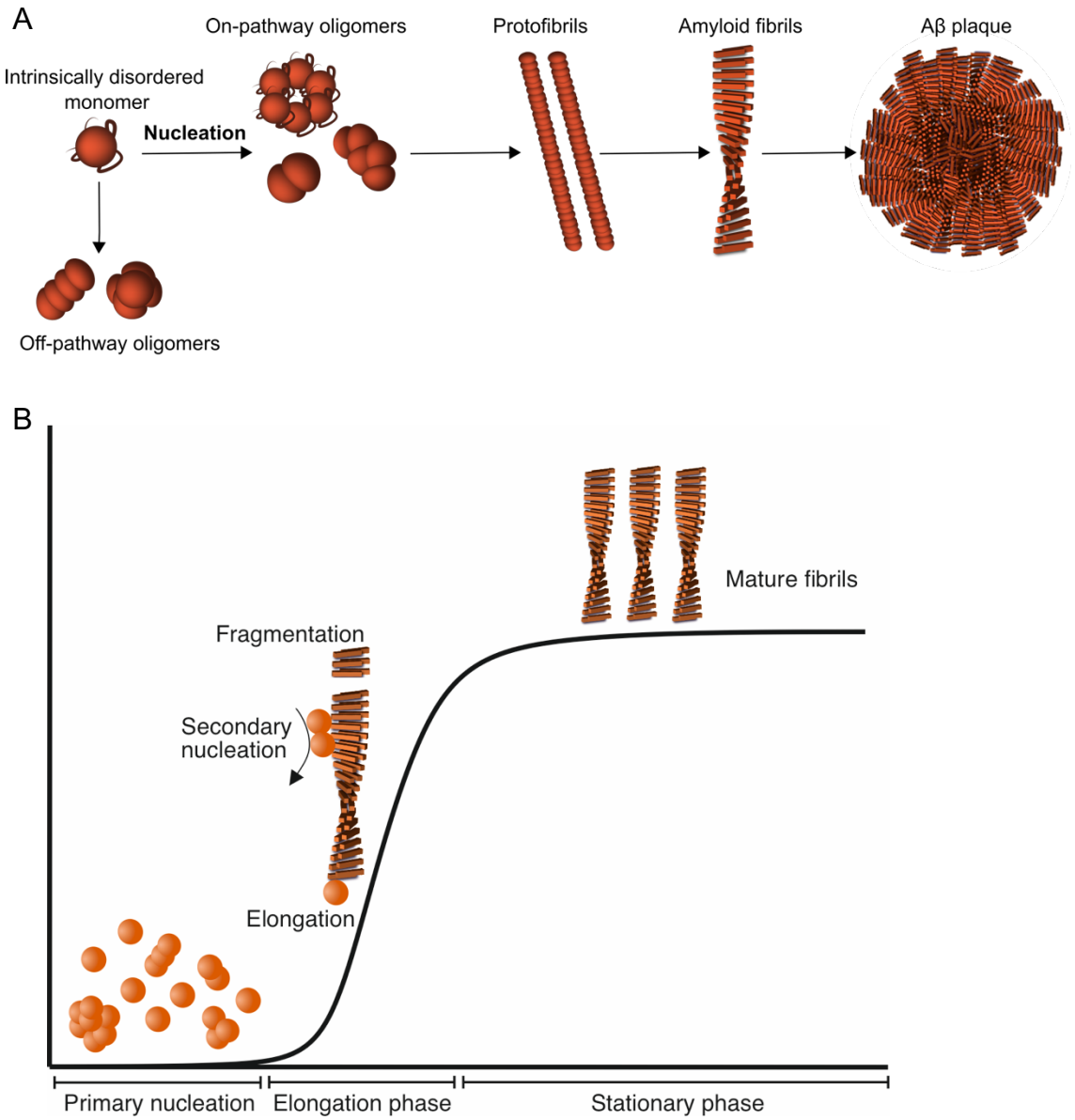

Figure 1.6. The pathway and mechanism of β-amyloid fibril formation
(A) The pathway of amyloid aggregation. (B) Mechanisms of amyloid fibril formation. Monomeric intrinsically disordered peptides self-associate to form nuclei in the early stages of amyloid fibril formation (Primary nucleation). Addition of peptides onto the nucleus results in the formation of an array of oligomeric intermediates. On-pathway oligomers go on to form protofibrils, which assoicate to form mature amyloid fibrils. It is these fibrils that make up the cores of Aβ plaques observed in the brains of AD patients. Monomeric peptide can elongate fibrils by adding directy onto fibril ends (Elongation phase). The fragmentation of fibrils results in more fibril ends on which elongation can occur. Monomers can also use the surface of existing fibrils to catalyse the formation of new fibrils and this is referred to as secondary nucleation. Multiple protofilaments can come together to form mature amyloid fibrils (Stationary phase).

This specific cross-β packing structure of amyloid fibrils results in distinct tinctorial properties, which allow the growth of amyloid fibrils to be monitored, and the presence of fibrils to be confirmed and measured. A number of dyes can be used for this including

Thioflavin T (ThT), Thioflavin S (ThS), congo red and luminescent-conjugated oligothiophenes (LCOs). ThT binds to the β-sheet structure of amyloid fibrils, and this sterically locks the dye by immobilising rotation of the molecule about the carbon-carbon bond between benzylamine and benzathiole rings. This immobilisation maintains the molecule in a more excited state, resulting in higher fluorescence (Biancalana and Koide, 2010). These dyes have been adapted for diagnostic use in amyloid diseases, for example ^{11}C-Pittsburgh compound B is a radioactive homolog of ThT that can be used in positron emission tomography (PET) scans to image Aβ load in patient brains.

1.2.3 Amyloid fibrils in disease

Protein misfolding into amyloid fibrils has been associated with more than 50 human diseases (Iadanza et al., 2018). This includes a number of the most common neurodegenerative diseases, including AD in which Aβ and tau both form amyloid structures. In Parkinson's disease (PD), α-synuclein aggregates to form amyloid fibrils that are the principal component of intraneuronal inclusions known as Lewy bodies. Huntington's disease is also associated with a polyglutamine expansion in the Huntingtin protein resulting in amyloid formation in affected neurons (Iadanza et al., 2018). A number of other neurodegenerative diseases are associated with amyloid deposits; superoxide dismutase (SOD) and TDP-43 are known to form amyloid aggregates in amyotrophic lateral sclerosis (ALS), and the aggregation of tau is observed in other tauopathies such as corticobasal degeneration (CBD) and frontotemporal degeneration (FTD).

Amyloidoses can also be systemic, affecting a range of tissues in the body (Iadanza et al., 2018). This includes amyloid light chain amyloidosis, in which the light chains of antibodies form amyloid deposits in cardiac and kidney tissue, and dialysis-related amyloidosis, in which β_2-microglobulin (β_2m), a component of the MHC class I complex, deposits as amyloid plaques in the joints (Koch, 1992). In addition, the aggregation of islet amyloid polypeptide (IAPP) in the islets of Langerhans is observed in type II diabetes (Westermark et al., 2011). More than one amyloid protein can also be found in a disease, with ~60% of AD patients found to also possess Lewy body pathology consisting of aggregated α-synuclein protein (Hamilton, 2000). With amyloid proteins implicated in numerous and devastating diseases, research into the role that the amyloid structure has to play in disease is imperative.

1.2.4 The role of Aβ in Alzheimer's disease

The amyloid cascade hypothesis of AD proposes that Aβ accumulation in the brain is the primary initiating event in AD pathogenesis, triggering the formation of tau tangles, neuroinflammation and ultimately neuronal death, resulting in disease. This is proposed to be due to an imbalance in the production and clearance of Aβ in the brain. There is strong evidence for this theory; all dominant mutations known to cause early-onset AD occur in APP or PSEN1/2, catalytic components of γ-secretase which cleaves APP to form Aβ (Figure 1.3) (Rogaev et al., 1995). Furthermore, these familial mutations principally result in the increased production of $A\beta_{42}$, the more aggregation-prone form of the peptide, directly implicating the aggregation of Aβ in disease. A key mutation identified in APP that links Aβ to the development of AD is A673T (A2T in the Aβ sequence), which has been shown to be protective against AD (Figure 1.4) (Jonsson et al., 2012). This mutation, located very closely to the β-secretase site of cleavage, was found to lower Aβ production, and protects against the development of AD and age-related cognitive decline (Jonsson et al., 2012). There is also evidence that Aβ deposition is significantly higher in carriers of dominant AD mutations compared to non-carriers from 19 years before expected disease onset, followed by metabolic decline and brain atrophy (Gordon et al., 2018). This suggests that Aβ could be an early triggering event of AD, occurring before other pathology.

In addition, an association between Down's syndrome and AD provides evidence for the involvement of Aβ in disease (Wiseman et al., 2015). Down's syndrome is a disorder that results from trisomy of chromosome 21, and patients have a striking increased susceptibility to developing early-onset AD. Aβ and tau pathology is consistently evident in Down's syndrome patient brains by the age of 40, and dementia symptoms develop in two thirds of patients over the age of 55 (Olson and Shaw, 1969; Zigman and Lott, 2007; Rubenstein et al., 2020). The APP gene is located on chromosome 21, therefore suggesting that the increased propensity of Down's syndrome patients to develop AD is due to the overexpression of APP in these individuals, thus resulting in overproduction of Aβ. Further to this theory, it was found that rare individuals who have small duplications in chromosome 21 that includes the APP gene (Dup-APP) develop AD, but individuals with duplications of parts of chromosome 21 excluding the APP gene do not (Rovelet-Lecrux et al., 2006; Sleegers et al., 2006; Korbel et al., 2009).

However, whilst Aβ clearly has a role to play in AD, the amyloid cascade hypothesis has since been criticized for being too simplistic and linear, based on a number of disparities (Herrup, 2015). For example, there is not a clear correlation between Aβ burden and the level of cognitive decline in patients (Nelson et al., 2012). Up to 40% of non-demented

elderly meet the criteria for AD in terms of brain pathology, and 10-30% of cognitively normal individuals have Aβ plaques, as shown by amyloid-PET scans (Knopman et al., 2003; Price et al., 2009; Chételat et al., 2013).

However, this lack of correlation could be explained by heterogeneity of the Aβ deposits themselves. In AD, Aβ oligomers have been implicated as important agents of toxicity, while Aβ fibrils have been shown to be less toxic in comparison (Hardy and Selkoe, 2002; Sengupta et al., 2016). Pools of soluble Aβ oligomers have been identified in the brains and CSF of AD patients and shown to have toxic effects towards neurons (Lambert et al., 1998; Hartley et al., 1999; McLean et al., 1999). Furthermore, the injection of Aβ oligomers in the absence of monomeric or fibrillar material was found to inhibit long-term potentiation (LTP) in rats, indicating that these species can lead to synaptic dysfunction (Walsh et al., 2002). A number of mechanisms of oligomer toxicity have been proposed, including receptor-mediated toxicity, association and perturbation of the cell membrane, and the generation of 'pore'-like structures (Kayed and Lasagna-Reeves, 2013; Serra-Batiste et al., 2016). However, the presence of mixtures of Aβ species makes it difficult to determine an exact oligomeric structure that is responsible for toxicity.

Despite oligomers being more implicated in toxicity than fibrils, there is also evidence that Aβ fibrils have several critical roles in AD pathogenesis. Firstly, it has been shown that various different amyloid fibrils interact with and perturb biological membranes (Tipping et al., 2015b). For Aβ, there is evidence that fibril interaction with biological lipids leads to the destabilisation and resolubilisation of mature amyloid fibrils, resulting in their conversion to a toxic species that was found to cause memory impairment in mice (Martins et al., 2008). Although molecular shedding of fibrils resulting in the formation of oligomeric species is slow, this could still be a relevant contributor to disease (Martins et al., 2008; Tipping et al., 2015a). There is evidence that the extent of this phenomenon is increased by changes in pH, therefore the reduction in pH encountered by fibrils when internalised by cells and trafficked via the endolysosomal pathway could result in the increased production of toxic oligomeric species (Goodchild et al., 2014; Tipping et al., 2015a).

Furthermore, a key study identified that senile plaques in an AD mouse model are surrounded by a 'halo' of oligomeric Aβ (Koffie et al., 2009). A 60% reduction in excitatory synapses was measured within this halo, and synapse density was shown to increase back to normal as distance from the plaque increased (Koffie et al., 2009). This evidence suggests that Aβ plaques, formed from a dense-core of Aβ fibrils, sequester oligomeric forms of Aβ which in turn lead to synapse loss. Furthermore, there is increasing evidence

that amyloid aggregates sequester proteins essential for cellular proteostasis, therefore destabilising this proteostasis network (Olzscha et al., 2011; Park et al., 2013).

Importantly, Aβ fibrils have been shown to activate microglial cells in the brain, therefore contributing to the widespread neuroinflammation that is observed in AD (Heneka et al., 2015a). Aβ fibrils have been shown to bind to and activate receptors on the cell surface of microglial cells including Toll-like receptors (TLRs) and scavenger receptors, resulting in the release of an array of pro-inflammatory cytokines (discussed in Section 1.4.3). Chronic exposure to Aβ pathology in the brain therefore results in a neurotoxic environment, contributing to neurodegeneration (Section 1.4.4). Together this evidence suggests that amyloid fibrils could be contributing to disease pathology through a number of processes and should not be treated as inert end-stage products of aggregation.

A lack of correlation between Aβ load and clinical severity of disease could also be explained by differences in the structure of the Aβ plaques that form. Dense-core neuritic plaques were recently shown to be more associated with changes in proteome solubility in mouse models of AD, whereas mouse models that formed diffuse plaques had few proteins that showed altered solubility (Xu et al., 2020). Plaques in AD brains have also been found to be more effective at sequestering Aβ oligomers than those in high-pathology controls, suggesting differences in their structure (Esparza et al., 2013). It is therefore possible that it is differences in the structure of Aβ plaques, and the proteins and cells that consequently interact with them, that confer varying levels of toxicity within the brain. Research into the molecular structure of Aβ fibrils and the identification of polymorphism could therefore be pivotal in understanding the role that Aβ has to play in AD. Critics of the amyloid cascade hypothesis suggest that research and therapeutic strategies should be redirected away from Aβ and towards targeting neuroinflammation (Makin, 2018). However, there is a clear interplay between these two disease hallmarks, and understanding this relationship is likely to be central in the progression of AD research (Leng and Edison, 2021).

1.2.5 The prion-like nature of Aβ

An important feature of Aβ fibrils is their ability to self-propagate, by the recruitment of Aβ monomers and their incorporation into amyloid structure in order to amplify and spread Aβ pathology throughout the brain (Meyer-Luehmann et al., 2006). *In vitro*, the addition of fibril ‘seeds’, short fibril fragments, to Aβ monomer removes the lag phase observed in Aβ aggregation kinetics, as elongation occurs by the addition of monomer to the ends of these seeds (Knowles et al., 2014). This seeding phenomenon has been demonstrated *in vivo* by inoculation experiments in which Aβ fibril-containing brain

homogenate is injected into the brains of transgenic AD mice models (Meyer-Luehmann et al., 2006; Langer et al., 2011; Stöhr et al., 2012). This was found to induce amyloidogenesis in the host, with the phenotype of amyloid deposition and spread depending not only on the host, but also on the source of the injected Aβ, suggesting the existence of polymorphic Aβ 'strains' that have distinct biological capabilities (Meyer-Luehmann et al., 2006; Langer et al., 2011; Stöhr et al., 2012).

This concept of Aβ strains is comparable to that of mammalian prion diseases such as Creutzfeldt-Jakob disease (CJD) in humans, and scrapie in sheep and goats. These diseases are a result of a misfolded conformer (PrP^{Sc}) of the host-expressed cellular protein PrP, which forms amyloid fibrils and self-propagates by inducing cellular PrP to misfold in the same way (Aguzzi and Polymenidou, 2004). Strains of PrP^{Sc} are associated with distinct phenotypes of disease, with differences in incubation time and the distribution and spread of pathology, and it has been found that these different prion strains exist as different structural conformations of PrP^{Sc} (Bessen et al., 1995; Telling et al., 1996; Safar et al., 1998). This link between structural conformation and phenotype also exists in yeast prions (Toyama et al., 2007). This raises the possibility that Aβ fibrils could also exist in different conformations, with different molecular structures that infer different biological properties, resulting in different clinical phenotypes in AD patients.

There is also some evidence that purified Aβ fibrils produced *in vitro* are sufficient to induce Aβ deposition, and that different synthetic fibril structures result in different patterns of this Aβ deposition (Stöhr et al., 2012, 2014). However, these fibrils were much less efficient in seeding compared to *in vivo* preparations, suggesting that co-factors present in the brain may be involved in propagation (Stöhr et al., 2012, 2014).

1.3 Amyloid fibril polymorphism

While all amyloid fibrils share a characteristic cross-β structure (Figure 1.5), polymorphism refers to differences in the molecular structure of the peptide within this cross-β subunit, and also the different number and arrangement of these cross-β subunits to make up a mature fibril (Tycko, 2015).

Polymorphism is now known to be a feature of a number of amyloid fibrils found in disease (Tycko, 2015). For example, cryo-electron microscopy (EM) analysis of tau fibrils revealed that fibrils observed to have paired helical and straight morphologies are formed by identical subunits, but in an alternative arrangement with different interactions between them (Fitzpatrick et al., 2017). A number of polymorphs have also been described for α-synuclein fibrils (Heise et al., 2005; Bousset et al., 2013; Gath et al., 2014; Tuttle et al., 2016; Fitzpatrick et al., 2017; Guerrero-Ferreira et al., 2018, 2019; Li

et al., 2018b). These polymorphs include two structures in which the same 'kernal' shaped subunit is packed differently, differing in protofilament interface interactions and resulting in distinctive fibril morphologies termed as 'rod' and 'twister' (Li et al., 2018a). Further analysis also suggests that mutations in α-synuclein that are associated with early-onset PD would lead to fibril structures that are distinct from wild-type fibrils (Li et al., 2018b). The evidence for polymorphism in Aβ fibrils *in vitro* and in AD patient brains and the significance of this will be discussed in more detail.

1.3.1 Aβ fibril polymorphism *in vitro*

Using primarily solid-state NMR (ssNMR) and cryo-EM, a number of structural models have been proposed for *in vitro* formed Aβ fibrils. This has revealed that subtle changes made to $A\beta_{40}$ fibril growth conditions can result in the formation of fibrils with distinct structures (Petkova et al., 2005). In one study, Aβ monomer was incubated either quiescently or with gentle circular agitation, and the resulting fibrils were analysed by transmission electron microscopy (TEM) and ssNMR. TEM measurements identified differences in morphology, but also differences in the structures of the Aβ fibrils at a molecular level.

2D ssNMR spectra for the two populations of fibrils showed significant differences in the cross-peak patterns produced (Petkova et al., 2005). These distinct spectra were also preserved in daughter and granddaughter fibrils produced by seeding (Petkova et al., 2005). This is comparable to prion strains and indicates that the different polymorphs are capable of recruiting monomeric Aβ structure and inducing it to adopt a specific molecular structure dependent on the structure of the seed. A molecular model was constructed for the fibrils produced under agitated conditions, based on constraints on internal and external quaternary contacts from ssNMR measurements (Petkova et al., 2006). This model comprises two molecular layers each made up of 2 β-strands (residues 10-22 and 30-40) separated by a 180˚ bend and form two in-register parallel β-sheets (Petkova et al., 2006). Residues 1-8 were not present in the resolved structure and this N-terminal region was considered to be structurally disordered (Petkova et al., 2006). This model proposes that most sidechain-sidechain interactions between the two β-sheets are hydrophobic or neutral, apart from a salt bridge formed between D23 and K28 (Petkova et al., 2005, 2006). Mass per length (MPL) values from TEM measurements indicate that these fibrils consist of two protofilaments (Petkova et al., 2005, 2006). This fibril structure will henceforth be referred to as the '2A', based on its 2-fold symmetry and growth under agitated conditions (Figure 1.7).

In subsequent experiments, fibrils were formed quiescently with occasional sonication for 9 days (Paravastu et al., 2008). Initially various fibril morphologies were exhibited, but

12 rounds of seeding resulted in a morphologically homogeneous population of fibrils. TEM was used to produce MPL values which indicate that the fibrils are made up of three molecular subunits, rather than the previously described two (Paravastu et al., 2008). 2D ^{13}C ssNMR spectra largely show a single set of ^{13}C chemical shifts, indicating a common structure of the fibrils. When combined with the MPL measurements, this ssNMR data indicates a molecular structure with 3-fold symmetry about the fibril growth axis (Paravastu et al., 2008). These fibrils are therefore termed '3Q' based on their 3-fold symmetry and formation under quiescent conditions (Figure 1.7). Both models describe nearly identical β-strand segments that form in-register parallel β-sheets, however there are differences between the structures in the conformation of the non-β-strand segments and some quaternary contacts (Petkova et al., 2005; Paravastu et al., 2008). Structural models of $A\beta_{40}$ fibrils are shown in Figure 1.7, and structural features of the fibrils are summarised in Table 1.1.

In addition to differences in structure formed from the same amino acid sequence, changes in the Aβ sequence can also lead to structural differences in the amyloid fibrils that form (Tomiyama et al., 2008; Tycko et al., 2009; Ovchinnikova et al., 2011; Schütz et al., 2015; Xiao et al., 2015; Wälti et al., 2016; Gremer et al., 2017). This is shown by structural determination of $A\beta_{42}$ fibrils, in which the resulting model is a 'double-horseshoe' structure with three β-strands per subunit rather than the two previously described for $A\beta_{40}$ (Xiao et al., 2015). These fibrils were not capable of cross-seeding $A\beta_{40}$ monomers, suggesting that $A\beta_{40}$ is not compatible with this triple β-sheet structure (Xiao et al., 2015). This is suggested to be due to Ala42 forming a salt-bridge with Lys28. As this C-terminal residue is not present in $A\beta_{40}$ this interaction is not possible, rendering $A\beta_{40}$ incapable of adopting this same molecular structure. This double-horseshoe structure was reproduced in later studies of $A\beta_{42}$ structure using similar but slightly altered conditions, however this structure showed two subunits per fibril rather than one, and there were some differences in side-chain packing (Figure 1.7) (Colvin et al., 2016).

Evidence for $A\beta_{42}$ polymorphism comes from the recent determination of the structure of $A\beta_{42}$ fibrils grown under distinct conditions; at pH 2 in 0.1% trifluoroacetic acid (TFA), using cryo-EM, ssNMR and x-ray diffraction (Gremer et al., 2017). Whilst these fibrils were shown to consist of two twisted protofilaments with a parallel in-register cross-β structure, the structure was strikingly different to that previously described for $A\beta_{42}$ (Gremer et al., 2017). The fibrils were described to have an 'LS-shaped structure' (shown in Figure 1.7 - $A\beta_{42}$ pH 2 structure). Fibrils were identified to possess 2_1 screw symmetry rather than C_2 symmetry, meaning that subunits within the fibril are staggered and interactions between them are therefore not truly dimeric. Another key difference in the structures is that the N-terminus forms part of the cross-β structure, whereas residues 1-

14 are thought to be disordered in fibrils formed at pH 8. The structural data suggests salt bridges between D1 and L28, D7 and N5, and E11 and H6/H13, with E11 salt bridges thought to stabilise the N-terminal turn. Three hydrophobic clusters were found to stabilize the subunit conformation of the pH 2 $A\beta_{42}$ fibrils: A2, V36, F4 and L34; L17, I31, and F19; and A30, I32, M35, and V40. *Gremer et al,* suggested that the A2T mutation, known to be protective in AD, could disrupt this hydrophobic cluster thus destabilising the fibrils, whereas the damaging A2V mutation would further stabilise this hydrophobic cluster therefore stabilising the fibrils (Figure 1.4) (Gremer et al., 2017). Other differences in this structure compared to previous $A\beta_{42}$ structures include differences in the dimer interface and turn-region residues 20-25. These residues are of note as it is in this section of the Aβ sequence that a number of pathogenic familial mutations associated with AD are located (Figure 1.4). This structure provides the first evidence of clear polymorphism in fibrils formed from $A\beta_{42}$, the more disease relevant form of Aβ. Whilst these fibrils were formed at very low pH, meaning that their physiological relevance is questionable, they still demonstrate the possibility of $A\beta_{42}$ fibril polymorphism resulting from altered growth conditions, which could be reflected in fibrils formed in different brain environments, and in different patients. Structural features of these two $A\beta_{42}$ fibril polymorphs are summarised in Table 1.3.

Further *in vitro* formed fibril structures that have been studied include fibrils formed from Aβ peptide harbouring relevant familial mutations which have been found to be associated with AD (Figure 1.4). The Japanese familial Osaka mutation (E22Δ) is associated with early-onset AD, and fibrils formed from $A\beta_{40}$ with this deletion were found to possess a distinct structure to those previously described for wild type peptide (Figure 1.7) (Ovchinnikova et al., 2011; Schütz et al., 2015). Key differences identified between this structure and the wildtype $A\beta_{40}$ fibril structure is a salt bridge between Glu3 and Lys28, an exclusively hydrophobic centre and a structured N-terminus (Table 1.2) (Schütz et al., 2015). In addition, salt bridge interactions were identified between four charged residues (V40, E11, H13, H6), similar to interactions observed in pH 2 $A\beta_{42}$ fibrils (Schütz et al., 2015; Gremer et al., 2017). In the mouse sequence of $A\beta_{42}$, H13 is replaced with an arginine, possibly preventing the stabilisation of this turn region, which could be linked to why mice do not naturally develop AD (Yamada et al., 1987). E22Δ Aβ peptide has been shown to be more neurotoxic in rat primary neuron cultures than wild-type $A\beta_{40}$, and aggregate more readily into fibrillary bundles (Ovchinnikova et al., 2011).

Another familial mutation in the Aβ peptide is D23N, known at the Iowa mutation, and is associated with early onset AD and cerebral amyloid angiopathy (CAA) (Grabowski et al., 2001). When fibrils were formed from $A\beta_{40}$ peptide with this mutation and examined

using EM, multiple different fibril morphologies were observed, and ssNMR measurements also indicate molecular polymorphism at a molecular level (Tycko et al., 2009). Furthermore, it was found that the majority of these fibrils contain antiparallel β-sheets, rather than the parallel in-register β-sheets reported for all other Aβ fibril structures (Table 1.2) (Tycko et al., 2009; Qiang et al., 2012). This unique feature of D23N fibrils could therefore have distinct effects in the brain, which could help to explain the pathological effects of this mutation. A series of seeding and filtration steps were used to produce a homogenous population of Iowa fibrils, all containing antiparallel β-sheets, and ssNMR and EM measurements were used to produce a structural model for these fibrils (Figure 1.7) (Qiang et al., 2012). This structure indicates a 'U-shaped' conformation of peptide with 2 β-strands, similar to 2A and 3Q fibrils (Qiang et al., 2012). Residues 1-14 were suggested to be disordered in the $A\beta_{40}$ Iowa fibrils, similar to $A\beta_{42}$ fibrils formed at pH 8, however residues 37-40 were also not included in the fibril structure of Iowa fibrils (Table 1.2) (Qiang et al., 2012; Wälti et al., 2016).

A number of post-translational modifications have been identified in Aβ fibrils that make up the Aβ plaques in the brains of AD patients (Kummer and Heneka, 2014). This includes fibrils made from peptide with an N-terminal phosphorylation at Serine-8 (pS8-$A\beta_{40}$) (Kumar et al., 2013; Rijal Upadhaya et al., 2014). The structure of fibrils formed from peptide with this phosphorylation were recently analysed using ssNMR (Figure 1.7) (Hu et al., 2019). Conditions used to generate the fibrils were similar to those used to form 2A fibrils from wild-type peptide; pH 7.4, 37°C with continuous gentle agitation, followed by generation seeding (Hu et al., 2019). The fibrils do share some structural features with 2A fibrils, including a striated morphology and 2-fold symmetry, however the fibrils were found to have a higher thermodynamic stability and possess a 5x higher seeding efficiency (Table 1.1) (Petkova et al., 2005; Hu et al., 2019). This higher seeding efficiency means that this fibril polymorph has the potential to be more dominant than other structures. Whilst residues 1-7 of the pS8-$A\beta_{40}$ fibrils were found to be disordered, strong intrastrand interactions were identified between the N-terminus and the fibril core, for example between pS9 and V24-G25. *Hu et al* proposed that these interactions could mean that the N-terminus is involved in the initial aggregation of these fibrils, helping to explain their higher seeding propensity compared to 2A fibrils which have a more dynamic N-terminus (Hu et al., 2019).

Limited comparisons have been made of the biological properties of these different Aβ fibril polymorphs, however it was reported that the pS8-$A\beta_{40}$ fibrils described above were more toxic towards neuronal and microglial cell lines than wild-type $A\beta_{40}$ fibrils (Hu et al., 2017). In addition, 3Q $A\beta_{40}$ fibrils were found to be more toxic towards primary rat neurons than 2A $A\beta_{40}$ fibrils when tested from 10-75 μM, further suggesting that structure

could confer differences in toxicity (Petkova et al., 2005). It has also been shown that heparin has a higher binding affinity for 3Q $A\beta_{40}$ fibrils than 2A $A\beta_{40}$ fibrils (Stewart et al., 2016). This suggests that differences in fibril structure present differences in binding sites for glycosaminoglycans (GAGs), which are found in Aβ plaques in the brain and can alter fibril resistance to proteolytic degradation (Valle-Delgado et al., 2010). This suggests that different fibrils may interact with other molecules to differing extents based on their structure, which would impact on their biological properties.

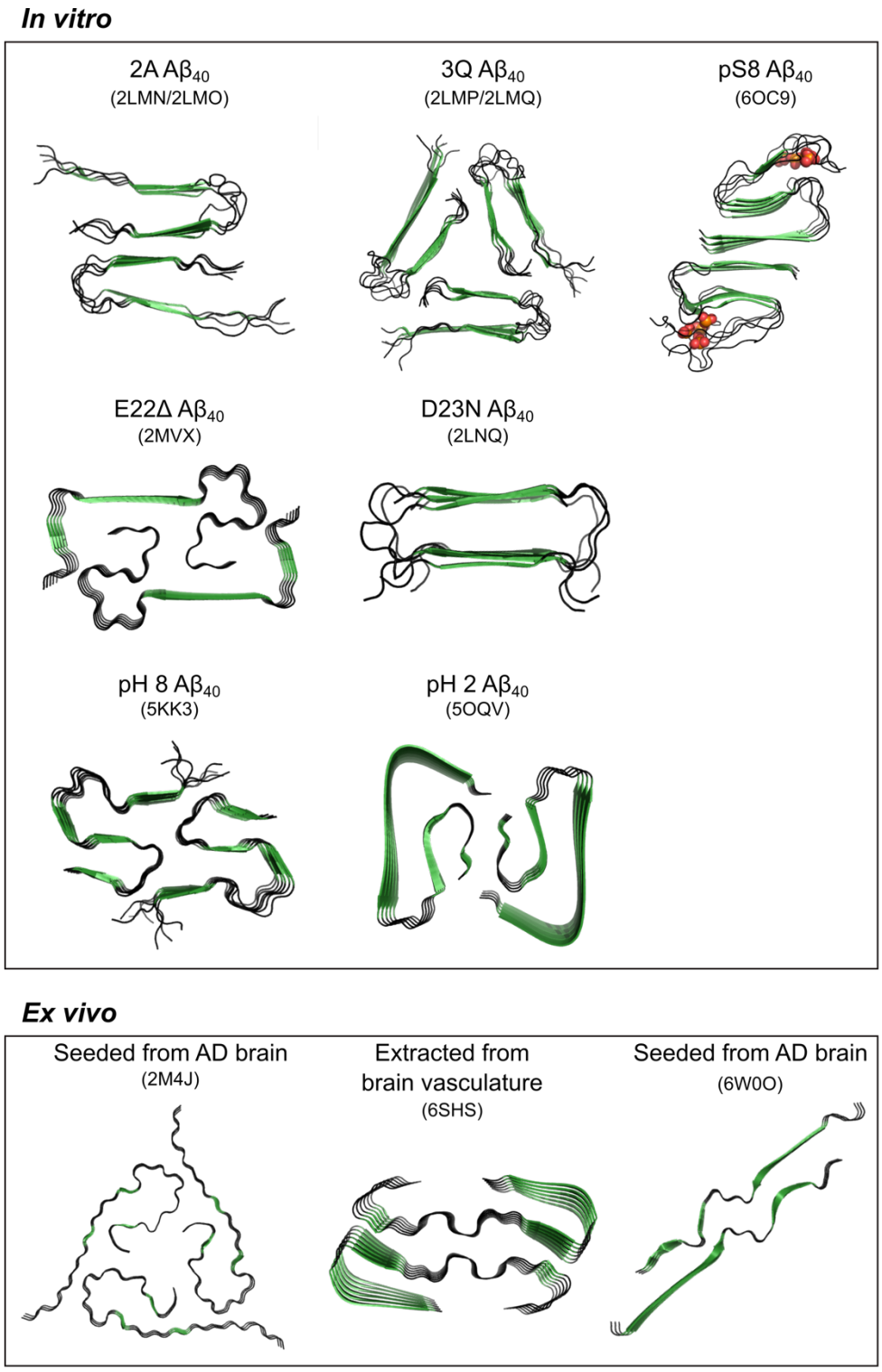

Figure 1.7. Molecular structures of Aβ fibril polymorphs
Schematics of molecular structural models of Aβ fibril polymorphs. Structures are shown for $A\beta_{40}$ fibrils, mutant $A\beta_{40}$ fibrils and $A\beta_{42}$ fibrils formed *in vitro*, and $A\beta_{40}$ fibrils generated from *ex vivo* material. PDB's are stated below structure names, green areas are representative of β-sheet structure and black areas are representative of loop regions.

	Aβ40		
Structure	**2A** (Petkova et al, 2005)	**3Q** (Paravastu et al, 2008)	**pS8-Aβ40** (Hu et al, 2019)
PDB	2LMN/2LMO	2LMP/2LMQ	6OC9
Growth conditions	Incubation of $A\beta_{1-40}$ in 10 mM sodium phosphate buffer, 0.01% NaN_3, pH 7.4 for 21 to 68 days in horizontal polypropylene tubes with gentle circular agitation at room temperature	Incubation of purified monomer in 10 mM sodium phosphate buffer, 0.01% NaN3, pH 7.4, in a bath sonicator with occasional sonication for 9 days at room temperature	Synthetic peptide, pH 7.4, 37°C with continuous gentle agitation followed by generation seeding
Method of structural analysis	Solid-state NMR	Solid-state NMR	Solid-state NMR
Morphology	Striated ribbon	Periodic twist	Striated
Number of protofilaments	2	3	2
Fold	Hairpin	Hairpin	-
Symmetry	2-fold	3-fold	2-fold
N-terminus	Residues 1-8 disordered, residues 9-15 not involved in fibril core but are highly dynamic	Disordered	Residues 1-7 disordered, strong intra-strand interactions between N-terminus and rest of amyloid core. N-terminus may participate in initial aggregation to form protofibrils
Number of cross-β sheets per peptide (residues)	2(12-24, 30-39)	2(11-22, 30-39)	3 (9-12, 17-22, 31-39)
Parallel cross-β sheets	Parallel in-register	Parallel in-register	Parallel in-register
Notable salt bridges	D23-K28	-	-
Notable interactions between residues	Close contacts between F19 and L34 sidechains	Close contacts between F19 and L34 sidechains	Intermolecular interactions between β2 and β3 strands

Table 1.1. Structural details of *in vitro* generated Aβ40 fibrils

	E22Δ $A\beta_{40}$	D23N $A\beta_{40}$
Structure	**Osaka** (Schütz et al, 2015)	**Iowa** (Qiang et al, 2012)
PDB	2MVX	2LNQ
Growth conditions	80 min incubation in 10 mM NaH_2PO_4-NaOH, 100 mM NaCl, pH 7.4, 700 rpm magnetic stirring at 37°C	Parent fibrils were obtained by quiescent incubation of monomer at 6 °C for 7 days in 10 mM sodium phosphate, pH 7.4, 0.01% NaN_3. Homogenous population obtained by a seeding and filtration protocol
Method of structural analysis	Solid-state NMR	Solid-state NMR
Morphology	-	Heterogeneous morphologies
Number of protofilaments	2	1
Fold	Cinnamon roll	U-shaped
Symmetry	2-fold	-
N-terminus	Ordered	Residues 1-14 disordered
Number of cross-β sheets per peptide (residues)	5 (4-8, 10-19, 26-28, 30-32, 34-36)	2 (17-21, 31-35)
Parallel cross-β sheets	Parallel in-register	Antiparallel
Notable salt bridges	E11 salt bridge stabilises N-terminal kink, K28-E3 salt bridge between subunits	Absence of K16-E22 bridge
Notable interactions between residues	-	Side chains of L17, F19, A21, A30, I32, L34 and V36 create a purely hydrophobic core

Table 1.2. Structural details of *in vitro* generated mutant $A\beta_{40}$ fibrils

	$A\beta_{42}$	
Structure	**pH 2** (Gremer et al, 2017)	**pH 8** (Colvin et al, 2016)
PDB	5OQV	5KK3
Growth conditions	Undisturbed incubation for several weeks in 30% v/v acetonitrile (ACN), 0.1% (v/v) trifluoroacetic acid (TFA) in water at room temperature	10−50 μM (0.05−0.25 mg/mL) solutions of recombinant $A\beta_{42}$ monomer in 20 mM sodium phosphate, 0.2 mM EDTA, 0.02% NaN_3, pH 8.0, incubated in 15 mL falcon tubes at room temperature overnight
Method of structural analysis	Cryo-EM	Solid-state NMR (magic angle spinning NMR)
Morphology	Twist	Twist
Number of protofilaments	2 - subunits arranged in staggered manner therefore not true dimeric interactions	2
Fold	LS-shaped	S-shaped
Symmetry	2_1 screw symmetry (rise of 4.67Å)	2-fold
N-terminus	Ordered and part of cross-β structure	Residues 1-14 dynamic
Number of cross-β sheets per peptide (residues)	2 (1-9, 11-21)	4 (16-20, 26-32, 35-36, 39-41)
Parallel cross-β sheets	Parallel in-register	Parallel in-register
Notable salt bridges	D1-L28; D7-N5; E11-H6-H13. E11 salt bridge stabilises N-terminal kink	A42-K28
Notable interactions between residues	Three hydrophobic clusters stabilize the subunit conformation: A2,V36, F4 and L34;L17, I31, and F19; and A30, I32, M35, and V40.	Contacts between I41−G29, I41−K28, F19−I32, F20−V24, and F19−A30 form two hydrophobic pockets that stabilise the S-shaped structure

Table 1.3. Structural details of *in vitro* generated $A\beta_{42}$ fibrils

1.3.2 Aβ fibril polymorphism *in vivo*

Importantly, there is also evidence for Aβ polymorphism in AD patients brains (Lu et al., 2013; Qiang et al., 2017). Brain extracts from two patients with distinct AD presentations were used to seed $A\beta_{40}$ fibril growth and the structures of the resulting fibrils analysed by ssNMR (Lu et al., 2013). Patient I had a tentative diagnosis of Lewy body dementia and autopsy revealed neuritic Aβ plaques, but only mild atrophy and few Lewy bodies. Patient II however had a diagnosis of probable AD, and autopsy revealed severe pathology with gross atrophy (Lu et al., 2013). SsNMR spectra showed sharp cross-peak signals in both patients indicative of a single dominant fibril structure, however these spectra were distinct from each other (Lu et al., 2013). This suggests that distinct Aβ polymorphs could be associated with variations in AD.

A structural model was created for patient I fibrils (Figure 1.7) (Lu et al., 2013). A key difference in this *ex vivo* structure is that there are strong NMR signals for N-terminal residues, indicative of this region being part of the ordered structure. There was evidence of a D23-K28 salt bridge as observed in 2A fibrils, however MPL values indicate a 3-fold symmetry similar to 3Q fibrils (Lu et al., 2013). Distinct features of this fibril structure include a kink at residue G33 that results in I32 and L34 sidechains being oriented in opposite directions, therefore able to make contacts with different $A\beta_{40}$ molecules (Lu et al., 2013). In addition, a twist in residues 19-23 means that the sidechains of F20 or E22 can be buried within the structure. These features result in an *ex vivo* structure that is more complex than the simple hairpin conformation of the 2A and 3Q $A\beta_{40}$ fibril structures (Table 1.4). The structure of these Aβ fibrils seeded from AD brain extract are therefore not directly comparable to any *in vitro* structures but do share some similar structural features.

More recently, cryo-EM was used to analyse the structure of $A\beta_{40}$ fibrils purified from the meninges of three AD patient brains (Kollmer et al., 2019). This analysis revealed that Aβ fibrils derived from patient brains are polymorphic. However, one polymorph termed ‘morphology I’ was more abundant relative to the others, and two other polymorphs ‘morphology II’ and ‘morphology III’ were also of high abundance (Kollmer et al., 2019). Together these three polymorphs made up 75% of fibril structures present in the samples. It was identified that these three polymorphs are made up of the same fundamental Aβ peptide conformation but vary in the number of subunits in each fibril, with morphology I consisting of 1 protofilament (PF), morphology II containing 2 PFs and morphology III containing 3 PFs (Figure 1.7). EM revealed that the fibrils have a twisted morphology, similar to fibrils formed *in vitro.* However, a key structural difference is the direction of this twist; the brain-derived fibrils have a right-handed twist whereas previous

in vitro formed fibrils were found to possess a left-handed twist (Petkova et al., 2005; Kollmer et al., 2019). The fibrils have a pseudo 2_1-screw symmetry, similar to $A\beta_{42}$ fibrils formed at pH 2 (Table 1.4). The structure of the peptide subunits within the fibril is described as 'C shaped', with N and C-termini forming arches and being more exposed, and the central peptide domain buried in the fibril core and forming the dimer interface (Kollmer et al., 2019). The N-terminus is ordered in this structure and the arch of the N-terminus is a unique feature of these fibrils. Most of the Aβ mutations associated with AD are located within this N-terminal arch (Figure 1.4). Four β-strands were identified, from residues 2-8, 10-13, 15-19 and 32-34, and the central contacts are residues 24-26, which is also a novel feature of these fibrils (Kollmer et al., 2019). The structure of these *ex vivo* brain-derived fibrils are distinct from those formed *in vitro*, likely reflecting the difference in growth conditions. However, the presence of different Aβ fibril polymorphs within AD brains raises the possibility of particular fibril structures being associated with pathology and clinical presentation of disease.

$A\beta_{40}$ is known to make up the majority of deposits in CAA, in which Aβ deposits form in the vasculature, in contrast to neuritic plaques in the AD brain which are predominantly formed from $A\beta_{42}$ (Charidimou et al., 2017). As the $A\beta_{40}$ fibrils in this research were extracted from the vasculature, their structure may be more representative of CAA Aβ fibrils rather than fibrils that make up the neuritic plaques in AD brains. It has been shown that subtle changes to growth conditions can alter the structure of the fibrils that form, therefore it is possible that different polymorphs arise from fibrils that form in blood vessels compared to those that form within other brain environments (Petkova et al., 2005; Paravastu et al., 2008; Venegas et al., 2017).

The molecular structure of an $A\beta_{40}$ fibril polymorph derived from cortical tissue of an AD patient was recently produced using a combination of cryo-EM, MPL measurements and ssNMR (Figure 1.7) (Ghosh et al., 2021). This structure is unique to all previously produced Aβ fibril structures. A perplexing feature of this structure is that MPL values are consistent with the presence of three Aβ subunits making up one fibril, however cryo-EM data indicates 2-fold symmetry (Ghosh et al., 2021). To account for this, a model was suggested in which $A\beta_{40}$ molecules are fully extended in inner layers, but the outer cross-β layers consist of Aβ molecules in β-hairpin conformations (Figure 1.7). The resulting structure is four-layered, with 2-fold screw symmetry about the fibril growth axis (Table 1.4) (Ghosh et al., 2021).

	Ex vivo $A\beta_{40}$		
Structure	**Brain derived patient I** (Lu et al, 2013)	**Meninges derived polymorph I** (Kollmer et al, 2019)	**AD patient brain derived** (Ghosh et al, 2021)
PDB	2M4J	6SHS	6W0O
Growth conditions	Seeded from brain extract	Extracted from 3 AD patients	Seeded from AD cortical tissue (parietal lobe/frontal lobe) from 2 patients
Method of structural analysis	Solid-state NMR	Cryo-EM	Cryo-EM, MPL and ssNMR
Morphology	Morphologically distinct from striated or ribbons - 'rod-like'	Right-handed twist	Left-handed twist
Number of protofilaments	3	1	3
Fold	-	C-shaped	4 layers - 2 inner layers are fully extended $A\beta_{40}$ molecules, outer layers are formed by $A\beta_{40}$ with β-hairpin conformations
Symmetry	3-fold	Pseudo 2_1 screw symmetry (Stacks offset by ~2.41 Å)	2_1 screw symmetry
N-terminus	Ordered	Ordered	Residues 1-9 disordered
Number of cross-β sheets per peptide (residues)	3 (12-13, ,18-19, 35-36)	4 (2-8, 10-13, 15-19, 32-34)	-
Parallel cross-β sheets	Parallel in-register	Parallel in-register	Parallel in-register
Notable salt bridges	D23-K28	E11-K16	D23–K28
Notable interactions between residues	Intermolecular contacts between the N terminus of one strand and the E22-A30 loop of adjacent strand	-	-

Table 1.4. Structural details of $A\beta_{40}$ fibril structures generated from *ex vivo* material

1.3.3 Association of amyloid fibril polymorphism with differences in the clinical presentation of disease

Expanding on initial evidence that different Aβ fibril polymorphs are present in different AD patient brains, a study was carried out in which brain extracts from three different subtypes of AD were used in Aβ seeding and the structures of the resulting fibrils compared (Qiang et al., 2017). This study used data collected from 37 cortical tissue samples, from a total of 18 individual brains. Typical AD (t-AD) was compared with two atypical forms of the disease – rapidly progressive AD (r-AD) and posterior cortical atrophy (PCA). A predominant $A\beta_{40}$ fibril structure was identified, which was common to all three AD subtypes. This structure accounted for 85% of $A\beta_{40}$ fibrils in PCA and t-AD, but only 65% in r-AD (Qiang et al., 2017). This indicates that there are a larger proportion of additional fibril structures in r-AD, which could be responsible for the rapid progression of AD in this form of the disease. Not only does this evidence support the notion of Aβ fibril polymorphism *in vivo*, it also suggests a clinical consequence of this, with different disease phenotypes being associated with different levels of Aβ fibril polymorphism in the brain.

Similar to this, distinct Aβ fibril conformations were identified in different AD subtypes when probed using LCOs (Rasmussen et al., 2017). LCOs bind to the repetitive cross-β structures of amyloid fibrils and display spectral differences based on the twisting of the flexible LCO backbone. The interaction of LCOs with different amyloid structures therefore imposes different rotational constraints on this backbone, leading to spectroscopic signatures that are indicative of these specific amyloid polymorphs. The resulting spectra of Aβ brain samples from familial AD patients, sporadic AD patients and patients with PCA were compared in this study. It was found that the spectra of these AD subtypes formed ‘clouds’ indicating distinct conformations (Rasmussen et al., 2017).

The association of different fibril morphologies with different disease phenotypes has been demonstrated for other amyloids. For example, the structure of tau fibrils in chronic traumatic encephalopathy (CTE), a tauopathy associated with repeated head impact, was recently found to be identical between three CTE patients, but is distinct from those in AD and Pick’s disease (Falcon et al., 2018b, 2018a, 2019). This shows that tau can adopt different conformations within the brain, depending on the disease.

Furthermore, α-synuclein forms Lewy bodies within neurons in AD and Dementia with Lewy bodies (DLB) but accumulates in oligodendrocytes as glial cytoplasmic inclusions in multiple system atrophy (MSA) (Goedert et al., 2017). It was found that the different cellular environments of neurons and oligodendrocytes result in the transformation of misfolded α-synuclein into different strains with distinct conformations and biological

properties (Peng et al., 2018). Analysis of the structural conformation of α-synuclein fibrils amplified from the brains of PD and MSA patient brains revealed polymorphism in the *ex vivo* fibrils (Strohäker et al., 2019). There was greater structural heterogeneity in fibrils derived from PD patients than those from MSA patients, perhaps indicative of the greater variability in disease phenotypes in PD. Different amyloid polymorphs being associated with differences in neuropathology and clinical features is comparable to prion strains and helps to explain how fibrils formed from the same protein can lead to a range of clinical phenotypes.

1.4 Neuroinflammation in Alzheimer's disease

Neuroinflammation has long been observed in mouse models of AD and in the brains of AD patients, characterised by the infiltration of immune cells such as microglia, and increased production of pro-inflammatory mediators (Itagaki et al., 1989; Frautschy et al., 1998; Simard et al., 2006). In addition to post-mortem analysis of AD brain tissue, developments in PET techniques have allowed the quantification of reactive microglia in the brain by targeting Translocator Protein 18kDa (TSPO), a marker of microglial activation (Gomez-Nicola and Boche, 2015; Knezevic and Mizrahi, 2018). This has further supported the increased presence of reactive microglia in AD patient brains compared to healthy controls, and TSPO binding has been found to correlate with the severity of disease (Kreisl et al., 2013). Furthermore, increased levels of inflammatory mediators including cytokines interleukin (IL)-1β, IL-6, IL-18 and tumour necrosis factor (TNF)-α, have been identified in AD brains (Griffin et al., 1989; Bauer et al., 1991; Ojala et al., 2009). This evidence for an inflammatory response in AD, alongside the identification of AD risk genes associated with innate immune functions suggests that rather than just a bystander of disease, this innate immune response contributes to the exacerbation and progression of the disease (Heneka et al., 2015b; McManus and Heneka, 2017). Further to this, Aβ may be a key trigger of this neuroinflammation, and the evidence for this will be discussed further (Ismail et al., 2020).

1.4.1 Insights from genetics

The most compelling evidence for the involvement of an immune response in AD comes from the study of AD genetics; a large number of genetic variants identified to be associated with AD are involved in the innate immune response and are highly expressed by microglial cells (Table 1.5). A number of these identified gene loci are in genes that encode proteins known to interact with Aβ, and particularly a number of proteins known to be involved in the clearance of Aβ (Table 1.5). Furthermore, analysis of gene regulatory networks in LOAD identified that immune and microglial molecular networks were most associated with LOAD (Zhang et al., 2013). This suggests that

immune cell dysfunction could play a key role in AD pathogenesis, and that targeting immune pathways could be a viable approach to the treatment of AD.

Gene locus	Associated protein	Functional information	Ref.
ABCA7	ATP-binding cassette sub-family A member 7	Involved in the phagocytosis of Aβ.	(Hollingworth et al., 2011)
ABI3	ABI gene family member 3	Highly expressed in microglia, suggested to play a role in interferon-mediated immune cell signalling and T-cell activation.	(Sims et al., 2017)
ADAM10	Disintegrin and metalloproteinase domain-containing protein 10	Cleaves TNF-α	(Mezyk-Kopeć et al., 2009; Jansen et al., 2019)
ApoE	Apolipoprotein E	Mainly expressed by astrocytes, involved in lipid transport. Binds to Aβ and involved in its clearance.	(Corder et al., 1993; LaDu et al., 1994)
CD33	Siglec-3-sialic acid binding Ig-like lectin 3	Expressed by myeloid cells and microglia, binds sialic acid-containing ligands to modulate immune cell functions, implicated in Aβ clearance.	(Hollingworth et al., 2011; Naj et al., 2011)
CLNK	Cytokine-dependent hematopoietic cell linker	An immune cell adaptor protein involved in the regulation of immunoreceptor signalling.	(Jansen et al., 2019)
CLU (APOJ)	Clusterin (Apolipoprotein J)	Stress-activated molecular chaperone, involved in lipid transport, modulates the complement system, interacts with Aβ.	(Harold et al., 2009; Lambert et al., 2009)
CR1	Complement receptor 1	Mediates cellular binding of immune complexes that activate the complement system.	(Lambert et al., 2009)
EPHA1	Ephrin type A receptor 1	Receptor tyrosine kinase - Involved in cell signalling in immunity and endocytosis. Expressed by T-cells and monocytes. Regulates neural development, angiogenesis, cell proliferation and BBB permeability.	(Hollingworth et al., 2011; Naj et al., 2011)
HLA-DRB5-DRB1	Major histocompatibility complex class II DRβ5/DRβ1	Role in antigen presentation in adaptive immunity.	(Lambert et al., 2013)
IL-34	Interleukin-34	Cytokine that plays roles in monocyte and macrophage cell survival and proliferation, important in the innate immune response and inflammation.	(Marioni et al., 2018)
INPP5D	Inositol polyphosphate-5-phosphatase	Specifically expressed in immune and hematopoietic cells, plays multiple roles in immune cell function including signalling, survival and proliferation.	(Lambert et al., 2013)
MS4A gene cluster	MS4A4A, MS4A4E, MS4A6E	Expressed in myeloid cells and monocytes, associated with the inflammatory response but poorly characterised.	(Hollingworth et al., 2011)
PLCG2	1-phosphatidylinositol 4,5-bisphosphate phosphodiesterase γ-2	A phospholipase highly expressed in microglia, involved in immune cell signalling in the hydrolysis of membrane bound PIP2 to IP3 and DAG.	(Sims et al., 2017; Marioni et al., 2018)

	(PLCγ2)		
PTK2B	Protein tyrosine kinase 2-beta	Regulation of the humoral immune response.	(Lambert et al., 2013)
SCIMP	SLP-adaptor and SCK-interacting membrane protein	A protein involved in MHC class II signal transduction.	(Liu et al., 2017b)
SHARPIN	Sharpin	Part of the LUBAC complex which synthesises and attaches M1-linked ubiquitin chains. Involved in NK-kB activation and regulation of inflammation.	(de Rojas et al., 2020)
SPPL2A	Signal peptide peptidase like 2A	Aspartic protease involved in TNF cleavage and signalling, may play role in both innate and adaptive immunity.	(Liu et al., 2017b)
TREM2	Triggering receptor expressed on myeloid cells 2	A myeloid cell receptor with multiple roles including phagocytosis and triggering the production of inflammatory cytokines. Binds Aβ.	(Jonsson et al., 2013; Chih Jin et al., 2014)
TREML2	Trem-like transcript protein 2	Immune cell surface receptor with possible roles in both innate and adaptive immunity, enhances T cell responses.	(Benitez et al., 2014)

Table 1.5. Genetic variants associated with AD that are linked to the immune response
Genetic variants are shown with corresponding protein and functional information.

1.4.1.1 ApoE4

Apolipoprotein E (ApoE) is a key cholesterol carrier, primarily produced by astrocytes in the brain, which facilitates the transport of lipids via receptors of the low-density lipoprotein receptor (LDLR) family. Three common isoforms of ApoE exist in humans; ε2 ε3 and ε4, with the ε4 allele of the ApoE gene (*APOE4)* being the strongest genetic risk factor for LOAD (Karch et al., 2014). ApoE4 increases the risk of developing AD 3-4 fold in heterozygotes, and 12-15 fold in homozygotes, compared to those carrying the ε3 allele (van der Lee et al., 2018). Conversely, the ε2 allele has a protective effect (Lambert et al., 2013). Whilst the molecular mechanism by which ApoE4 mediates its pathological effect is not yet well-defined, ApoE has been found to bind to Aβ and is implicated in mediating its clearance, with evidence suggesting that ApoE4 binds to Aβ with lower affinity, resulting in less efficient clearance (LaDu et al., 1994; Castellano et al., 2011). There is also evidence that ApoE4 accelerates early seeding of amyloid pathology (Huynh et al., 2017; Liu et al., 2017a).

1.4.1.2 TREM2

The strongest risk factor for LOAD other than ApoE4 is Triggering receptor expressed on myeloid cells 2 (TREM2) (Deczkowska et al., 2020). TREM2 is an immune receptor of the immunoglobulin family, which is expressed by microglia in the brain (Deczkowska et al., 2020). This plasma membrane receptor forms signalling complexes with the adaptor protein DNAX-activating protein of 12 kDa (DAP12) and is important in the

phagocytosis of apoptotic neurons and the negative regulation of inflammatory responses (Hamerman et al., 2005, 2006; Takahashi et al., 2005; Piccio et al., 2007; Hsieh et al., 2009). TREM2 sequence variants R47H and R62H have been found to increase the risk of developing late-onset AD (Jonsson et al., 2013; Chih Jin et al., 2014). There is evidence that in the absence of functional TREM2, the early deposition of Aβ is accelerated, and this is suggested to be a result of reduced phagocytic clearance of Aβ. It was recently found that deleting TREM2 increased tau pathology and brain atrophy in an AD mouse model, but only if Aβ is present (Lee et al., 2021). A damaging microglial response was also found to result from Aβ pathology in a TREM2-dependent manner (Lee et al., 2021).

1.4.2 Cells involved in the immune response to Aβ

Immune cells in the brain can be activated by Aβ, but they can also contribute to its clearance. Conversely, there is also evidence that inflammatory pathways can contribute to the aggregation of Aβ (Webers et al., 2020). This suggests a mutual, bidirectional relationship between Aβ pathogenesis and neuroinflammation. This relationship will be discussed in more depth.

1.4.2.1 Microglia

Microglial cells have been found to be key contributors to the neuroinflammation observed in AD. These are innate immune cells that make up 0.5-16% of cells in the human brain, depending on the brain region (Mittelbronn et al., 2001; Ajami et al., 2007). These myeloid lineage cells are recruited to the brain during early development where they play a phagocytic role (Ginhoux et al., 2010). When in a resting state microglia have a ramified morphology with multiple fine processes projecting from the cell body, with which the cells survey the local brain environment (Nimmerjahn et al., 2005). Upon activation microglia migrate to the location of injury or infection and adopt a ‘reactive’ phenotype, consisting of conversion to an amoeboid morphology and changes in receptor expression (Davalos et al., 2005).

Reactive microglia are observed in AD brains, where they surround and infiltrate Aβ plaques and release pro-inflammatory mediators (Itagaki et al., 1989). Transgenic mouse models of AD have also been used to show that microglia are activated and recruited to Aβ plaques, as quickly as within a day of plaque formation, with a 2-5 fold increase in microglia at the site of plaques compared to other neighbouring areas (Frautschy et al., 1998; Simard et al., 2006; Meyer-Luehmann et al., 2008).

A correlation was identified in AD mice models between Aβ load and levels of inflammatory cytokines, including TNF-α, IL-6 and GM-CSF (Patel et al., 2005). In addition, the inhibition of IL-12/IL-23 signalling was found to lead to a reduction in Aβ pathology and cognitive decline, further highlighting an important link between inflammation, amyloid and degeneration (Vom Berg et al., 2012).

1.4.2.2 Astrocytes

Astrocytes are the most abundant glial cell in the brain, they are specialised cells with numerous crucial roles in maintaining and regulating neuronal function and signal transmission (Perez-Nievas and Serrano-Pozo, 2018). Like microglia, astrocytes can react to pathogenesis by adopting a reactive phenotype, and this reactive astrogliosis is observed in AD brains, mostly observed to be surrounding Aβ plaques (Nagele et al., 2003; Braak et al., 2007; Hurtley, 2009; Palpagama et al., 2019). In addition to this astrogliosis, there is evidence that astrocytes are capable of internalising and degrading different amyloid proteins, and that they can also contribute to the formation of plaques (Nagele et al., 2003; Wyss-Coray et al., 2003). A number of AD risk genes are also highly expressed by astrocytes, such as ApoE4, further implicating these cells in disease (Table 1.5).

1.4.2.3 T-cells

Most research into the immune response in AD has focused on the innate immune system, and much less is known about the contribution of the adaptive branch of the immune system. However, there are reports of the presence of T-cells in AD brains, and also that T-cells from AD patients are more reactive to Aβ, recognising Aβ as an immunogenic antigen to which a response is stimulated, than those from healthy subjects (Togo et al., 2002; Monsonego et al., 2003). A more recent study also identified increased numbers of a $CD8^+$ T effector memory $CD45RA^+$ (T_{EMRA}) cell population to be associated with AD and MCI (Gate et al., 2020). It was confirmed in a separate cohort that an increase in $CD8^+$ T_{EMRA} cells was associated with a decline in cognition (Gate et al., 2020). Further investigation revealed $CD8^+$ T-cells in the perivascular space of blood vessels but not control brains, and significantly more of these cells in AD hippocampi compared to control brains. Notably, these $CD8^+$ T-cells were detected adjacent to Aβ plaques (Gate et al., 2020).

1.4.3 Mechanisms of immune cell activation by Aβ fibrils

Pattern recognition receptors (PRRs) are receptors on the surface of immune cells that have evolved to recognise components of foreign pathogens known as pathogen-

associated molecular patterns (PAMPs) and molecules produced by damaged or apoptotic cells called damage-associated molecular patterns (DAMPs) (Li and Wu, 2021). Oligomeric and fibrillar amyloid structures are recognised by PRR's, resulting in the activation of an immune response. This is speculated to be due to amyloid fibrils resembling functional amyloids such as curli fibres, expressed on the surface of enteric bacteria including *Escherichia coli* (*E. coli)* and *Salmonella* (Epstein and Chapman, 2008).

1.4.3.1 NLRP3 inflammasome

One key pathway of immune cell activation involved in the response to amyloid fibrils is the NOD-like receptor family, pyrin domain containing 3 (NLRP3) inflammasome. This inflammasome is a multiprotein complex present in myeloid-lineage cells (Swanson et al, 2019). The NOD-like receptor present in this complex is NALP3, which consists of an N-terminal pyrin domain (PYD) a central NACHT domain and a C-terminal leucine-rich repeat domain (LRR) (Figure 1.10).

The activation of the NLRP3 inflammasome is a two-step process which first requires a priming stimulus. This priming stimulus can be PAMPs such as lipopolysaccharide (LPS), or cytokines such as TNF and IL-1β. This priming step induces the transcriptional upregulation of NALP3 and inactive forms of IL-1β, IL-18 and caspase-1 (Bauernfeind et al., 2009; Franchi et al., 2009). A second activating stimulus is then required in order to trigger IL-1β and IL-18 cleavage and release from cells (Swanson et al., 2019). This activating stimulus can be ATP, pore-forming toxins that result in low intracellular K^+, crystallised structures such as uric acid and silica, and amyloid fibrils including Aβ fibrils (Mariathasan et al., 2006; Martinon et al., 2006; Halle et al., 2008). The second activating stimulus of the inflammasome results in the oligomerisation of NLRP3, and recruitment of adaptor protein apoptosis-associated speck-like protein containing a CARD (ASC). The polymerisation of ASC into helical filaments and ultimately into large macromolecular structures known as 'specks' is triggered, and caspase-1 is recruited to these ASC structures via a caspase recruitment (CARD) domain. Caspase-1 undergoes activating autoproteolytic cleavage which activates it so it can subsequently cleave and thus activate cytokines IL-1β and IL-18. These cytokines are released from cells, contributing to a neurotoxic inflammatory environment (Swanson et al., 2019). A further consequence of NLRP3 inflammasome activation is the induction of an inflammatory form of cell death known as pyroptosis (Swanson et al., 2019). Activated caspase-1 is also capable of cleaving a protein called gasdermin D. Gasdermin D subsequently inserts into the cell membrane, forming pores which results in the induction of pyroptosis (Swanson et al., 2019). The NLRP3 inflammasome pathway is outlined in Figure 1.8.

It was first shown that Aβ fibrils are capable of activating the NLRP3 inflammasome *in vitro* using primary microglial cells and this activation was found to be dependent on Aβ phagocytosis, subsequent damage to lysosomes and the release of cathepsin B into the cytosol (Halle et al, 2008). A further study then identified that NLRP3 or caspase-1 knock-out in transgenic APP/PS1 AD model mice, IL-1β activation was substantially reduced (Heneka et al., 2013). This provides *in vivo* support for the role of this activation pathway in AD. Moreover, increased levels of cleaved caspase-1 were identified in hippocampal and cortical lysates from AD patient brains compared with controls, further implicating the NLRP3 inflammasome in AD (Heneka et al, 2013).

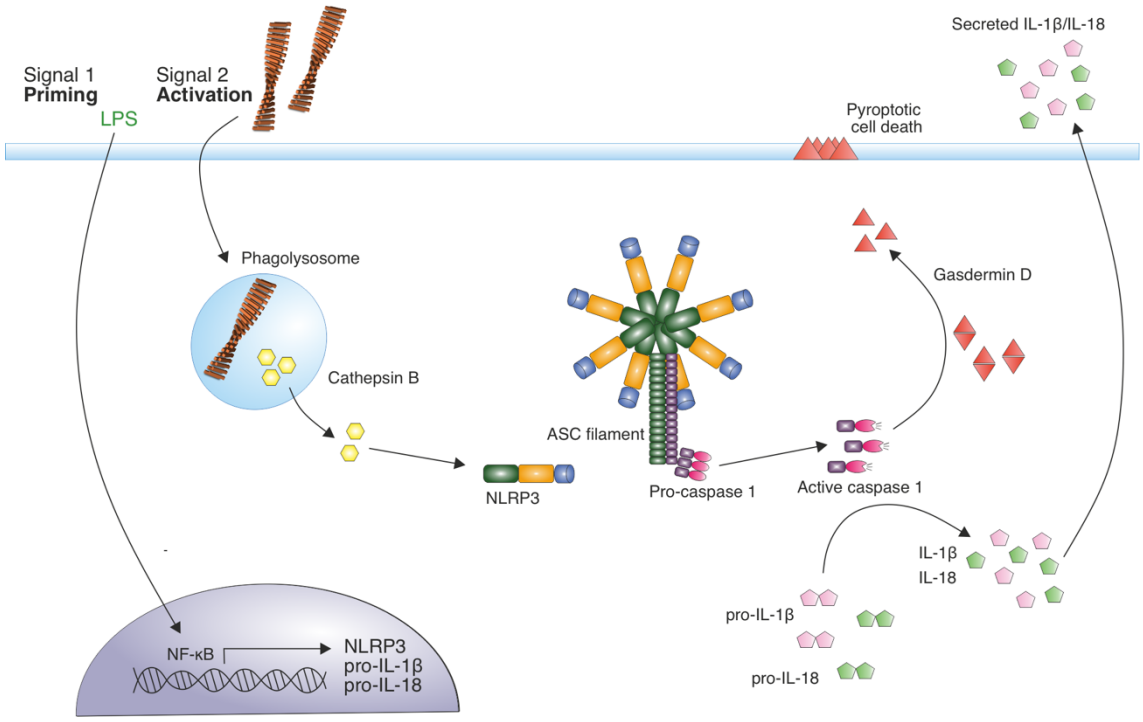

Figure 1.8. The NLRP3 inflammasome pathway
A priming signal such as LPS leads to the increased expression of NLRP3 and precursor forms of inflammatory cytokines IL-1β and IL-18. Amyloid fibrils can act as a second activating stimulus via their internalisation and disruption of lysosomes leading to the release of cathepsin B into the cytosol. This triggers the assembly of the NLRP3 inflammasome complex. This complex recruits ASC adaptor protein which forms filaments. ASC filaments interact with pro-caspase-1 via CARD domains, resulting in caspase-1 activation. Active caspase-1 cleaves precursor forms of IL-1β and IL-18 which are secreted from immune cells in their active form, contributing to neuroinflammation. Caspase 1 also cleaves Gasdermin D, which forms pores in the cell membrane resulting in pyroptotic cell death (Brown et al, 2020)

There is evidence linking fibrils of a number of other amyloidogenic proteins to inflammasome activation, suggesting that this activation is dependent on the amyloid fibril structure. PrP fibrils were found to be potent activators of the NLRP3 inflammasome in microglia, whereas oligomeric and monomeric forms of the protein had no activating effect (Shi et al, 2012/Hafner-Bratkovic et al, 2012). Similarly, human IAPP, but not the non-amyloidogenic rat IAPP, was found to trigger NLRP3 inflammasome activation in

macrophages and dendritic cells, helping to explain the elevated IL-1β observed in type 2 diabetes (Masters et al, 2010). It has been found that both fibrillar and monomeric α-synuclein promote the expression of pro-IL-1β in monocytes, and this is dependent on binding to the TLR2 receptor (Codolo et al., 2013). However, only fibrillar α-synuclein led to the release of mature IL-1β, via inflammasome activation (Codolo et al., 2013). NLRP3 activation has also been identified in FTD patients and Tau22 mice models. It was previously found that fibrillar tau is capable of activating the NLRP3 inflammasome, which in turn leads to the exacerbation of tau deposition in a tau transgenic mouse model *in vivo (*Stancu et al, 2019). However, a different study reported that the inflammasome was only activated in response to monomeric and oligomeric forms of tau, not tau fibrils (Ising et al, 2019).

In addition to the activation of the NLRP3 inflammasome by amyloid fibrils, evidence is emerging for an effect of this inflammasome activation on amyloid formation (Venegas et al., 2017). As described previously, NLRP3 inflammasome activation results in the formation of ASC specks which can be up to a micrometre in size (Masumoto et al., 1999; Franklin et al., 2014; Lu et al., 2014). These specks are released from cells when the NLRP3 inflammasome is activated and it has been found that after their release, ASC specks bind to $A\beta_{42}$ peptide (Venegas et al., 2017). *In vitro* experiments found that the addition of ASC specks to both $A\beta_{40}$ and $A\beta_{42}$ peptide accelerated their aggregation. This result is indicative of cross-seeding activity, and this effect was found to be dependent on the PYD domain of ASC (Venegas et al., 2017). Furthermore, when purified ASC specks were injected into the hippocampus of APP/PS1 mice, more Aβ deposits were observed, and an ASC-speck antibody was capable of reducing this Aβ deposition (Venegas et al., 2017). This suggests that the activation of the NLRP3 inflammasome by Aβ fibrils in turn results in increased aggregation of Aβ, creating a positive-feedback effect (Figure 1.9).

It was recently found that in the presence of ASC-Aβ composite complexes the uptake of Aβ was reduced by 35% and Aβ degradation was inhibited (Friker et al., 2020). This suggests that NLRP3 inflammasome activation has a negative effect on Aβ clearance, in addition to a positive effect on Aβ aggregation. ASC-Aβ composites were also shown to be capable of activating the NLRP3 inflammasome and inducing pyroptotic death in microglia (Friker et al, 2020). IL-1β release induced by ASC-Aβ composites was reduced with the neutralisation of TLR2 and TLR4, implicating these receptors in the recognition of Aβ by microglial cells (Figure 1.10) (Friker et al., 2020). One suggested hypothesis is that clustering of Aβ on the ASC specks may allow the Aβ to interact with multiple cell surface receptors therefore amplifying inflammatory activation.

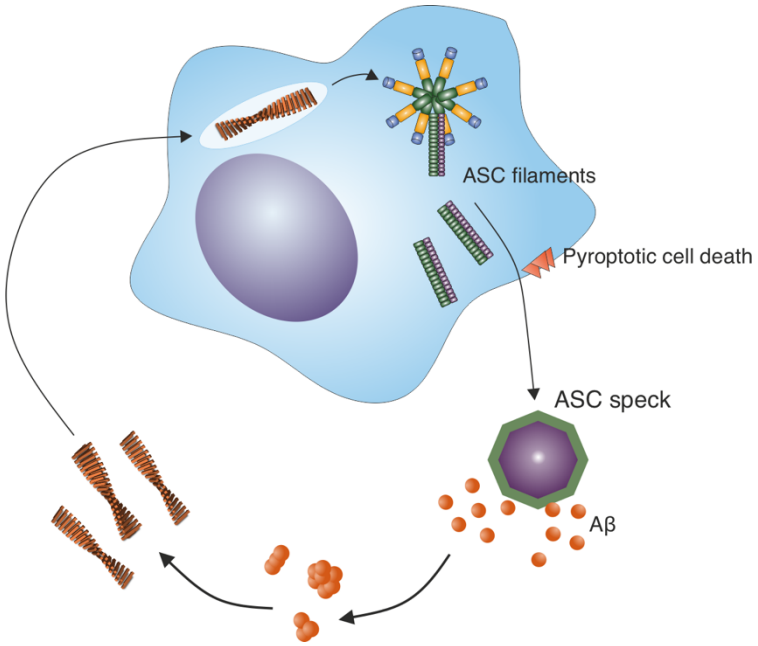

Figure 1.9. The bidirectional relationship between NLRP3 inflammasome activation and Aβ fibril formation
Activation of the NLRP3 inflammasome by Aβ fibrils leads to the release of ASC specks. These spekcs cross-seed the aggregation of Aβ peptide, resulting in the formation of more Aβ fibrils. These Aβ fibrils can activate the NLRP3 in other microglial cells, therefore amplifying this effect. (Brown et al, 2020).

1.4.3.2 Toll-like receptors and scavenger receptors

TLRs are a class of PRRs that recognize conserved microbial structures and have identified to be involved in the immune response to Aβ fibrils (Kawasaki and Kawai, 2014). These receptors are type I integral membrane receptors which form dimers when interacting with a ligand via their LRR ectodomains, leading to downstream signalling (Botos et al., 2011). The expression of six TLR genes (1,2,4,5,6,8) was found by RNAseq to be upregulated in the temporal cortex of AD patients compared to control brains, likely resulting from increased microgliosis (Chakrabarty et al., 2018).

There is evidence that Aβ fibrils trigger inflammatory signalling through a heterodimer of TLR4 and TLR2, regulated by CD14 signalling (Reed-Geaghan et al., 2009). CD14, a TLR co-receptor, has been shown previously to bind to fibrillar Aβ (fAβ), with a 20-fold higher affinity than the interaction between non-fibrillar Aβ and CD14 (Reed-Geaghan et al., 2009). Additionally, increased expression of CD14 and TLR2 has been identified in AD mouse models and AD patient tissue (Fassbender et al., 2004; Liu et al., 2005; Letiembre et al., 2009). Levels of inflammatory mediators TNF-α, IL-1β, IL-10 and IL-17 were found to be increased in AD mice compared to wild-type littermates, but this increase was no longer evident in TLR4 deficient AD mice, demonstrating a role for TLR4 in cytokine upregulation in AD (Jin et al., 2008). All components of this TLR signalling complex were shown to be necessary for stimulation of an inflammatory response (Reed-Geaghan et al., 2009).

Scavenger receptors are highly expressed in microglia and have also been found to be involved in the response to Aβ fibrils (Christie et al., 1996; Wilkinson and El Khoury, 2012). It was originally identified that Class A scavenger receptors, which possess an extracellular collagen domain, are capable of binding to Aβ fibrils (Paresce et al., 1996). Further experiments using SR-A1 deficient microglia confirmed that SR-A1 and also SR-B1 receptors bind to Aβ fibrils (Husemann et al., 2001).

Another TLR complex implicated in the activation of microglia by Aβ is a heterodimer of TLR4 and TLR6 regulated by CD36, a class B scavenger receptor (Stewart et al., 2010). It has been shown that CD36 is expressed by microglia in AD brains, binds to fAβ and is important in the consequent mediation of a microglial inflammatory response via a Src-kinase dependent signalling pathway (Husemann et al., 2001; Coraci et al., 2002; Moore et al., 2002). Microglia from CD36-null mice were found to secrete reduced levels of cytokines, chemokines and reactive oxygen species (ROS) in response to Aβ fibrils (El Khoury et al., 2003). Similarly, deficiency of TLR4, TLR6 or CD36 in microglia abolished $A\beta_{42}$-mediated ROS and nitric oxide (NO) production, inflammatory mediators that contribute to neurotoxicity in AD (Stewart et al., 2010). Consistent with this, neuronal cell death was observed when microglial and neuronal cocultures were treated with $A\beta_{42}$, however this neurotoxic effect was lost with CD36 -/-, TLR4 -/- or TLR6 -/- microglia (Stewart et al., 2010).

CD36 has also been suggested to be a regulator of NLRP3 inflammasome activation, facilitating the uptake of soluble Aβ which then forms fibrils at the lysosome and triggers NLRP3 activation (Sheedy et al., 2013). However, this does not agree with studies that report the amyloid fibril structure to be key to triggering NLRP3 inflammasome activation

in microglia (Gustot et al., 2015). Receptor complexes identified to be involved in the response of immune cells to Aβ fibrils are shown in Figure 1.10.

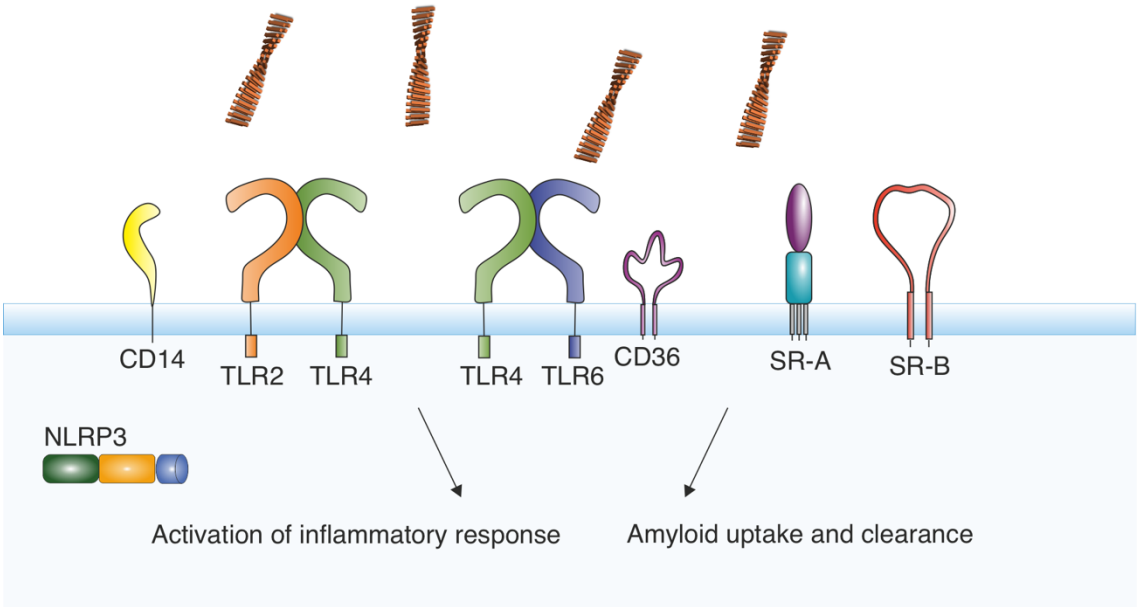

Figure 1.10. Immune cell receptors involved in the response to Aβ fibrils
A number of receptors have been identified in immune cells that are involved in the recognition of the fibrillar form of Aβ, including Toll-like receptor (TLR) complexes, scavenger receptors and the NALP3 receptor of the NLRP3 inflammasome. The activation of these receptors has been shown to lead to the activation of an inflammatory response, but in some cases also triggers the uptake and clearance of the fibrils.

1.4.3.3 Complement system

The identification by genome-wide association studies (GWAS) of an association between components of the complement cascade, complement receptor 1 (CR1) and Clusterin (CLU) and risk of AD implicates the complement system in disease (Lambert et al., 2009).

Studies have shown that Aβ can activate the classical and alternative complement pathways, via binding to C1q and C3b components of the complement system respectively, and this was shown to be dependent on the aggregated state of Aβ (Rogers et al., 1992; Jiang et al., 1994; Webster et al., 1997; Bradt et al., 1998). It was reported that a deficiency in the C3 component of the complement pathway in APP/PS1 transgenic mice increased Aβ load, but reduced plaque-related neuronal death, cognitive decline and activated glia despite this, suggesting that the complement system is somehow modulating the response to Aβ. This evidence suggests that inhibition of C3 signalling could be a potential target for AD treatment (Shi et al., 2017). Further to this, C3 was found to be a marker of the so called A1 astrocyte phenotype which was found to be neurotoxic, and C3 upregulation was identified in astrocytes from both AD and PD post-mortem tissue (Liddelow et al., 2017).

1.4.4 The neurotoxic consequences of immune cell activation by Aβ

The release of cytokines and other inflammatory mediators in a short-term inflammatory response results in the activation of additional microglial cells, recruitment of these cells to the site of damage, and consequently enhanced uptake and clearance of the invading pathogen, protein or molecule. However, long-term exposure to a stimulus such as Aβ in AD brains results in a chronic inflammatory response. This persistent release of pro-inflammatory mediators creates a neurotoxic environment (Sarlus and Heneka, 2017).

There is evidence that pro-inflammatory mediators can lead to synaptic dysfunction, including loss of synapse function and plasticity. For example, IL-1β production has been shown to lead to the loss of synaptic connections as a result of sensitisation of NMDA receptors, key excitatory receptors in the brain (Mishra et al., 2012). It has also been shown that IL-18 inhibits LTP in the dentate gyrus *in vitro*, and other inflammatory mediators including cyclooxygenase-2 (COX-2) and NO are involved in this (Cumiskey et al., 2007). There is also evidence that pro-inflammatory cytokines inhibit neurogenesis, with a correlation between the number of hippocampal microglia and impairment of neurogenesis (Ekdahl et al., 2003). In addition, many of the signalling molecules produced in excess during an inflammatory response in the brain, for example TNF-α, mediate pro-apoptotic pathways, therefore directly implicating neuroinflammation in neuronal death (Harry et al., 2008). Other pro-inflammatory mediators have also been found to lead to neuronal apoptosis indirectly, for example NO has been shown to kill neurons by inhibiting neuronal respiration, which results in glutamate release and subsequent excitotoxicity (Bal-Price and Brown, 2001). Degeneration of neurons leads to further activation of immune cells, further amplifying this inflammatory response. In this chronic inflammation, clearance of the stimulus can be impaired. The relationship between Aβ fibrils, microglia and neurons is outlined in Figure 1.11.

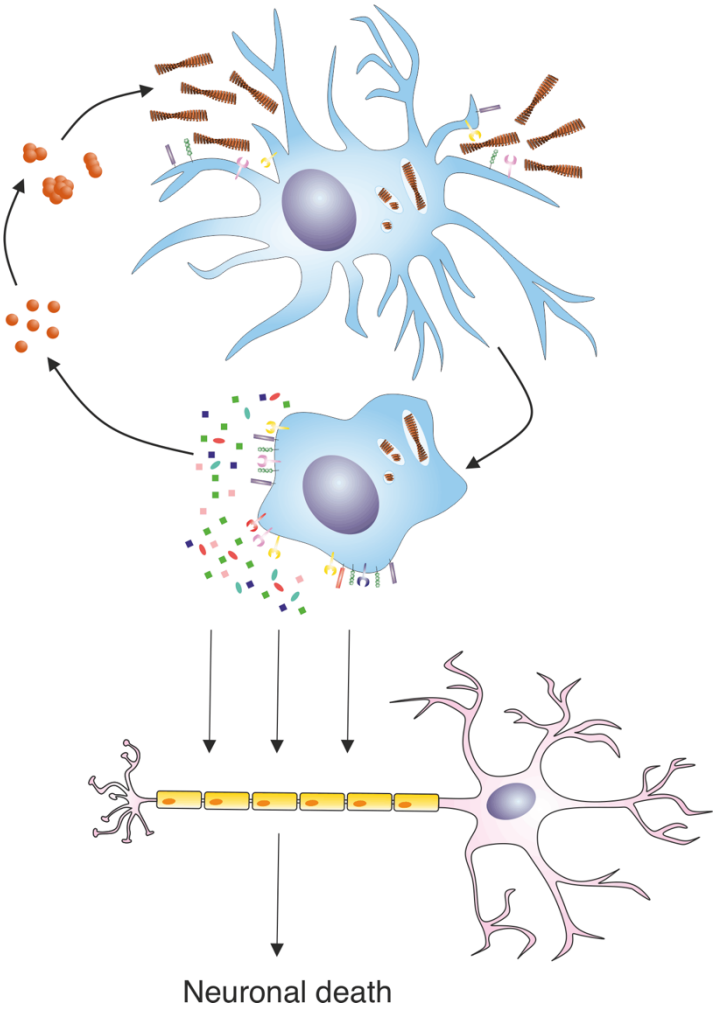

Figure 1.11. Summary schematic of how microglial activation by Aβ fibrils contributes to neurodegeneration
Aβ monomers aggregate to form an array of soluble oligomer intermediates, protofibrils then amyloid fibrils with a cross-β structure. These various amyloid structures bind to different receptors on microglial cells in the brain. This results in the uptake and clearance of Aβ but can also result in the activation of microglial cells. When activated, microglial cells adopt a 'reactive' phenotype consisting of a more amoeboid morphology and changes in receptor expression. Activated microglia secrete cytokines and other inflammatory mediators, which creates a neurotoxic environment for neurons, contributing to neurodegeneration. Immune cell activation can alter amyloid formation and propagation, creating a cycle.

1.4.5 Clearance of Aβ fibrils by immune cells

In addition to the activation of immune cells by Aβ fibrils, these cells can also contribute to the clearance of Aβ deposits. This can be by via the uptake and degradation of fibrils intracellularly, or via the secretion of degradative enzymes (Rogers et al., 2002). A number of the risk genes associated with LOAD have been found to be involved in the clearance of Aβ, demonstrating the importance of this process in AD (Table 1.5) (Kleinberger et al., 2014; Ulrich et al., 2018; Griciuc et al., 2019).

1.4.5.1 Cellular uptake of Aβ fibrils

As with activation, a number of PRR's expressed by immune cells have been implicated in the clearance response to Aβ fibrils. This includes TLR's, some of which were previously discussed to be involved in the inflammatory response to Aβ. A direct molecular interaction was identified between fAβ and CD14, which was found to facilitate the internalisation of fAβ into microglial cells (Fassbender et al., 2004; Reed-Geaghan et al., 2009). This internalisation response occurred at significantly lower concentrations than that required for cell activation, suggesting that CD14 could be involved in the phagocytosis of Aβ at low concentrations, but increased levels of Aβ in AD results in inflammatory activation (Liu et al., 2005). Further to this, TLR4 deficiency in AD mouse models has been shown to result in increased Aβ deposition, and stimulation of BV-2 microglial cells with TLR2 and TLR4 ligands significantly increased the internalisation of Aβ *in vitro* (Tahara et al., 2006; Song et al., 2011).

There is also evidence for the involvement of SR's in Aβ clearance; it was shown that coincubation of microglia with SR ligands such as acetyl-low density lipoprotein (Ac-LDL) reduced Aβ uptake, and CHO cells transfected with class A, or class B SR's showed enhanced Aβ uptake, suggesting that SRs are important in the uptake and clearance of Aβ (Paresce et al., 1996). $\alpha_6\beta_1$-integrin and the integrin-associated protein CD47 in microglia. Studies have reported that the interaction of Aβ fibrils with a receptor complex made up of CD36, $\alpha_6\beta_1$-integrin and the integrin-associated protein CD47 in microglia is involved in the phagocytic uptake of fibrils by microglia (Coraci et al., 2002; Koenigsknecht and Landreth, 2004).

The complement pathway is also implicated in the clearance of Aβ. CR1 has been suggested to modulate the effect of the Apoε4 allele, with significantly higher amyloid burden in Apoε4 individuals who are carriers of the CR1 risk allele rs3818361 than noncarriers (Thambisetty et al., 2013). Complement receptor 3 (CR3), a major phagocytic receptor expressed by microglia, was also found more recently to regulate Aβ levels, with a reduction in Aβ deposition observed in CR3 deficient APP transgenic mice (Czirr et al., 2017). CR3 deficient microglial cells were found to be more efficient at Aβ degradation, and this was suggested to be a result of increased secretion of Aβ-degrading enzymes (Czirr et al., 2017).

Numerous studies have reported that astrocytes are also able to internalise Aβ, with evidence for the accumulation of $A\beta_{42}$ within activated astrocytes (Nagele et al., 2003; Wyss-Coray et al., 2003). Cultured astrocytes were shown to migrate towards CCl-2, a chemokine present at AD plaques, and subsequently bind to Aβ, however the receptors involved in this binding were not identified (Wyss-Coray et al., 2003). In a study using

AD brain tissue, the identification of neuron-specific markers alongside Aβ material within astrocytes suggests that this material is derived from the phagocytosis of debris from damaged neurons (Nagele et al., 2003).

1.4.5.2 Amyloid-degrading enzymes

One mechanism by which immune cells are thought to contribute to the clearance of amyloid is via the secretion of amyloid-degrading enzymes. Enzymes identified to cleave Aβ include the metalloendopeptidases insulin-degrading enzyme (IDE) and neprilysin (NEP) (Leissring et al., 2003). However, these enzymes are not thought to be capable of degrading the fibrillar form of Aβ, but are limited to the degradation of monomeric peptide (Qiu et al., 1998; Farris et al., 2003; Leissring et al., 2003). Enzymes that are capable of cleaving fibrillar Aβ have however been identified. Matrix metalloprotease-9 (MMP-9) is a zinc-dependent metalloprotease expressed by neurons, astrocytes, microglia and vascular cells in the brain (Vafadari et al., 2016). It was shown using ThT and TEM that incubation of fAβ with MMP-9 leads to fibril degradation (Yan et al., 2006). Analysis of resulting fibril fragments by mass spectrometry revealed species corresponding to Aβ(1-20) and Aβ(1-30), suggesting Phe20-Ala21 and Ala30-Ile31 as cleavage sites (Yan et al., 2006). These sites must therefore be accessible in the fibril structure to MMP-9. Importantly, MMP-9 was also found to degrade compact Aβ plaques in brain sections from APP/PS1 mice (Yan et al., 2006).

Another matrix metalloprotease, MMP-2, is also implicated in Aβ degradation, with increased Aβ identified in the brains of KO MMP-2 mice compared to wild-type controls (Yin et al., 2006). Astrocytes are suggested to be involved in this MMP-2/MMP-9 secretion (Deb et al., 2003; Yin et al., 2006). A further MMP implicated in Aβ fibril degradation is membrane type-1 (MT1) MMP. This protease was found to be expressed in reactive astrocytes close to Aβ deposits, and degraded Aβ plaques in an APP mouse model (Liao and Van Nostrand, 2010). MT1-MMP also cleaved Aβ fibrils *in vitro*, confirmed by ThT and TEM analysis (Liao and Van Nostrand, 2010).

Certain proteases present in lysosomes are also capable of degrading Aβ. Cathepsin B, a lysosomal cysteine protease, was found to accumulate in neuritic plaques in AD model mice (Mueller-Steiner et al., 2006). Cathepsin B activity was highest in supernatant taken from primary microglial cell cultures, compared to neurons and astrocytes, suggesting that these cells act as a source of cathepsin B as they surround Aβ plaques (Mueller-Steiner et al., 2006). $Aβ_{42}$ monomeric peptide, nonfibrillar assemblies and fibrils were all found to be cleaved by cathepsin B, resulting in the production of Aβ(1-40), Aβ(1-38) and Aβ(1-33) fragments (Mueller-Steiner et al., 2006). This suggests an anti-amyloidogenic role for cathepsin B, via the C-terminal truncation of Aβ.

Another lysosomal protease, tripeptidyl peptidase 1 (TPP-1) was more recently identified as an enzyme capable of cleaving Aβ fibrils. *In vitro* digestions of $A\beta_{42}$ fibrils were carried out and resulting peptide fragments revealed a number of different cleavage sites (Solé-Domènech et al., 2018). A number of these sites were within the β-sheet domains, and molecular dynamics simulations suggested that these cleavages lead to destabilisation of the β-sheet fibril structure (Solé-Domènech et al., 2018).

1.4.5.3 The failure of microglia to clear Aβ in Alzheimer's disease

The amyloid deposition observed in AD brains implies that microglia may be limited in their ability to clear Aβ. There is evidence to suggest that this clearing capability of microglia may be impaired as a result of ageing and disease (Brown et al., 2020). For example, microglia from older PS1-APP AD model mice have a 2-6-fold reduction in expression of Aβ-binding receptors SR-A and CD36 compared to WT control mice, in addition to significant reductions in the expression of Aβ-degrading enzymes IDE, NEP and MMP-9 (Hickman et al., 2008). These older PS1-APP mice were found to have increased expression of inflammatory cytokines TNF-α and IL-1β, indicating that in parallel to impaired clearance pathways, there is also a damaging inflammatory response to Aβ (Hickman et al., 2008).

A later study also found that the phagocytic activity of microglia in AD mice was significantly impaired compared to WT controls, and this impairment correlated with increased Aβ deposition (Krabbe et al., 2013). Reducing Aβ load by vaccination was shown to restore the phagocytic capacity of microglia, suggesting that the microglial dysfunction is a result of this Aβ pathology present in AD (Krabbe et al., 2013). Importantly, when production and clearance rates of $A\beta_{40}$ and $A\beta_{42}$ were tracked in AD patients using metabolic labelling, it was found that clearance rates for both peptides were reduced in AD compared to controls, but no differences in production rates were identified (Mawuenyega et al., 2010). This suggests that AD could be a result of the failure of microglia to clear Aβ.

Recent developments in microglial research has revealed that microglia undergo a number of morphological, transcriptional and functional changes in disease (Deczkowska et al., 2018). For example, myeloid cells show changes in their morphology and function in response to the Aβ-rich environment of an AD brain (Drost et al., 2020). Furthermore, a number of different subset populations of microglia with distinct transcriptional profiles and phenotypes have been identified in aging and AD brains (Keren-Shaul et al., 2017; Krasemann et al., 2017; Marschallinger et al., 2020). These include 'damage associated microglia' (DAM) which are proposed to play a protective role in disease, and microglia characterised by a loss of homeostatic function which are

associated with neurodegeneration (Krasemann et al., 2017). APOE signalling induced by TREM2 was found to be responsible for the conversion of microglia to this impaired neurodegenerative phenotype, further implicating these pathways and microglial dysfunction in AD (Krasemann et al., 2017). An additional unique population of microglia with a distinct transcriptional signature was recently identified in the aging brain, termed 'lipid-droplet-accumulating microglia' (LDAM) (Marschallinger et al., 2020). These cells are characterised by an accumulation of lipid droplets and show defects in phagocytosis alongside increased levels of pro-inflammatory cytokine release (Marschallinger et al., 2020). LDAM were found to account for up to 50% of microglia in the hippocampus of aged mice, but the presence of LSAM in AD models or brains has yet to be confirmed (Marschallinger et al., 2020).

Another distinct population of microglia termed 'activated response microglia' (ARMs) have been shown to occur naturally in aging mice and human brains, but the presence of Aβ plaques accelerates the conversion of microglia to this state (Frigerio et al., 2019). A number of AD risk genes have also been found to be upregulated in ARMs, including ApoE (Frigerio et al., 2019). Given the association of the ApoE4 allele with AD, future studies should investigate the effect of this allele on the occurrence of the ARM phenotype (Lambert et al., 2013). Manipulating microglia to encourage the conversion from dysfunctional and damaging phenotypes to a protective phenotype such as DAM is a potential therapeutic strategy that could be utilised to restore microglial function and enhance the clearance of Aβ.

1.5 Project aims

Despite the evidence for Aβ fibril polymorphism both *in vitro* and *ex vivo*, the functional consequences of Aβ fibril polymorphism are not well understood. This is crucial information as differences in the functional properties of Aβ fibrils in the brain could link to differences in the presentation of disease. This project aims to address this missing link by investigating the biological consequences of different Aβ fibril structures.

The functional properties of Aβ fibril structures will be explored from an immune perspective. This is because interactions between Aβ fibrils and immune cells such as microglia could be playing a key role in AD. The effects of Aβ fibrils on these immune cells determine the balance between the activation of the cells and the production of pro-inflammatory mediators resulting in a neurotoxic environment, but also the uptake and clearance of the fibrils.

The work in this thesis is based on the hypothesis that differences in the molecular structure of Aβ fibrils, i.e. fibril polymorphism, could determine the extent to which the fibrils activate an inflammatory response in immune cells and also the extent to which the fibrils are taken up by immune cells and degraded.

In the first results chapter of this thesis, the production and characterisation of distinct populations of Aβ fibrils *in vitro* is described. For this, Aβ peptides are purified, and previously defined conditions shown to result in fibrils with distinct and characterised structures are reproduced. The fibril preparations are then characterised using a number of biophysical methods.

The second results chapter of this thesis then studies the toxicity of the Aβ fibril preparations produced towards microglial, macrophage-like and monocytic cell lines. In addition, the immune cell activation in response to the different Aβ fibrils is investigated, and the pathway of this inflammatory activation explored.

Finally, the last results chapter of this thesis explores differences in the cell association, uptake and degradation of the different Aβ fibril preparations by a microglial cell line, in order to determine whether differences in Aβ fibril structure can affect their clearance by microglia.

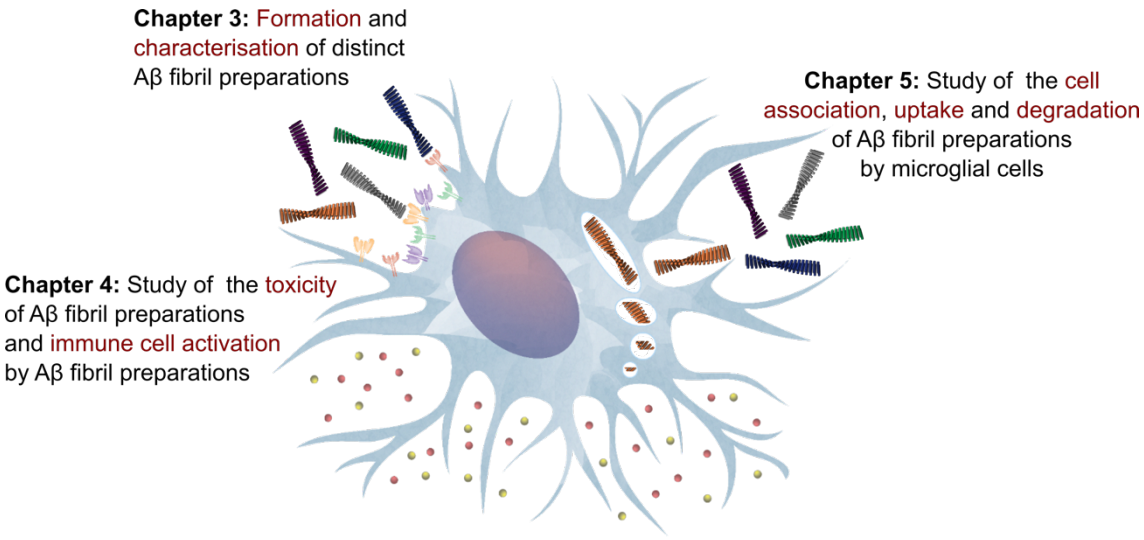

Figure 1.12. Summary schematic of project aims
The first results chapter of this thesis (Chapter 3) aims to produce distinct preparations of Aβ fibrils and characterise these. The second results chapter (Chapter 4) then aims to assess the effect of these Aβ fibril preparations on cell viability. Also in this chapter, the ability of the Aβ fibril preparations to activate an immune response resulting in the release of inflammatory cytokines will be investigated. Finally, the third results chapter (Chapter 5) aims to compare the level of association of the different Aβ fibril preparations, and their subsequent uptake and degradation by microglial cells.

2 Materials and Methods

2.1 Materials

2.1.1 Reagents

All reagents were purchased from Merck (Sigma-Aldrich, Germany) unless stated otherwise.

2.1.2 Buffers

Buffer A	10 mM Tris, 1 mM EDTA (pH 8.5)
Buffer B	10 mM Tris, 1 mM EDTA, pH 8.0
SDS-PAGE loading buffer	50 mM Tris.HCl pH 6.8, 100 mM DTT, 2% (w/v) SDS, 0.1% (w/v) bromophenol blue, 10% (v/v) glycerol
Anode buffer	200 mM Tris HCl (pH 8.9)
Cathode buffer	100 mM Tris HCl, 100 mM Tricine, 0.1% *w/v* SDS, (pH 8.25)
NHS-ester labelling reaction buffer	25 mM sodium phosphate (pH 8.3)
$A\beta_{40}$ fibrillation buffer	25 mM sodium phosphate, 0.01% NaN_3 (pH 7.5)
$A\beta_{40}$ E22Δ fibrillation buffer	10 mM NaH_2PO_4-NaOH (pH 7.4), 100 mM NaCl
pH 2 $A\beta_{42}$ fibrillation buffer	30% (*v/v*) acetonitrile, 0.1% (*v/v*) TFA in water (pH 2)
pH 8 $A\beta_{42}$ fibrillation buffer	20 mM sodium phosphate, 0.2 mM EDTA, 0.02% NaN_3, (pH 8.0)
Cellular fractionation homogenisation buffer (1X)	10 mM Triethanolamine, 10 mM acetic acid, 1 mM EDTA- Na_2, 6.66 % (*v/v*) sucrose, (pH 7.4)
N-acetylglucosaminidase (NAGA) substrate buffer	100 mM citric acid, 0.2 % (*v/v*) Triton X-100, (pH 4.5)
NAGA stop buffer	200 mM glycine, (pH 10.3)
Alkaline phosphatase assay buffer	5 mM magnesium acetate, 70 mM KCl, 5 mM glycine and 0.2 % (*v/v*) Triton X-100, (pH 9.0)

2.2 Recombinant DNA methods

2.2.1 Site-directed mutagenesis

Site-directed mutagenesis was used to introduce an E22 deletion into the Met($A\beta_{40}$) pETSac plasmid, provided by Professor Sara Linse (Lund University, Sweden) using Q5 mutagenesis (New England Biolabs, UK). Primers were designed using the NEB online tool (http://nebasechanger.neb.com) and purchased from Eurofins Genomics. The primers used for Q5 mutagenesis are shown in Table 2.1.

Met($A\beta_{40}$) pETSac E22Δ	**Sequence**	**Annealing temperature**
Forward primer	GACGTGGGTTCTAACAAG	60˚C
Reverse primer	AGCGAAGAACACCAGCTT	64˚C

Table 2.1. Primers used for site-directed mutagenesis

A PCR reaction was performed with the components outlined below, using the cycling conditions in Table 2.2.

Q5 Hot Start High-Fidelity 2X Master Mix	12.5 µL
Forward primer	0.5 µM
Reverse primer	0.5 µM
Met($A\beta_{40}$) pETSac vector	16.5 ng
Nuclease-free water	To 25 µL

Step	**Temperature (°C)**	**Time (s)**
Initial denaturation	98	30
Denaturation, annealing and elongation (25 cycles)	98	10
	64	30
	72	150
Final extension	72	120

Table 2.2. Cycling conditions used in PCR for site-directed mutagenesis

The PCR product was subsequently treated with kinase, ligase and *Dpn* I (KLD) enzymes to simultaneously phosphorylate and ligate amplified DNA, whilst degrading template DNA. The components of the reaction are outlined below and were mixed well by pipetting before incubation for 10 min at room temperature.

2X KLD Reaction buffer	5 µL
10X KLD Enzyme Mix	1 µL
PCR product	1 µL
Nuclease-free water	3 µL

2.2.2 Transformation

For Q5 mutagenesis, 50 µL of DH5α competent *E. coli* were transformed with 5 µL of KLD reaction mixture and incubated on ice for 30 min. Cells were heat shocked at 42°C for 45 s before incubation on ice for a further 5 min. Cells were then added to 950 µl Super Optimal broth with Catabolite (SOC) media and incubated at 37 °C for 1 h with shaking at 200 rpm. The transformation reaction was centrifuged at 3000 xg for 5 min, the pellet resuspended in 200 µL SOC and 40 µL of this was spread onto LB agar plates containing carbenicillin (100 µg/mL).

For protein expression, BL21(DE3) competent cells were transformed with 1 µL (100 ng) pETSAc vector containing Met($A\beta_{40}$), Met($A\beta_{40}$ E22Δ) or Met($A\beta_{42}$) sequences, provided by Professor Sara Linse (Lund University, Sweden), and incubated on ice for 30 min. Cells were then heat shocked at 42°C for 45 s before incubation on ice for a further 10 min. Cells were added to 500 µL LB media and incubated at 37 °C for 30 min with shaking at 200 rpm. 200 µL of culture was then plated onto LB agar plates containing carbenicillin (100 µg/mL).

2.2.3 Purification and sequencing of plasmid DNA

Single colonies were picked from transformation plates and used to inoculate 10 mL cultures of LB containing carbenicillin (100 µg/mL). Cultures were then incubated overnight at 37 °C with shaking at 200 rpm. Overnight cultures were pelleted at 4,000 g for 5 min and plasmid DNA was extracted using Wizard Plus SV Minipreps DNA Purification System (Promega, UK), according to manufacturer's instructions. DNA was eluted in 50 µL nuclease-free water and the concentration was measured using a NanoDrop 2000 spectrophotometer. Plasmid DNA was diluted to 100 ng/µL and sequenced by GENEWIZ using T7 primers.

2.3 Peptide expression, purification and labelling

$A\beta_{40}$, $A\beta_{40}$ E22Δ and $A\beta_{42}$ peptides with an additional methionine at the N-terminus were expressed and purified recombinantly using the following methods.

2.3.1 Expression of $A\beta_{40}$, $A\beta_{40}$ E22Δ and $A\beta_{42}$ in *E. coli*

100 mL cultures of LB containing carbenicillin (100 µg/mL) were inoculated with a single colony of transformed BL21(DE3) cells (Section 2.2.2) and incubated overnight at 37 °C with shaking at 200 rpm. Glycerol stocks were generated by adding 500 µL of this culture to 500 µL sterile 50% glycerol. Glycerol stocks were snap-frozen and stored at -80 °C. 5 mL of starter culture was used to inoculate 11 x 0.5 L flasks of LB containing carbenicillin (100 µg/mL). 0.5 L cultures were incubated at 37 °C with shaking at 200 rpm until an OD_{600} of 0.5 was reached (approximately 2 h). Protein expression was then induced by the addition of 500 µL 1M isopropyl-β-D-thiogalacto-pyranoside (IPTG). Cultures were incubated at 37 °C with shaking at 200 rpm for a further 4-5 h, until an OD_{600} plateau was reached. Cells were harvested by centrifugation at 7000 xg for 17 min at 4 °C (Avanti J-26 XP – JLA 8.1 Rotor, Beckman Coulter, CA, USA). Pellets were combined and stored at -20 °C until purification.

2.3.2 Isolation of inclusion bodies

2.3.2.1 Inclusion body isolation of $A\beta_{40}$ and $A\beta_{40}$ E22Δ

Inclusion bodies were isolated by the method described in (Walsh et al., 2009). Cell pellets were thawed on ice and 25 mL Buffer A (Section 2.1.2) was added containing 1 mM phenylmethylsulfonyl fluoride (PMSF), and 15 µg/mL deoxyribonuclease from bovine pancreas. The pellet was homogenised by magnetic stirring for 1 h at 4 °C, before being passed through a 1 ½" blunt syringe needle. The homogenate was subsequently sonicated at 22% amplitude for 30 sec (Sonics VCX 130 PB with 630-0435 probe) before centrifugation at 26,500 xg for 15 min at 4 °C (Avanti J-26 XP – JA 25.50, Beckman Coulter, CA, USA). Pellets were resuspended in Buffer A and the homogenisation, sonication and centrifugation steps repeated. Samples of the supernatants were taken. The pellet was then resuspended in Buffer A containing 8M urea to isolate inclusion bodies. This homogenate was stirred, sonicated and centrifuged as previously, but the supernatant was retained and the pellet discarded.

2.3.2.2 Inclusion body isolation of $A\beta_{42}$

Inclusion bodies were isolated as described in Yoo et al., 2018. Cell pellets were thawed on ice and resuspended in Buffer B (Section 2.1.2). This suspension was homogenised by sonication on ice for 2 min at 40% amplitude (50% duty cycle), then centrifuged at 4 °C for 25 min at 26,500 x g (Avanti J-26 XP – JA 25.50, Beckman Coulter, CA, USA). This cycle of sonication and centrifugation was repeated twice more before the final pellet was resuspended in 7mM NaOH (20 mL/g pellet). The solution was then sonicated as

described above, until it appears clear. The solution could then be filtered through a 0.22 μm Durapore non-sterile hydrophilic polyvinylidene fluoride (PVDF) filter (Merck, UK), although this step is not essential.

2.3.3 Anion-exchange chromatography

Purification of $A\beta_{40}$ and $A\beta_{40}$ E22Δ was performed as described in (Walsh et al., 2009). This first step of this was two rounds of batch mode anion-exchange (IEX) chromatography, using Q-sepharose Fast Flow resin (GE healthcare, UK). 50 mL of this resin was equilibrated with Buffer A before supernatant obtained in Section 1.3.2.1 was added to the resin and allowed to bind for 30 min at 4 °C with rocking. This mixture was then added to a Buchner funnel with Whatman 70 mm filter paper and a Whatman 250 mL glass open top funnel. Fractions were filtered and collected, the first fraction being flowthrough, followed by a wash step with 50 mL Buffer A then a wash step with 25 mM NaCl in Buffer A. The peptide was eluted from the resin in 5 fractions using 125 mM NaCl in Buffer A. A final elution step used an increased NaCl concentration of 250 mM in Buffer A, before remaining peptide was removed from resin using 1M NaCl in Buffer A and finally 1M NaCl and 8M urea in Buffer A. These purification steps were repeated with the flowthrough and first wash fractions to optimise yield. Samples from each fraction were taken and analysed using SDS-PAGE.

2.3.4 Dialysis and lyophilisation

Elution fractions were dialysed in SnakeSkin Dialysis tubing (3500 MWCO) against 50 mM ammonium bicarbonate for 2 days, with 5 buffer changes during this period. The sample was then aliquoted into 25 mL fractions and snap-frozen. Samples were then lyophilised for 3 days (Heto PowerDry PL3000).

2.3.5 Size-exclusion chromatography

Size-exclusion chromatography (SEC) was used as a second purification step of $A\beta_{40}$ and $A\beta_{40}$ E22Δ, following IEX purification, dialysis and lyophilisation. SEC was performed at 4 °C using a Superdex 75 16/60 column (GE healthcare, UK) connected to an ÄKTA prime plus chromatography system. The column was first washed with 1 column volume H_2O, NaOH and 50 mM ammonium bicarbonate. Lyophilised peptide was solubilised in 50 mM Tris, pH 8.5, 7M guanidine HCL and centrifuged for 10 min at 16,873 xg (5418 R, Eppendorf) at 4 °C to pellet any insoluble material. Supernatant was pulled through a needle before injection into the ÄKTA system using a 5 mL loop. The ÄKTA system was run at 2 mL/min for 180 min, collecting 4 mL fractions. Fractions corresponding to $A\beta_{40}$ or $A\beta_{40}$ E22Δ monomer were collected and aliquots taken for analysis by mass

spectrometry and concentration determination. The remaining samples were snap-frozen and lyophilised as previously described for 3 days.

2.3.6 High performance liquid chromatography (HPLC)

HPLC was performed with the help of Dr Martin Walko in the School of Chemistry at the University of Leeds, using a Kinetex EVO C18 (250x21.2) column (Phenomenex, UK). A 10%-30% acetonitrile gradient was used in water containing 0.1% ammonia to maintain basic conditions. 5 mL of sample was injected per purification run and a flow rate of 10 mL /min was used, for 30 min. $A\beta_{42}$ elutes between 20 to 25 min. Mass directed chromatography software Masshunter by ChemStation and Agilent 6120 Quadropole Liquid chromatography-mass spectrometry (Agilent Technologies, CA, USA), which separates the eluents at a defined m/z, were used to collect the fractions corresponding to $A\beta_{42}$. Collected fractions were freeze-dried and stored at -20 ºC until use.

2.3.7 Fluorescent labelling of peptide

$A\beta_{40,}$ $A\beta_{40}$ E22Δ and $A\beta_{42}$ monomers were labelled with ATTO 594 dye in the following manner. 1 mg of lyophilised monomeric peptide was solubilised in 2 mL 25 mM sodium phosphate buffer (pH 8.3), resulting in a final monomer concentration of 100 µM for $A\beta_{40}$ and $A\beta_{40}$ E22Δ, and 10 µM for $A\beta_{42}$ to prevent aggregation. ATTO 594 NHS ester was resuspended in dimethyl sulfoxide (DMSO) and added to the rehydrated monomer in a 4X molar excess. The reaction was incubated overnight at 4˚C with gentle rocking on a rocking table. The reaction was then quenched with a 10X molar excess of Tris over the ATTO 594 dye. The labelled monomer was purified by SEC using a Superdex 75 analytical column 10/300 (GE healthcare, UK). The resulting protein was eluted in 50 mM ammonium bicarbonate and lyophilised before storage at -20˚C.

2.4 Protein analysis

2.4.1 Determination of protein concentration

Protein concentration was determined by solubilisation of an aliquot of lyophilised sample in 50 mM Tris, pH 8.5, 7M guanidine HCL and measurement of A_{280}, and A_{340} using a quartz cuvette and UV-1800 UV spectrophotometer (Shimadzu, UK). A_{340} was subtracted from A_{280} to calculate corrected absorbance. This was divided by the extinction coefficient for Aβ (ε: 1490 M^{-1} cm^{-1}) to obtain molar concentration.

2.4.2 Mass spectrometry

To confirm that the correct peptides were purified, and to assess purity of $A\beta_{40}$ and $A\beta_{40}$ E22Δ peptide electrospray ionisation mass spectrometry (ES-MS) was performed in the mass spectrometry facility within the Faculty of Biological Science at the University of Leeds. Purity of $A\beta_{42}$ peptide was determined by liquid-chromatography mass spectrometry (LC-MS) in the School of Chemistry at the University of Leeds.

2.4.3 Sodium dodecyl sulphate polyacrylamide gel electrophoresis (SDS-PAGE)

Tris-tricine buffered SDS-PAGE gels were used to separate proteins according to their molecular weight. Two glass plates were assembled separated by a 1.5 mm spacer (ATTO, Japan) and resolving and stacking solutions were prepared as described in Table 2.3. The resolving gel was poured leaving a 2 cm gap at the top of the glass plates and the stacking gel was then immediately poured on top of the resolving gel. A 12-well comb was inserted, and the gels were left to set for 1 h.

Solution component	**Resolving gel volume (mL)**	**Stacking gel volume (mL)**
30% (*w/v*) acrylamide: 0.8% (*w/v*) bis-acrylamide	7.5	0.83
H_20	0.44	3.72
3M Tris-HCl, 0.3% (*w/v*) SDS pH 8.45	5	1.55
50% glycerol	2	0
10% ammonium persulfate (APS)	0.05	0.1
Tetramethylethylenediamine (TEMED)	0.01	0.005

Table 2.3. Components of tris-tricine buffered SDS-PAGE gels

Gel cassettes were inserted into the gel tank according to manufacturer's instructions (ATTO, Japan) and cathode and anode buffers (Section 2.1.2) were added to the inner and outer chambers respectively. Protein samples were diluted 1:2 in 2X SDS-PAGE loading buffer (Section 2.1.2), boiled for 5 min and 20 µL of sample added to wells. 5 µL of Precision Plus Protein Dual Xtra Standard (Bio-Rad, CA, USA) molecular weight marker was loaded into one lane for use in molecular weight estimation. Gels were run at a current of 30 mA until the samples entered the resolving gel, then the current was increased to 60 mA. The electrophoresis was stopped when the dye front reached the bottom of the gel, the gels removed from the casts and stained with Instant Blue Coomassie. Gels were imaged using a Syngene InGenius gel documentation system

(Syngene, UK). The absorbance of gels at 594 nm was measured using a G:Box gel doc system (Syngene, UK).

2.5 Aβ fibril formation

2.5.1 Formation of *de novo* $A\beta_{40}$ fibrils

Lyophilised $A\beta_{40}$ monomer was resuspended in 25 mM sodium phosphate, 0.01% NaN_3 (pH 7.5) to a final concentration of 0.9 mg/mL. This was aliquoted into a Costar 3881 half volume 96-well plate, with 100 µL in each well. This plate was incubated at 37˚C with orbital shaking in a Clariostar microplate reader (BMG Labtech) for 48 h. Fibril synthesis was monitored using 10 µM final concentration ThT.

2.5.2 Seeded growth of 2A and 3Q $A\beta_{40}$ fibrils

2A and 3Q $A\beta_{40}$ fibrils were produced using seeding reactions as described previously (Paravastu et al., 2008; Madine et al., 2012; Stewart et al., 2016), using original 2A and 3Q fibrils seeds kindly provided by Dr R. Tycko (NIH, Bethesda, USA). Lyophilised monomeric $A\beta_{40}$ and 5% (*v/v*) fibril seed of the desired morphology was resuspended in 25 mM sodium phosphate buffer (pH 7.5) to a final concentration of 0.9 mg/mL. This solution was sonicated 5 seconds on, 45 seconds off for 3 cycles at 22% amplitude (Sonics VCX 130 PB with 630-0422 probe). The sample was then incubated quiescently overnight at room temperature. After 18 h, the sample was sonicated again for 5 seconds at amplitude 22%. 2A and 3Q fibrils were stored at 4 °C until use.

2.5.3 Production of 2A and 3Q $A\beta_{40}$ fibril seeds

To maintain stocks of 2A and 3Q fibril seeds, fibril samples were sonicated 5 seconds on, 45 seconds off for three cycles one week after fibril synthesis. Fibril seeds were stored at -20 °C until use.

2.5.4 Formation of $A\beta_{40}$ E22Δ fibrils

$A\beta_{40}$ E22Δ fibrils were produced using conditions previously described in Schütz et al., 2015. Lyophilised $A\beta_{40}$ E22Δ monomer was resuspended in a reaction buffer of 10 mM NaH_2PO_4-NaOH pH 7.4, 100 mM NaCl to a final concentration of 60 µM. This was transferred to a 2 mL sterile glass vial and a sterile magnetic stirrer bar added. The vial was sealed and placed on a heater/stirrer in a mineral oil bath to maintain a constant temperature. The protein was stirred at 700 rpm, 37˚C for 24 h.

2.5.5 Formation of $A\beta_{42}$ fibrils

For the pH 2 $A\beta_{42}$ fibril preparation, fibrillation conditions described in Gremer et al., 2017 were reproduced. $A\beta_{42}$ monomer was solubilised in 30% (*v/v*) acetonitrile, 0.1% (*v/v*) TFA in water (pH 2) to a final concentration of 120.5 µM. This solution was left at room temperature to incubate quiescently for 48 h.

For the pH 8 $A\beta_{42}$ fibril preparation, fibrillation conditions described in Colvin et al., 2016 were reproduced. $A\beta_{42}$ monomer was solubilised in 20 mM sodium phosphate, 0.2 mM EDTA, 0.02% NaN_3, pH 8.0 to a final concentration of 50 µM. This solution was left at room temperature to incubate quiescently for 48 h.

2.5.6 Production of fluorescently labelled Aβ fibrils

To produce fibrils that are fluorescently labelled with ATTO 594, 1% of labelled $A\beta_{40}$ monomer was added into fibril reactions described above. Fibrils were then pelleted by centrifugation (as in Section 2.6.2). This was to identify the location of the labelled monomer, which appears as a clear blue colour. A blue pellet indicates that the labelled monomer has been incorporated into fibrillar material.

2.5.7 Sterile precautions taken in fibril preparation

To minimise the risk of microbial contamination all fibril preparations were carried out around a flame or in a laminar flow hood to ensure sterile conditions. All buffers were filter sterilised with a 0.22 µm syringe filter immediately before fibril preparation. The sonicator probe was autoclaved before use when making seeded fibrils. To check for microbial contamination, the LAL endotoxin test was performed on Aβ fibril samples (Section 2.6.5). Results of this test found endotoxin levels of fibril samples to consistently be below 1 EU/mL, with no significant differences between fibril samples. To further check for microbial contamination, samples of Aβ fibrils were added to agar plates and incubated at 37 °C for 72 h. Microbial growth was then monitored and results from this showed no significant differences in microbial growth between fibril preparations and buffer-alone, or between fibril samples. These precautions and evidence underlie a confident conclusion that the Aβ samples used in the experiments of this thesis lack microbial contamination.

2.6 Aβ fibril characterisation

2.6.1 Thioflavin T (ThT) aggregation assay

Fibril growth kinetics were monitored using ThT fluorescence. ThT was added to a final concentration of 10 μM to wells of a half volume 96-well plate (Costar 3881) containing 100 μL samples of fibril reactions described above (Section 2.5). Fluorescence was measured in a Clariostar microplate reader (BMG Labtech, Germany) set to bottom optics with excitation and emission filters of 440 nm and 475 nm respectively. The plate reader was set to 37 °C with orbital shaking at 600 rpm for monitoring $A\beta_{40}$ *de novo* fibril growth, whereas seeded reactions and $A\beta_{42}$ fibrils were monitored quiescently at room temperature.

2.6.2 Fibril yield assay

To identify how much of the Aβ monomer has been incorporated into an insoluble fibril form, fibril yield assays were performed. 100 μL of fibril sample was taken and 10 μL of this removed as the 'whole' fraction. The remaining 90 μL was then centrifuged at 16,873 xg (5418 R, Eppendorf) for 40 min. The supernatant was removed, being careful not to disturb the pellet, and 10 μL of this was set aside as the supernatant fraction. The pellet was then resuspended in 90 μL of 25 mM sodium phosphate (pH 7.5) buffer and 10 μL of this taken as the pellet fraction. These fractions were run on an SDS-PAGE gel, as outlined in Section 2.4.3.

2.6.3 Transmission electron microscopy (TEM)

Aβ fibrils were imaged by TEM using negative stain. Carbon-coated copper grids were prepared by Martin Fuller in the Astbury Biostructure Laboratory. Grids were glow-discharged before use, and 2% uranyl acetate was centrifuged for 5 min at 16,873 xg to clear any crystals. 10 μL of fibril sample was added to each grid and incubated for 30 sec. Grids were then washed twice in distilled water before staining with 2% uranyl acetate for 45 sec. Grids were then blotted and allowed to dry for at least 5 min. Images were acquired using a JEOL 1400 microscope with a 120 keV Lab6 filament and Gatan US1000XP 2k x 2k CCD camera, in the Astbury Biostructure Laboratory.

2.6.4 Oligothiophene fluorescence assays

Samples of fibril preparations were pelleted as described in Section 2.6.2 and resuspended in 25 mM sodium phosphate to a final concentration of 20 μM. 100 μL of samples were added to wells of a half volume 96-well plate (Costar 3881) and Amytracker dyes (Amytracker 480/Amytracker 520 – EbbaBiotech, Sweden) were added

at a final concentration of 0.5 μM. Samples were left for 10 min to equilibrate before emission spectra were recorded using a Clariostar microplate reader (BMG Labtech, Germany). For Amytracker 480, samples were excited at 430 nm and an emission spectrum recorded from 450-650 nm. For Amytracker 520, an excitation wavelength of 470 nm was used, and an emission spectrum was recorded from 490 – 640 nm.

2.6.5 Endotoxin measurements

Endotoxin levels of fibril samples were measured using the Pierce *Limulus* Amebocyte Lysate (LAL) Chromogenic Endotoxin Quantitation Kit (Thermo Scientific, MA, USA). All samples were measured at a final concentration of 1 μM. This assay was carried out as outlined in the manufacturers protocol and the absorbance read on a Clariostar microplate reader (BMG Labtech, Germany) at 405 nm. Endotoxin-free water was used as a blank and taken as 0 EU/mL and a series of endotoxin standards were used to plot a standard curve from which endotoxin values of experimental samples were calculated. 3 repeats were carried out for all samples, standards and blanks.

2.7 Cell culture

Details of the cell lines and the cell media used for the culture of each in this study are outlined in Table 2.4. All cells were maintained in T75 flasks (Corning, Germany) and incubated at 37 °C, 5 % CO_2. BV-2 and RAW 264.7 cells were cultured in Dulbecco's Modified Eagles media (DMEM), supplemented with 10% (*v/v*) foetal bovine serum (FBS Gold – PAA), 1% (*v/v*) 20 units/mL penicillin, 20 mg/mL streptomycin (Pen/Strep) and 1% GlutaMAX (Gibco, Thermo Scientific, MA, USA). All three THP-1 cell lines were cultured in Roswell Park Memorial Institute (RPMI) 1640 Medium (Gibco, Thermo Scientific, MA, USA), supplemented with 10% (*v/v*) FBS, 1% (*v/v*) Pen/Strep and 1% GlutaMAX. THP-1 ASCDef cells were also cultured in 100 μg / mL Zeocin (InvivoGen, France), and THP-1 ASC-GFP reporter cells were cultured with 200 μg / mL Hygromycin (InvivoGen, France). For imaging, phenol red-free DMEM/RPMI was used (Gibco, Thermo Scientific, MA, USA).

BV-2 cells were passaged by the removal of cell media and incubation with 5 mL of 1% trypsin-EDTA (Gibco, Thermo Scientific, MA, USA) for 5 min. Trypsin activity was quenched by the addition of 5 mL of cell media and cells were centrifuged for 5 min at 500 x g (5810R centrifuge, Eppendorf, UK). The cell pellet was resuspended in fresh cell media and split 1:20, to a final flask volume of 10 mL. RAW 264.7 cells were passaged by the removal of all but 5 mL of cell media, then by use of a cell scraper to remove cells from the flask surface. The cell suspension was then split 1:5 to a final flask volume of 20 mL. THP-1 cells are a suspension cell line, therefore were passaged by the

centrifugation of the cell media suspension and resuspension of the cell pellet in fresh cell media. This suspension was split 1:5 to a final flask volume of 20 mL.

Cell line name	Cell type	Source
BV-2	Murine microglial cells	Dr Ian Wood – University of Leeds. Authenticated by IDEXX BioAnalytics.
RAW 264.7	Murine macrophage leukaemia	American Type Culture Collection (ATCC)
THP-1	Human monocytic leukaemia	European Collection of Authenticated Cell Cultures (ECACC)
THP-1 ASCDef	Human monocytic leukaemia stably expressing an ASC:GFP fusion protein	InvivoGen
THP-1 ASC-GFP reporter cells	Human monocytic leukaemia with ASC Knockdown	InvivoGen

Table 2.4. Details of cell lines used in this study

2.8 Measurement of cell viability

For cell viability assays, 10,000 cells/well (BV-2/RAW 264.7 cells) or 30,000 cells/well (THP-1 cells) were plated into clear sterile 96-well plates (CytoOne, Starlab, UK) in 200 µL cell media. BV-2 and RAW 264.7 cells were incubated for 24 h before treatment to allow attachment, whereas THP-1 cells were treated immediately. Cells were treated with Aβ fibril preparations or the same volume of fibrillation buffers as negative control samples (100% viability). Cells were incubated with Aβ fibril or control samples for 48 h before the cell viability assays described below were performed. Positive control cells were lysed with 1% Triton X-100 (LDH lysis buffer – Thermo Scientific, MA, USA) 45 min before assays as a readout of 0 % viability.

To measure the effect of endotoxin on cell viability, endotoxin provided in the Pierce LAL Chromogenic Endotoxin Quantitation Kit (Thermo Scientific, MA, USA) was vortexed vigorously for 15 min before addition to cells at final concentrations of 0.1, 1, 3, 5 or 10 EU/mL. Cells were incubated for 48 h before cell viability assays described below were performed.

2.8.1 3-(4,5-Dimethylthiazol-2yl)-2,5-diphenyltetrazolium Bromide (MTT) Cell Viability Assay

20 µL of MTT (5 mg/mL) was added to cells following 48 h incubation with sample, and the plate incubated for a further 1 h at 37˚C, 5% CO_2. Cell media was then removed and replaced with 200 µL DMSO. The absorbance was then measured at 570 nm on a

Clariostar microplate reader (BMG Labtech, Germany) and the background signal at 650 nm subtracted from this.

2.8.2 ATP assay

The ATPLite Luminescence ATP detection system (PerkinElmer Life Sciences, UK) was used to measure cellular ATP levels. The assay was performed according to the manufacturer's instructions, in a white 96-well plate (Greiner Bio-One, UK). Luminescence was then measured on an OPTIMA plate reader (BMG Labtech, Germany).

2.8.3 LDH release assay

The Pierce LDH Cytotoxicity Assay Kit (Thermo Scientific, MA, USA) was used to measure LDH release from cells. This assay was performed according to the manufacturer's instructions, in a black Costar 96-well plate with a clear bottom. Absorbance was then measured on a Clariostar microplate reader (BMG Labtech, Germany) at 490 nm and the background signal absorbance at 680 nm subtracted from this.

2.8.4 Analysis of cell viability data

Data was normalised using cells treated with fibrillation buffers (Section 2.1.2) as 100% viability and values from lysed cells as 0% viability. GraphPad Prism Version 8 software was used to create graphs, with error bars representing standard error of the mean. A one-way ANOVA test and Tukey's multiple comparison test were used to determine statistical differences between Aβ fibril preparations, and a one-way ANOVA test with Sidak's multiple comparisons test was used to compare the viability of cells after incubation with Aβ fibrils compared to the viability of cells incubated with the equivalent volume of the corresponding fibril growth buffer.

2.9 Measurement of inflammatory activation

2.9.1 Enzyme-linked immunosorbent assays (ELISA)

For measurements of cytokine release, 5 x 10^4 cells/well THP-1 cells or 5 x10^3 cells/well BV-2 cells were plated in into clear sterile 96-well plates in 200 µL cell media. BV-2 cells were incubated for 24 h before treatment to allow attachment. For measurement of IL-1β release via the NLRP3 inflammasome, cells were primed for 3 h with 1 µg/ml LPS. Plates were then centrifuged for 5 min at 500 xg (5810R centrifuge, Eppendorf, UK), cell media removed and replaced with fresh media. Aβ fibril preparations or equivalent

volumes of fibrillation buffers were added to a final concentration of 2 μM and cells were incubated for a further 72 h at 37 ºC, 5% CO_2. Control cells were primed with 1 μg/ml LPS after 68 h for 3 h then were centrifuged for 5 min at 500 xg and replaced with fresh media. These control samples were then treated with 5 μM nigericin for 1 h incubation at 37 ºC, 5% CO_2. 72 h after fibril treatment, plates were centrifuged as previously described and supernatants were collected and stored at -80 ºC until use. Other cytokines (TNF-α and IL-6) were tested using the same protocol, but in the absence of an LPS priming step. Human IL-1β/IL-1F2 DuoSet ELISA, Human/Mouse TNF-α Duoset ELISAs and Human/Mouse IL-6 DuoSet ELISAs (R&D systems, UK) were performed according to the manufacturer's instructions, using 100 μL of cell supernatant, and read on a PowerWave XS2 microplate reader set to 450 nm (BioTek, UK).

2.9.2 Measurement of oxidative stress

THP-1/BV-2 cells were plated in clear sterile 96-well plates, as described in Section 2.9.1 and incubated with Aβ fibril preparations or fibril buffers for 24-72 h. H_2O_2 was added at a final concentration of 200 μM as a positive control, 1 h before the assay was carried out. CellRox Green (Thermo Fisher Scientific, MA, USA) was added at a final concentration of 5 μM to wells and the plates were incubated for 30 min at 37 °C. The cell media was then removed from all wells and cells were washed X3 with PBS before measurement on a Clariostar microplate reader (BMG Labtech, Germany) at 520 nm.

2.9.3 Confocal microscopy of ASC specks

5 x 10^5 THP-1 ASC-GFP reporter cells were plated in individual 35 mm diameter, 10 mm well glass-bottom dishes (FluoroDish™, Fisher Scientific, UK) in 2 mL of culture medium per dish. Cells were primed with 1 μg/mL LPS for 3 h then the cell media was removed, and cells were washed X1 in PBS. Cell media was then replaced with 2 mL phenol-red free cell media. Fibril preparations were added to dishes to a final concentration of 1 μM, or the equivalent volume of fibril buffer was added as a negative control. Cells were incubated for 72 h at 37 ºC before live-cell imaging was performed on samples. 4 h before imaging, positive control samples were primed for 3 h with 1 μg/ml LPS then treated with 5 μM nigericin to induce ASC speck formation. All samples were treated with 10 μg/mL Hoechst nuclear stain for a further 30 min at 37 ºC. Confocal imaging was performed on either an inverted Zeiss LSM880 or inverted Zeiss LSM700 microscope, using 10x/0.3 Ph1 Plan-Neofluar, M27, 20x/0.5 Ph2 Plan Neofluar, M27 and 40/1.3 Oil DIC Plan Apochromat, M27 objectives.

Laser and filter combinations were selected based on the fluorophores being used and gain settings were adjusted using control samples to remove any background signal.

Laser and gain settings were then kept consistent for all samples throughout the experiment. Images were processed and scale bars added in ZenBlack software. Analysis of speck number was carried out in Fiji software and data analysed using GraphPad Prism 8 software.

2.9.4 Measurement of the expression of activation markers using flow cytometry

125,000 THP-1 cells were plated in 48-well plates (Corning, Germany) and Aβ fibril preparations were added to a final concentration of 1 μM, 2 μM or 5 μM, or the equivalent volume of fibril buffer was added as a negative control. Interferon-γ (IFN- γ) (20 ng/mL) was added to cells as a positive control to induce expression of CD80 and MHC class II. Cells were incubated for 72 h at 37 ºC, 5% CO_2 before staining.

Cells were transferred to individual Eppendorf tubes and centrifuged for 5 min at 400 xg at 4 °C in a microcentrifuge (5418 R centrifuge, Eppendorf, UK). The supernatant was removed carefully by pipetting, and the cell pellet resuspended in 1 mL PBS 0.1 % bovine serum albumin (BSA) with mixing my pipetting. Centrifugation and wash steps were repeated X3 before cells were resuspended in 100 μL primary antibody diluted 1:100 in PBS 0.1 % BSA (CD80 Monoclonal Antibody MEM233 – Invitrogen / L243- anti-human HLA-DR Monoclonal Antibody – Invitrogen, Thermo Fisher, MA, USA). Cells were incubated for 1 h on ice then 3X centrifugation and wash steps were performed as described previously. Cells were then resuspended in 10 μL Goat anti-Mouse IgG Secondary antibody, Alexa Fluor 488 (Thermo Fisher, MA, USA). Samples were incubated for 1 h on ice, then 3X centrifugation and wash steps were repeated as previously before a final resuspension in 100 μL PBS 0.1 % BSA.

Cell-associated fluorescence was analysed by a CytoFLEX S flow cytometer using a 488 nm laser and 525/40 band pass filter. CytExpert software was used to record and analyse flow cytometry data. Control cells were used to gate the cell population to exclude debris. 10,000 gated events were recorded per sample, 3 flow cytometry experiments were performed in triplicate.

2.10 Assessing fibril uptake and degradation by cells

2.10.1 Live-cell imaging of Aβ fibril uptake and degradation by microglial cells

3 x 10^5 BV-2 cells were plated in individual 35 mm diameter, 10 mm well glass-bottom dishes (FluoroDish™, Fisher Scientific, UK) in 2 mL of culture medium per dish. Cells

were incubated for 24 h at 37 ºC before the addition of fibrils samples. 1% ATTO-594-Aβ fibrils were added to dishes to a final concentration of 1 μM, for 4 h. Control cells were incubated with non-labelled Aβ fibrils for the same period. Cells were then washed x 2 with PBS to remove non-cell associated ATTO-594-Aβ fibrils. Cells were either imaged immediately or incubated for a further 24 or 72 h in fresh culture medium at 37 ºC, 5% CO_2. Prior to imaging, cell media was replaced with 2 mL phenol-free media and incubated with a 1 μM final concentration of LysoTracker Green DND-26 (Thermo Fisher, MA, USA) and 10 μg/mL Hoechst nuclear stain for a further 30 min at 37 ºC. Confocal imaging was performed on either an inverted Zeiss LSM880 or inverted Zeiss LSM700 microscope, using a 40/1.3 Oil DIC Plan Apochromat, M27 objective.

Laser and filter combinations were selected based on the fluorophores being used and gain settings were adjusted using control samples to remove any background signal. Laser and gain settings were then kept consistent for all samples throughout the experiment. Images were processed and scale bars added in ZenBlack software.

2.10.2 Flow cytometry of Aβ fibril uptake and degradation by microglial cells

BV-2 cells were plated in 24-well plates (Corning, Germany) and incubated for 24 h at 37 ºC, 5% CO_2 before the addition of fibrils samples. 1% ATTO-594-Aβ fibrils were added to dishes to a final concentration of 1 μM, for 4 h. Control cells were incubated with non-labelled Aβ fibrils for the same period. Cells were then washed X2 with PBS to remove non-cell associated ATTO-594-Aβ fibrils. Cells were either analysed by flow cytometry immediately, or after 24 h or 48 h further incubation at 37 ºC, 5% CO_2. Cells were dissociated using Cell Dissociation Buffer (Gibco, Thermo Scientific, MA, USA).

Cell-associated fluorescence was analysed by a CytoFLEX S flow cytometer (Beckman Coulter, MA, USA) using a 561 nm laser with a 610-20 band pass filter. CytExpert software was used to record and analyse flow cytometry data. Control cells were used to gate the cell population to exclude debris and place a gate, above which cells were considered to be associated with ATTO-594 Aβ fibrils. 10,000 gated events were recorded per sample, 3 flow cytometry experiments were performed in triplicate.

2.11 Degradation of fibrils by lysosomal fractions

2.11.1 Subcellular fractionation and lysosome isolation

Lysosomes were isolated from BV-2 cells by subcellular fractionation on Percoll gradients as previously described but in the absence of carrier cells (Davidson et al.,

1990). ~1.0 x 10^8 BV-2 cells were homogenised in 1X homogenisation buffer (Section 2.1.2) by 10 passes through a stainless-steel ball bearing homogeniser with 10 µm clearance. A sample of homogenate was taken for use as a positive control in enzyme assays. The cell lysate was centrifuged for 10 min at 400 xg at 4 ºC in a microcentrifuge (5418 R centrifuge, Eppendorf, UK), and the supernatant was loaded onto 9 mL of 27% (*v/v*) Percoll in homogenisation buffer. Samples were then centrifuged for 1 h at 4 ºC, 36,289 xg in an Avanti J-HC centrifuge (Beckman Coulter, CA, USA) with a 70.1 Ti rotor. 20 x 0.5 mL fractions were collected and stored at 4 ºC while enzyme assays were carried out to identify lysosomal fractions. The NAGA and alkaline phosphatase enzyme activities were measured as described in Sections 2.11.2.1 and 2.11.2.2 respectively.

Fractions with the highest NAGA activity were pooled and centrifuged for 1 h at 214,000 xg in an Optima Ultracentrifuge equipped with a TLA110 rotor (Beckman Coulter, CA, USA). The resulting concentrated lysosomal fraction was extracted and stored at -80 ºC. Lysosomes were freeze-thawed x3 before use to disrupt the membranes and thus release their contents.

2.11.2 Assays of marker enzymes in gradient fractions

2.11.2.1 NAGA assay

The activity of NAGA, a lysosomal marker, was determined in each subcellular fraction (2.11.1) to identify lysosomal fractions and quantify lysosomal activity. 10 µL of each subcellular fraction was added to 100 µL of 2 mM NAGA substrate (4-nitrophenyl N-acetyl-β-D-glucosaminide) in NAGA substrate buffer (Section 2.1.2) in a clear, sterile 96-well plate (CytoOne – Starlab). Crude homogenate or homogenisation buffer were used as positive and negative control respectively. The plate was incubated at 37 ºC for 30 min and the reaction stopped with 200 µL of NAGA stop buffer (Section 2.1.2). The absorbance of the samples was read at 405 nm using a Clariostar plate reader (BMG Labtech, Germany).

2.11.2.2 Alkaline phosphatase assay

The activity of alkaline phosphatase, a membrane marker, was measured in each subcellular fraction (Section 2.11.1) to assess the purify of fractions. 10 µL of each subcellular fraction was added to 100 µL 5 mM alkaline phosphatase substrate (4-nitrophenyl phosphate) in alkaline phosphatase substrate buffer (Section 2.1.2). The plate was incubated at 37 ºC for 30 min and the absorbance of the samples read at 405 nm using a Clariostar platereader (BMG Labtech, Germany).

2.11.3 Degradation of Aβ fibrils by lysosomal fractions

NAGA units were used to standardize the amount of lysosomal enzymes added to each experiment. The NAGA activity of 0.1 µL lysosome extract was measured in 100 µL NAGA substrate as described above. A NAGA unit is defined as the absorbance of this sample read at 405 nm after 30 min incubation at 37 °C. Fibril samples were pelleted by centrifugation at 16,873 xg for 40 min (5418 R centrifuge, Eppendorf) and resuspended in 100 mM ammonium acetate, pH 4.5, at a final concentration of 200 µM. Fibrils were incubated in the presence of lysosome extract containing 0.083 NAGA units in a total volume of 60 µL, at 37 ºC for 0-48 h. 15 µL samples were taken at 0 h, 4 h, 24 h and 48 h and added to equal volumes of SDS-PAGE loading buffer (Section 2.1.2). Samples were then boiled for 5 min and resolved on 15% Tris-Tricine gels (Section 2.4.3) to analyse digestion products. Densitometry was performed using Fiji software and the percentage reduction in the main Aβ peptide band was calculated in relation to 0 h samples.

3 Formation of distinct Aβ fibril preparations

3.1 Introduction

Distinct molecular structures have been identified for Aβ fibrils both *in vitro* and *ex vivo,* suggesting that Aβ fibril polymorphism occurs in the diseased brain (Petkova et al., 2005; Paravastu et al., 2008; Lu et al., 2013; Qiang et al., 2017; Rasmussen et al., 2017; Kollmer et al., 2019). However, the significance of this polymorphism in Alzheimer's is not well understood. Whilst *in vitro* structures differ from those extracted from patient tissue, the conditions used to form *in vitro* structures, and structural models of the fibrils resulting from these conditions, are well defined. Therefore, this work used fibrils made *in vitro*, made under conditions which had previously been shown to produce populations of fibrils with distinct structures. These distinct Aβ polymorph preparations were then compared in order to determine if they exhibit functional differences and thus whether structural polymorphism of fibrils is a key determinant of their biological properties.

Preparations of fibrils formed by the two most prominent Aβ peptides in Alzheimer's disease, $A\beta_{40}$ and $A\beta_{42}$, were analysed in this study. The $A\beta_{40}$ fibrils studied in this work were seeded from 2A and 3Q fibrils, and a *de novo* fibril population produced in the absence of seeding was also studied. The 2A fibrils were originally formed under agitated conditions and resulted in fibrils with a 2-fold symmetry, whereas 3Q fibrils were produced under quiescent conditions and resulted in fibrils with a 3-fold symmetry (Petkova et al., 2002; Paravastu et al., 2008, 2009). The structural models for these fibril polymorphs were produced using measurements from ssNMR and TEM (shown in Figure 3.1). 2A and 3Q fibrils have been reproduced in-house using seeds of these fibrils kindly provided by Dr R. Tycko (NIH Bethesda USA) and the ssNMR spectra of these were reported to be consistent with the published 2A and 3Q structural models (Stewart et al., 2017).

Differences between the 2A and 3Q fibril structures exist beyond symmetry, in some quaternary contacts and the conformation of non-β strand segments (Table 1.1). The *de novo* fibril preparation is formed under agitated conditions and is thought to contain a mixture of fibril polymorphs (Petkova et al., 2005; Stewart et al., 2017), however the ^{13}C-^{13}C dipolar assisted rotational rationale ssNMR spectrum has been shown to differ for these fibrils compared to those for 2A and 3Q populations (Madine et al., 2012).

In addition, a fibril polymorph preparation formed from $A\beta_{40}$ with the familial Osaka AD mutation, E22Δ, was also studied (Figure 3.1) (Schütz et al., 2015). The familial Osaka mutation results in the deletion of residue 22 in the Aβ sequence (APP E693Δ), and has been associated with early-onset AD (Tomiyama et al., 2008). Fibrils formed from $A\beta_{40}$

with this E22Δ mutation have been structurally characterised using ssNMR, and the resulting structural model is distinct from that for all other $A\beta_{40}$ structures formed from the full-length peptide (Figure 3.1) (Petkova et al., 2002, 2005; Paravastu et al., 2008, 2009; Ovchinnikova et al., 2011; Schütz et al., 2015). This indicates that the deletion of this residue alters the arrangement of Aβ monomer within the fibril structure, resulting in a distinct fibril population. These Osaka $A\beta_{40}$ fibrils were therefore also used to explore the biological consequences of fibril polymorphism.

$A\beta_{42}$ is often considered to be more relevant in Alzheimer's disease due to its higher hydrophobicity and rate of aggregation (Jarrett et al., 1993; Iwatsubo et al., 1994). Therefore, two *in vitro* formed $A\beta_{42}$ fibril preparations were produced and analysed in this study. One was formed at pH 2, and the other formed at pH 8, with the resultant fibrils shown to possess distinct morphologies (Figure 3.1) (Colvin et al., 2016; Gremer et al., 2017). These fibril populations were formed under quiescent incubation of $A\beta_{42}$ monomer either in 30% v/v acetonitrile, 0.1% (v/v) TFA (pH 2) or in sodium phosphate (pH 8) (Colvin et al., 2016; Gremer et al., 2017). The resulting structures both consist of two subunits, but in the pH 2 $A\beta_{42}$ fibrils these subunits are staggered and arranged in an LS-shape with 2_1 screw symmetry, whereas those in the pH 8 fibrils are in an S-shaped arrangement, with 2-fold symmetry (Colvin et al., 2016; Gremer et al., 2017).

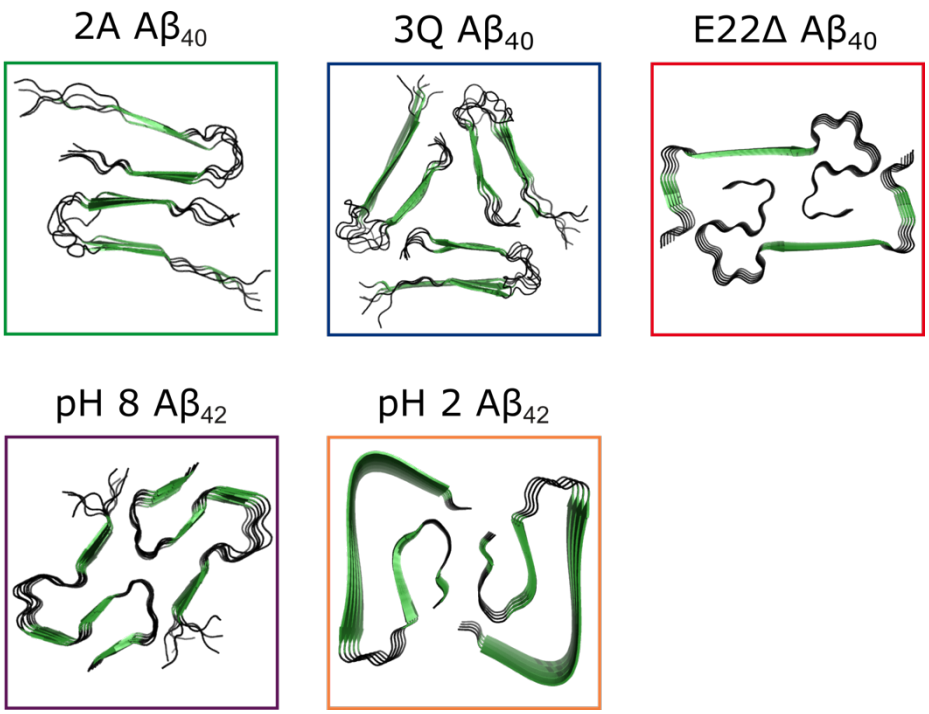

Figure 3.1 $A\beta_{40}$, $A\beta_{40}$ E22Δ and $A\beta_{42}$ fibril polymorphs
Molecular structures of Aβ fibril polymorphs formed under the conditions used in this study. From left to right - 2A $A\beta_{40}$ (PDB 2LMN/2LMO), 3Q $A\beta_{40}$ (PDB 2LMP/2LMQ), Osaka E22Δ $A\beta_{40}$ fibrils (PDB 2MVX), $A\beta_{42}$ fibrils formed at pH 8 (PDB 5KK3) and $A\beta_{42}$ fibrils formed at pH 2 (PDB 5OQV). green areas are representative of β-sheet structure and black areas are representative of loop regions.

3.2 Expression of Aβ peptides

In order to produce Aβ fibril polymorph preparations, the $A\beta_{40}$, $A\beta_{40}$ E22Δ and $A\beta_{42}$ peptides were expressed in *E. coli* and purified (Walsh et al., 2009). This involved the transfection of BL21 (DE3) *E. coli* with a pET-Sac vector containing either the $A\beta_{40}$ or $A\beta_{42}$ sequence, as described in Section 2.3.1. For the E22Δ peptide, site-directed mutagenesis was used to delete the nucleotides encoding residue 22 from the $A\beta_{40}$ DNA sequence (Section 2.2.1), and then BL21 (DE3) were transformed with the resultant pET-Sac E22Δ vector. Amino acid sequences of the three peptides expressed are shown in Figure 3.2.

$A\beta_{40}$ M-DAEFRHDSGYEVHHQKLVFFAEDVGSNKGAIIGLMVGGVV

E22Δ $A\beta_{40}$ M-DAEFRHDSGYEVHHQKLVFFADVGSNKGAIIGLMVGGVV

$A\beta_{42}$ M-DAEFRHDSGYEVHHQKLVFFAEDVGSNKGAIIGLMVGGVVIA

Figure 3.2. Amino acid sequences of $A\beta_{40}$, E22Δ $A\beta_{40}$ and $A\beta_{42}$ peptides

An ATG initiation codon was included at the start of all three Aβ sequences, in order to facilitate expression of the peptides. Therefore, all of the Aβ peptides had an exogenous N-terminal methionine. However, it has been previously shown that this N-terminal Met does not affect the kinetics of fibril formation of $A\beta_{40}$ or $A\beta_{42}$, or the morphology of the fibrils produced (Walsh et al., 2009). In addition, recombinant Met-$A\beta_{40}$ and Met-$A\beta_{42}$ aggregates led to nearly identical levels of MTT reduction in hippocampal neurons as those formed in the same way but without an N-terminal Met (Walsh et al., 2009). This shows that the natural N-terminal aspartic acid does not govern toxicity (Walsh et al., 2009). Furthermore, ^{13}C chemical shifts obtained from 3Q fibrils formed from Met($A\beta_{40}$) expressed in this way were consistent with those previously obtained for 3Q fibrils, showing that expressing Aβ using this system does not alter fibril structure (Stewart et al., 2017). Met($A\beta_{40}$) peptide will henceforth just be referred to as $A\beta_{40}$ for simplicity.

After transformation a single colony was used to inoculate cultures which were then grown on a large scale and expression was induced using IPTG (Section 2.3.1). Cultures were allowed to grow for a further 4-5 hours after induction, and expression was confirmed using SDS-PAGE (Figure 3.3).

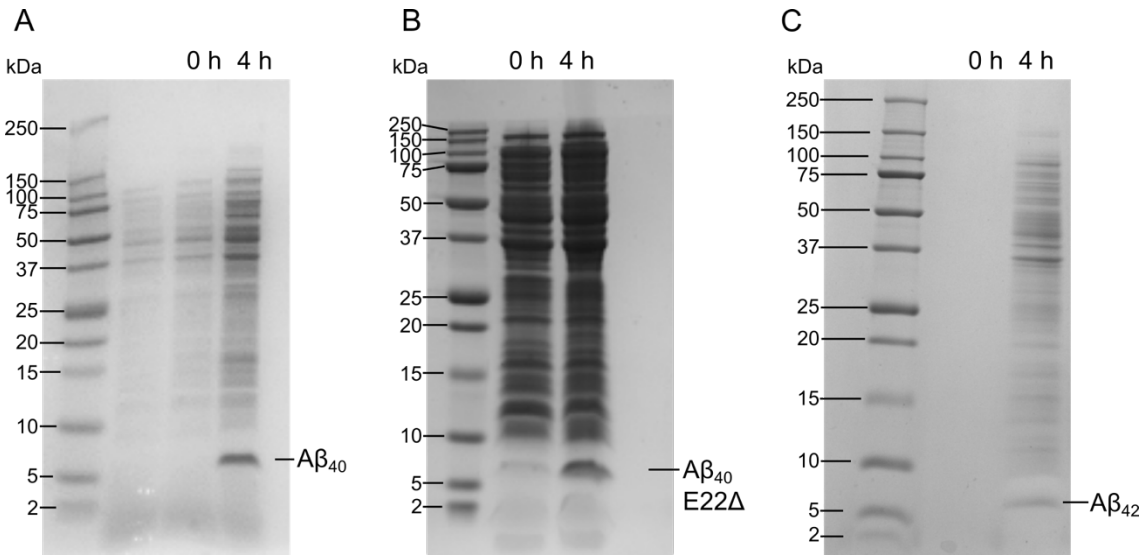

Figure 3.3. Expression of Aβ peptides in *E. coli*
BL21 (DE3) *E. coli* were transformed with (A) pET-Sac vector containing Met($A\beta_{40}$) sequence (B) pET-Sac vector containing Met($A\beta_{40}$-E22Δ) sequence or (C) pET-Sac vector containing Met($A\beta_{42}$) sequence and cultured in LB media. Expression was induced in cultures with 0.1M IPTG and cells were cultured for a further 4h at 37°C, shaking at 200 rpm after induction. Samples were taken before and after induction and resolved using SDS-PAGE on a 15% Tris-Tricine gel stained with Instant Blue Coomassie.

3.3 Purification of Aβ peptides

Aβ peptides aggregate into inclusion bodies when expressed in *E. coli*, therefore the first step in each purification required the isolation of these inclusion bodies. The methods used to purify $A\beta_{40}$ and $A\beta_{42}$ peptides then diverge and are summarised in Figure 3.4.

3.3.1 Purification of $A\beta_{40}$ and $A\beta_{40}$ E22Δ

The same methods of purification were used for both $A\beta_{40}$ and $A\beta_{40}$ E22Δ and are based on methods described by *Walsh et al, (2009)*. In order to isolate inclusion bodies two rounds of homogenisation, sonication and centrifugation steps were performed on harvested *E.coli* cultures (Section 2.3.2.1). 8M urea was then used for inclusion body solubilisation, followed by a final sonication and centrifugation step. Batch mode ion-exchange (IEX) chromatography was then performed, as described in Section 2.3.3, using a Q-Sepharose resin. A series of wash steps were performed before 125 mM NaCl was used to elute Aβ peptide from the resin. Samples were taken after each step of this process and analysed using SDS-PAGE in order to monitor the presence of Aβ peptide in each fraction (Figure 3.5). This showed that less $A\beta_{40}$ E22Δ peptide was eluted than wild type $A\beta_{40}$ peptide under the same conditions, indicating that the loss of the E22 residue causes $A\beta_{40}$ to bind more strongly to the Q-Sepharose resin and a higher concentration of NaCl should be used for elution of E22Δ $A\beta_{40}$ in future (Figure 3.5B). This analysis confirms the successful elution of $A\beta_{40}$ peptide, but also shows the

presence of impurities, highlighting the requirement for further purification steps (Figure 3.5).

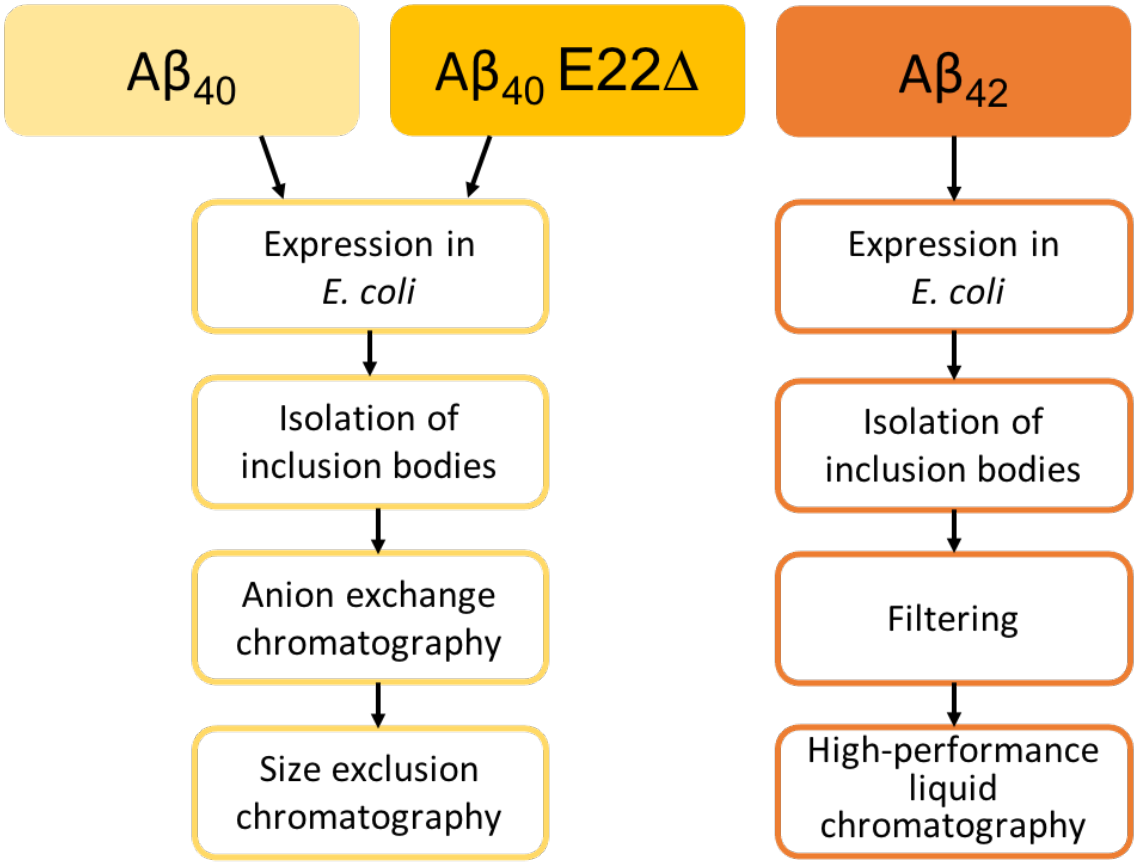

Figure 3.4 Steps of Aβ peptide purification
Different purification methods were used to purify recombinantly expressed $A\beta_{40}$ and $A\beta_{42}$ peptides from *E. coli*. After isolation of inclusion bodies, $A\beta_{40}$ and $A\beta_{40}$ E22Δ samples were processed by anion exchange chromatography followed by size-exclusion chromatography. $A\beta_{42}$ samples were instead first filtered, then purified by HPLC.

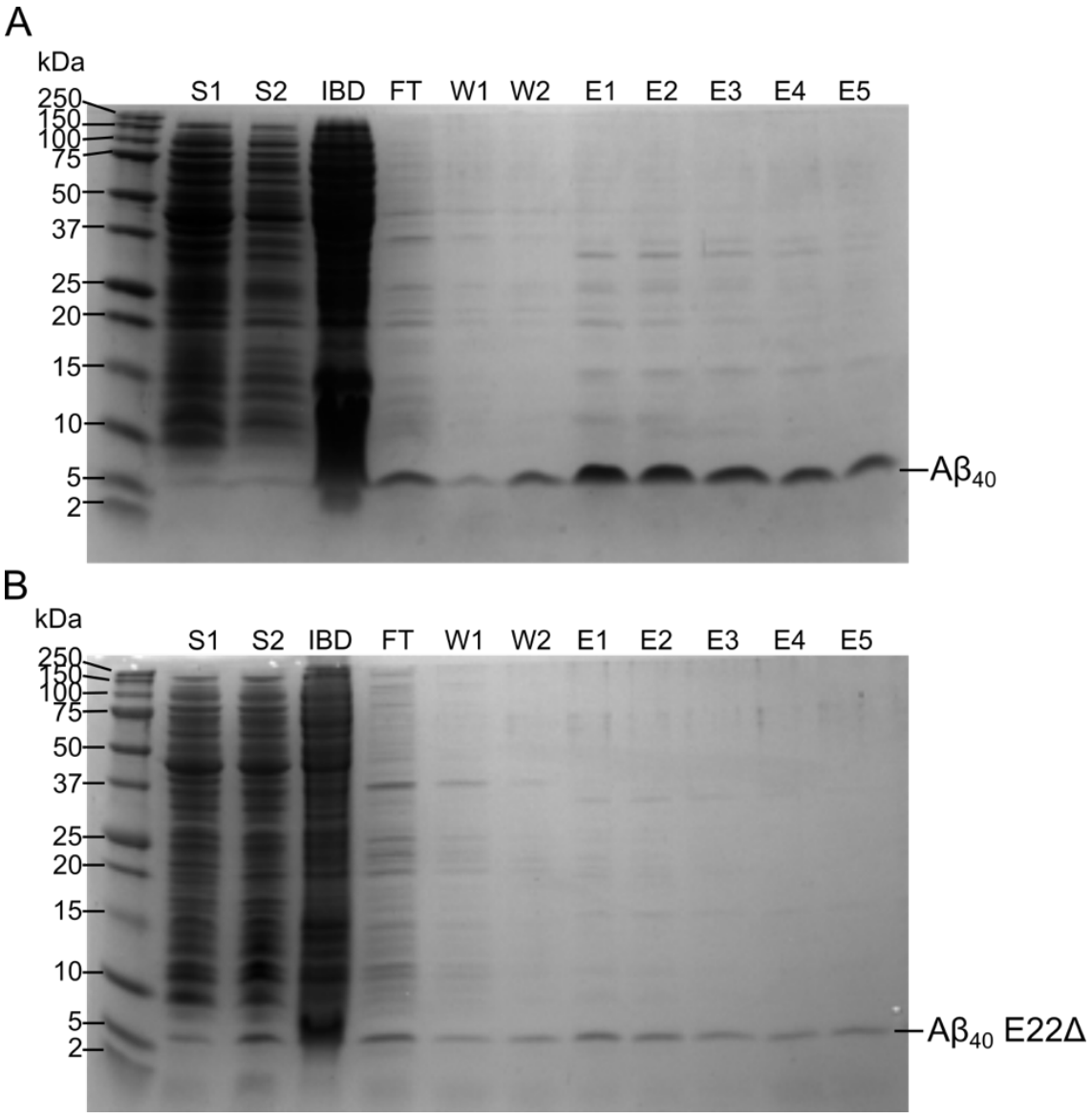

Figure 3.5. Inclusion body solubilisation and ion-exchange chromatography of Aβ40 and Aβ40 E22Δ peptides

E. coli cultures were harvested 4 h after induction of expression of (A) Aβ40 and (B) Aβ40 E22Δ, and subjected to sonication and centrifugation cycles to isolate inclusion bodies. Samples of supernatant from these steps were collected (S1/S2). Inclusion bodies were then solubilised using 8M urea (IBD – inclusion body denaturant). The resulting solution was allowed to bind to Q-Sepharose resin before ion exchange chromatography was performed in batch mode, with samples taken from flowthrough (FT), wash steps (W1/W2) and elution steps (E1-E5). W1 was performed with 10 mM Tris HCl, 1 mM EDTA, pH 8.5 (Buffer A). W2 was performed with 25 mM NaCl in Buffer A. Elution steps E1-E5 were performed using 125 mM NaCl in Buffer A.

Following IEX, $A\beta_{40}$ and $A\beta_{40}$ E22Δ samples were dialysed and lyophilised (Section 2.3.4). In order to eliminate remaining impurities, samples were then resuspended in buffer containing 7M guanidine HCl and subjected to size exclusion chromatography (SEC). This process was previously reported to be efficient in obtaining a homogenous monomeric Aβ solution (Walsh et al., 2009). The predicted elution volume for $A\beta_{40}$ corresponds to the prominent peak shown on the SEC trace in Figure 3.6A, at 210 mL. Fractions corresponding to this peak were collected and samples taken from these for SDS-PAGE analysis. Figure 3.6B shows that a single band results from these samples, just above 5 kDa, as expected for $A\beta_{40}$. These samples were analysed by electrospray ionisation mass spectrometry, which confirmed a mass of 4460 ± 1 Da, consistent with the predicted mass of Met-$A\beta_{40}$ (4459.21 Da) (Figure 3.6C).

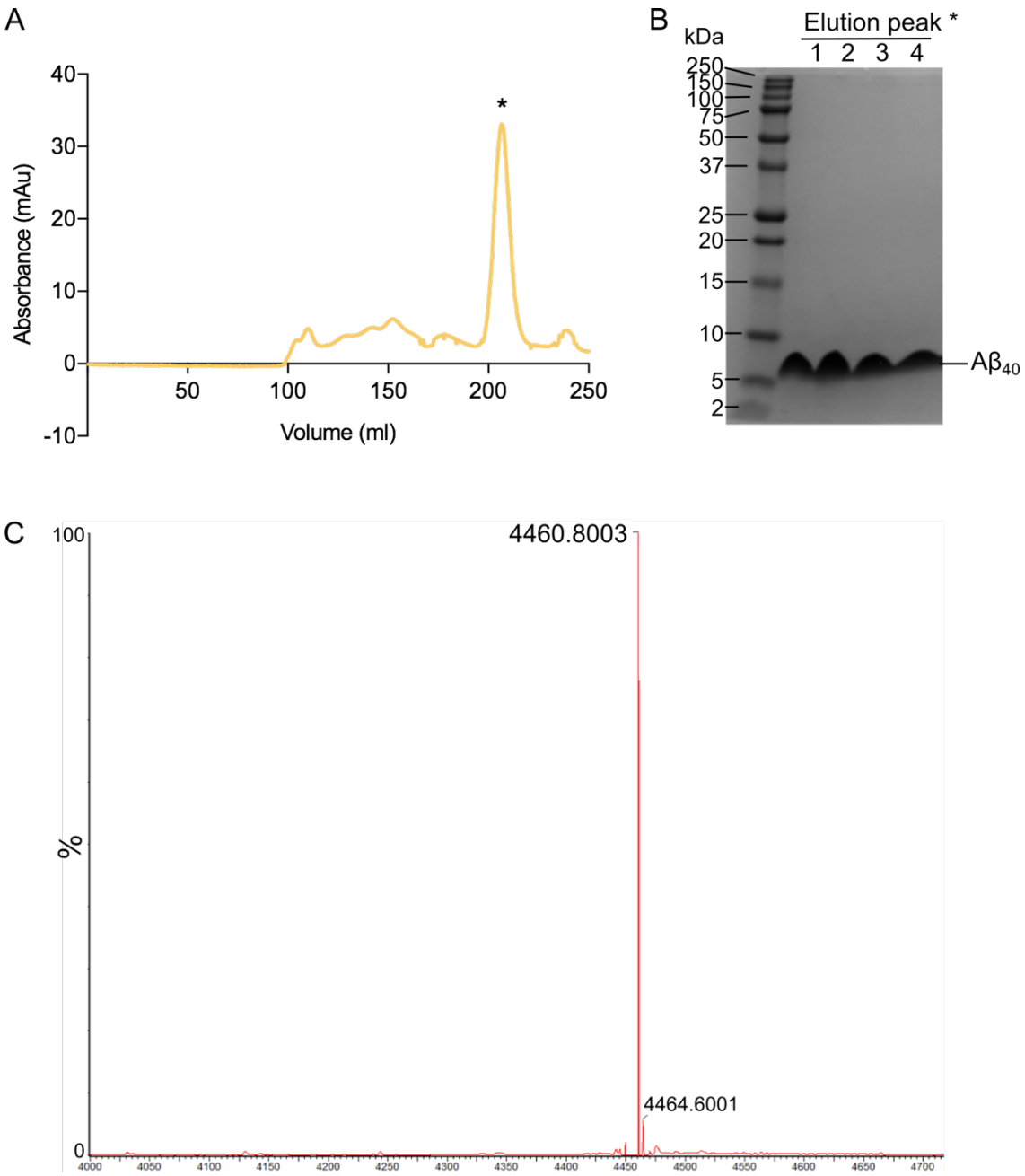

Figure 3.6. SEC purification of Aβ$_{40}$ peptide
Aβ$_{40}$ samples following IEX were dialysed, lyophilised and resuspended in buffer containing 7M guanidine HCl. 5 mL of sample was injected per run into an AKTA prime purification system connected to a Superdex 75 16/60 SEC column equilibrated in 50 mM ammonium bicarbonate at 4 °C (A) Chromatogram of one 5 mL sample run through the SEC column. Monomeric Aβ$_{40}$ elution is evident at the prominent peak at 210 mL, marked * (B) Aβ$_{40}$ peaks (*) were collected from 4 consecutive 5 mL sample runs through the SEC column (1-4) and samples from these were analysed on a 15% Tris-Tricine SDS-PAGE gel. A single band evident just above the 5 kDa marker is consistent with Aβ$_{40}$ (C) Deconvoluted mass spectrum from ESI-MS of collected sample (*) confirms a molecular weight of 4460 Da, as expected for Met-Aβ$_{40}$ monomer.

SEC was carried out on post-IEX $A\beta_{40}$ E22Δ samples as described for $A\beta_{40}$ (Figure 3.7). SDS-PAGE confirmed the presence of a single species, which when analysed by mass spectometry had a mass of 4331 ±1 Da, consistent with the predicted mass of 4331.93 Da for Met($A\beta_{40}$) E22Δ (Figure 3.7). As can be seen when comparing Figures 3.6 and 3.7, the yield of $A\beta_{40}$ E22Δ peptide was lower than that for the wild type $A\beta_{40}$ protein, with typical yields for wild-type peptide ~2-3 mg/L, compared to ~1 mg/L for $A\beta_{40}$ E22Δ.

Both $A\beta_{40}$ and $A\beta_{40}$ E22Δ peptides were lyophilised and stored at -20 °C until use.

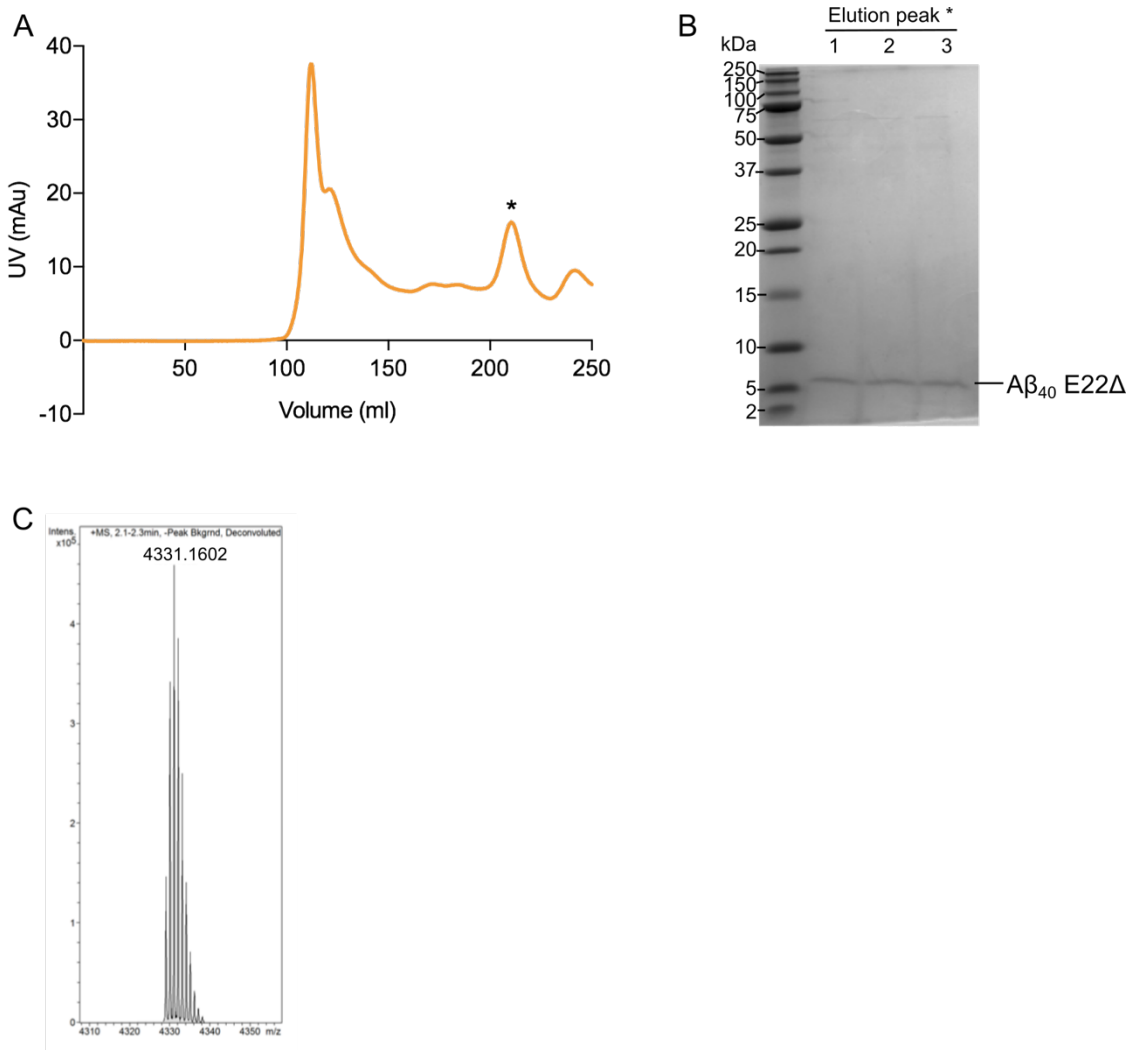

Figure 3.7. SEC purification of $A\beta_{40}$ E22Δ peptide
$A\beta_{40}$ E22Δ samples following IEX were dialysed, lyophilised and resuspended in buffer containing 7M guanidine. 5 mL of sample was injected per run into an AKTA prime purification system connected to a Superdex 75 16/60 SEC column equilibrated in 50 mM ammonium bicarbonate at 4 °C (A) Chromatogram of one 5 mL sample run through the SEC column. Monomeric $A\beta_{40}$ E22Δ elution is evident at the prominent peak at 210 mL, marked *. (B) $A\beta_{40}$ E22Δ peaks (*) were collected from 3 consecutive 5 mL sample runs through the SEC column (1-3) and samples from these were analysed on a 15% Tris-Tricine SDS-PAGE gel. A single band evident just above the 5 kDa marker is consistent with $A\beta_{40}$ E22Δ (C) Deconvoluted mass spectrum from LC-ESI-MS of collected sample (*) confirms a molecular weight of 4331 Da, as expected for Met-$A\beta_{40}$ E22Δ monomer.

3.3.2 Purification of $A\beta_{42}$

A different approach was used to purify $A\beta_{42}$ peptide, which was based on methods described in *Yoo et al, 2018.* As for $A\beta_{40}$, this method also produces recombinant peptide containing an exogenous N-terminal methionine – Met($A\beta_{42}$). This Met($A\beta_{42}$) will henceforth just be referred to as $A\beta_{42}$ for simplicity. The presence of this N-terminal Met has been shown to have no demonstratable effect on $A\beta_{42}$ aggregation or fibril structure (Silvers et al., 2017). This method resulted in significantly higher yields of $A\beta_{42}$ than the previous method used for $A\beta_{40,}$ and requires only half of the preparation time, making it more efficient.

Following bacterial expression of $A\beta_{42}$, cells were lysed and inclusion bodies isolated by a series of four repeated sonication and centrifugation steps (Section 2.3.2.2). Some $A\beta_{42}$ peptide was lost in this process (Figure 3.8A), leading to optimisation of the protocol involving only 2-3 wash steps. The final inclusion body pellet was originally resuspended in 8M urea in early purifications and filtered through a 0.22 µm PVDF filter (Merck) before HPLC purification (Section 2.3.6). However, this step was optimised, and the protocol adapted so that the inclusion body pellet was instead dissolved in 7mM NaOH. This solution was sonicated and centrifuged before loading directly onto an HPLC column as outlined in Section 2.3.2.2 (Figure 3.8B).

HPLC of the dissolved inclusion bodies (Section 2.3.6) resulted in three peaks observable on the HPLC trace, and LC-MS indicated that the first peak (*) at ~3.5 min corresponds to $A\beta_{42}$ monomer (Figure 3.8B). Running the HPLC purified $A\beta_{42}$ peptide again on the HPLC column resulted in a single peak, consistent with the first peak seen in the HPLC of crude solution (Figure 3.8C). Purified peptide from this peak was analysed by LC-MS, confirming a mass of 4644.25 Da, consistent with the predicted mass for Met-$A\beta_{42}$ of 4645 Da (Figure 3.8D). This shows that pure $A\beta_{42}$ has been obtained for use in fibril reactions. Ion-adducts visible in the mass spectrum are very low abundance and did not affect fibrillation. A yield of ~7 mg/L bacterial culture of pure $A\beta_{42}$ was obtained using this purification method. Purified peptide was lyophilised and stored at -20 °C until use.

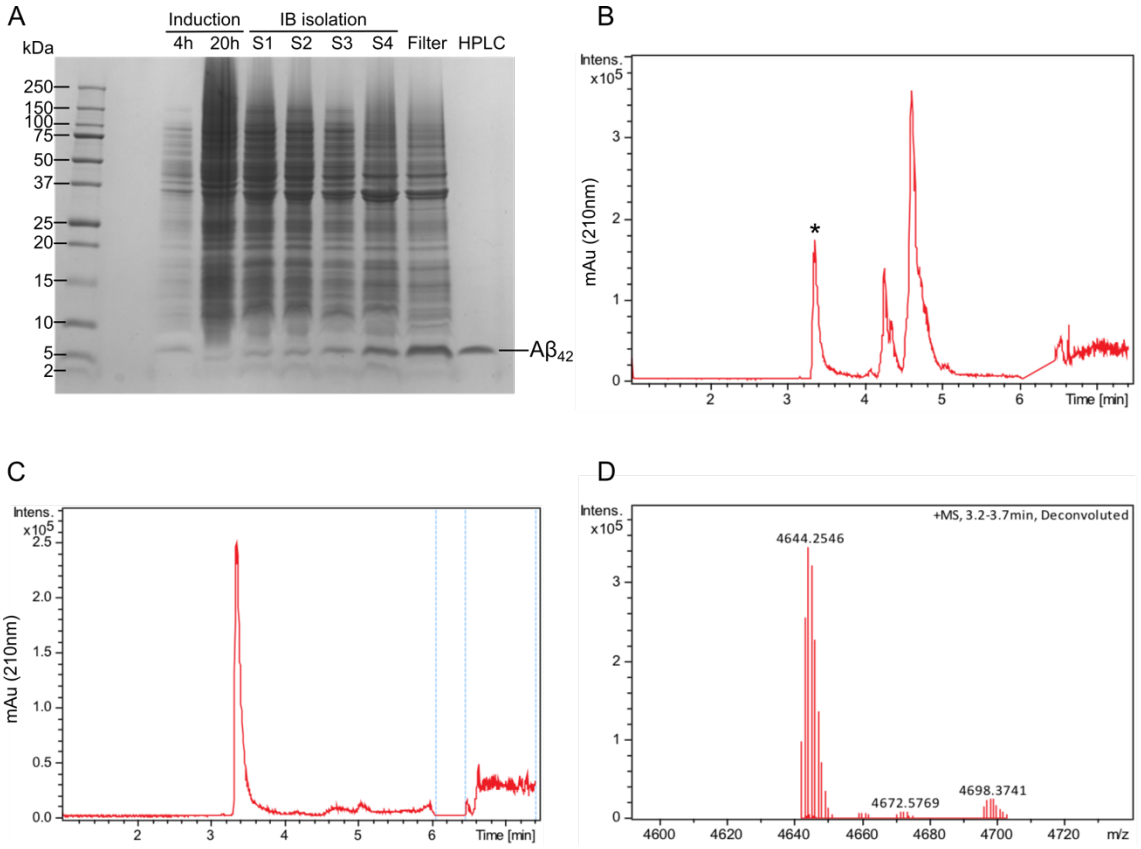

Figure 3.8. Purification of Aβ$_{42}$ peptide by preparative HPLC
Samples were taken from steps of Aβ$_{42}$ purification and resolved by SDS-PAGE on a 15% Tris-Tricine gel (A) Met(Aβ42) expression was induced in *E. coli* and cells harvested after 20 h (Induction). Four cycles of sonication and centrifugation were then carried out in order to isolate inclusion bodies (S1-S4). Inclusion bodies were solubilised using 8M urea and the solution filtered through a PVDF membrane (Filter). This crude solution was loaded onto a Kinetex EVO C18 column and HPLC performed using a 10-30% acetonitrile gradient in water with 0.1% ammonia (HPLC). The first eluting peak (*) on the LC trace (210 nm mAu) of the filtered solution was shown to correspond to Aβ$_{42}$ monomer (B). HPLC of purified Aβ$_{42}$ shows a single peak consistent with * (C). Deconvoluted mass spectrum of purified Aβ$_{42}$ confirms the observed mass is consistent with the predicted mass of 4645 Da for the Met- Aβ$_{42}$ monomer (D). Metal ion adducts were observed in a low abundance after purification (4672.5 and 4698.3 Da). HPLC was performed with the help of Dr Martin Walko (School of Chemistry - University of Leeds).

3.4 Fibril formation and characterisation

Following the production of pure recombinant Aβ$_{40}$, Aβ$_{40}$ E22Δ and Aβ$_{42}$ monomers, these peptides were used in fibril reactions to form Aβ fibril preparations for use in experiments to study cellular responses. Conditions were used which were described previously to result in fibrils with structures that are distinctive (Paravastu et al., 2008, 2009; Schütz et al., 2015; Colvin et al., 2016; Gremer et al., 2017).

3.4.1 Formation of Aβ$_{40}$ fibrils

Three fibril populations were formed from the Aβ$_{40}$ peptide: *de novo*, 2A and 3Q fibrils. *De novo* fibrils were formed by the simple shaking of Aβ$_{40}$ monomer in solution at 37°C

as desribed in Section 2.5.1 (Stewart et al., 2017), whereas 2A and 3Q fibrils were produced in seeding reactions with seed provided by Dr R.Tycko (NIH, Bethesda, USA). Seeding reactions consisted of 5% (v/v) seed of the desired fibril structure (2A or 3Q), added to purified $A\beta_{40}$ monomer. This removes the nucleation phase of fibril growth and results in the propagation of fibrils with the same intrinsic molecular structure as the seed (Petkova et al., 2005; Paravastu et al., 2008, 2009; Qiang et al., 2013; Tycko, 2014). A member of the Radford lab has previously demonstrated that 3Q fibrils produced using this seeding method were consistent with the structure of 3Q fibrils originally described when analysed by ssNMR (Stewart et al., 2017).

The kinetics of fibril growth was monitored for all fibril preparations with ThT, a widely used amyloid-specifc dye (Biancalana and Koide, 2010). ThT binds to the beta-sheet structure of amyloid fibrils, sterically locking the dye by immobilising rotation of the molecule about the carbon-carbon bond between benzylamine and benzathiole rings (Figure 3.9A) (Biancalana and Koide, 2010). This increases the lifetime of the excited state, resulting in increased fluorescence. Monitoring with ThT confirms that monomeric Aβ has aggregated into amyloid species with a cross-β structure and was also used to check consistency and reproducibility of fibril growth kinetics between fibril batches.

ThT monitoring of *de novo* fibril assembly reactions shows that fibrillation of $A\beta_{40}$ monomer has a lag time of ~5 hours at the 200μM concentration used in these experiments (Figure 3.9B). When the experimental data are fitted to a sigmoidal function and lag time (t_{lag}) defined as the point in time where the signal relative to the pre-transition base line reaches 10% amplitude, t_{lag} is calculated to be 4.58 h. A number of factors including protein concentration, salt, pH, temperature and shaking can all affect the length of the lag phase, making it difficult to compare between studies, however this lag time is within the expected range for $A\beta_{40}$ (Walsh et al., 2009; Bunce et al., 2019).

$A\beta_{40}$ fibril seeds were produced by diluting fibrils of the 2A or 3Q morphology (originally gifted from Dr R. Tycko) to 5% (v/v) in $A\beta_{40}$ fibrillation buffer and sonicating for 5 s “on,” 45 s “off” for 3 cycles at amplitude 20%. This results in shortened fibrils, which are then used to form full-length fibrils by elongation (Paravastu et al., 2008; Stewart et al., 2017). When 5% (v/v) fibril seed (2A or 3Q) is added to the $A\beta_{40}$ fibril assembly reaction, a loss of lag phase is observed and a rapid and immediate increase in ThT fluorescence occurs, indicating that the fibril seeds are elongated by $A\beta_{40}$ monomer. This is shown for 2A fibril growth in Figure 3.9C and is representative of ThT growth kinetics seen for both 2A and 3Q fibril growth. This trace is consistent with that of a seeding reaction, confirming the propagation of 2A and 3Q fibril seeds rather than the formation of fibrils ‘*de novo’* (Figure 3.9C) (Arosio et al., 2015; Stewart et al., 2017).

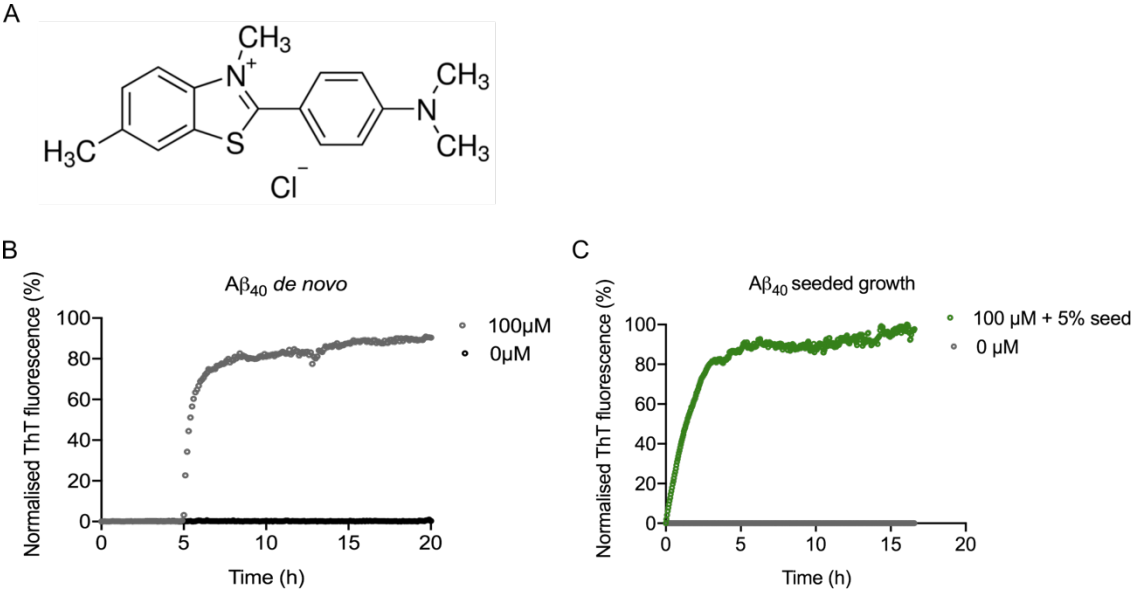

Figure 3.9. ThT monitoring of *de novo* and seeded Aβ$_{40}$ fibril growth
(A) Molecular structure of ThioFlavin T (ThT). (B) Fibril growth kinetics of 100 μM monomeric Aβ$_{40}$ incubated at 37°C with orbital shaking, exhibiting a lag time of ~5 h and reaching a plateau within 8 h. (C) Fibril growth kinetics of 100 μM monomeric Aβ$_{40}$ with 5% (v/v) 2A fibril seed at room temperature showing immediate entry into the growth phase as fibril seeds are propagated. A growth plateau is reached at ~5 h. Both reactions were carried out in 25 mM sodium phosphate buffer (pH 7.5) with 10 μM final concentration ThT. 0 μM samples represent buffer without the addition of Aβ$_{40}$ monomer.

3.4.2 Characterisation of Aβ$_{40}$ fibrils

Following fibril formation, further characterisation of fibrils was carried out. Fibril yields were determined by the centrifugation of fibril samples, separation of the supernatant and pellet and the analysis of the Aβ$_{40}$ content of these fractions using SDS-PAGE (as described in Section 2.6.2) (Figure 3.10A). This allows the quantification of the relative proportion of soluble and insoluble Aβ material.

Analysis of fibril yields confirmed the conversion of soluble Aβ$_{40}$ monomer into insoluble material, with an average of 96.5%, 96.8% and 93.2% of protein in the pellet fraction for 2A, 3Q and *de novo* Aβ$_{40}$ fibrils respectively (Figure 3.10B).

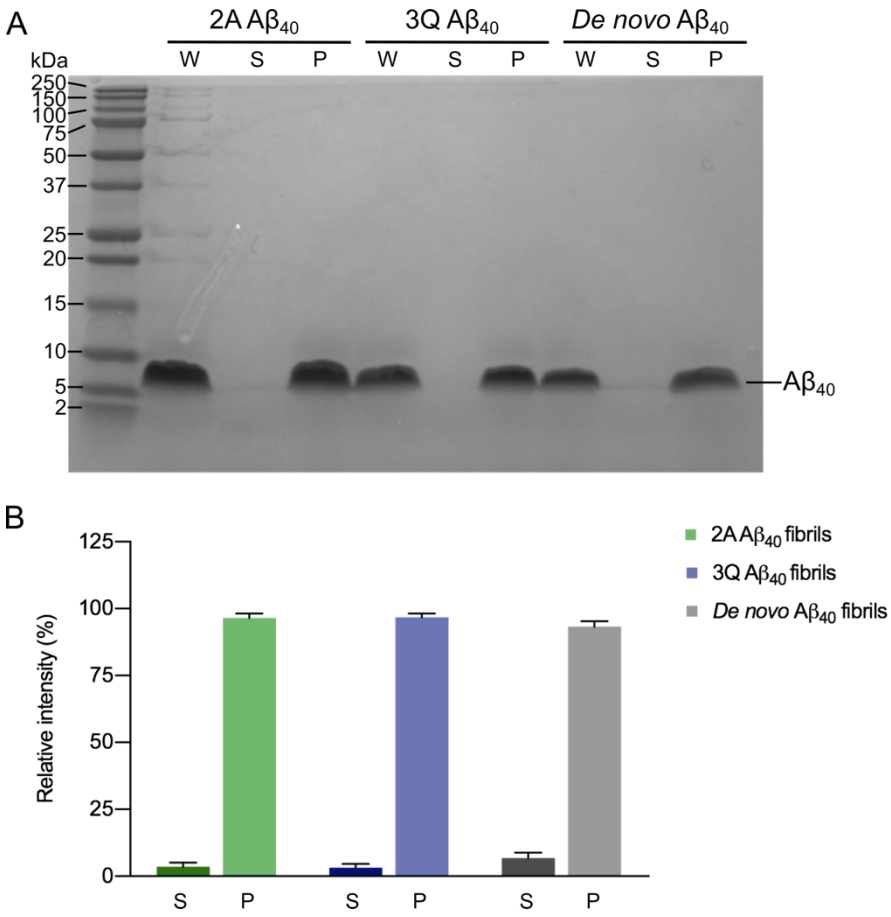

Figure 3.10. Fibril yields of Aβ40 fibril polymorphs confirm conversion of Aβ40 monomer to insoluble material
(A) Fibril samples were centrifuged at 16,873 xg for 40 min, the supernatant subsequently removed and the pellet resuspended in fresh 25 mM sodium phosphate buffer (pH 7.5). Equal volumes of the whole sample before centrifugation (W), the supernatant fraction after centrifugation (S) and the resuspended pellet fraction (P) were analysed using SDS-PAGE on a 15% Tris-Tricine gel. (B) Densitometry was carried out in order to quantify Aβ40 levels in each fraction. Error bars represent mean ± SEM (n=2). Statistical analysis using Tukey's multiple comparison test showed no significant difference in the formation of insoluble aggregates by the three different Aβ40 polymorphs.

To confirm that the insoluble Aβ40 is fibrillar and to assess fibril morphology, negative stain EM imaging of *de novo*, 2A and 3Q fibrils was performed (Figure 3.11). All three preparations were shown to consist of fibrils, with no evidence of amorphous aggregates present. This combination of data provides clear evidence for the formation of amyloid fibrils; the Aβ40 material is insoluble, ThT positive and shown to have a fibrillar structure by EM.

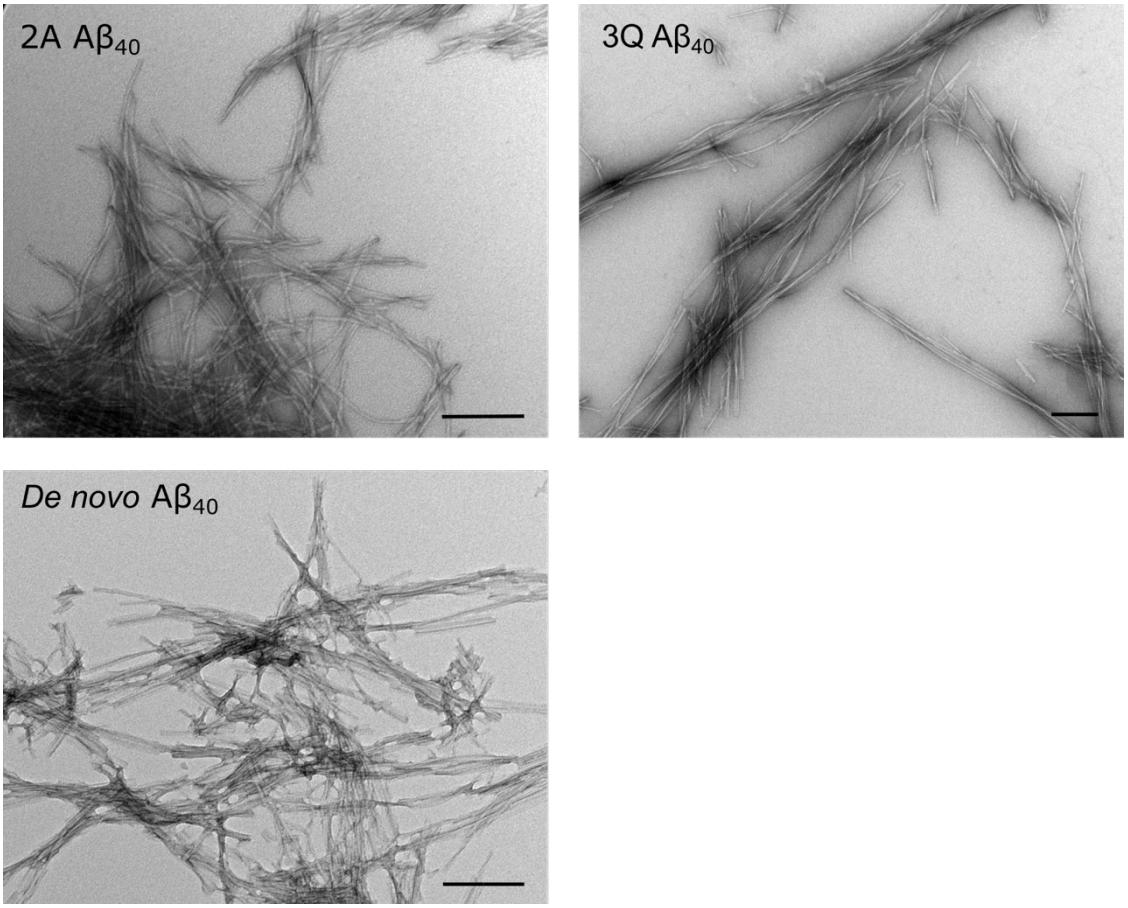

Figure 3.11. Negative stain electron micrographs of $A\beta_{40}$ fibril polymorphs
Samples of Aβ fibril polymorphs (100 μM monomer-equivalent concentration) were imaged by negative stain EM on a JEOL 1400 microscope. Scale bar = 200 nm

Re-determining the structure of all the different Aβ fibril preparations by ssNMR or cryo-EM is unfeasible for this project, but the use of amyloid dyes is a more practical method that may allow differences to be observed. To demonstrate polymorphism between 2A and 3Q $A\beta_{40}$ fibrils, luminescent-conjugated oligothiophene (LCO) probes were used (Nilsson et al., 2007; Klingstedt et al., 2013). LCO's are amyloid-specific dyes which are also sensitive to amyloid conformation. In contrast to ThT, which is sterically locked upon binding to amyloid, these dyes have a flexible thiophene backbone which have different emission spectra based on their geometry. Binding to amyloid fibrils of different conformations therefore results in different rotational constraints on the backbone and consequently different spectral signatures (Nilsson et al., 2007; Rasmussen et al., 2017).

Two commercially available LCOs were used in these studies to compare fibril preparations; Amytracker 480 and Amytracker 520 (Ebba Biotech, Sweden). No differences were observed between the binding of 2A and 3Q fibrils to Amytracker 480 (Figure 3.12A-C). However, 2A and 3Q $A\beta_{40}$ fibrils showed a clear difference when bound to Amytracker 520, suggesting a difference in binding site availability (Figure 3.12D). An unpaired t-test of the mean Amytracker 520 fluorescence intensity (FI) showed a significant difference between 2A and 3Q fibrils (Figure 3.12F). When the spectra are

normalised, there are no clear spectral shifts, however minor visual differences can be observed (Figure 3.12E).

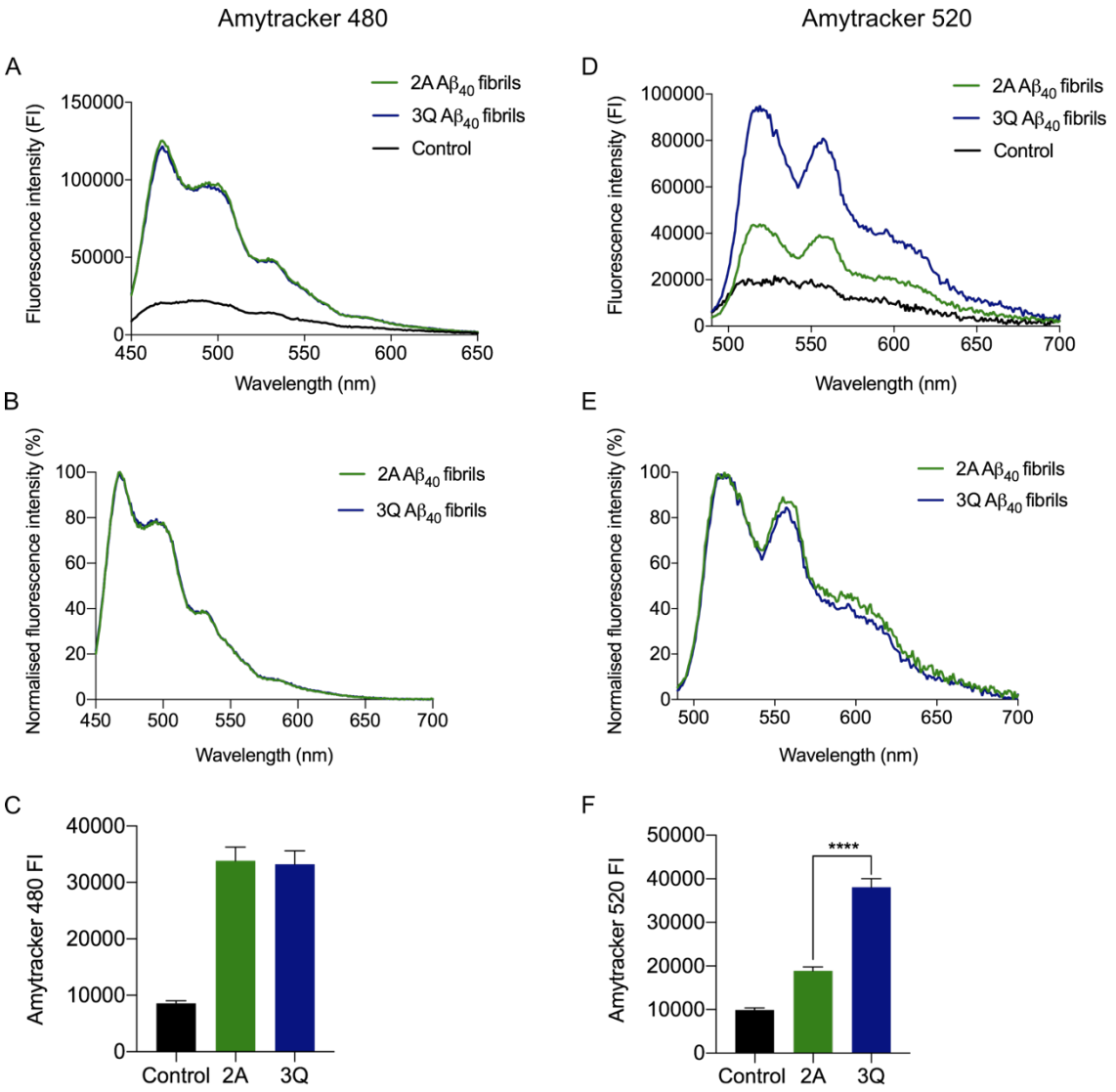

Figure 3.12. Comparison of Amytracker dye binding to 2A and 3Q Aβ40 fibril preparations (A) Average fluorescence spectra of Amytracker 480 upon binding to 2A and 3Q Aβ40 fibrils. Control sample is Amytracker 480 in buffer alone in the absence of Aβ40 fibrils (B) Normalised Amytracker 480 spectra upon binding to 2A and 3Q Aβ40 fibrils, normalised to the smallest and largest value in each data set. (C) Mean Amytracker 480 fluorescence intensity upon binding to 2A and 3Q Aβ40 fibrils. (D) Average fluorescence spectra of Amytracker 520 upon binding to 2A and 3Q Aβ40 fibrils. Control sample is Amytracker 520 in buffer alone in the absence of Aβ40 fibrils (E) Normalised Amytracker 520 spectra upon binding to 2A and 3Q Aβ40 fibrils, normalised to the smallest and largest value in each data set. (F) Mean Amytracker 520 fluorescence intensity upon binding to 2A and 3Q Aβ40 fibrils. Error bars represent mean ± SEM (n=4). Unpaired t-test, ****, p≤0.0001. Experiments were performed in 25 mM sodium phosphate (pH 7.5). For Amytracker 480, samples were excited at 430 nm and for Amytracker 520 samples were excited at 470 nm, using a Clariostar microplate reader (BMG Labtech, Germany).

3.4.3 Formation of Aβ40 E22Δ fibrils

To produce Aβ40 E22Δ fibrils, conditions were reproduced from *Schütz et al., 2015*, from which the PDB 2MVX structure was determined. This involved the resuspension of purified Aβ40 E22Δ monomer at a final concentration of 60 μM in 10 mM sodium phosphate, 100 mM NaCl (pH 7.4). 1 mL of this solution was incubated at 37°C under constant agitation with a magnetic stirrer bar (700 rpm) in a 2 mL glass vial (Fisher Scientific) for 48 h to ensure that the fibrillation reaction was complete. Fibril growth was monitored using ThT fluorescence (Figure 3.13A), and shows a slower aggregation rate than the *de novo* Aβ40 fibrils, with a lag time of ~20 hours (t_{lag} = 18h). However, the E22Δ fibrils were formed at a lower monomer concentration than used herein for *de novo* Aβ40 fibrils (200 μM) which would be predicted to reduce the rate of aggregation. The concentration of monomer in the fibril reaction was kept consistent to that described previously for E22Δ fibril formation, so as not to alter the kinetics of fibril growth, rather than adapting conditions to form fibrils at the same concentration as wild-type Aβ40 fibrils (Schütz et al., 2015).

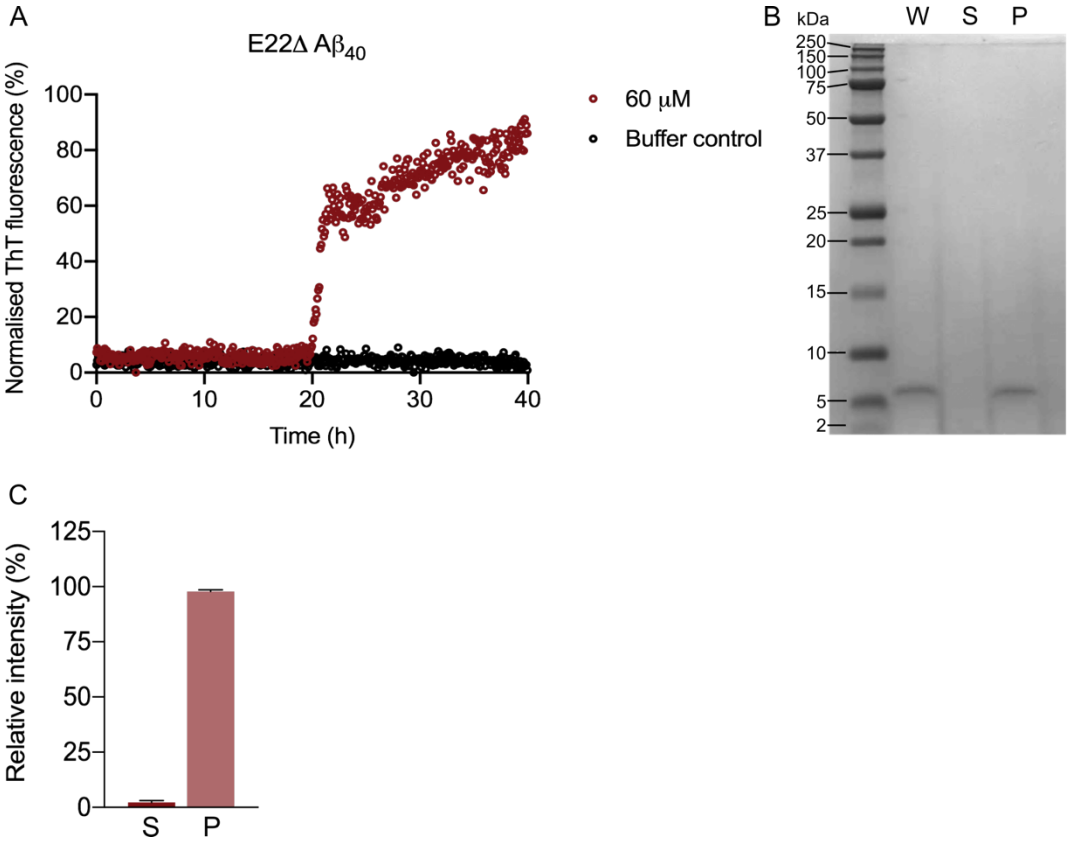

Figure 3.13. ThT monitoring and fibril yield analysis of Aβ40 E22Δ fibrils
(A) ThT fluorescence of Aβ40 E22Δ fibril growth was monitored over time. The fibril growth reaction consisted of 60 μM Aβ40 E22Δ monomer incubated in 10 mM sodium phosphate, pH, temp, 100 mM NaCl, 10 μM ThT (B) Aβ40 E22Δ fibrils were centrifuged at 16,873 xg for 40 min, the supernatant subsequently removed and the pellet resuspended in fresh buffer. Equal volumes of the whole sample before centrifugation (W), the supernatant fraction after centrifugation (S) and the resuspended pellet fraction (P) were analysed using SDS-PAGE on a 15% Tris-Tricine gel. C) Densitometry was carried out in order to quantify Aβ40 levels in each fraction. Error bars represent mean ± SEM (n=2).

3.4.4 Characterisation of Aβ$_{40}$ E22Δ fibrils

As with wild-type Aβ$_{40}$ fibrils, fibril yields of Aβ$_{40}$ E22Δ fibrils were determined (Figure 3.13B and C). This confirmed that the majority (97.8%) of soluble monomeric Aβ$_{40}$ E22Δ peptide has been converted into insoluble material at the endpoint of the fibrillation reaction. The morphology of this endpoint material was assessed using negative stain EM imaging (Figure 3.14). These EM images confirm that the samples consist of amyloid fibrils.

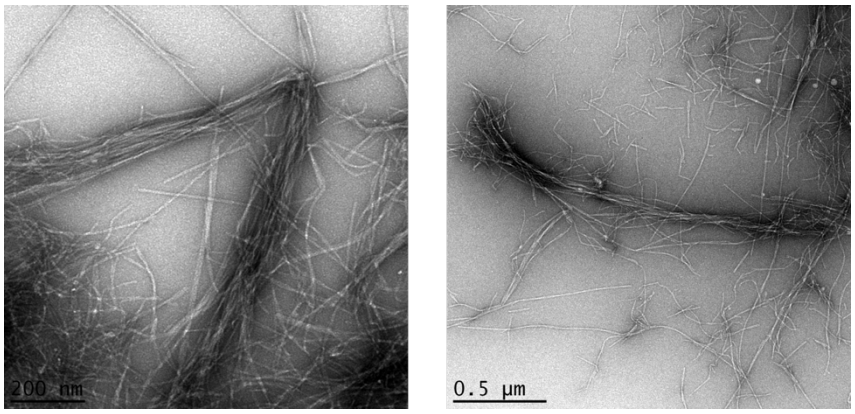

Figure 3.14. Negative stain electron micrographs of Aβ$_{40}$ E22Δ fibrils
Samples of Aβ$_{40}$ E22Δ fibrils (60 µM monomer-equivalent concentration) were imaged by negative stain EM on a JEOL 1400 microscope. Scale bar = 200 nm (left), 0.5 µm (right)

3.4.5 Formation of Aβ$_{42}$ fibrils

Two Aβ$_{42}$ fibril preparations were compared in this study, formed under distinct fibrillation conditions. The main distinction between these conditions is the pH of the reaction buffer used; one population of Aβ$_{42}$ fibrils was formed at pH 2, whereas the other population was formed at pH 8. The pH 2 Aβ$_{42}$ fibrils were formed by reproducing the conditions used in *Gremer et al, 2017,* from which the cryo-EM structure PDB 5OQV was solved (Gremer et al., 2017). Briefly, this involved the resuspension of previously purified recombinant Aβ$_{42}$ monomer in 30% v/v acetonitrile, 0.1% (v/v) TFA in water, at a concentration of 120.5 µM. This solution was incubated quiescently at room temperature. Whilst in the original study this solution was left undisturbed for 'several weeks', monitoring of aggregation with ThT showed that the reaction reached a plateau within ~35 h (Figure 3.15). Therefore, the pH 2 Aβ$_{42}$ fibrils were incubated for 48 h in subsequent reactions before use in experiments with cells. ThT monitoring revealed a calculated t_{lag} of 6.52 h for Aβ$_{42}$ monomer under these conditions (Figure 3.15).

The pH 8 fibril polymorph was formed by reproducing conditions described in *Colvin et al, 2016,* which were used to generate fibrils from which the ssNMR structure PDB 5KK3 was modelled (Colvin et al., 2015). pH 8 fibrils were formed from the same $A\beta_{42}$ monomeric peptide that was used to produce pH 2 fibrils, but the monomer was resuspended instead in 20 mM sodium phosphate, 0.2 mM EDTA, 0.02% (w/v) NaN_3, pH 8.0. This solution was then incubated quiescently at room temperature in 1.5 mL Eppendorf tubes. Monitoring of growth kinetics with ThT shows that aggregation occurs more quickly than for the pH 2 $A\beta_{42}$ fibril polymorph, with a calculated t_{lag} of 38 min, and a growth plateau reached in 1 h (Figure 3.15).

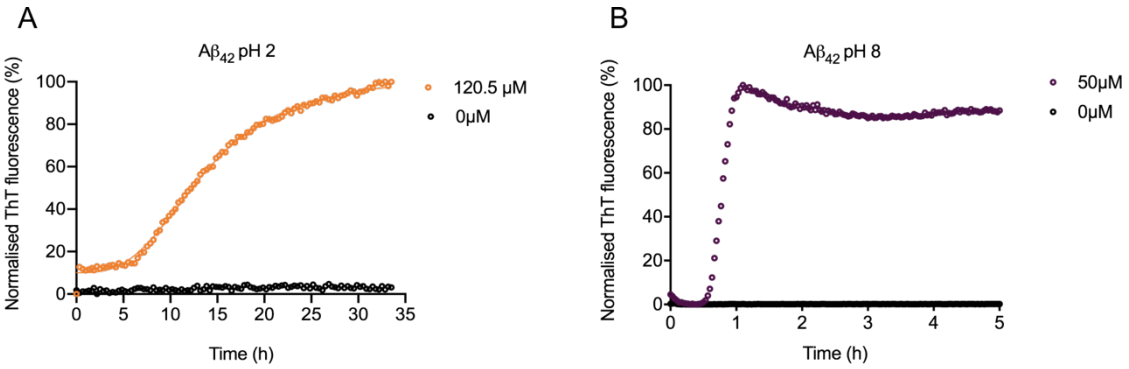

Figure 3.15. ThT monitoring of $A\beta_{42}$ fibril formation at pH 2 or pH 8
ThT fluorescence was measured over time to monitor fibril growth kinetics of (A) 120.5 μM monomeric $A\beta_{42}$ incubated quiescently at room temperature in 30% v/v acetonitrile, 0.1% (v/v) TFA in water (pH 2). (B) 50 μM monomeric $A\beta_{42}$ incubated quiescently at room temperature in 20 mM sodium phosphate, 0.2 mM EDTA (pH 8.0). 10 μM final concentration ThT was used in both samples and 0 μM samples represent the respective buffer without the addition of $A\beta_{42}$ monomer.

3.4.6 Characterisation of $A\beta_{42}$ fibril preparations

As with the other fibril preparations, fibril yield experiments were carried out to determine the proportion of soluble $A\beta_{42}$ that has formed insoluble aggregates at the end of the fibrillation reaction time (Figure 3.16). This showed that an average of 84% and 89% of peptide was in the insoluble fraction for the pH 2 and pH 8 $A\beta_{42}$ fibril preparations respectively. Analysis by an unpaired t-test showed no significant difference between the two $A\beta_{42}$ fibril populations in their formation of insoluble material (Figure 3.16B).

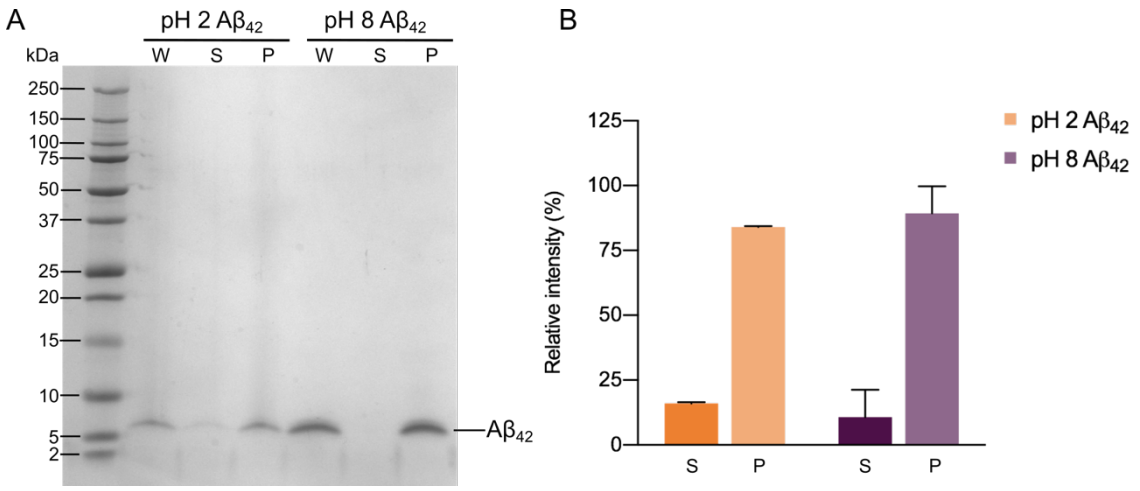

Figure 3.16. Fibril yield analysis of pH 2 and pH 8 Aβ42 fibril preparations
(A) Aβ42 fibrils formed at pH 2 and pH 8 were centrifuged at 16,873 xg for 40 min, the supernatants subsequently removed and the pellets resuspended in fresh buffer. Equal volumes of the whole sample before centrifugation (W), the supernatant fraction after centrifugation (S) and the resuspended pellet fraction (P) were analysed using SDS-PAGE on a 15% Tris-Tricine gel. (B) Densitometry was carried out in order to quantify Aβ42 levels in each fraction. Error bars represent mean ± SEM (n=2).

The morphology of the resulting Aβ42 fibril samples was analysed using negative stain EM. This confirmed the formation of amyloid fibrils as expected (Figure 3.17).

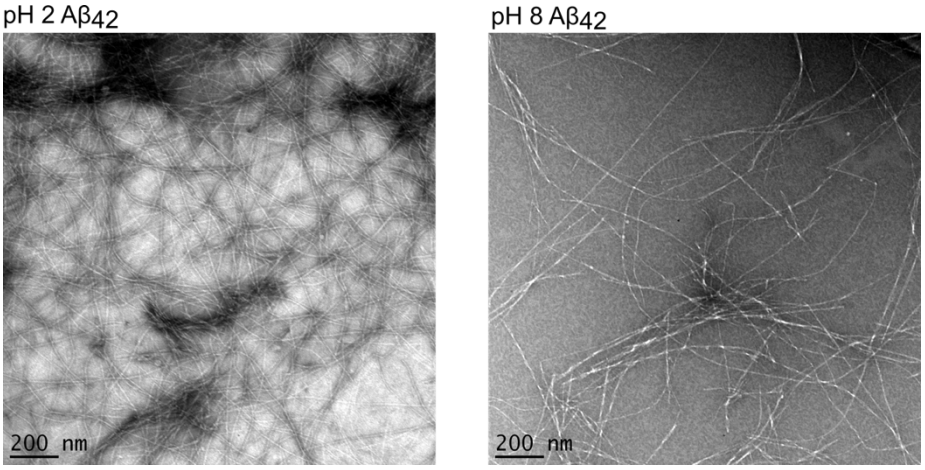

Figure 3.17. Negative stain electron micrographs of Aβ42 fibril preparations
Samples of pH 2 Aβ42 fibrils (120.5 μM monomer-equivalent concentration) and pH 8 Aβ42 fibrils (50 μM monomer-equivalent concentration) were imaged by negative stain EM on a JEOL 1400 microscope. Scale bar = 200 nm

To demonstrate that the two Aβ42 fibril preparations formed contained structurally distinct fibrils, two LCO probes were used as previously for Aβ40 fibrils. The spectrum of Amytracker 480 binding shows a clear shift when bound to pH 2 Aβ42 fibrils compared with when bound to pH 8 Aβ42 fibrils (Figure 3.18A). This indicates conformational differences between the two fibril preparations. This shift is also evident when the data are normalised to the highest and lowest values in each data set (Figure 3.18B). No significant difference in the mean fluorescence of Amytracker 480 was identified between

pH 2 and pH 8 $A\beta_{42}$ fibrils (Figure 3.18C). The spectra for Amytracker 520 did not show a clear shift when bound to the two different fibril preparations (Figure 3.18D/E). However, analysis by an unpaired t-test found FI to be significantly higher when bound to pH 2 $A\beta_{42}$ fibrils compared to pH 8 $A\beta_{42}$ fibrils ($p \leq 0.0001$) (Figure 3.18D/F). A similar effect was identified for $A\beta_{40}$ fibrils and could be indicative of differences in binding site availability.

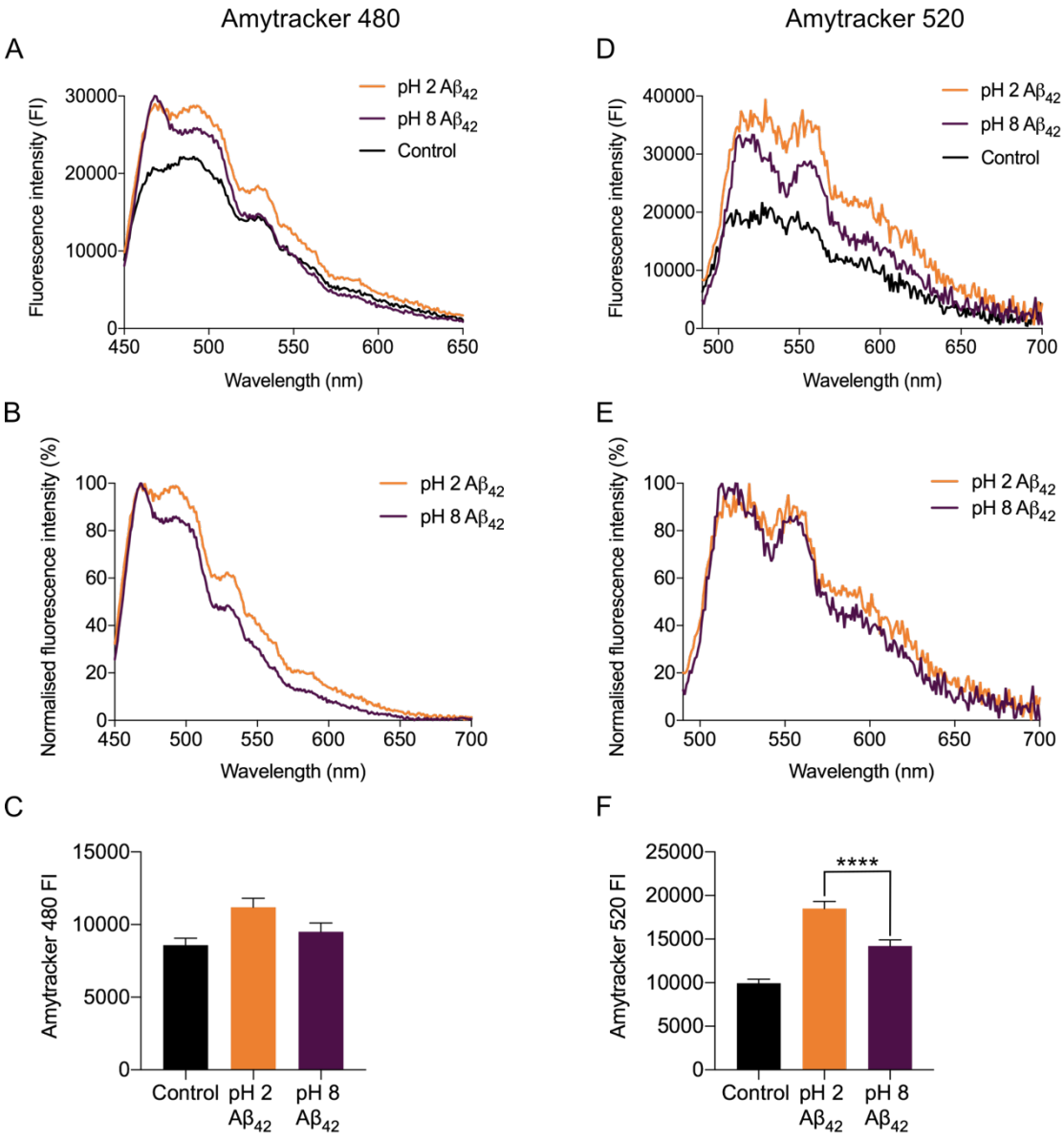

Figure 3.18. Comparison of Amytracker dye binding to pH 2 and pH 8 Aβ42 fibrils
(A) Average fluorescence emission spectra of Amytracker 480 upon binding to pH 2 and pH 8 Aβ42 fibrils. (B) Normalised Amytracker 480 spectra upon binding to pH 2 and pH 8 Aβ42 fibrils, normalised to the smallest and largest value in each data set. (C) Mean Amytracker 480 fluorescence intensity upon binding to pH 2 and pH 8 Aβ42 fibrils. (D) Average fluorescence spectra of Amytracker 520 upon binding to pH 2 and pH 8 Aβ42 fibrils, (E) Normalised Amytracker 520 spectra upon binding to pH 2 and pH 8 Aβ42 fibrils, normalised to the smallest and largest value in each data set. (F) Mean Amytracker 480 fluorescence intensity upon binding to pH 2 and pH 8 Aβ42 fibrils. Error bars represent mean ± SEM (n=3). Unpaired t-test, ****, p≤0.0001, Control samples are Amytracker dyes in buffer alone in the absence of Aβ42 fibrils. Experiments were performed in 25 mM sodium phosphate (pH 7.5). For Amytracker 480, samples were excited at 430 nm and for Amytracker 520 samples were excited at 470 nm, using a Clariostar microplate reader (BMG Labtech, Germany).

3.5 Measurement of endotoxin levels in Aβ fibril preparations

Before Aβ fibril preparations were used in cell experiments (Chapters 4 and 5), endotoxin tests were carried out on the fibril samples. As the protein used to produce these fibrils was expressed and purified from *E. coli*, there is potential for endotoxin contamination, which could impact cells and the results of cell viability and inflammatory activation measurements. The LAL endotoxin test was performed on peptide and fibril samples, as described in Section 2.6.5, in order to measure endotoxin levels.

The endotoxin level of recombinantly produced Aβ monomer (Section 3.2), was first compared to that of Aβ monomer that was synthetically produced (kindly provided by Dr Martin Walko). This showed no significant difference in endotoxin levels between peptide produced in these two systems (Figure 3.19A). Three separate batches of all six fibril populations were then also tested for endotoxin; this showed that all fibril samples had an endotoxin concentration under 1 EU/mL when tested at a final concentration of 1 μM, and importantly there were no significant differences in the levels of endotoxin between any of the fibril samples (Figure 3.19B). This makes it unlikely that endotoxin contamination could be responsible for any differences in toxicity or inflammatory activation observed in later cell experiments. Fibrils formed from another recombinantly expressed amyloid protein, α-synuclein, were also tested in triplicate as a comparison (Figure 3.19B).

For reference, the LAL endotoxin test is an FDA recognised method for endotoxin measurements, and a level of 5 EU/kg of body weight is the threshold for pharmacological preparations (Bacterial Endotoxins/Pyrogens | FDA).

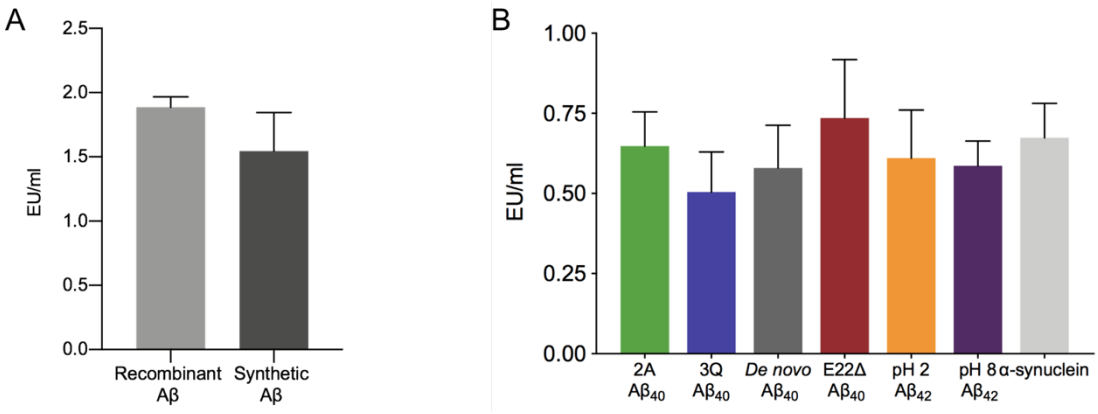

Figure 3.19. Endotoxin testing of Aβ$_{40}$ monomer and fibril preparations
Endotoxin levels were tested using a Limulus Amebocyte Lysate (LAL) Chromogenic Endotoxin Quantification assay. (A) Endotoxin levels of Aβ monomer produced either recombinantly in *E. coli* or synthetically. (B) Endotoxin levels of all six fibril preparations measured at a final concentration of 1 μM. Endotoxin levels of an independent amyloid protein, α-synuclein was also tested. Error bars represent mean ± SD (n=3)

3.6 Discussion

In this chapter, the methods for Aβ$_{40}$, Aβ$_{40}$ E22Δ and Aβ$_{42}$ peptide purification were described. These were shown by mass spectrometry and SDS-PAGE to result in the production of pure monomeric peptide for all three Aβ sequences. The purity of peptide is important in ensuring the reproducible formation of Aβ fibrils, as contaminants could affect the aggregation kinetics and potentially the structure of the fibrils resulting (Bunce et al., 2019; Madine, 2019). Different methods were used to produce Aβ$_{40}$ and Aβ$_{42}$ peptides, both of which were shown to be efficient (Figure 3.4). However, the HPLC protocol used to produce Aβ$_{42}$ resulted in a greater yield (~7 mg/L of bacterial growth compared to ~2-3 mg/L of bacterial growth), despite lower expression in *E. coli* (Figure 3.3). Some of the peptide can be seen to be lost in flow-through and wash steps of the ion-exchange chromatography method used to purify Aβ$_{40}$. As the HPLC method requires fewer stages of purification, and does not involve this ion-exchange method, less peptide is lost resulting in a higher yield. Further to this, the HPLC protocol was optimised to resuspend the inclusion body pellet in NaOH and remove the filtering step, further improving yield. These basic conditions also ensure that the peptide remains monomeric throughout the HPLC process. In addition, the HPLC method is a much quicker protocol than the protocol used to purify Aβ$_{40}$, taking ~1.5 weeks compared to ~3 weeks, making it more efficient. The purification of Aβ$_{40}$ using this same method would therefore be advisable in future studies.

The formation of Aβ fibrils from purified peptide was performed under defined conditions, and fibrillation was demonstrated using a range of methods. ThT analysis of all Aβ fibril preparations showed an increase in ThT fluorescence indicative of ThT binding to the

cross-β structure of amyloid fibrils. This confirms the formation of amyloid structures from monomeric peptide. ThT kinetics of fibril formation were as expected for *de novo* formed fibrils and seeded (2A/3Q) reactions (Figure 3.9), confirming the elongation of fibril seeds (Biancalana and Koide, 2010; Arosio et al., 2015). This seeding has been shown to result in the self-propagation of fibrils with the same intrinsic structure through generations (Petkova et al., 2005; Paravastu et al., 2008, 2009; Tycko, 2014). The lag time of $A\beta_{42}$ fibril formation at pH 8 was much shorter (t_{lag} = 38 mins) than that of $A\beta_{40}$ formed at a similar pH (t_{lag} = 4.58 h), despite $A\beta_{40}$ being at a higher concentration, at 37°C and under shaking conditions. This is expected, as $A\beta_{42}$ is more hydrophobic and prone to aggregation (Jarrett et al., 2002).

Fibril yields showed that for all fibril preparations, ≥84% of peptide was in the insoluble fraction, with $A\beta_{42}$ samples appearing to have more soluble material remaining than $A\beta_{40}$ samples (Figure 3.10, Figure 3.13, Figure 3.16). However, there was no significant difference in the proportion of insoluble material formed between $A\beta_{40}$ preparations or between $A\beta_{42}$ preparations, therefore eliminating any differential effect of remaining soluble species. It is also possible that material observed in the 'soluble' fraction could be smaller fibrils that were not efficiently pelleted under the centrifugation conditions used. EM was used to confirm that the insoluble material detected from fibril yield experiments was in a fibrillar form, as suggested by ThT. Amyloid fibrils were observed for all fibril preparation samples imaged by EM, without any evidence of amorphous aggregates or contaminants. This means that any differences identified in the biological properties of the fibrils are likely to be due to differences in fibril structure.

The resolution of negative stain EM was not sufficient to confirm the structures of fibril preparations, however some observations could be made. The originally reported twisted morphology of 3Q fibrils could not be identified (Petkova et al., 2005). This has been noted in the past, but the ssNMR spectra still confirmed that the propagated fibril structure was consistent with that originally reported (Stewart et al., 2017). The $A\beta_{40}$ fibril preparations appeared to be of similar lengths, but the $A\beta_{40}$ E22Δ fibrils contained a larger proportion of short fibrils (Figure 3.14), likely resulting from the magnetic stirring method used in their formation. There was no observable difference between the lengths of the two $A\beta_{42}$ fibril preparations, but the $A\beta_{42}$ fibrils can be seen to be longer than $A\beta_{40}$ fibrils. This could result from the quiescent conditions used to form the $A\beta_{42}$ fibrils, in the absence of shaking or fibril seeds. These differences in length will be taken into account in subsequent experiments when interpreting results that could be affected by fibril length, for example in cellular uptake experiments. Fibrils were not processed using methods such as sonication to all be the same length, as length is an inherent property

of the fibril resulting from the growth conditions, and therefore could be significant in the effect that a particular fibril polymorph has on cells.

As ssNMR and cryo-EM experiments are not an efficient way to regularly and routinely assess structure, conformation-sensitive amyloid dyes LCO's (Amytracker 480 and Amytracker 520) were used to demonstrate the polymorphism of the Aβ fibril populations produced. The mean fluorescence intensity of Amytracker 520 was found to be significantly higher for 3Q $A\beta_{40}$ samples compared with 2A $A\beta_{40}$ fibril samples (Figure 3.12), suggesting increased binding resulting from increased availability of binding sites for this dye. However, when normalised, the Amytracker 520 spectra profiles look similar for 2A and 3Q fibrils. This increased fluorescence but similar spectra could be because 2A and 3Q fibrils are formed from similar subunits, but 3Q fibrils have three of these subunits whereas 2A fibrils only have two (Paravastu et al., 2008, 2009).

Differences between $A\beta_{42}$ fibril preparations were also observed in LCO binding spectra (Figure 3.18). A clear shift can be seen in the spectra of Amytracker 480 bound to pH 2 $A\beta_{42}$ fibrils compared with when bound to pH 8 $A\beta_{42}$ fibrils (Figure 3.18A/B), suggesting that differences in the conformation of pH 2 and pH 8 fibrils are inflicting different rotational constraints on the thiophene backbone (Nilsson et al., 2007). The Amytracker 520 spectra for $A\beta_{42}$ fibril preparations showed only minor differences in signatures, but the mean FI was significantly higher for pH 2 $A\beta_{42}$ fibrils compared to pH 8 $A\beta_{42}$ fibrils, suggesting different binding affinities of the dye (Figure 3.18D/E/F).

In summary, Aβ fibrils were formed *in vitro* using previously defined conditions, to produce 6 distinct populations of fibrils. These fibril preparations will be compared in subsequent cell experiments in order to assess biological differences that fibril structure can convey.

4 Analysis of the effect of Aβ fibril preparations on the viability and activation of microglial and monocytic cells

4.1 Introduction

Whilst the library of different Aβ fibril structures continues to grow, the biological significance of these different structures is not well understood. The phenomenon of Aβ fibril polymorphism both *in vitro* and *ex vivo* is now widely documented and accepted, however whether these different fibril structures affect cells differently within the brain environment is not known. Microglial cells would be in close contact with Aβ fibrils in the brain, with the potential to either improve or exacerbate disease (Section 1.4.2).

One fundamental property of the different Aβ fibril preparations that is compared in this study is their toxicity towards monocytic and microglial cells. There is some evidence suggesting that there could be differences in toxicity between Aβ fibril polymorphs for other cell types; a significantly greater reduction in the number of viable neurons was observed when primary rat embryonic hippocampal neuron cultures were incubated with 3Q $A\beta_{40}$ fibrils compared to those incubated with 2A $A\beta_{40}$ fibrils (Petkova et al., 2005). However, this was tested using concentrations from 10-75 μM, and using only a single measure of viability, counting viable neurons. This does not provide information about the metabolic activity, cellular stress or functional capabilities of the remaining neurons. In other work, fibrils with a distinctive structure formed from $A\beta_{40}$ that is phosphorylated at the Ser-8 residue (pS8-$A\beta_{40}$ – shown in Figure 1.7) were found to be more toxic than wild-type $A\beta_{40}$ fibrils towards neuronal N2a and microglial BV-2 cell lines. This was measured using an MTT assay, a measure of cellular metabolic activity, and the greatest differences were observed at the lower concentrations tested, from 0.001-0.01 μM (Hu et al., 2017). This further implicates a role for fibril structure in cytotoxicity and as this fibril polymorph was also found to have a higher seeding efficiency, it is likely that these fibrils would be more detrimental in the brain than other polymorphs with lower seeding capabilities and cytotoxicity.

Further evidence for differences in the toxicity of distinct fibril polymorphs comes from studies of other amyloidogenic proteins, such as α-synuclein. Two structurally distinct α-synuclein polymorphs termed ‘fibrils’ and ‘ribbons’ were structurally and functionally characterized (Bousset et al., 2013). The polymorph termed ‘fibrils’ were generated under physiological salt conditions and have a cylindrical aspect, whereas ‘ribbons’ were formed under low salt concentrations or in the presence of 2.5 mM EDTA, and are flat with a twist (Bousset et al., 2013). The toxicity of the fibril polymorphs towards the SH-SY5Y neuroblastoma cell line was measured by the MTT assay and cell counting, which

revealed that the 'fibril' polymorph is more toxic than the 'ribbon' polymorph towards these cells (Bousset et al., 2013). This shows that differences in amyloid fibril structure can convey differences in cytotoxicity, which could contribute *in vivo* to different clinical presentations or severity of disease.

Further to this, recent research used brain homogenate from Parkinson's Disease (PD), Multiple System Atrophy (MSA) and Dementia with Lewy Bodies (DLB) patients to seed monomeric α-synuclein *in vitro* and investigated differences between the resulting fibril 'strains' (Van der Perren et al., 2020). This seeding resulted in fibrils of different disease-specific morphologies, with those from PD and MSA patients resembling previously described 'ribbons', and those from DLB resembling the 'fibril' polymorph. Differences in toxicity towards dopaminergic neurons were observed when injected in the substantia nigra of rats, with MSA and DLB samples leading to the highest proportion of neuronal loss compared to PD samples (Van der Perren et al., 2020). In addition, differences in the pattern of spread of pathology were observed between sample groups (Van der Perren et al., 2020). This suggests that different fibril morphologies have different toxicities and are likely to be associated with different disease presentations.

In addition to comparing the toxicity of different fibril preparations towards monocytic and microglial cells, this thesis chapter aims to investigate the extent to which different fibril preparations can elicit an inflammatory response from these cells. It is known that the Aβ fibrils that make up amyloid plaques in the AD brain closely interact with microglial cells, resulting in the activation of these cells and the subsequent release of pro-inflammatory mediators, contributing to neuroinflammation in AD (Section 1.4). A number of microglial receptors have been implicated in this process (Figure 1.10) along with the NLRP3 inflammasome pathway (Figure 1.8) (Halle et al., 2008; Heneka, 2017). The question remains, however, as to whether certain Aβ fibril structures are more capable of eliciting this immune response than others. This is critical as Aβ fibrils that result in an amplified pro-inflammatory response will be more damaging in the brain than other fibril structures that are less efficient in eliciting this response.

Whilst the immune cell activation capabilities of different Aβ fibril polymorphs has not previously been investigated, recent research compared this for two structurally distinct protein oligomers of the model amyloidogenic protein HypF-N (Mannini et al., 2019). Although not examined for fibrils, distinct oligomeric structures (Type A and Type B) were shown to elicit different levels of immune response activation in microglial cells (Mannini et al., 2019). The oligomers both have a core structure based on a β-sheet scaffold and were both shown to bind to ThT, but differ in their overall flexibility and the solvent exposure of hydrophobic residues. The Type A oligomer structure had more solvent-

exposed hydrophobic residues and was shown to be more toxic towards N13 microglial cells compared to Type B oligomers (Mannini et al., 2019). The levels of pro-inflammatory cytokines IL-1β, TNF-α and IL-6, and anti-inflammatory cytokine IL-10 were measured after incubation with the two oligomer polymorphs. This revealed distinct cytokine profiles, with Type B oligomers found to be stronger inducers of pro-inflammatory cytokine release at lower concentration ranges than the Type A oligomers (Mannini et al., 2019).

As discussed above, *Van der Perren et al* recently investigated the effects of structural differences of distinct α-synuclein fibril polymorphs originating from different synucleinopathies (PD, MSA, DLB) (Van der Perren et al., 2020). A key novel finding from this was the identification of differential levels of immune response activation elicited by the different fibril polymorphs. α-synuclein fibrils derived from MSA patients induced the strongest immune response when injected into the substantia nigra of rats overexpressing human α-synuclein, measured by the number of cells positive for Iba1, a marker of microglial activation, and the number of large reactive phagocytic microglia after 150 days (Van der Perren et al., 2020). This was followed by PD and DLB originated fibril samples. MHC class II expression by reactive microglia was induced by fibrils from all three disease groups, but MSA samples again were found to induce the highest expression (Van der Perren et al., 2020). This pattern was the same for the number of $CD4^+$ and $CD8^+$ T-cells, indicating an increased capability of an adaptive immune response being triggered in mice injected with MSA-derived fibrils compared to those injected with PD or DLB-derived fibrils (Van der Perren et al., 2020). With α-synuclein fibrils previously shown to act as antigenic epitopes which trigger a T-cell response, this evidence suggests that different structures of the fibrils do so to differing extents, resulting in varying levels of immune activation in the brain (Sulzer et al., 2017; Van der Perren et al., 2020).

Further evidence for differential immune cell activation by amyloid fibril polymorphs comes from a recent study in which it was found that the level of activation of primary monocytes and BV-2 microglial cells varied in response to five α-synuclein polymorphs, measured by pro-inflammatory cytokine release (Grozdanov et al., 2019).

This chapter aims to examine the relationship between Aβ fibril structure and biological function by comparing the effects of different Aβ fibril preparations on immune cells. The toxicities of the fibril polymorphs towards microglial and monocytic cell lines are analysed using a combination of assays for cell viability. In addition, the activation of these immune cells elicited by the distinct Aβ fibril populations is compared by measuring cytokine

release, ROS production, NLRP3 inflammasome activation and cell surface markers of activation.

4.2 Cellular toxicity of $A\beta_{40}$, $A\beta_{40}$ E22Δ and $A\beta_{42}$ fibril preparations

The first biological property of the different Aβ fibril preparations that was compared was the effect of the fibrils on immune cell viability. For this, a number of different cell lines were used (see Table 2.4 for details). As microglial cells are the resident immune cells of the brain these cells are arguably the most relevant to use in this context (discussed in Section 1.4.2.1). The toxicity of the fibril preparations towards BV-2 microglial cells was therefore tested. However, with evidence of BBB breakdown in AD patients and the possible involvement of peripheral monocytes in the response to Aβ the macrophage cell line RAW 264.7 was also used in these experiments (Majumdar et al., 2008). Finally, as the previous two cell lines described are both murine, the toxicity of the different Aβ fibril preparations on a human monocytic cell line, THP-1, was also tested.

To assess the toxicity of the different Aβ fibril preparations towards immune cells, three different measures of cell viability were used (Figure 4.1). Cellular ATP levels were quantified using a commercial ATP assay (ATPLite Luminescence ATP detection system - PerkinElmer Life Sciences). This assay uses firefly luciferase, an oxidative enzyme that uses ATP and D-Luciferin substrate to produce oxyluciferin product, inorganic pyrophosphates (PPi) and bioluminescence as a side product (Figure 4.1A). Luminescence is measured as a readout of ATP levels.

Lactate dehydrogenase (LDH) release from cells was also measured. LDH is an enzyme normally located in the cytoplasm of cells, whereas its presence in the cell culture media is indicative of plasma membrane damage. The LDH release assay used here is based on a two-step reaction (Figure 4.1B). First, LDH reduces lactate into pyruvate, resulting also in the conversion of NAD+ to NADH. This NADH then reduces iodonitrotetrazolium (INT), a commonly used tetrazolium salt, via diaphorase catalysis to produce a red formazan dye. This red formazan can then be dissolved, and the absorbance measured.

Finally, cellular metabolism was measured using the 3-(4,5-Dimethylthiazol-2yl)-2,5-diphenyltetrazolium Bromide (MTT) assay. This assay depends on the activity of mitochondrial reductases within the cell reducing MTT into purple MTT formazan crystals (Figure 4.1C). This formazan can then be dissolved, and the absorbance measured as a colorimetric readout of cellular metabolic activity.

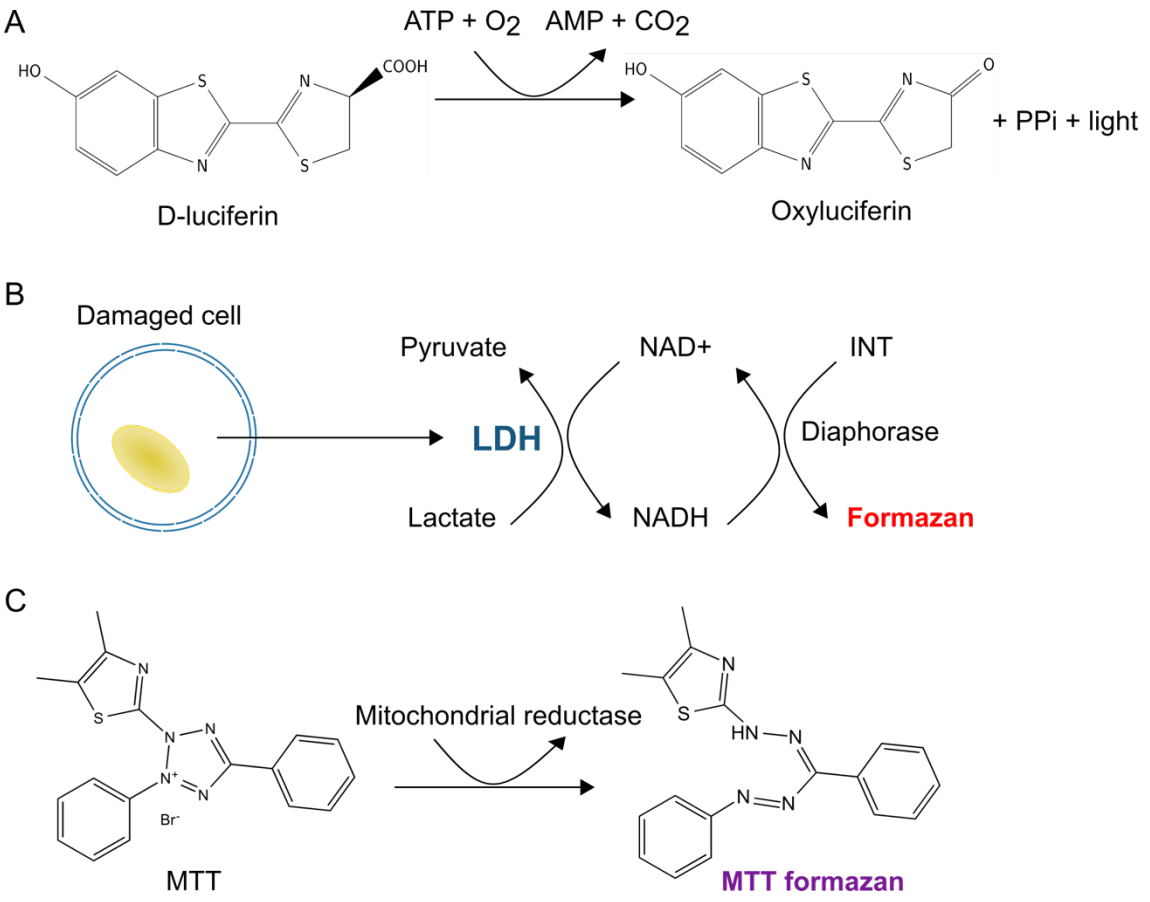

Figure 4.1. Mechanisms of viability assays used to measure Aβ fibril toxicity
Three viability assays were used to measure the cellular toxicity of Aβ fibril preparations. (A) In the ATP assay, D-luciferin substrate is converted to oxyluciferin by firefly luciferase catalysis, resulting in luminescence which is measured as a readout of cellular ATP levels. (B) In the LDH assay, LDH released from cells with membrane damage catalyses the conversion of lactate to pyruvate, also resulting in NADH formation. NADH reduces INT to a red formazan via diaphorase catalysis. This formazan is used as a colorimetric readout of cell membrane damage. (C) In the MTT assay cellular NADases located in the mitochondria reduce MTT into formazan crystals which are dissolved and measured as a colorimetric readout of cellular metabolic activity.

Before testing fibril toxicity, BV-2 cells were incubated with increasing concentrations of endotoxin (1-10 EU/mL) for 48 h and ATP levels and LDH release were measured (Figure 4.2). This was to identify any effect of the ~1 EU/ mL endotoxin previously measured in 1 μM samples of Aβ fibril preparations (Figure 3.19) on cell viability. Both assays showed no significant effect on cell viability at this concentration of endotoxin, although ATP levels were reduced at the highest endotoxin concentration tested (10 EU/mL) (Figure 4.2).

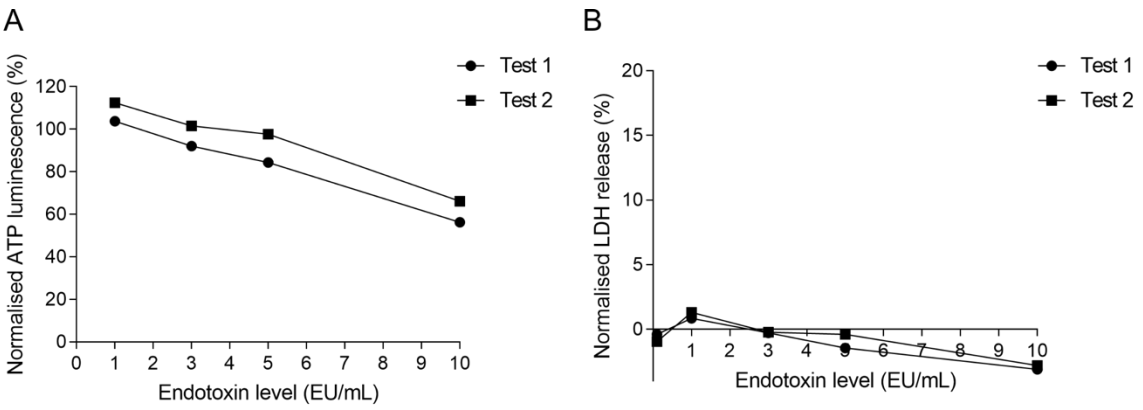

Figure 4.2. The effect of endotoxin on BV-2 cell viability
BV-2 cells were incubated with increasing concentrations of purified endotoxin standard (final concentration 1-10 EU/mL) for 48 h before ATP (A) and LDH release (B) assays were performed Results are normalised using lysed cells as 0% viability and untreated cells as 100% viability.

Cells were then incubated with 0.1 – 5 μM (monomer-equivalent concentration) of the fibril preparations or the equivalent volume of the corresponding fibrillation buffer (Section 2.1.2) for 48 h, before cell viability assays were performed. Differences in results of cell viability assays for cells incubated with Aβ fibrils compared to those incubated with the corresponding fibril buffer were calculated and are shown in Tables 4.1-4.9. The effects of different Aβ fibril preparations formed from the same peptide sequence on cell viability were also compared, and significant differences are shown on graphs in Figure 4.3- Figure 4.5.

In BV-2 cells, there was no observable effect on ATP levels or LDH release after incubation with the 2A, 3Q or *de novo* $A\beta_{40}$ fibril preparations, suggesting no effect on cell viability (Figure 4.3/Tables 4.1-4.3). This was also observed for RAW 264.7 and THP-1 cells (Figure 4.3/Tables 4.4-4.9). Decreases in MTT reduction were observed in BV-2 cells and RAW 264.7 cells incubated with $A\beta_{40}$ fibril preparations (Table 4.3/Table 4.6). However, there were no significant differences between the three $A\beta_{40}$ fibril populations (Figure 4.3). These results indicate that the fibrils are having an effect on cellular reductase activity, but do not cause cell death. This has been previously reported for β_2m amyloid fibrils, in which a decrease in MTT was measured but no other effects on cell viability were identified (Jakhria et al., 2014). It is therefore important to use a combination of multiple viability assays in the context of amyloid, to confirm any effects observed in the MTT assay.

In contrast to wild-type $A\beta_{40}$ fibril preparations, incubation with $A\beta_{40}$ E22Δ fibrils led to a significant reduction in cellular ATP levels of BV-2 microglial cells with increasing fibril concentration (Figure 4.4). An increase in LDH release and decrease in MTT reduction was also observed in BV-2 cells incubated with increasing concentrations of $A\beta_{40}$ E22Δ

fibrils (Figure 4.4). Together this data indicates that the $A\beta_{40}$ E22Δ fibrils are having a toxic effect on the BV-2 cells. This toxic effect of $A\beta_{40}$ E22Δ fibrils was also observed in RAW 264.7 cells (Figure 4.4), but no significant effect was observed in THP-1 cells (Figure 4.4).

All three viability assays showed a difference between the $A\beta_{42}$ fibril preparations formed at pH 2 and pH 8 in their toxicity to BV-2 cells. This difference was observed at 5 μM, with pH 8 fibrils being significantly more toxic than pH 2 fibrils (Figure 4.5). Incubation with 5 μM pH 8 $A\beta_{42}$ fibrils led to on average a 50% reduction in BV-2 cellular ATP levels and a 9% increase in LDH release, compared to cells incubated with buffer alone (Figure 4.5/Table 4.1-Table 4.2). MTT reduction in BV-2 cells also decreased by an average of 45% after incubation with 5 μM of the pH 8 $A\beta_{42}$ fibrils, compared to only a ~5% decrease in cells treated with the same concentration of pH 2 $A\beta_{42}$ fibrils (Figure 4.5/Table 4.3).

This differential toxicity between the two $A\beta_{42}$ fibril preparations was also observed in RAW 264.7 cells (Figure 4.5). The observed toxicity effect of the pH 8 fibrils was greater in these cells, with a 74% reduction in ATP and a 25% increase in LDH release resulting from incubation with 5 μM pH 8 $A\beta_{42}$ fibrils. pH 2 $A\beta_{42}$ fibrils again had no noticeable effect on cell viability. In THP-1 cells, ATP and LDH assays again showed a significantly greater effect on cell viability of pH 8 $A\beta_{42}$ fibrils compared to pH 2 $A\beta_{42}$ fibrils (Figure 4.5). This difference between the two $A\beta_{42}$ fibril preparations was observed at lower concentrations in these assays, however a smaller decrease in viability was observed resulting from 5 μM pH 8 $A\beta_{42}$ fibrils compared to other cell types, with an average of 25 % decrease in ATP. LDH release from THP-1 cells resulting from incubation with pH 8 $A\beta_{42}$ fibrils at 5 μM was similar to that in BV-2 cells at ~10% increase compared to buffer, however in these cells the pH 2 fibrils also resulted in some LDH release, meaning that there is not a significant difference between the fibrils at this concentration (Figure 4.5).

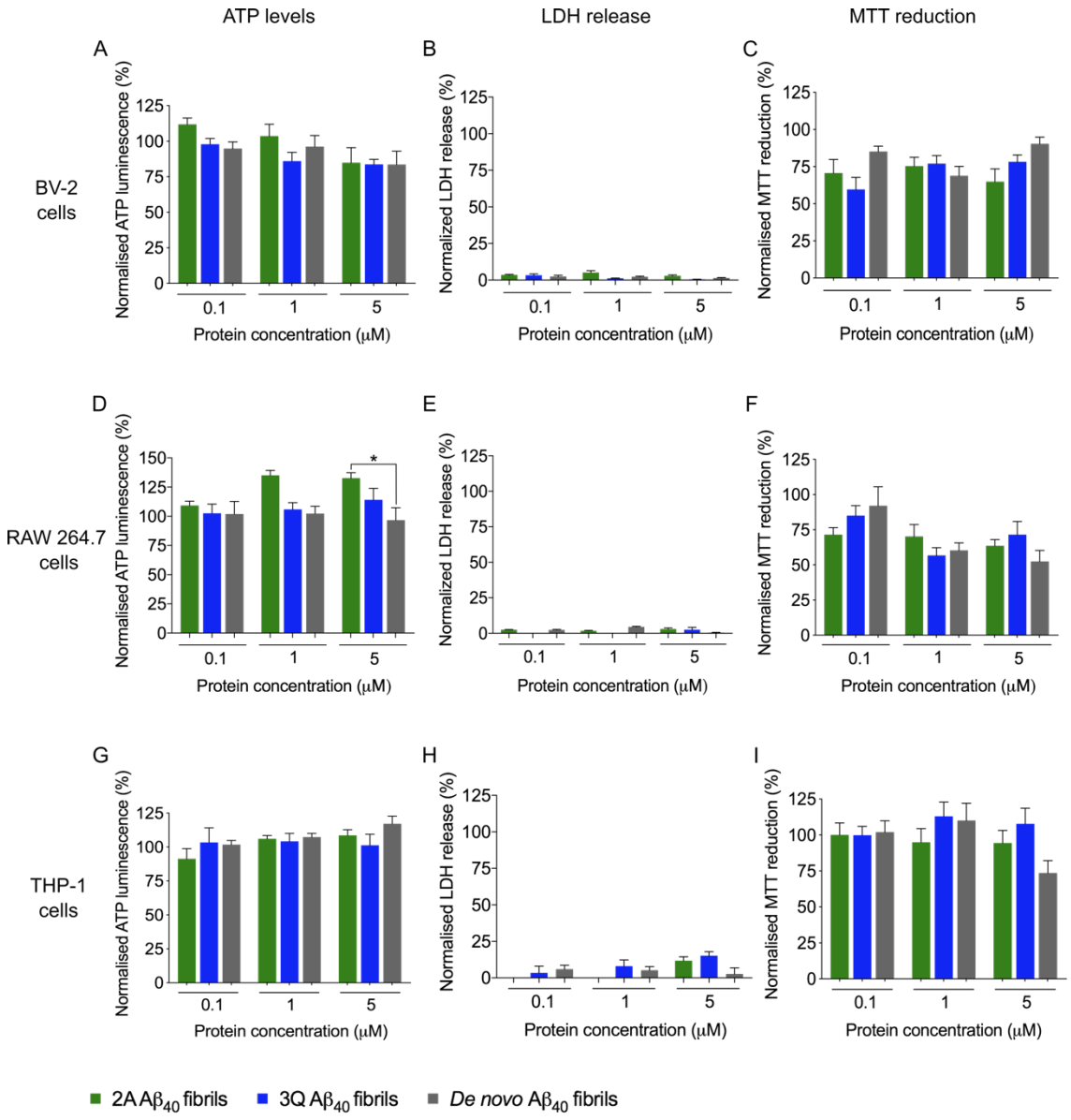

Figure 4.3. Analysis of the effect of Aβ40 fibril preparations on the viability of BV-2, RAW 264.7 and THP-1 cells

(A-C) BV-2 cells were incubated with 0.1, 1 or 5 μM of 2A, 3Q and *de novo* Aβ40 fibril preparations for 48 h before cellular ATP (A), LDH (B) and MTT (C) viability assays were performed (D-F) RAW 264.7 cells were incubated with 0.1, 1 or 5 μM of 2A, 3Q and *de novo* Aβ40 fibril preparations for 48 h before cellular ATP (D), LDH (E) and MTT (F) viability assays were performed. (G-I) THP-1 cells were incubated with 0.1, 1 or 5 μM of 2A, 3Q and *de novo* Aβ40 fibril preparations for 48 h before cellular ATP (G), LDH (H) and MTT (I) viability assays were performed. LDH release data are normalised to cells treated with lysis buffer after the same incubation period and ATP/MTT data are normalised to cells incubated with corresponding fibril growth buffer. Error bars represent mean ± SEM (n=3). One-way ANOVA with Tukey's multiple comparisons test was used to compare between fibril preparations, *, p≤0.05. All fibril concentrations are monomer-equivalent.

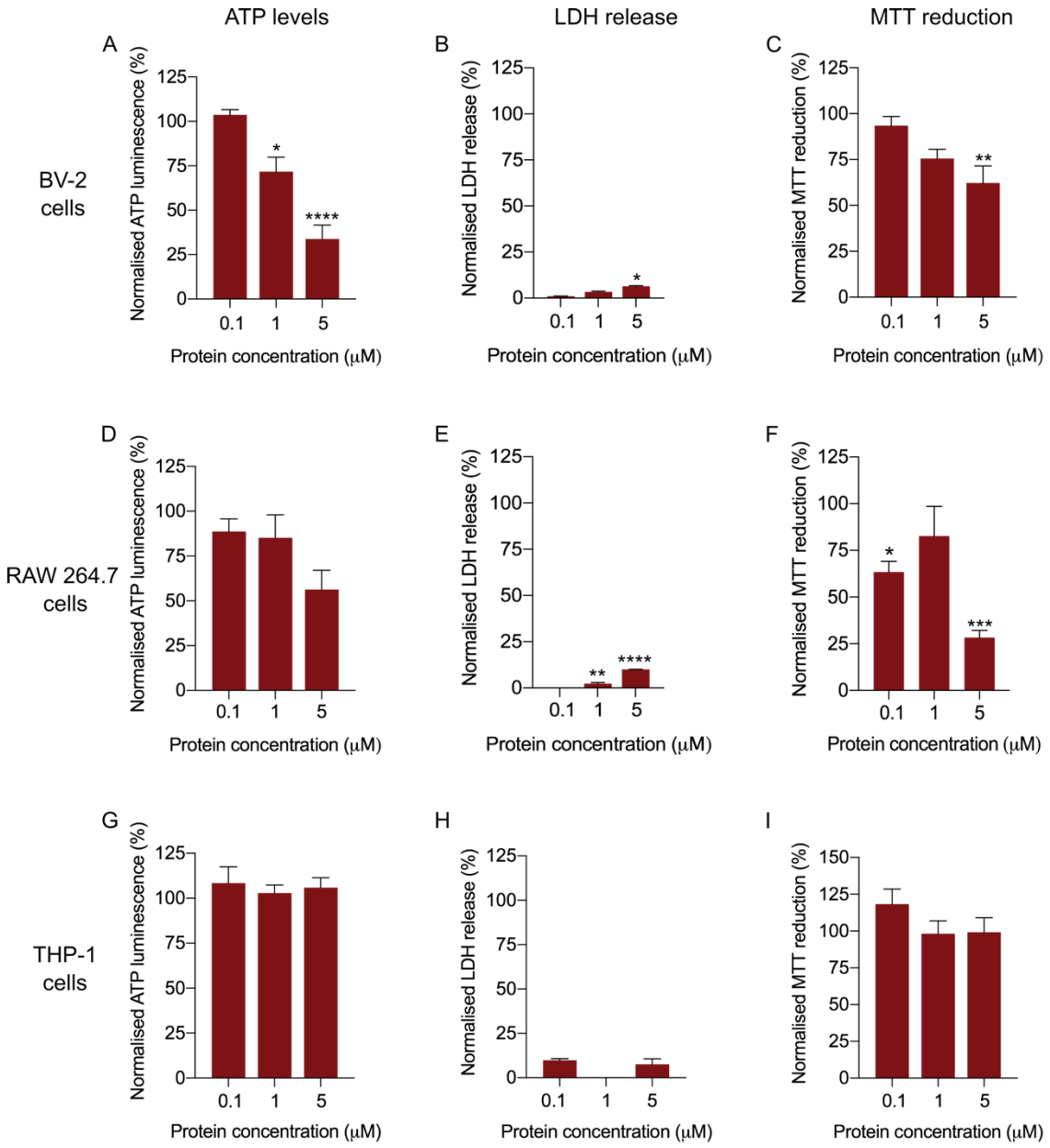

Figure 4.4 Analysis of the effect of $A\beta_{40}$ E22Δ fibrils on the viability of BV-2, RAW 264.7 and THP-1 cells

(A-C) BV-2 cells were incubated with 0.1, 1 or 5 μM of $A\beta_{40}$ E22Δ fibril preparations for 48 h before cellular ATP (A), LDH (B) and MTT (C) viability assays were performed D-F) RAW 264.7 cells were incubated with 0.1, 1 or 5 μM of $A\beta_{40}$ E22Δ fibril preparations for 48 h before cellular ATP (D), LDH (E) and MTT (F) viability assays were performed. (G-I) THP-1 cells were incubated with 0.1, 1 or 5 μM of $A\beta_{40}$ E22Δ fibril preparations for 48 h before cellular ATP (G), LDH (H) and MTT (I) viability assays were performed. LDH release data are normalised to cells treated with lysis buffer after the same incubation period and ATP/MTT data are normalised to cells incubated with corresponding fibril growth buffer. Error bars represent mean ± SEM (n=3). Significance is relative to buffer treated controls calculated using one-way ANOVA with Sidak's multiple comparisons test, *, $p \leq 0.05$, **, $p \leq 0.01$, ****, $p \leq 0.0001$. All fibril concentrations are monomer-equivalent.

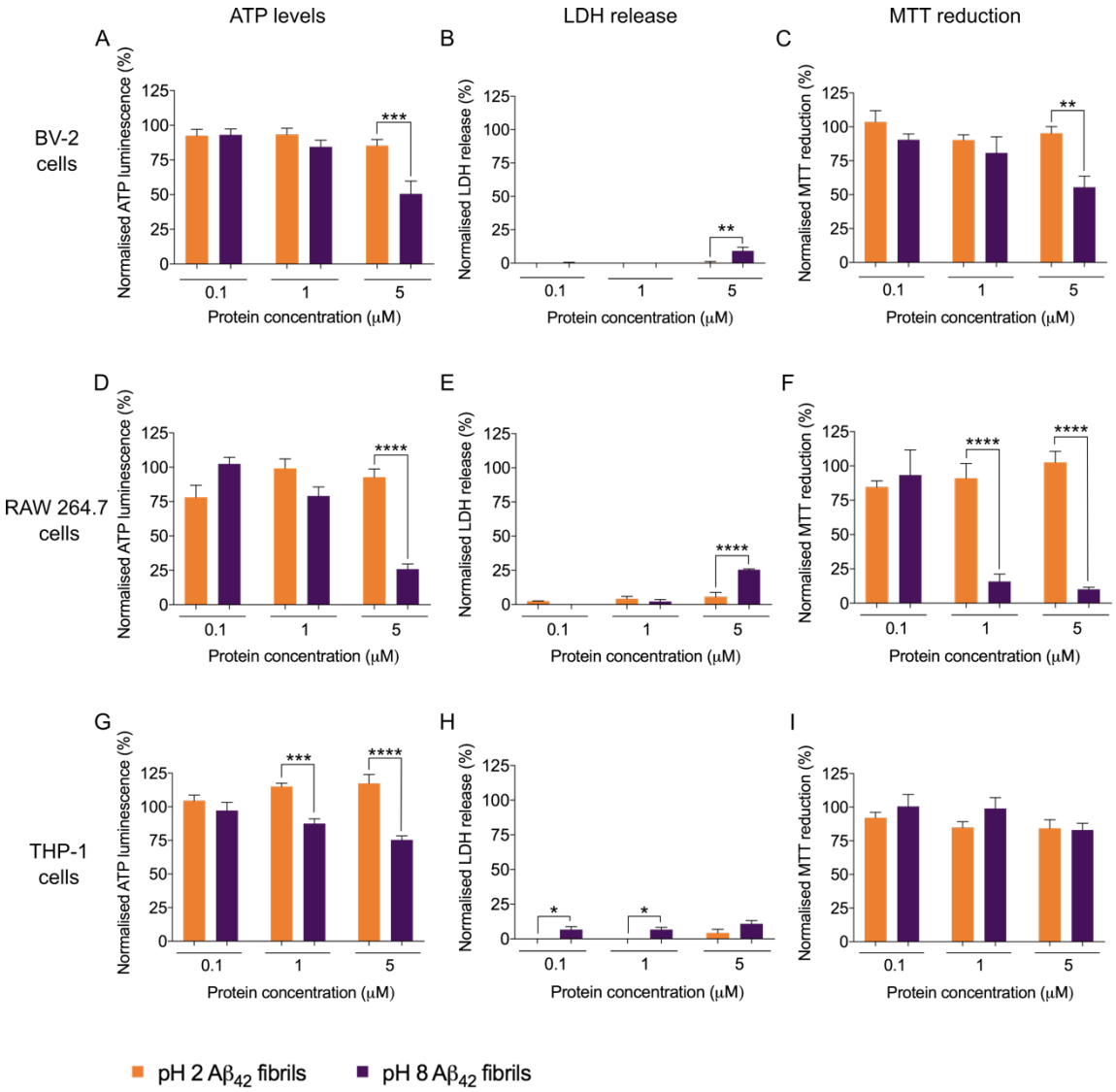

Figure 4.5 Analysis of the effect of Aβ42 fibril preparations on the viability of BV-2, RAW 264.7 and THP-1 cells

(A-C) BV-2 cells were incubated with 0.1, 1 or 5 μM of pH 2 or pH 8 Aβ42 fibril preparations for 48 h before cellular ATP (A), LDH (B) and MTT (C) viability assays were performed D-F) RAW 264.7 cells were incubated with 0.1, 1 or 5 μM of pH 2 or pH 8 Aβ42 fibril preparations for 48 h before cellular ATP (D), LDH (E) and MTT (F) viability assays were performed. G-I) THP-1 cells were incubated with 0.1, 1 or 5 μM of pH 2 and pH 8 Aβ42 fibril preparations for 48 h before cellular ATP (G), LDH (H) and MTT (I) viability assays were performed. LDH release data are normalised to cells treated with lysis buffer after the same incubation period and ATP/MTT data are normalised to cells incubated with corresponding fibril growth buffer. Error bars represent mean ± SEM (n=3). One-way ANOVA with Tukey's multiple comparisons test was used to compare between fibril preparations, *, p≤0.05.**, p≤0.01, ***, p≤0.001, ****, p≤0.0001. All fibril concentrations are monomer-equivalent.

BV-2 cells – ATP assay	0.1 μM	1 μM	5 μM
	p value (vs buffer control)	p value (vs buffer control)	p value (vs buffer control)
2A $A\beta_{40}$	ns	ns	ns
3Q $A\beta_{40}$	ns	ns	ns
De novo $A\beta_{40}$	ns	ns	ns
$A\beta_{40}$ E22Δ	ns	0.0162 (*)	<0.0001 (****)
pH 2 $A\beta_{42}$	ns	ns	ns
pH 8 $A\beta_{42}$	ns	ns	<0.0001 (****)

Table 4.1. P values for the effects of Aβ fibril preparations on ATP levels in BV-2 cells compared to buffer controls
Values for ATP levels in BV-2 cells after 48 h incubation with Aβ fibrils were compared to those in cells incubated with the equivalent volume of the corresponding fibril buffer to identify significant effects using one-way ANOVA with Sidak's multiple comparisons test

BV-2 cells – LDH assay	0.1 μM	1 μM	5 μM
	p value (vs buffer control)	p value (vs buffer control)	p value (vs buffer control)
2A $A\beta_{40}$	ns	ns	ns
3Q $A\beta_{40}$	ns	ns	ns
De novo $A\beta_{40}$	ns	ns	ns
$A\beta_{40}$ E22Δ	ns	ns	0.0269 (*)
pH 2 $A\beta_{42}$	ns	ns	ns
pH 8 $A\beta_{42}$	ns	ns	<0.0001 (****)

Table 4.2. P values for the effects of Aβ fibril preparations on LDH release in BV-2 cells compared to buffer controls
Values for LDH release in BV-2 cells after 48 h incubation with Aβ fibrils were compared to those in cells incubated with the equivalent volume of the corresponding fibril buffer to identify significant effects using one-way ANOVA with Sidak's multiple comparisons test.

BV-2 cells - MTT assay	0.1 μM	1 μM	5 μM
	p value (vs buffer control)	p value (vs buffer control)	p value (vs buffer control)
2A $A\beta_{40}$	ns	ns	0.0276 (*)
3Q $A\beta_{40}$	0.0051 (**)	ns	ns
De novo $A\beta_{40}$	ns	ns	ns
$A\beta_{40}$ E22Δ	ns	ns	0.0038 (**)
pH 2 $A\beta_{42}$	ns	ns	ns
pH 8 $A\beta_{42}$	ns	ns	<0.0001 (****)

Table 4.3. P values for the effects of Aβ fibril preparations on MTT reduction in BV-2 cells compared to buffer controls
Values for MTT reduction in BV-2 cells after 48 h incubation with Aβ fibrils were compared to those in cells incubated with the equivalent volume of the corresponding fibril buffer to identify significant effects using one-way ANOVA with Sidak's multiple comparisons test.

RAW 264.7 cells – ATP assay	0.1 μM	1 μM	5 μM
	p value (vs buffer control)	p value (vs buffer control)	p value (vs buffer control)
2A $A\beta_{40}$	ns	0.0174 (*)	0.0216 (*)
3Q $A\beta_{40}$	ns	ns	ns
De novo $A\beta_{40}$	ns	ns	ns
$A\beta_{40}$ E22Δ	ns	ns	ns
pH 2 $A\beta_{42}$	ns	ns	ns
pH 8 $A\beta_{42}$	ns	ns	0.0020 (**)

Table 4.4. P values for the effects of Aβ fibril preparations on ATP levels in RAW 264.7 cells compared to buffer controls
Values for ATP levels in RAW 264.7 cells after 48 h incubation with Aβ fibrils were compared to those in cells incubated with the equivalent volume of the corresponding fibril buffer to identify significant effects using one-way ANOVA with Sidak's multiple comparisons test.

RAW 264.7 cells – LDH assay	0.1 μM	1 μM	5 μM
	p value (vs buffer control)	p value (vs buffer control)	p value (vs buffer control)
2A $A\beta_{40}$	ns	ns	ns
3Q $A\beta_{40}$	ns	ns	ns
De novo $A\beta_{40}$	ns	ns	ns
$A\beta_{40}$ E22Δ	ns	0.0042 (**)	<0.0001 (****)
pH 2 $A\beta_{42}$	ns	ns	ns
pH 8 $A\beta_{42}$	ns	ns	<0.0001 (****)

Table 4.5. P values for the effects of Aβ fibril preparations on LDH release in RAW 264.7 cells compared to buffer controls
Values for LDH release in RAW 264.7 cells after 48 h incubation with Aβ fibrils were compared to those in cells incubated with the equivalent volume of the corresponding fibril buffer to identify significant effects using one-way ANOVA with Sidak's multiple comparisons test.

RAW 264.7 cells – MTT assay	0.1 μM	1 μM	5 μM
	p value (vs buffer control)	p value (vs buffer control)	p value (vs buffer control)
2A $A\beta_{40}$	ns	ns	0.0439 (*)
3Q $A\beta_{40}$	ns	0.0232 (*)	ns
De novo $A\beta_{40}$	ns	0.0110 (*)	0.0042 (*)
$A\beta_{40}$ E22Δ	0.0270 (*)	ns	0.0002 (***)
pH 2 $A\beta_{42}$	ns	ns	ns
pH 8 $A\beta_{42}$	ns	0.0005 (***)	0.0002 (***)

Table 4.6. P values for the effects of Aβ fibril preparations on MTT reduction in RAW 264.7 cells compared to buffer controls
Values for MTT reduction in RAW 264.7 cells after 48 h incubation with Aβ fibrils were compared to those in cells incubated with the equivalent volume of the corresponding fibril buffer to identify significant effects using one-way ANOVA with Sidak's multiple comparisons test.

THP-1 cells - ATP assay	0.1 µM	1 µM	5 µM
	p value (vs buffer control)	p value (vs buffer control)	p value (vs buffer control)
2A $A\beta_{40}$	ns	ns	ns
3Q $A\beta_{40}$	ns	ns	ns
De novo $A\beta_{40}$	ns	ns	ns
$A\beta_{40}$ E22Δ	ns	ns	ns
pH 2 $A\beta_{42}$	ns	ns	ns
pH 8 $A\beta_{42}$	ns	ns	0.0105 (*)

Table 4.7. P values for the effects of Aβ fibril preparations on ATP levels in THP-1 cells compared to buffer controls
Values for ATP levels in THP-1 cells after 48 h incubation with Aβ fibrils were compared to those in cells incubated with the equivalent volume of the corresponding fibril buffer to identify significant effects using one-way ANOVA with Sidak's multiple comparisons test.

THP-1 cells - LDH assay	0.1 µM	1 µM	5 µM
	p value (vs buffer control)	p value (vs buffer control)	p value (vs buffer control)
2A $A\beta_{40}$	ns	ns	ns
3Q $A\beta_{40}$	ns	ns	0.0119 (*)
De novo $A\beta_{40}$	ns	ns	ns
$A\beta_{40}$ E22Δ	ns	ns	ns
pH 2 $A\beta_{42}$	ns	ns	ns
pH 8 $A\beta_{42}$	ns	ns	0.0053 (**)

Table 4.8. P values for the effects of Aβ fibril preparations on LDH release in THP-1 cells compared to buffer controls
Values for LDH release in THP-1 cells after 48 h incubation with Aβ fibrils were compared to those in cells incubated with the equivalent volume of the corresponding fibril buffer to identify significant effects using one-way ANOVA with Sidak's multiple comparisons test.

THP-1 cells - MTT assay	0.1 µM	1 µM	5 µM
	p value (vs buffer control)	p value (vs buffer control)	p value (vs buffer control)
2A $A\beta_{40}$	ns	ns	ns
3Q $A\beta_{40}$	ns	ns	ns
De novo $A\beta_{40}$	ns	ns	ns
$A\beta_{40}$ E22Δ	ns	ns	ns
pH 2 $A\beta_{42}$	ns	ns	ns
pH 8 $A\beta_{42}$	ns	ns	ns

Table 4.9. P values for the effects of Aβ fibril preparations on MTT reduction in THP-1 cells compared to buffer controls
Values for MTT reduction in THP-1 cells after 48 h incubation with Aβ fibrils were compared to those in cells incubated with the equivalent volume of the corresponding fibril buffer to identify significant effects using one-way ANOVA with Sidak's multiple comparisons test.

In addition to measuring ATP levels, LDH release and MTT reduction, for BV-2 microglial cells microscopy images were taken after 48 h incubation with Aβ fibril preparations to assess the effects of the different fibril preparations on cellular morphology. No pronounced changes in cell morphology were observed in the cells incubated with either 2A, 3Q or *de novo* $A\beta_{40}$ fibril preparations compared to those incubated with fibril growth buffers (Figure 4.6). The majority of cells appear to be approximately spherical in shape, with some cells extending processes towards others, as expected for BV-2 cells (Blasi et al., 1990). This is consistent with the results from viability assays for these fibrils in which no pronounced effect was observed (Figure 4.3).

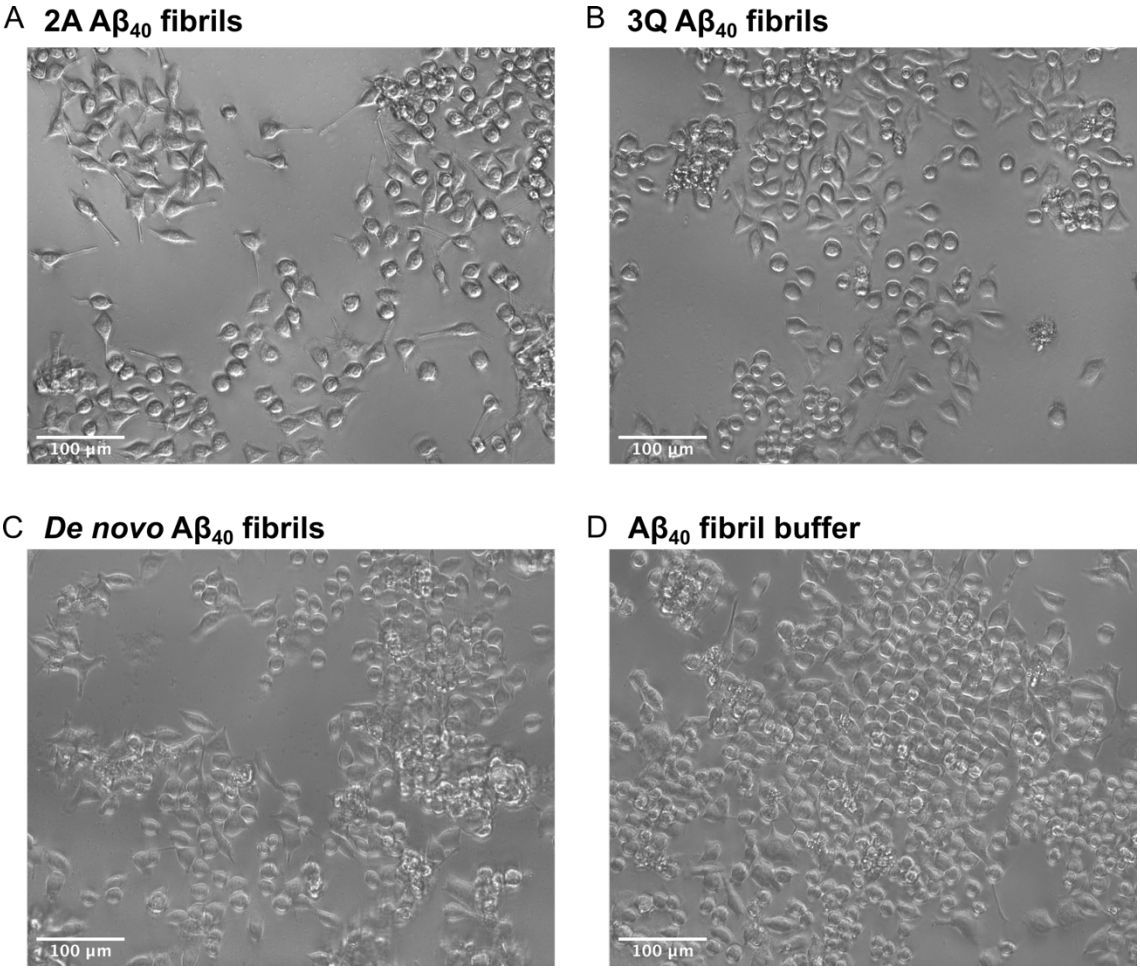

Figure 4.6. BV-2 microglial cell morphology after 48 h incubation with $A\beta_{40}$ fibril preparations
BV-2 cells were incubated for 48 h with 5 µM monomer-equivalent concentration of (A) 2A, (B) 3Q, (C) *de novo* $A\beta_{40}$ fibril preparations or (D) fibril growth buffer alone before imaging using an EVOS microscope with 20x objective. Representative phase-contrast images are shown. Scale bar = 100 µm

In contrast to cells incubated with $A\beta_{40}$, the most notable feature in images of BV-2 cells incubated with 5 μM of $A\beta_{40}$ E22Δ fibrils is the presence of cellular debris in areas between remaining cells, suggestive of cell damage (Figure 4.7A). Some remaining cells can also be seen to have lost the spherical shape of the cell body and are more swollen and irregular in shape than those incubated only with buffer (Figure 4.7). There is also evidence of clusters of floating cells in samples incubated with $A\beta_{40}$ E22Δ fibrils (Arrow in Figure 4.7). These changes to BV-2 cell morphology suggest that the $A\beta_{40}$ E22Δ fibrils are having a deleterious effect on these cells, which is consistent with the observations above (Figure 4.4).

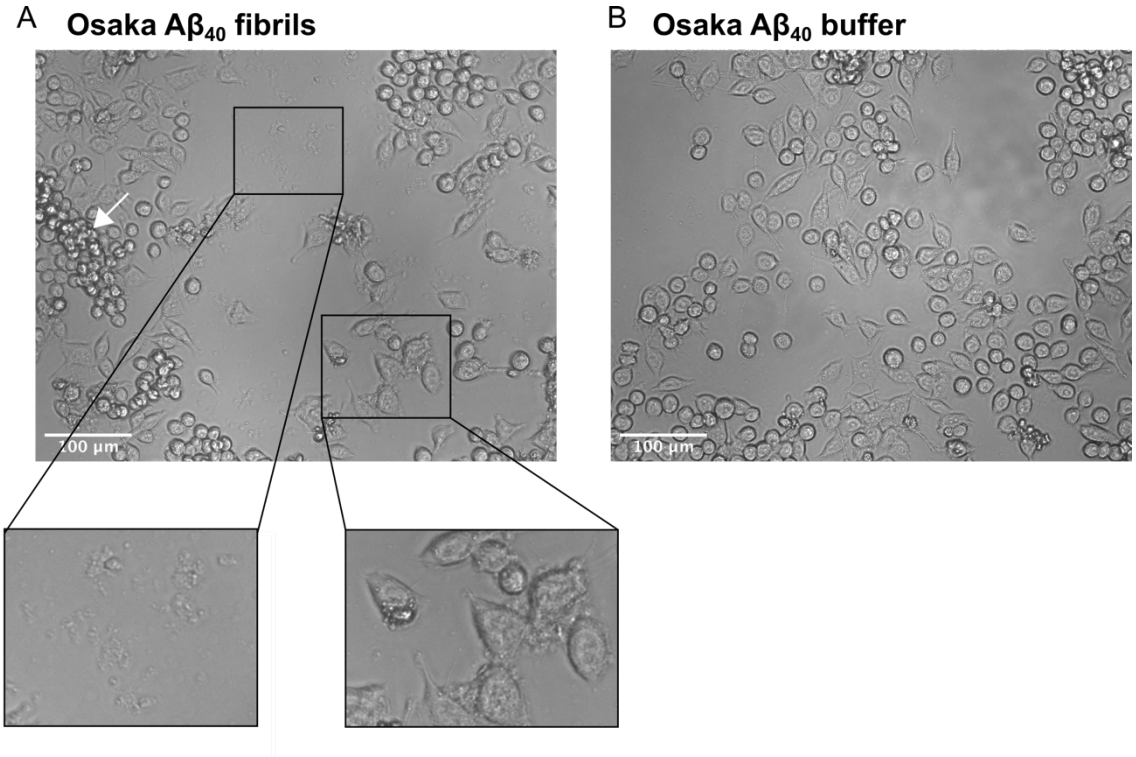

Figure 4.7. BV-2 microglial cell morphology after 48 h incubation with $A\beta_{40}$ E22Δ fibrils
(A) Image of BV-2 cells after 48 h incubation with 5 μM monomer-equivalent concentration of $A\beta_{40}$ E22Δ fibrils. Higher magnification image on the left highlights cellular debris. Higher magnification image on right highlights cells with swollen and irregular morphology. White arrow indicates populations of detached cells. (B) Image of BV-2 cells after 48 h incubation with equivalent volume of $A\beta_{40}$ E22Δ fibril growth buffer. Images are representative and were taken using an EVOS microscope with 20x objective. Scale bar = 100 μm.

BV-2 cells incubated with 5 μM $A\beta_{42}$ fibrils formed at pH 2 are indistinguishable from those incubated with buffer alone, (Figure 4.8A/B), consistent with no effect of the fibrils on cell viability observed in the ATP, LDH and MTT assays (Figure 4.5). However, differences can be observed in BV-2 cells incubated with 5 μM $A\beta_{42}$ fibrils formed at pH 8 compared to those treated with buffer alone (Figure 4.8C/D). The number of cells that could be observed in these images was reduced. This aligns with the results of the viability assays above (Figure 4.5) and is consistent with the cells dying as a consequence of incubation with these $A\beta_{42}$ pH 8 fibrils. As observed for cells treated with

$A\beta_{40}$ E22Δ fibrils, there is also evidence of cell debris in the gaps between remaining cells (Figure 4.8C). The cells that remain are similar in morphology to expected healthy cells, although there are some cells with more amorphous cell bodies and longer processes (Arrows in Figure 4.8C).

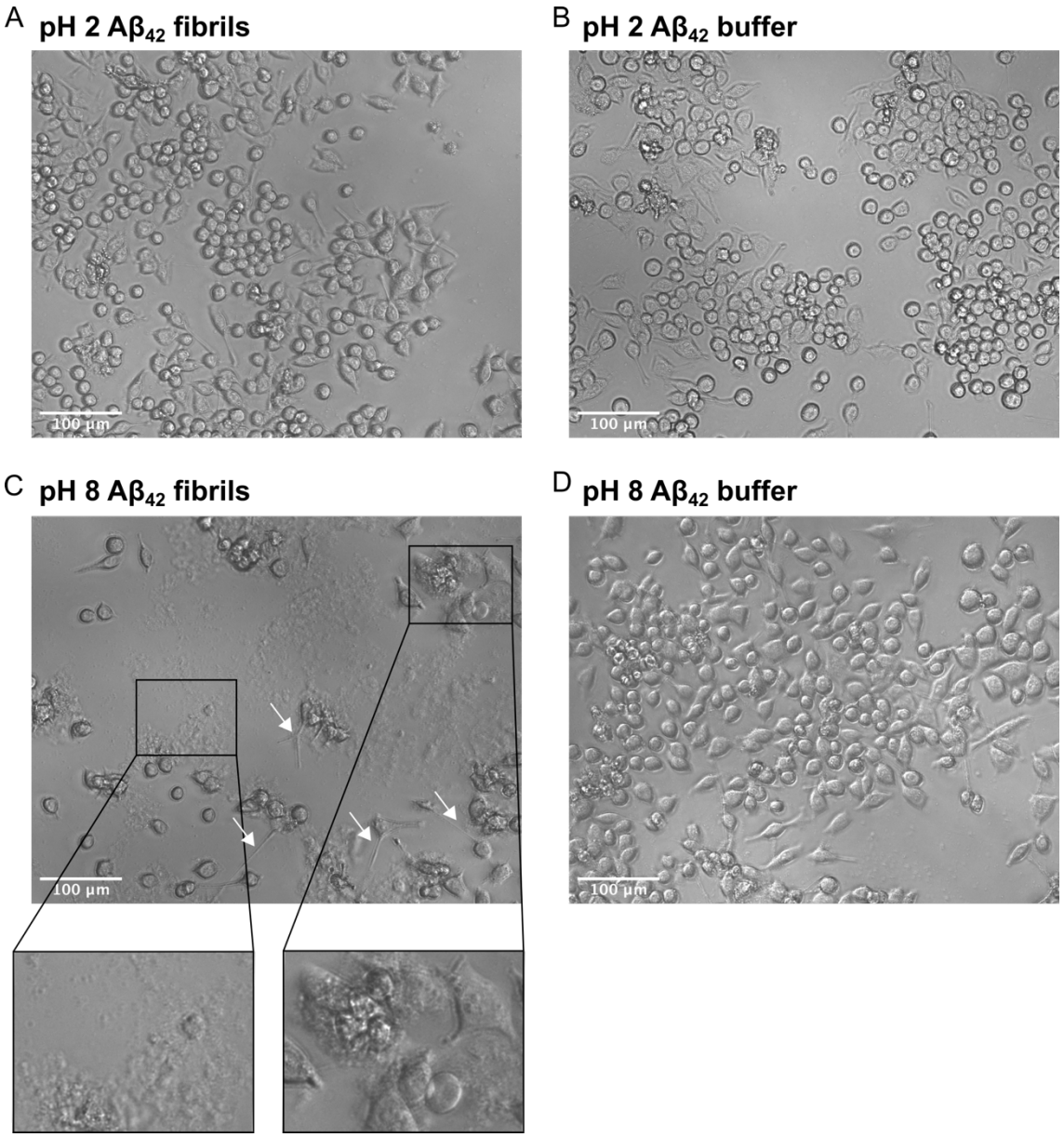

Figure 4.8. BV-2 microglial cell morphology after 48 h incubation with $A\beta_{42}$ fibril preparations
(A) Image of BV-2 cells after 48 h incubation with 5 µM monomer-equivalent concentration of pH 2 $A\beta_{42}$ fibrils. (B) Image of BV-2 cells after 48 h incubation with the equivalent volume of pH 2 $A\beta_{42}$ fibril growth buffer. (C) Image of BV-2 cells after 48 h incubation with with 5 µM monomer-equivalent concentration of pH 8 $A\beta_{42}$ fibrils. Left higher magnification image highlights cellular debris and right higher magnification image shows amorphous cells. White arrows indicate the presence of long processes extending from cells. (D) Image of BV-2 cells after 48 h incubation with equivalent volume of pH 8 $A\beta_{42}$ fibril growth buffer alone. Phase-contrast images shown are representative and were taken using an EVOS microscope with a 20x objective. Scale bar = 100 µm

Taken together, these data suggest that $A\beta_{40}$ E22Δ and pH 8 $A\beta_{42}$ fibril preparations are toxic towards the immune cell lines analysed, with the greatest effect being observed at the 5 μM Aβ monomer-equivalent concentration. However, research into the toxic form of Aβ has implicated oligomers as the principal toxic species of Aβ assembly reactions (Sengupta et al., 2016) (Section 1.2.4). Further experiments were therefore performed to confirm whether the fibrils were indeed responsible for the observed toxicity. For this, first $A\beta_{40}$ E22Δ fibril samples were centrifuged at 16,873 xg to pellet fibrillar material. Supernatant and pellet fractions were then separated, and the pellet resuspended in fresh fibril buffer. The pellet fraction will contain insoluble fibrillar material, whereas any small proportion of soluble oligomeric or monomeric species will be present in the supernatant fraction. To test the toxicity of these different fractions, equal volumes of whole sample, supernatant and pellet fractions added to BV-2 cells for 48 h and ATP/LDH assays performed (Figure 4.9).

Results from these assays show that the pellet fraction containing fibrillar material was toxic to cells, leading to a decrease in cellular ATP levels and an increase in LDH release (Figure 4.9). The supernatant fraction did cause a reduction in ATP at the highest volume added, but no significant increase in LDH release was detected. This suggests that the fibrils themselves are toxic. Moreover, although smaller non-sedimentable species in the supernatant fraction may also be toxic, these could be smaller fibrils in the sample that were not efficiently pelleted.

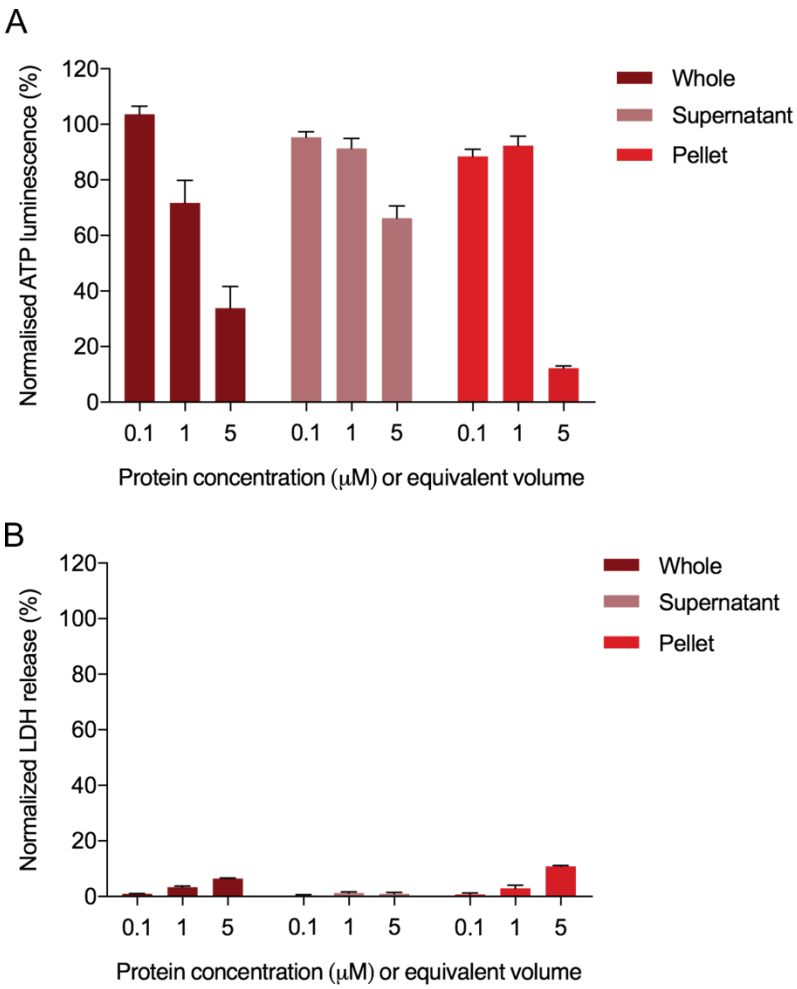

Figure 4.9. Analysis of the effect of $A\beta_{40}$ E22Δ fibril pellet and supernatant fractions on the viability of BV-2 cells
$A\beta_{40}$ E22Δ fibrils were centrifuged for 40 min at 16,873 xg to separate insoluble (pellet) and soluble (supernatant) material. The pellet was resuspended in fresh fibril buffer and 0.1, 1 or 5 μM of the whole sample or the equivalent volume of supernatant or pellet fractions was added to BV-2 cells and incubated for 48 h. (A) ATP and (B) LDH assays were then performed on cells. LDH release data are normalised to cells treated with lysis buffer after the same incubation period and ATP data are normalised to cells incubated with fibril growth buffer. Error bars represent mean ± SEM (n=3). All fibril concentrations are monomer-equivalent.

The pH 8 $A\beta_{42}$ fibril preparations were also centrifuged to pellet insoluble fibril material (as described in Section 2.6.2), and the separated fractions added to BV-2 cells for 48 h before viability assays were performed (Figure 4.10). These experiments showed that the pellet fraction of pH 8 $A\beta_{42}$ fibrils exhibited the same effect on ATP levels and LDH release on BV-2 cells as the whole non-centrifuged fibril sample. This indicates that the fibrils are toxic to BV-2 cells (Figure 4.10). The first supernatant did show some toxic effect in both viability assays; however, this was not observed when the sample is centrifuged again (Supernatant 2). This suggests that this toxicity resulted from residual fibrils remaining in the sample.

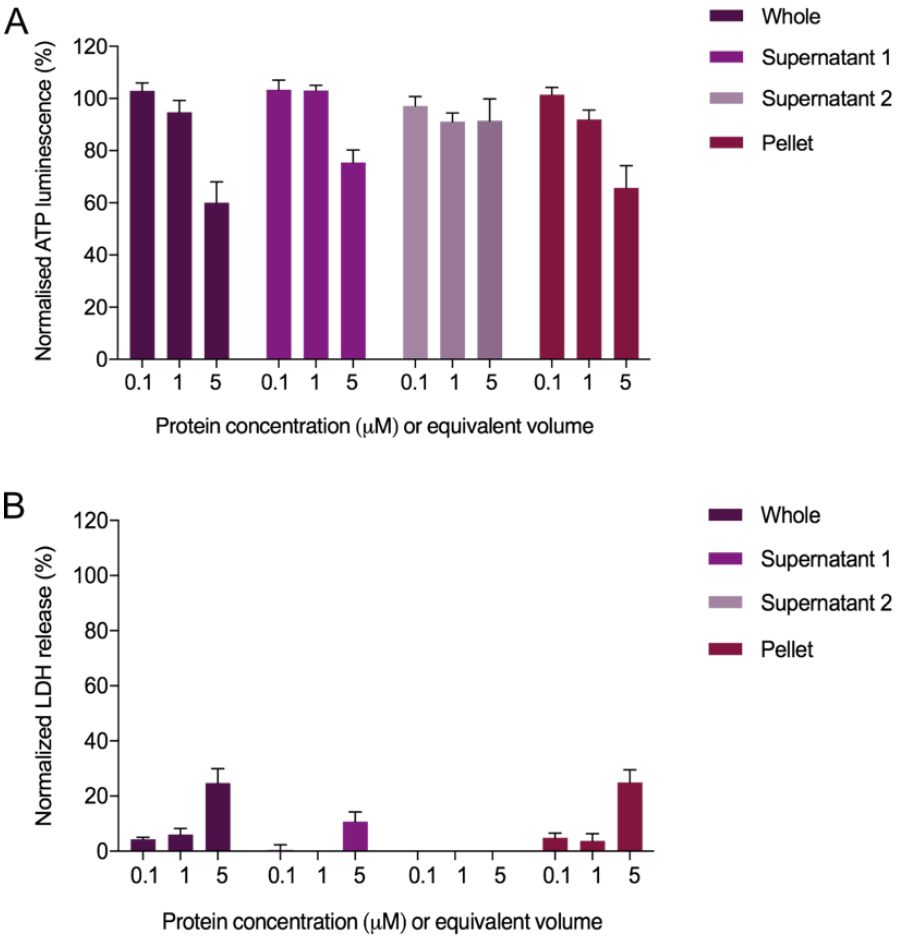

Figure 4.10. Analysis of the effect of pH 8 Aβ$_{42}$ fibril pellet and supernatant fractions on the viability of BV-2 cells
pH 8 Aβ$_{42}$ fibrils were centrifuged for 40 min at 16,873 xg to separate insoluble and soluble material. The pellet was resuspended in fresh fibril buffer, and samples of the supernatant taken (Supernatant 1) before centrifugation was repeated under the same conditions (Supernatant 2). 0.1, 1 or 5 μM of the whole sample or the equivalent volume of supernatant or pellet fractions was added to BV-2 cells and incubated for 48 h. (A) ATP and (B) LDH assays were then performed on cells. Error bars represent mean ± SEM (n=3). All fibril concentrations are monomer-equivalent.

In summary, the use of ATP, LDH and MTT viability assays in combination with microscopy indicate that the 2A, 3Q and *de novo* Aβ$_{40}$ fibrils have no observable effect on the viability of BV-2, RAW 264.7 or THP-1 cells (Figure 4.3). However, results from these experiments indicate that Aβ$_{40}$ E22Δ fibrils are toxic towards BV-2 microglial cells and RAW 264.7 macrophage cells, with no observable effects on THP-1 cells (Figure 4.4). In addition, a differential effect on cell viability was identified between Aβ$_{42}$ fibril preparations, with pH 2 Aβ$_{42}$ fibrils having no observable effect on cell viability, whereas pH 8 Aβ$_{42}$ fibrils were toxic to all three cell lines tested (Figure 4.5). These results are summarised in Table 4.10.

Both Aβ$_{42}$ fibril populations were formed from the same initial Aβ$_{42}$ monomeric peptide but were resuspended in distinct buffers. Furthermore, for all assays a negative control

was carried out in which cells were incubated with these fibrillation buffers in the absence of fibrils, and this value was subtracted from experimental values. The differential toxicity identified therefore cannot be attributed to differences in the peptide or buffer in the samples, implicating differences in fibril structure as the causative factor.

	2A $A\beta_{40}$	**3Q $A\beta_{40}$**	**De novo $A\beta_{40}$**	**$A\beta_{40}$ E22Δ**	**pH 2 $A\beta_{42}$**	**pH 8 $A\beta_{42}$**
BV-2 cells	Not toxic	Not toxic	Not toxic	Toxic	Not toxic	Toxic
RAW 264.7 cells	Not toxic	Not toxic	Not toxic	Toxic	Not toxic	Toxic
THP-1 cells	Not toxic	Not toxic	Not toxic	Not toxic	Not toxic	Toxic

Table 4.10. Summary of fibril preparation toxicities from viability experiments and microscopy

4.2.1 Measurement of reactive oxygen species (ROS) generation in response to Aβ fibril preparations

ROS production is an indicator of cellular stress and ROS are also key signalling molecules in the inflammatory response (Nathan and Cunningham-Bussel, 2013). Therefore, ROS generation was measured in response to the different Aβ fibril preparations. This was measured using a cell permeant dye (CellRox Green, Thermo Fisher Scientific). This dye is weakly fluorescent in the reduced state but becomes more fluorescent when oxidised by ROS and binds to DNA. Green fluorescence of cell samples is therefore measured using a plate reader as a readout of cellular ROS levels.

For this assay optimisation experiments were first required to identify the timescale of incubation and concentration of Aβ fibril required in subsequent ROS measurements. 2A $A\beta_{40}$ and pH 8 $A\beta_{42}$ fibrils were used for these preliminary tests, as from viability experiments these fibrils would be predicted to have the least and greatest effect on cells, allowing clearer identification of any differences. Monomer-equivalent concentrations of fibrils from 1-10 μM were tested at 24, 48 and 72 h timepoints (Figure 4.11).

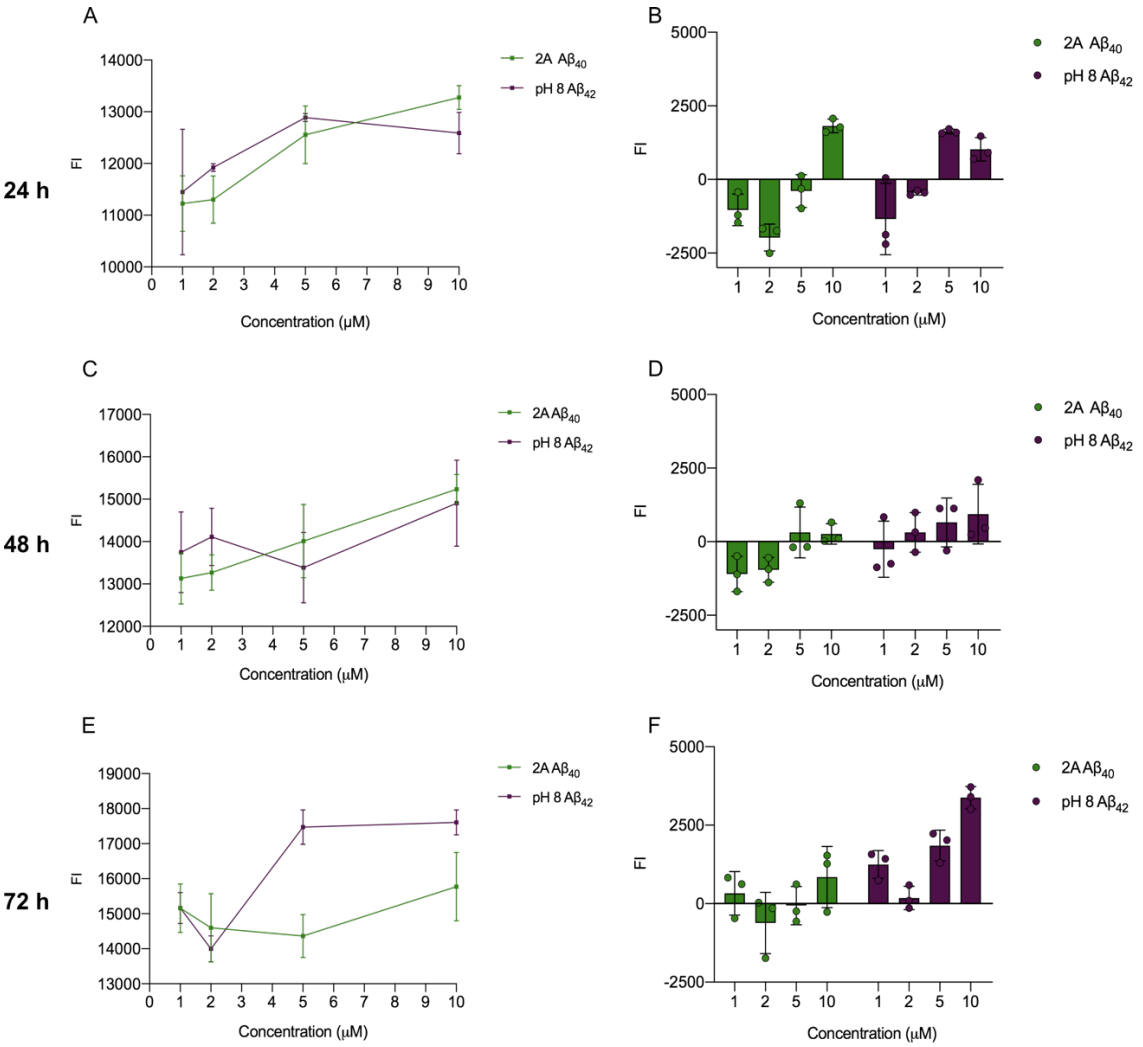

Figure 4.11. Time course and concentration series of ROS generation from BV-2 cells in response to 2A $A\beta_{40}$ and pH 8 $A\beta_{42}$ fibrils
BV-2 cells were incubated with 1, 2, 5 or 10 μM (monomer-equivalent concentration) of 2A $A\beta_{40}$ or pH 8 $A\beta_{42}$ fibril preparations for (A/B) 24 h (C/D) 48 h or (E/F) 72 h. Cells were then incubated with 5 μM CellRox dye for 30 min at 37 °C. Cells were washed x2 in PBS to remove excess dye. Samples were excited in a Clariostar platereader (BMG Labtech) at 485 nm and emission measured at 520 nm. Error bars represent mean ± SD over a total of 3 replicates (n=1). ROS release from cells treated with buffer controls has been subtracted from samples in the right panel (B/D/F)

These experiments showed that increasing concentrations of both Aβ fibrils above 2 μM (monomer-equivalent concentration) leads to increased ROS generation. However, a difference in ROS generation was only observed between cells incubated with pH 8 $A\beta_{42}$ fibrils compared to 2A fibrils after 72 h. Based on this, subsequent experiments were performed using 5 μM monomer-equivalent concentration of Aβ fibrils for 72 h (Figure 4.12).

Results from these experiments showed only small increases in ROS generation compared to buffer treatment; this increase was significant for all Aβ fibril preparations apart from the pH 8 $A\beta_{42}$ fibrils (Figure 4.12A). However, there were no significant differences in the levels of ROS generation induced in response to the different Aβ fibril

polymorphs (Figure 4.12B). The *de novo* $A\beta_{40}$ fibrils had the greatest effect on ROS production. This fibril preparation was not previously observed to have an effect in viability experiments.

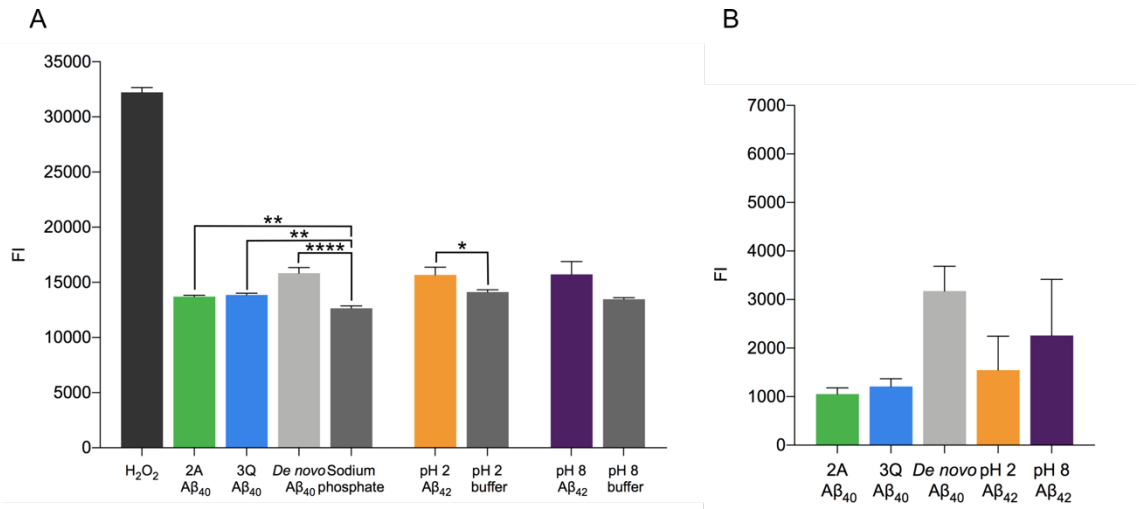

Figure 4.12. ROS generation in BV-2 cells after incubation with Aβ fibrils for 72 h
BV-2 cells were incubated with 5 μM (monomer-equivalent concentration) of Aβ fibril preparations for 72 h. Cells were then incubated with 5 μM CellRox dye for 30 min at 37 °C. Cells were washed x2 in PBS to remove excess dye before fluorescence was measured at 488 nm. Cells were treated with 200 μM H_2O_2 as a positive control for ROS measurement. (A) ROS release in response to Aβ fibrils is compared to cells incubated with corresponding fibril growth buffer. Error bars represent mean ± SEM (n=3), Unpaired t-test *, p≤0.05, **, p≤0.01, ****, p≤0.0001. (B) ROS generation resulting from incubation with fibril polymorphs with corresponding buffer values subtracted. Comparisons between fibril preparations were made using one-way ANOVA test with Tukey's multiple comparisons.

4.3 Inflammatory activation of immune cells elicited by distinct Aβ fibril preparations

Having identified differences in the toxicity of distinct Aβ fibrils towards microglial and monocytic cell lines, differences in the inflammatory response elicited from these cells in response to the fibrils was next explored. The release of pro-inflammatory cytokines was measured, as these inflammatory mediators are involved in the damaging neuroinflammation that is observed in AD brains (discussed in Section 1.4.4) (Sarlus and Heneka, 2017).

4.3.1 Measurement of pro-inflammatory cytokine release in response to Aβ fibril preparations

For cytokine release experiments, both BV-2 microglial cells and THP-1 monocytic cells were used. First, it was necessary to investigate the timescale in which Aβ fibrils lead to cytokine release from cells. For this, a time course was carried out in which THP-1 cells were incubated with fibril preparations for 24, 48 or 72 h, and the levels of TNF-α released from cells measured by ELISA (Figure 4.13). A monomer-equivalent concentration of 2

μM fibril preparation was used, which is similar to that used in previously published work using THP-1 cells and was found produce a measurable cytokine response (Yates et al., 2000; Cohen et al., 2015).

A

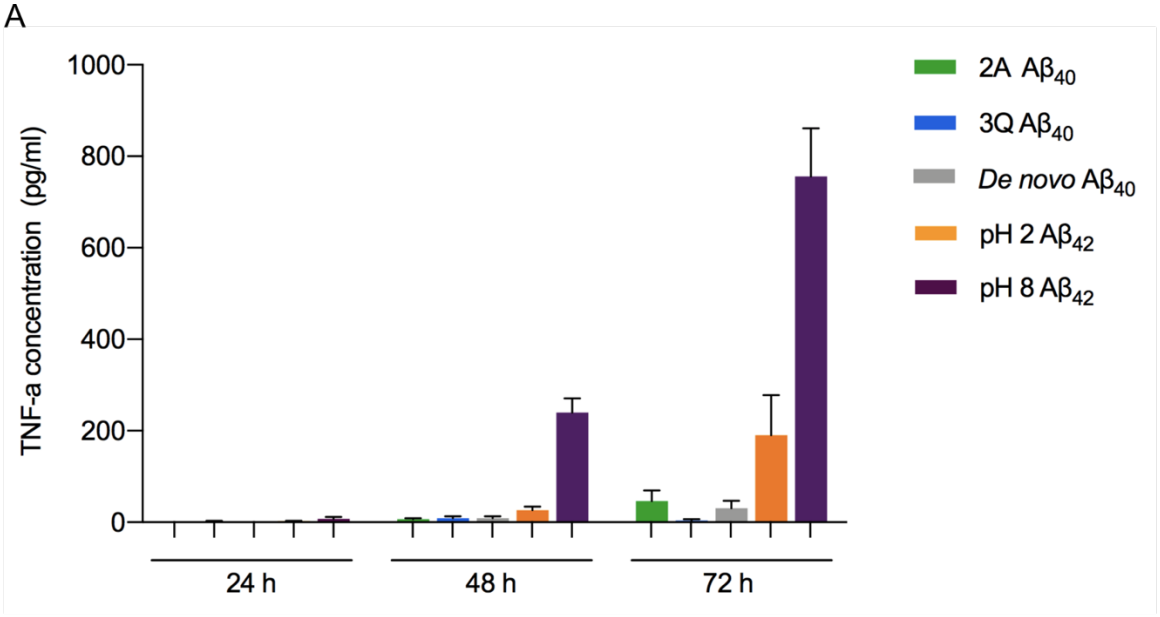

B

24 h

	2A Aβ40	3Q Aβ40	De novo Aβ40	pH 2 Aβ42	pH 8 Aβ42
2A Aβ40					
3Q Aβ40	ns				
De novo Aβ40	ns	ns			
pH 2 Aβ42	ns	ns	ns		
pH 8 Aβ42	ns	ns	ns	ns	

C

48 h

	2A Aβ40	3Q Aβ40	De novo Aβ40	pH 2 Aβ42	pH 8 Aβ42
2A Aβ40					
3Q Aβ40	ns				
De novo Aβ40	ns	ns			
pH 2 Aβ42	ns	ns	ns		
pH 8 Aβ42	<0.0001 (****)	<0.0001 (****)	<0.0001 (****)	<0.0001 (****)	

D

72 h

	2A Aβ40	3Q Aβ40	De novo Aβ40	pH 2 Aβ42	pH 8 Aβ42
2A Aβ40					
3Q Aβ40	ns				
De novo Aβ40	ns	ns			
pH 2 Aβ42	ns	ns	ns		
pH 8 Aβ42	<0.0001 (****)	<0.0001 (****)	<0.0001 (****)	<0.0001 (****)	

Figure 4.13. Time course of TNF-α release from THP-1 cells upon incubation with Aβ fibrils
(A) THP-1 cells were incubated with 2 μM monomer-equivalent concentration of the different Aβ fibril preparations for 24, 48 or 72 h. Samples of the cell media were taken and TNF-α concentrations measured by ELISA. Concentrations were calculated from a standard curve. Error bars represent the mean ± SEM (n=3). (B-D) p values for differences between Aβ fibril preparations in TNF-α release calculated using one-way ANOVA with Tukey's multiple comparison test after (B) 24 h, (C) 48 h, (D) 72 h incubation with Aβ fibrils.

This time course experiment showed that there was minimal TNF-α release from THP-1 cells after 24 h incubation with Aβ fibrils (Figure 4.13A/B). After 48 h, higher TNF-α release was measured for all samples but more so for cells incubated with $Aβ_{42}$ fibrils than $Aβ_{40}$ fibrils. Further to this, significantly more TNF-α release was measured from

cells incubated with pH 8 $A\beta_{42}$ fibrils than all other fibril preparations, including pH 2 $A\beta_{42}$ fibrils (Figure 4.13C/D). At 72 h, cytokine release was found to have increased ~4-fold from 48 h, but the trend remained the same for the different fibril preparations (Figure 4.13).

Based on these results, BV-2 and THP-1 cells were incubated with Aβ fibril preparations for 72 h for subsequent experiments measuring cytokine release. Concentrations of pro-inflammatory cytokines IL-6 and TNF-α were measured in cell supernatants using ELISAs (Figure 4.14). A consistent finding from these experiments was that $A\beta_{42}$ fibrils produced a much greater release of IL-6 and TNF-α from these cell lines than $A\beta_{40}$ fibrils. The other key finding from these experiments is the differential effect of $A\beta_{42}$ fibrils formed under different fibrillation conditions. Incubation of cells with pH 8 $A\beta_{42}$ fibrils elicited a larger release of IL-6 and TNF-α than incubation with pH 2 $A\beta_{42}$ fibrils. This difference was significant for IL-6 and TNF-α release from BV-2 cells, and TNF-α release from THP-1 cells (Figure 4.14). P values of differences identified between the different Aβ fibril preparations are shown in Figure 4.14E-H.

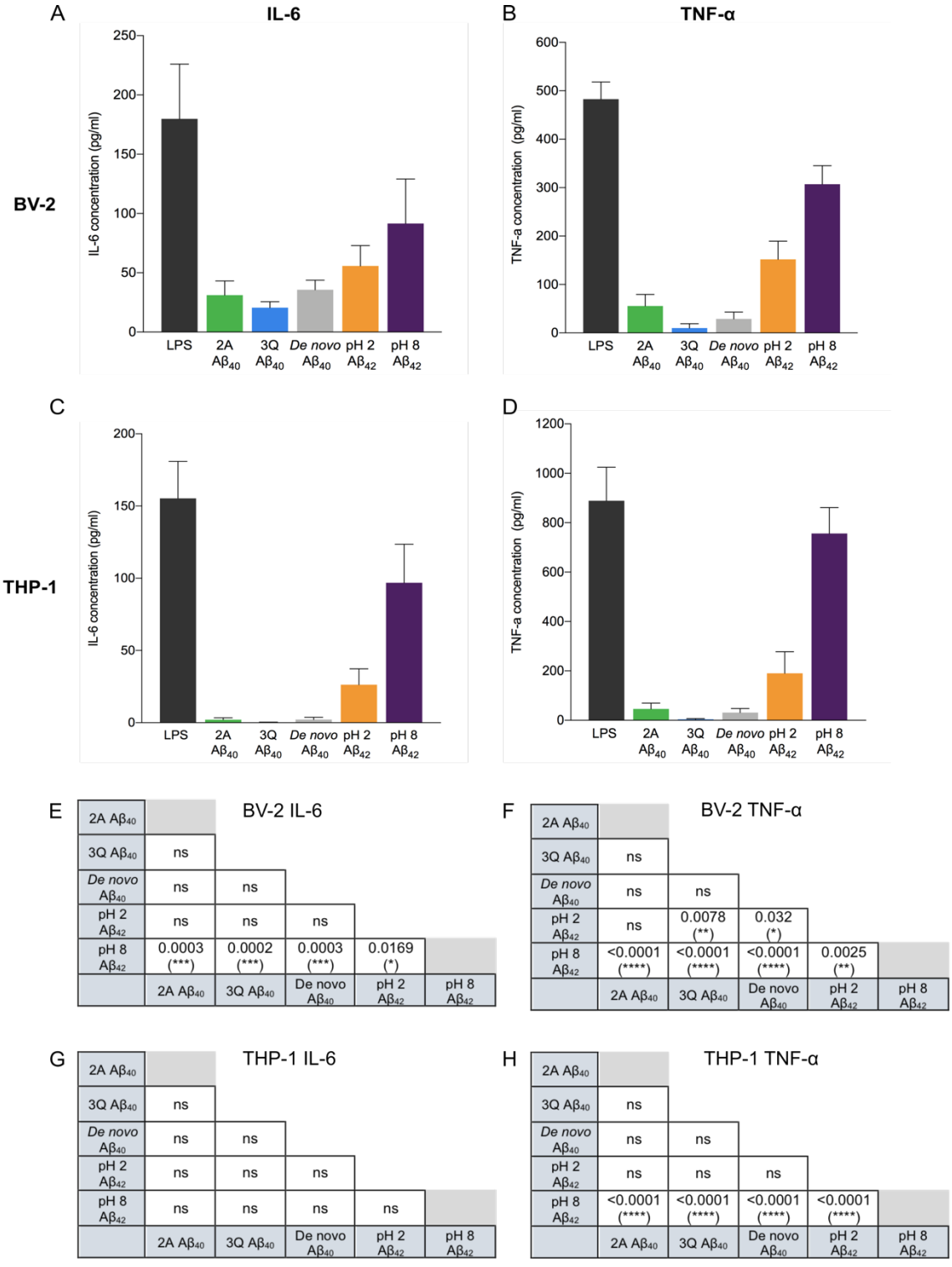

E	2A Aβ40	3Q Aβ40	De novo Aβ40	pH 2 Aβ42	pH 8 Aβ42
3Q Aβ40	ns				
De novo Aβ40	ns	ns			
pH 2 Aβ42	ns	ns	ns		
pH 8 Aβ42	0.0003 (***)	0.0002 (***)	0.0003 (***)	0.0169 (*)	

F	2A Aβ40	3Q Aβ40	De novo Aβ40	pH 2 Aβ42	pH 8 Aβ42
3Q Aβ40	ns				
De novo Aβ40	ns	ns			
pH 2 Aβ42	ns	0.0078 (**)	0.032 (*)		
pH 8 Aβ42	<0.0001 (****)	<0.0001 (****)	<0.0001 (****)	0.0025 (**)	

G	2A Aβ40	3Q Aβ40	De novo Aβ40	pH 2 Aβ42	pH 8 Aβ42
3Q Aβ40	ns				
De novo Aβ40	ns	ns			
pH 2 Aβ42	ns	ns	ns		
pH 8 Aβ42	ns	ns	ns	ns	

H	2A Aβ40	3Q Aβ40	De novo Aβ40	pH 2 Aβ42	pH 8 Aβ42
3Q Aβ40	ns				
De novo Aβ40	ns	ns			
pH 2 Aβ42	ns	ns	ns		
pH 8 Aβ42	<0.0001 (****)	<0.0001 (****)	<0.0001 (****)	<0.0001 (****)	

Figure 4.14. IL-6 and TNF-α release from BV-2 and THP-1 cells after 72 h incubation with distinct Aβ fibril preparations

BV-2 cells (A and B) and THP-1 cells (C and D) were incubated with 2 μM monomer-equivalent concentration of Aβ fibril preparations for 72 h. Cell media was then collected and IL-6 (A and C) and TNF-α levels (B and D) measured by ELISA. 1 μg/mL LPS was added to cells as a positive control for the same incubation to stimulate cytokine release. Cytokine release from cells incubated with fibril buffers alone was subtracted from fibril samples to isolate effects of the fibrils. Error bars represent mean ± SEM (n=3). (E-F) p values for differences between Aβ fibril preparations in cytokine release calculated using one-way ANOVA with Tukey's multiple comparison test.

As pH 8 $A\beta_{42}$ fibrils were previously shown to be toxic towards BV-2 and THP-1 cells, it could be suggested that the cells are not actively releasing these cytokines, but the presence of cytokines in the cell media is just a result of cell membrane damage. To investigate this, the same number of untreated cells as used in cytokine experiments were lysed after 72 h incubation and the concentration of TNF-α released was measured by ELISA (Figure 4.15). This showed very minimal TNF-α release from lysed untreated cells, suggesting that the fibrils are inducing the production of cytokines.

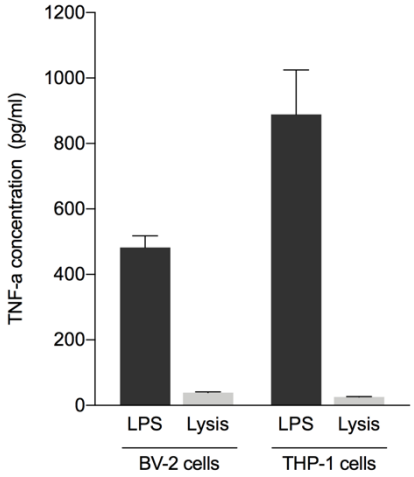

Figure 4.15. The concentration of TNF-α from lysed BV-2 and THP-1 cells
Untreated BV-2 and THP-1 cells were incubated for 72 h then lysed with 1% Triton X-100. Cell debris was removed by centrifugation and the concentration of TNF-α in samples measured using ELISA. TNF-α concentration released from cells treated with 1 μg/mL LPS are shown as comparison. Error bars represent mean ± SEM (n=2).

4.3.2 Measurement of IL-1β release in response to Aβ fibril preparations

One of the key pro-inflammatory mediators released in an inflammatory response is IL-1β, and this cytokine has been found to accumulate around Aβ plaques in AD brains (Griffin et al., 1989). IL-1β levels have also found to be elevated in the CSF and circulation of AD patients (Italiani et al., 2018). IL-1β release was therefore measured in response to the different Aβ fibril preparations (Figure 4.16).

For IL-1β measurements, cells were first primed for 3 h with LPS, as this priming signal is required to induce transcription of pro-IL-1β (Swanson et al., 2019). For consistency with previous cytokine release experiments cells were then incubated with Aβ fibrils for 72 h at a monomer-equivalent concentration of 2 μM (Figure 4.16A/B). However, under these conditions little IL-1β release was detected in the samples. A higher concentration of fibrils (10 μM monomer-equivalent) was therefore tested (Figure 4.16C/D). This resulted in an increased and differential cytokine release response from the cells (Figure 4.16C/D). When this higher concentration of fibrils was used in IL-1β experiments, the same observation from previous cytokine experiments was made; $A\beta_{42}$ fibrils elicit a greater response than $A\beta_{40}$ fibrils. In addition, cells incubated with pH 8 $A\beta_{42}$ fibrils

release a higher level of IL-1β compared to cells incubated with pH 2 $A\beta_{42}$ fibrils (Figure 4.16). The difference in IL-1β release is significant between the two $A\beta_{42}$ fibril preparations when pairwise comparisons are made between fibrils formed from the same peptide (Figure 4.16F).

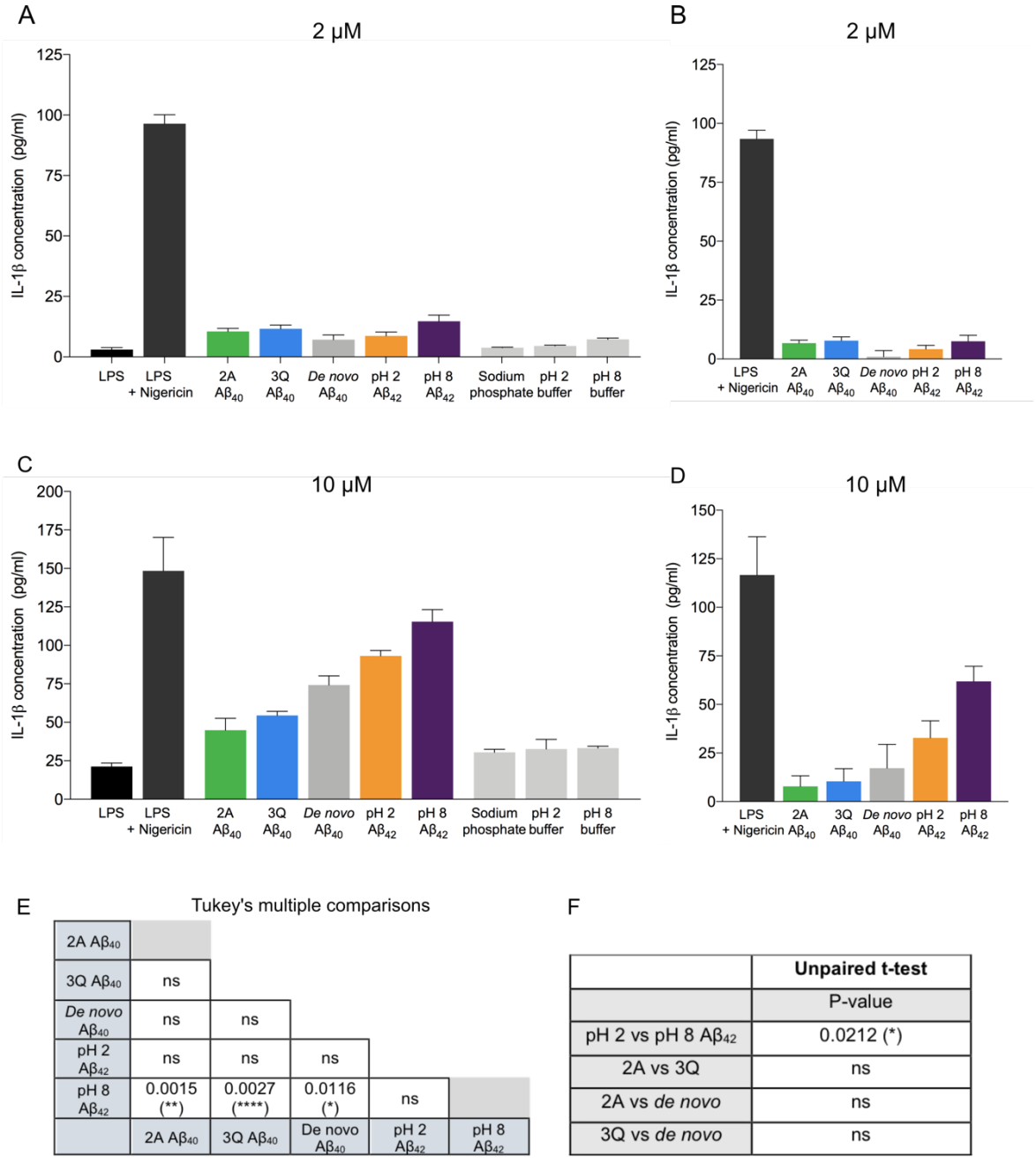

E

Tukey's multiple comparisons

2A $A\beta_{40}$					
3Q $A\beta_{40}$	ns				
De novo $A\beta_{40}$	ns	ns			
pH 2 $A\beta_{42}$	ns	ns	ns		
pH 8 $A\beta_{42}$	0.0015 (**)	0.0027 (****)	0.0116 (*)	ns	
	2A $A\beta_{40}$	3Q $A\beta_{40}$	De novo $A\beta_{40}$	pH 2 $A\beta_{42}$	pH 8 $A\beta_{42}$

F

	Unpaired t-test
	P-value
pH 2 vs pH 8 $A\beta_{42}$	0.0212 (*)
2A vs 3Q	ns
2A vs *de novo*	ns
3Q vs *de novo*	ns

Figure 4.16. IL-1β release from THP-1 cells after 72 h incubation with Aβ fibril preparations THP-1 cells were primed for 3 h with 1 μg/mL LPS before incubation with Aβ fibril preparations for 72 h. Samples of the cell media were taken and IL-1β concentration measured by ELISA. For a positive control of IL-1β release, cells were subjected to the same priming step followed by treatment with 5 μM nigericin for 30 min (LPS + Nigericin). (A) IL-1β release from cells incubated with 2 μM monomer-equivalent concentration of Aβ fibril preparations (B) Values in A with corresponding buffer values subtracted. (C) IL-1β release from cells incubated with 10 μM monomer-equivalent concentration of Aβ fibril preparations. (D) Values in C with corresponding buffer values subtracted. Error bars represent mean ± SEM (n=3). (E) p values for differences between Aβ fibril preparations in IL-1β release calculated using one-way ANOVA with Tukey's multiple comparison test. (F) p-values from pairwise comparisons between fibril preparations formed from the same peptide using unpaired t-test.

To confirm that the Aβ fibrils are responsible for the IL-1β release measured, samples of Aβ peptide were digested using Proteinase K (PK). If Aβ is not the trigger for IL-1β release then an IL-1β response would expected to still be observed when incubated with these digested samples. Aβ peptide was incubated with increasing concentrations of PK and samples analysed on an SDS-PAGE in order to demonstrate digestion. From this, the lowest concentration of 5 µg/mL was determined to be sufficient for peptide digestion, as demonstrated by the loss of a band seen at the expected MW for full-length Aβ at ~5 KDa (Figure 4.17A). This digested form of Aβ was incubated with cells for 72 h after LPS priming and IL-1β release measured as previously (Figure 4.17B).

In addition, to confirm that the IL-1β release measured from cells is not as a result of endotoxin in the Aβ fibril samples, THP-1 cells were incubated with 1 EU/mL endotoxin for 72 h after LPS priming and IL-1β release measured (Figure 4.17B). Results showed that there was no significant difference between cells treated with LPS alone to those subsequently treated with 1 EU/mL endotoxin or 10 µM PK-digested Aβ (Figure 4.17B).

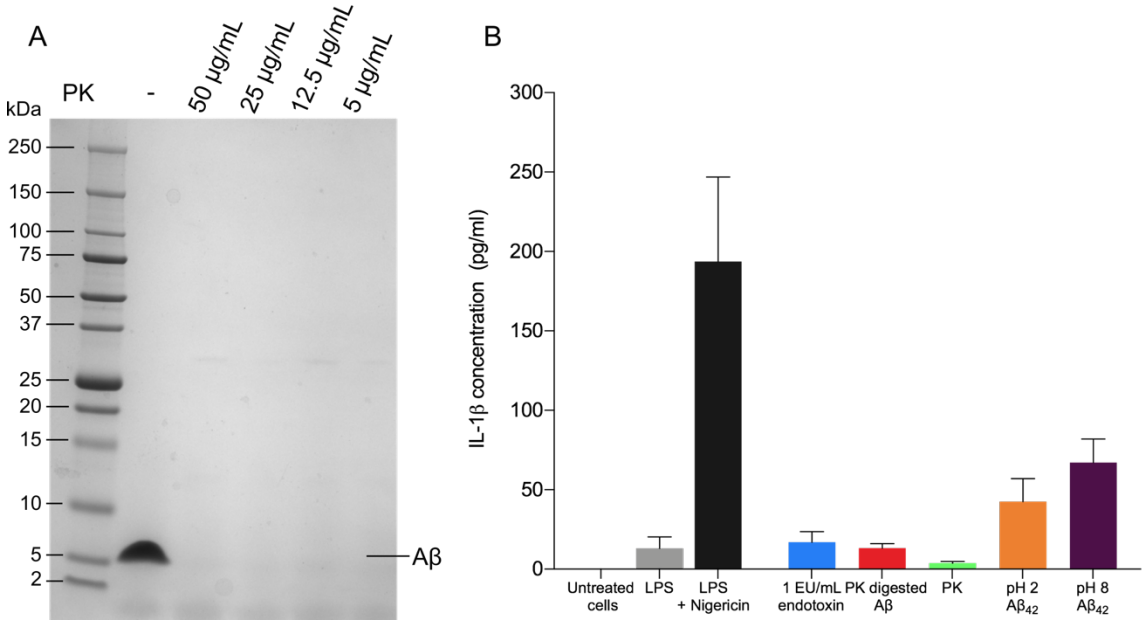

Figure 4.17. IL-1β release from THP-1 cells resulting from digested Aβ and endotoxin
(A) 200 µM Aβ peptide was incubated with 0-50 µg/mL Proteinase K (PK) for 30 min at 37 °C then samples analysed using SDS-PAGE on a 15% Tris-Tricine gel. The first lane shows Aβ incubated in the absence of PK. Aβ can be seen to have been digested at all concentrations of PK. (B) THP-1 cells were primed with 1 µg/mL LPS for 3h before treatment with 5 µM nigericin, 1 EU/mL (final concentration) endotoxin, 10 µM Aβ monomer digested for 30 min with 5 µg/mL PK, PK alone or 10 µM monomer-equivalent concentration $Aβ_{42}$ fibril preparations. Error bars represent mean ± SEM (n=3).

4.3.3 Measurement of NLRP3 inflammasome activation in response to Aβ fibril preparations

IL-1β is released after cleavage into an active form by caspase-1, as a result of NLRP3 inflammasome activation (Figure 4.18). The NLRP3 inflammasome is known to be involved in the inflammatory response to the fibrillar form of Aβ, and can also result in an inflammatory form of cell death known as pyroptosis (Halle et al., 2008; Heneka et al., 2013; Venegas et al., 2017). This pathway was further investigated in this study to identify if different Aβ fibril preparations activate the inflammasome to differing extents. The NLRP3 inflammasome pathway is shown in Figure 4.18 with the components of the pathway that were measured in this study highlighted in red.

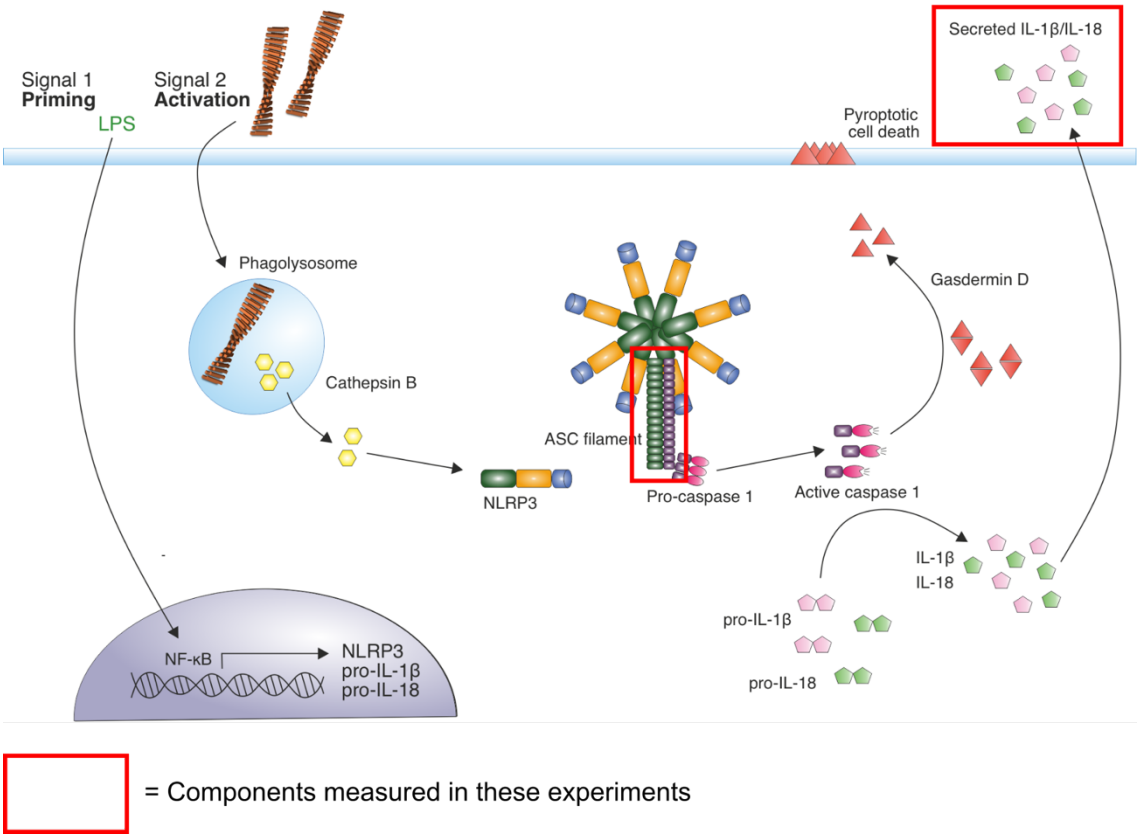

Figure 4.18. Components of the NLRP3 inflammasome pathway
The pathway of NLRP3 inflammasome activation is outlined. In these experiments, LPS is used as an initial 'priming' signal, and Aβ fibrils are added to cells as a secondary 'activation' signal. The priming signal leads to the upregulation of transcription of NLRP3 pathway components, NLRP3, pro-IL-1β and pro-IL-18. Aβ fibrils are proposed to lead to cathepsin release via lysosomal disruption, which triggers the formation of the NLRP3 complex. ASC adaptor protein interacts with NLRP3 via its pyrin domain, and forms ASC filaments. Pro-caspase 1 is recruited via the CARD domain of ASC, leading to autoproteolytic cleavage and activation of caspase-1. Caspase-1 cleaves precursor forms of IL-1β and pro-IL-18 which are released from cells. Caspase-1 also cleaves Gasdermin D, which forms pores in the cell membrane, leading to pyroptotic cell death. In these studies, secreted IL-1β and the formation of ASC complexes are measured as readouts of inflammasome activation, as highlighted in red.

For inflammasome activation THP-1 cells were used. This is because it is known that these cells express NLRP3 inflammasome components, numerous studies have used these cells in experiments to investigate the NLRP3 inflammasome, and NLRP3 reporter cells are readily available in this cell line (Yates et al., 2000; Kim et al., 2016; Guzova et al., 2019).

To investigate the inflammasome pathway, an ASC knockdown THP-1 cell line was used (ASCDef). ASC is a protein adaptor important in the canonical inflammasome response pathway, made up of a PYD domain and a CARD domain (Figure 4.18). This bipartite structure allows interaction with NLRP3 via PYD domains, and with pro-caspase 1 via CARD domains. As NLRP3 does not contain a CARD domain, ASC is essential in this pathway for the recruitment of caspase-1 and consequent cleavage of pro-IL-1β, pro-IL-18 and Gasdermin D. The ASC deficient cell line used (THP-1 ASCDef) exhibits a knockdown of ASC gene expression and has been previously shown by qPCR to exhibit up to a 3-fold reduction in ASC expression (ASC KO & KD THP-1 Cells | Inflammasome test monocytes | InvivoGen; Bedient et al., 2020; Svadlakova et al., 2020).

To first test the knockdown of these cells, wild type and ASCDef THP-1 cells were treated with LPS for 3 h followed by treatment with inflammasome activator nigericin for 30 min, and the resulting IL-1β release measured by ELISA (Figure 4.19). This showed that IL-1β release is significantly reduced in ASCDef cells compared to wildtype in response to LPS and nigericin treatment. However, it was observed that there can be a large variation in the amount of IL-1β that is released from LPS and nigericin treated THP-1 cells.

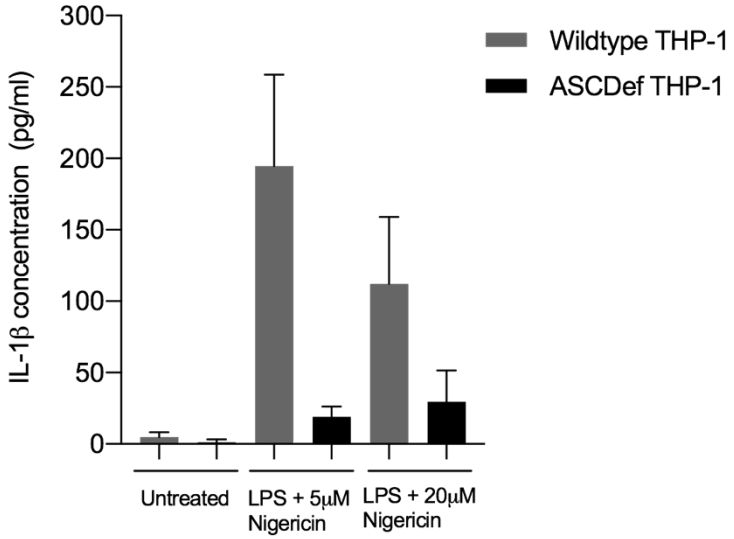

Figure 4.19. IL-1β release from wildtype and ASCDef THP-1 cells
Wildtype THP-1 cells and ASCDef THP-1 cells were treated for 3 h with 1 μg/mL LPS, followed by 5 μM or 20 μM of nigericin for 30 min, to activate the NLRP3 inflammasome. This inflammasome activation was measured by quantification of IL-1β in the cell media. Error bars represent mean ± SD (n=1, 3 replicates)

ASCDef THP-1 cells were then primed with LPS and treated with 10 μM (monomer-equivalent concentration) of Aβ fibril preparations for 72 h, and IL-1β measured (Figure 4.20). This revealed a reduction in the concentration of IL-1β released from ASCDef THP-1 cells in response to all of the Aβ fibril preparations compared to wild-type THP-1 cells, however these differences did not reach significance (Figure 4.20). It was also noted that over the course of the 3 individual experiments, ASCDef cells started to display a greater IL-1β response to LPS and nigericin treatment, indicating that the knockdown of ASC may have gradually been losing efficiency.

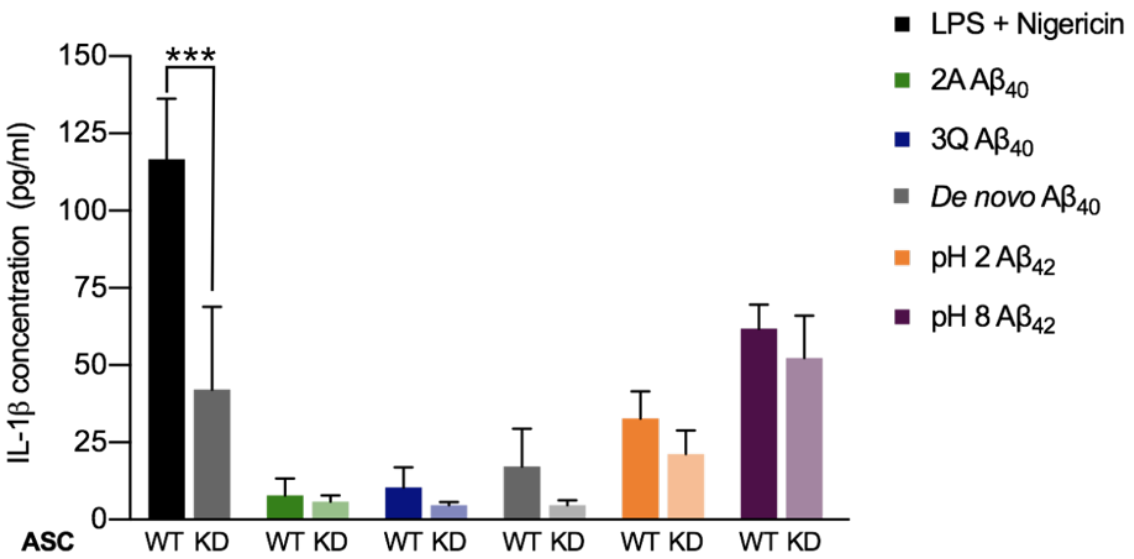

Figure 4.20. IL-1β release from ASCDef THP-1 cells after incubation with Aβ fibril preparations
ASCDef THP-1 cells were primed for 3 h with 1 μg/mL LPS before incubation with 10 μM monomer-equivalent concentration of Aβ fibril preparations for 72 h. Samples of the cell media were then taken and IL-1β concentration measured by ELISA. For a positive control of IL-1β release, cells were subjected to the same priming step followed by treatment with 5 μM nigericin for 30 min (LPS + Nigericin). Error bars represent mean ± SEM (n=3). IL-1β release from cells incubated with buffer have been subtracted from fibril values. One-way ANOVA with Sidak's multiple comparisons test, *** p≤0.001

NLRP3 activation leads to ASC filament formation (Figure 4.18). These filaments then coalesce to form a macromolecular structure known as a 'speck'. In most cells, only one ASC speck forms upon NLRP3 activation, therefore speck formation can be used as a readout of inflammasome activation (Franklin et al., 2014). In these experiments, an ASC speck reporter cell line was used, in which THP-1 cells stably express an ASC::GFP fusion protein (Mehto et al., 2019; Sousa et al., 2020). The expression of this fusion protein is under the control of an NF-κB-inducible promoter. The expression of this GFP fusion protein is therefore induced by the first inflammasome priming signal, in this case LPS. This ASC::GFP protein then polymerises in response to a second inflammasome activation signal to form a speck structure up to 1 μM in size, which can be visualised using confocal microscopy (Outlined in Figure 4.21).

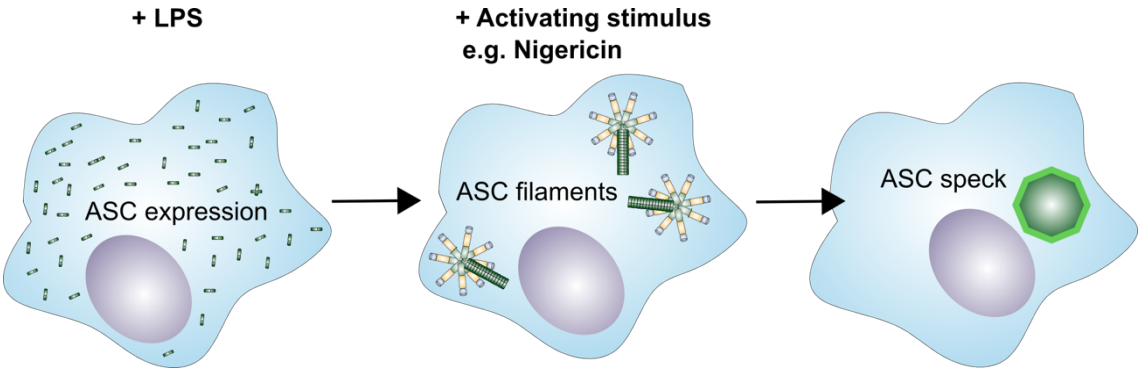

Figure 4.21. GFP-ASC THP-1 cell system
Expression of the GFP::ASC fusion protein is induced in GFP-ASC cells by LPS treatment, via the NF-κB pathway. A second activating stimulus of the NLRP3 inflammasome then induces the formation of NLRP3 inflammasome complexes including ASC filaments. Filaments then self-associate to form a macromolecular structure called a 'speck' which can be visualised and quantified by fluorescence microscopy.

This cell system was used to compare the speck formation induced by incubation with different Aβ fibril preparations. Control cells were used alongside fibril treated cells in all experiments to ensure that the ASC-GFP cell system was functioning correctly (Figure 4.22). Treatment with 1 µg/mL LPS resulted in a diffuse expression of the GFP fusion protein in the cell cytoplasm. Subsequent treatment with nigericin, an inflammasome activator, resulted in the formation of small perinuclear speck structures with increased fluorescence intensity (Figure 4.22).

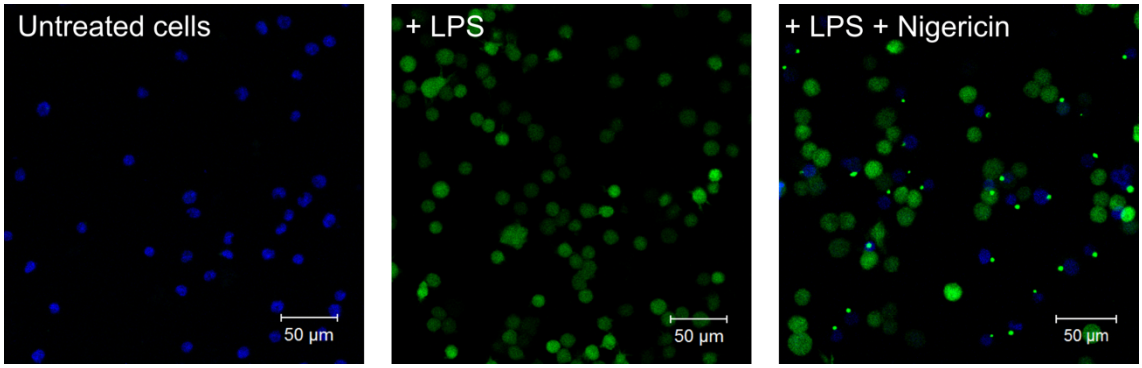

Figure 4.22. Imaging ASC speck formation in GFP-ASC THP-1 cells
GFP-ASC THP-1 cells were plated in individual glass imaging dishes and either left untreated (left), treated for 3 h with 1 µg/mL LPS (middle), or treated for 3 h with 1 µg/mL LPS followed by 30 min treatment with 5 µM nigericin (right). Nuclei were stained with Hoechst stain (blue) and cells were imaged by live-cell imaging on a Zeiss LSM700 confocal microscope with a 20x objective. Representative images are shown, scale bar = 50 µm

GFP-ASC cells were then incubated with 1 μM monomer-equivalent concentration of the different fibril preparations for 72 h before live-cell confocal imaging was performed on samples to visualise and quantify the resulting ASC speck formation (Figure 4.23). Cells were treated with Hoechst stain to visualise nuclei, and both ASC-GFP specks and nuclei were counted to produce speck/cell values in response to the different Aβ fibrils. Tilescan images were taken in order to maximise cell sample size (Figure 4.23). This revealed that incubation with Aβ fibrils led to an increase in the production of ASC specks compared to buffer-treated cells for all samples, however this difference only reached significance for 3Q $A\beta_{40}$, pH 2 $A\beta_{42}$ and pH 8 $A\beta_{42}$ fibrils (Figure 4.24A). In addition, a difference was only identified in the number of ASC specks produced in response to 2A $A\beta_{40}$ fibrils compared to pH 2 $A\beta_{42}$ fibrils, with no significant differences between fibrils formed from the same peptide, under these conditions (Figure 4.24B).

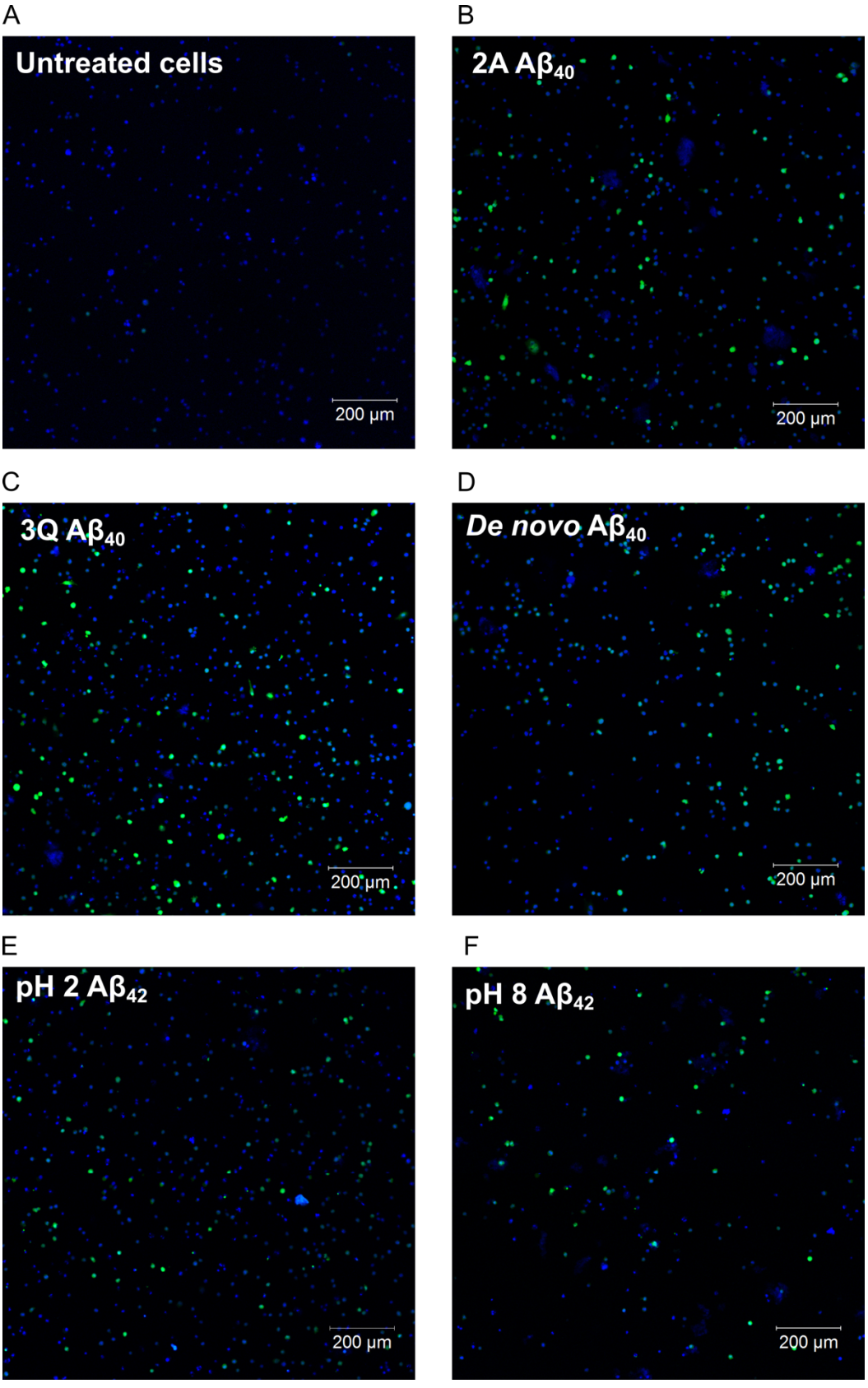

Figure 4.23. ASC speck formation in response to incubation with Aβ fibril preparations
(A) Representative tilescan confocal images of untreated GFP-ASC THP-1 cells. (B-F) GFP-ASC THP-1 cells after 3 h treatment with 1 µg/mL LPS followed by 72 h incubation with 1 µM monomer-equivalent concentration of (B) 2A $A\beta_{40}$ fibrils (C) 3Q $A\beta_{40}$ fibrils (D) *De novo* $A\beta_{40}$ fibrils (E) pH 2 $A\beta_{42}$ fibrils (F) pH 8 $A\beta_{42}$ fibrils. Cells were treated with Hoechst stain 30 min before live-cell imaging using a Zeiss LSM700 confocal microscope with a 20x objective. Representative images are shown, scale bar = 200 µm

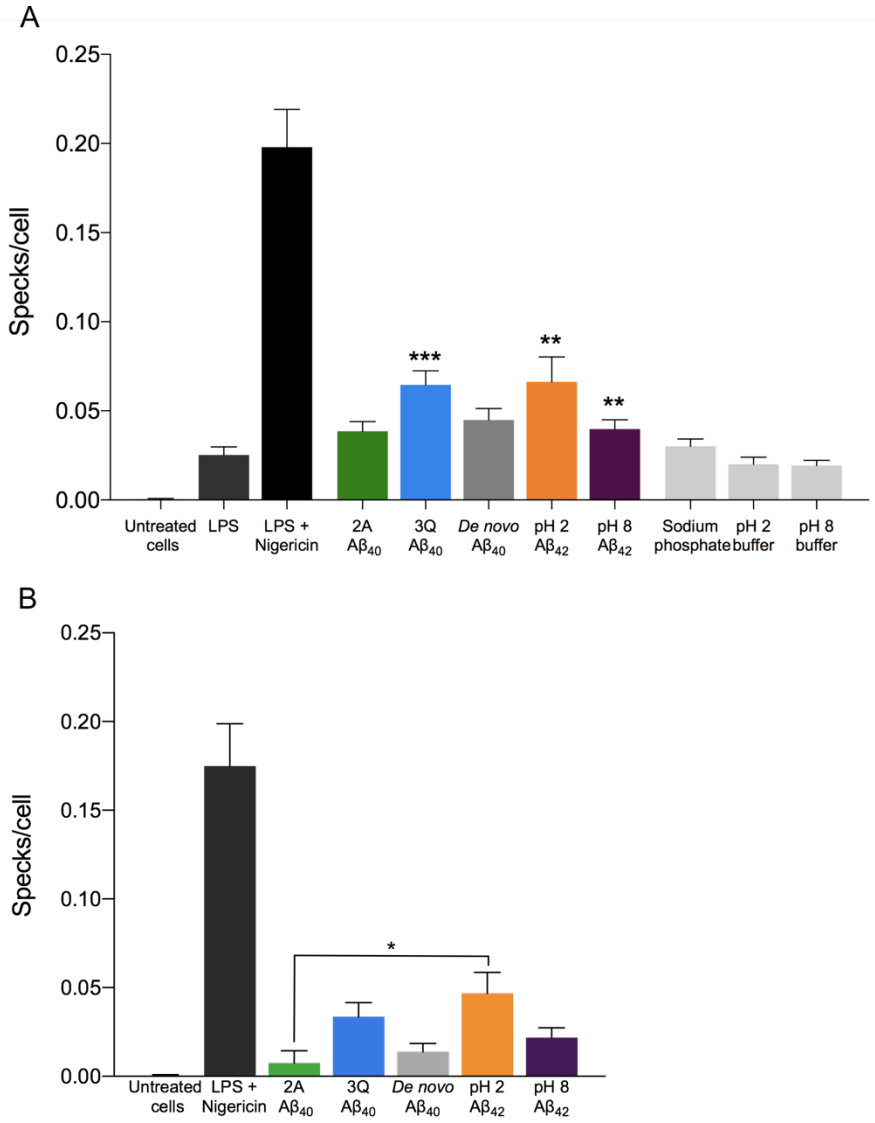

Figure 4.24. Quantification of GFP-ASC specks formation in response to Aβ fibril preparations
(A) The number of GFP-ASC specks per cell resulting from incubation with Aβ fibril preparations. Error bars represent mean ± SEM over a total of 12 tilescan images each with an average of 350 cells (n=3). Significance values represent differences to corresponding buffer-treated samples. Unpaired t-test *, p≤0.05, **, p≤0.01, ***, p≤0.001. (B) The number of GFP-ASC specks formed per cell with corresponding buffer values subtracted. The number of specks formed in response to the five different Aβ fibril preparations was compared using one-way ANOVA with Tukey's multiple comparison test *, p≤0.05

In summary, a differential IL-1β release is observed from THP-1 cells in response to Aβ fibril preparations, but this requires a higher concentration of fibril than for the release of previously measured cytokines. $Aβ_{42}$ fibrils resulted in a greater IL-1β release than $Aβ_{40}$ fibrils, and pH 8 $Aβ_{42}$ fibrils triggered a significantly greater IL-1β release compared to pH 2 $Aβ_{42}$ fibrils. Although there is evidence for NLRP3 inflammasome activation in response to the Aβ fibrils, a differential NLRP3 activation effect corresponding to the IL-1β release observed by the different Aβ fibrils was not demonstrated.

4.4 Measuring changes in the expression of MHC class II and CD80 molecules in response to Aβ fibril preparations

As infiltration of T-cells has previously been observed in response to amyloid fibrils, along with an increase in MHC class II expression indicative of enhanced antigen presentation, molecules involved in the triggering of an adaptive immune response were also explored (Hopperton et al., 2017; Gate et al., 2020). For this, the expression of two cell surface markers – MHC class II and CD80, was measured. MHC class II presents antigens to CD4 T-cells and CD80 provides a co-stimulatory signal in T-cell activation (Smith-Garvin et al., 2009). The upregulation of these proteins will therefore enhance the detection of antigens by T-cells. For these experiments, THP-1 cells were treated with 2 μM monomer-equivalent concentration of Aβ fibril preparations for 72 h, then cell-staining was carried out using antibodies specific for HLA-DR, one of three types of MHC class II molecule, and CD80. Cell-associated fluorescence was subsequently measured using flow cytometry.

These experiments showed that CD80 expression was significantly increased in response to all Aβ fibril preparations, compared to CD80 expression in cells treated with buffer alone (Figure 4.25B/C). Similar to results for ROS generation, the *de novo* $A\beta_{40}$ fibrils were found to induce the greatest increase in CD80 expression, with differences in the mean fluorescence of cells incubated with the different Aβ fibril preparations shown in Figure 4.25D.

MHC class II expression, however, was not increased to the same extent as CD80, with only $A\beta_{40}$ fibrils found to have a significant effect over buffer alone when measuring the mean fluorescence of cells (Figure 4.26C). No differences in MHC class II expression in response to incubation with the different Aβ fibril preparations were identified (Figure 4.26D).

In summary, these results identified an increase in CD80 expression in response to all Aβ fibril preparations, with *de novo* fibrils leading to the greatest increase, and pH 2 $A\beta_{42}$ fibrils leading to the smallest increase in expression. This indicates that increasing CD80 expression is a general cellular response to Aβ fibrils, but some fibrils can result in a greater increase than others. MHC class II expression was not increased to the same extent as CD80, indicating that different conditions such as higher concentrations of Aβ fibril may be required for clear changes to be measured in MHC class II expression.

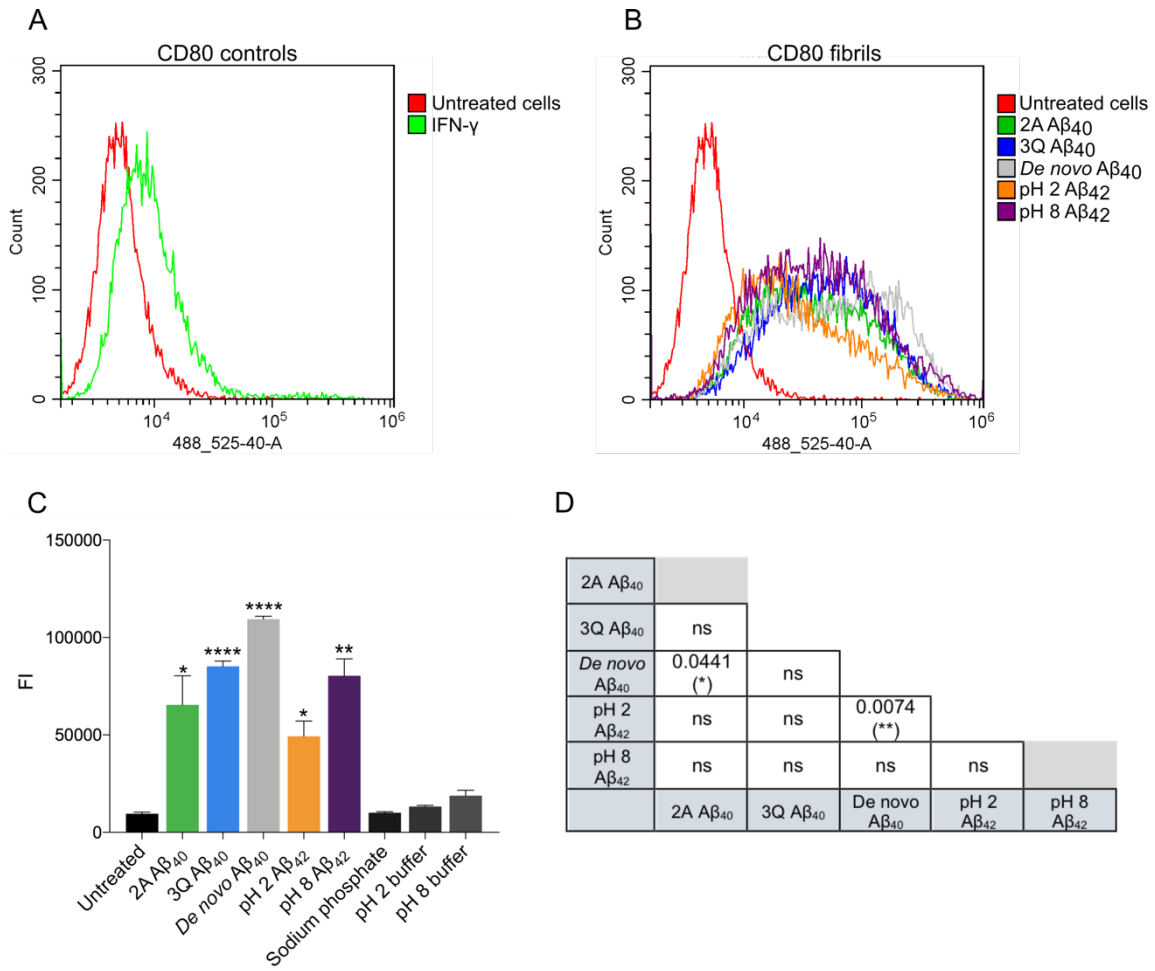

Figure 4.25. CD80 expression in THP-1 cells treated with Aβ fibril preparations
THP-1 cells were stained using a CD80 antibody and an Alexa-488-conjugated secondary antibody. Cell associated fluorescence is therefore indicative of CD80 expression. (A) Flow cytometry trace showing cell-associated fluorescence after staining untreated THP-1 cells or cells treated with IFN-γ for CD80. (B) Representative flow cytometry trace of THP-1 cell associated fluorescence after incubation with 2 μM Aβ fibril preparations for 72 h. (C) Mean fluorescence of THP-1 cells incubated with Aβ fibril preparations or buffers and stained for CD80. Error bars represent mean ± SEM (n=3), 10,000 cells were recorded per replicate. Pairwise comparisons were made between values for cells incubated with Aβ fibrils and values resulting from incubation with the corresponding fibril buffer to identify significant changes in expression. Student's t-test *, p ≤0.05, **,p ≤0.01, ****, p ≤0.0001 (D) p values of significant differences identified in the mean fluorescence of cells after incubation with the different Aβ fibril preparations. One-way ANOVA with Tukey's multiple comparisons test *, p ≤0.05, **,p ≤0.01

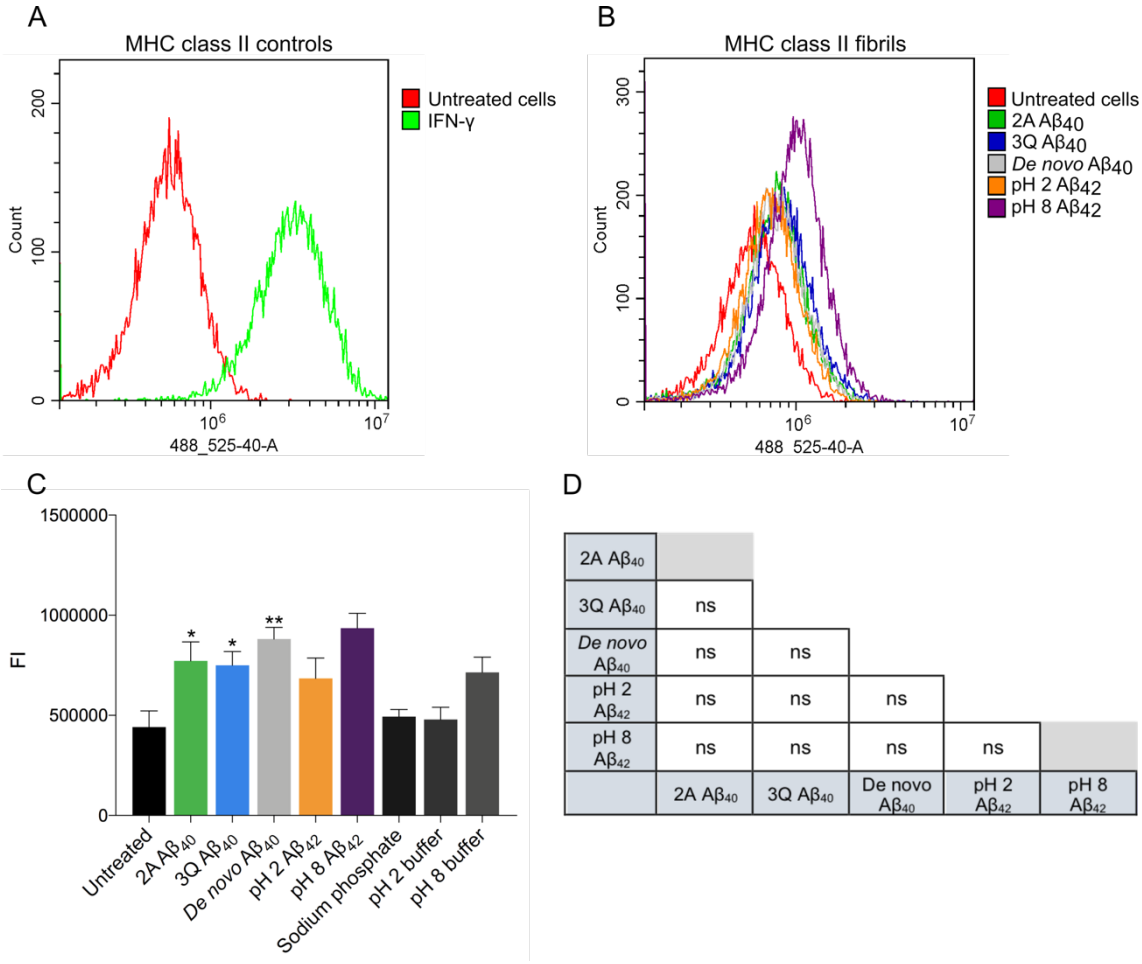

Figure 4.26. Expression of MHC class II in THP-1 cells treated with Aβ fibril preparations
THP-1 cells were stained using an MHC class II antibody and an Alexa-488-conjugated secondary antibody. Cell associated fluorescence is therefore indicative of MHC class II expression. (A) Flow cytometry trace showing cell-associated fluorescence after staining untreated THP-1 cells or cells treated with IFN-γ for MHC class II. (B) Representative flow cytometry trace of THP-1 cell associated fluorescence after incubation with 2 μM Aβ fibril preparations for 72 h. (C) Mean fluorescence of THP-1 cells incubated with Aβ fibril preparations or buffers and stained for MHC class II. Error bars represent mean ± SEM (n=3), 10,000 cells were recorded per replicate. Pairwise comparisons were made between values for cells incubated with Aβ fibrils and values resulting incubated with the corresponding fibril buffer to identify significant changes in expression. Student's t-test *, p ≤0.05, **,p ≤0.01, (D) p values of significant differences identified in the mean fluorescence of cells after incubation with the different Aβ fibril preparations. One-way ANOVA with Tukey's multiple comparisons test.

A summary of the effects identified in THP-1 cells in response to the different fibril preparations tested are summarised in Table 4.11.

	2A $A\beta_{40}$	**3Q $A\beta_{40}$**	***De novo* $A\beta_{40}$**	**pH 2 $A\beta_{42}$**	**pH 8 $A\beta_{42}$**
ROS assay	+	+	+	+	+
TNF-α release	-	-	-	++	++++
IL-6 release	-	-	-	++	++++
IL-1β release	+	+	+	++	+++
ASC speck formation	+	+	+	+	+
CD80 expression	+	+	++	+	+
MHC II expression	-	-	-	-	-

Table 4.11. Summary of the effects of different Aβ fibril preparations on assays performed to measure the inflammatory response in THP-1 cells
The effects of Aβ fibril preparations in assays performed in this thesis in relation to the inflammatory response are compared. '-' indicates that the Aβ fibril preparation had no effect in the corresponding assay, and increasing numbers of '+' symbols indicate increasing strength of the effect observed in the corresponding assay resulting from the Aβ fibril preparation.

4.5 Discussion

In this chapter the effects of six Aβ fibril preparations on immune cell viability and inflammatory activation were explored. The first key finding was the differential toxicity of Aβ fibril preparations towards monocytic and microglial cell lines (Figure 4.3-6). 2A, 3Q and *de novo* $A\beta_{40}$ fibril preparations were not found to be toxic towards BV-2, RAW 264.7 and THP-1 cell lines, whereas $A\beta_{40}$ E22Δ fibrils were toxic towards BV-2 microglial cells and to a lesser extent RAW 264.7 macrophage cells. It has been previously shown that the $A\beta_{40}$ E22Δ peptide has toxic effects on neuronal cell viability, however the conformation of the protein that was responsible for this toxic effect was not identified (Ovchinnikova et al., 2011). The increased toxicity of fibrils formed from mutant E22Δ peptide compared to wild-type $A\beta_{40}$ peptide towards monocytic and microglial cells could in part explain why this mutation is associated with early-onset disease (Tomiyama et al., 2008). Further to these findings, $A\beta_{42}$ fibrils formed at pH 8 were found to be toxic to all cell lines tested, however this toxic effect was not observed for $A\beta_{42}$ fibrils formed at pH 2.

Further experiments are required to explore the mechanism of fibril toxicity. These experiments could involve determining whether the toxicity of $A\beta_{40}$ E22Δ fibrils and pH 8 $A\beta_{42}$ fibrils is dependent on the uptake of the fibrils by cells, or if interaction with the plasma membrane is sufficient. Increased initial interaction of Aβ fibrils with cells could result in an enhanced toxic effect. In relation to this, experiments were carried out in this work (Chapter 5), which investigate the relationship between the different Aβ fibrils and cell association, uptake and degradation. Work in this chapter identified that the pH 8 $A\beta_{42}$ fibrils associate more with cell surfaces than pH 2 $A\beta_{42}$ fibrils, which could help to explain the increased toxicity of these fibrils. The disruption of cell membranes by the fibrils is one possible mechanism of fibril toxicity, a phenomenon that has been previously described in the context of amyloid fibrils (Xue et al., 2009; Milanesi et al., 2012; Goodchild et al., 2014). The toxicity of a distinct α-synuclein fibril polymorph was found to be a result of binding and permeabilization of membrane lipid bilayers, and previous research has also shown that the interaction of mature Aβ fibrils with cell lipids can result in their destabilisation and resolubilisation into more toxic species (Martins et al., 2008; Pieri et al., 2012; Bousset et al., 2013). In addition, Aβ fibrils have also been shown by electron tomography to penetrate into tubular invaginations of the plasma membrane (Han et al., 2017). However, fibril toxicity in this previous study was hypothesised to result from damage to intracellular membranes, as lysosomal leakage was observed (Han et al., 2017). This damage to intracellular membrane structures has also been demonstrated in a study using amyloid fibrils formed from polyglutamine-expanded huntingtin protein, in which ER membranes were shown to be deformed, and ER

organisation and dynamics altered (Bäuerlein et al., 2017). Experiments in the current work identified increased LDH release from cells in response to pH 8 fibrils, which is consistent with damage to the cell membrane. More in-depth analysis of the interactions of the Aβ fibrils used in this thesis with membrane lipid bilayers would be an interesting line of research (Martins et al., 2008; Bäuerlein et al., 2017; Han et al., 2017).

The second key finding in this chapter was the differential release of cytokines in response to the Aβ fibrils. Increased release of two pro-inflammatory cytokines, IL-6 and TNF-α, was observed in response to $A\beta_{42}$ fibrils when compared to $A\beta_{40}$ fibrils. Further to this, a significantly greater release of IL-6 and TNF-α was measured from cells treated with pH 8 $A\beta_{42}$ fibrils compared to pH 2 $A\beta_{42}$ fibrils. This difference in cytokine release suggests that the pH 8 $A\beta_{42}$ fibril population activates a greater pro-inflammatory response in immune cells than the pH 2 $A\beta_{42}$ fibrils.

The release of these pro-inflammatory cytokines were investigated as they are released from microglial cells and have been found to be elevated in AD brains, linking them to neuroinflammation (Griffin et al., 1989; Bauer et al., 1991; Ojala et al., 2009). The transcription of IL-6 and TNF-α is enhanced in response to recognition of stimuli by PRR's on immune cells such as the microglia and monocytes used in these experiments (Tanaka et al., 2014). A number of these PRR's, such as TLR's, have been shown previously to be involved in the immune response to Aβ fibrils (Fassbender et al., 2004; Reed-Geaghan et al., 2009). With a different set of amino acid side chains exposed on the surface of different amyloid fibril polymorphs, it is possible that the fibrils will interact to differing extents with these receptors on immune cells, thus resulting in different levels of immune cell activation via the pathways discussed in Section 1.4.3. This is consistent with results presented in Chapter 5 of this thesis, in which increased interaction of pH 8 $A\beta_{42}$ fibrils with cell surfaces is demonstrated compared to the pH 2 $A\beta_{42}$ fibrils. This increased cell association could be indicative of increased engagement of these fibrils with cell surface receptors, which in turn would result in amplified receptor activation and consequent cell signalling. If binding to receptors involved in the inflammatory response, this could explain the increased release of inflammatory mediators from monocytic and microglial cells in response to pH 8 $A\beta_{42}$ fibrils compared to the pH 2 fibrils. Future experiments to develop this hypothesis would involve measuring the activation of signalling pathways to determine if the activation of these pathways is amplified in proportion to fibril cell surface interactions. For example, intracellular Ca^{2+} levels that result from fibril binding could be measured, indicative of cell signalling. Further experiments are required to identify the receptors that are involved in the differential immune response observed between fibril polymorphs, but TLR2, TLR4, TLR6, SR-A and SR-B receptors are potential candidate receptors that could be investigated

(Bamberger et al., 2003; El Khoury et al., 2003; Tahara et al., 2006; Reed-Geaghan et al., 2009; Stewart et al., 2010). Cells deficient in these receptors could be utilised for this, before protein-protein interactions between receptors and the different fibril structures could be investigated in more detail (Reed-Geaghan et al., 2009).

The release of IL-1β was also investigated in this work, as this cytokine has been found to accumulate around Aβ plaques in AD brains and levels have found to be elevated in the CSF and circulation of AD patients (Griffin et al., 1989; Italiani et al., 2018). IL-1β is therefore implicated in AD. Measurement of IL-1β release revealed that a greater concentration of Aβ fibril (10 μM monomer-equivalent concentration) was required in order to elicit similar levels of IL-1β release from BV-2 and THP-1 cells as TNF-α and IL-6 release. This concentration of Aβ fibrils has been used previously in experiments to measure resulting IL-1β release from THP-1 cells, and these experiments also demonstrated the same 72 h timepoint of release after incubation with the fibrils (Yates et al., 2000). These experiments detected a greater concentration of IL-1β release from cells than in the current work, however LPS was incubated with the fibrils throughout the experiment rather than just 3 h priming, and cell numbers used were not described (Yates et al., 2000). In the present work, this higher 10 μM concentration of fibril resulted in the same pattern of IL-1β release as previously observed with TNF-α and IL-6, with $A\beta_{42}$ fibrils eliciting a greater IL-1β release than $A\beta_{40}$ fibrils, and pH 8 $A\beta_{42}$ fibrils having a greater effect compared to pH 2 $A\beta_{42}$ fibrils.

The mechanism of this differential IL-1β release was explored, focusing on the NLRP3 inflammasome. This pathway has been shown to be activated by Aβ fibrils resulting in the release of IL-1β, and can also result in cell death via pyroptosis (Halle et al., 2008; Heneka et al., 2013; Shi et al., 2015; Swanson et al., 2019). Differential activation of this inflammasome would therefore provide a link helping to explain both the enhanced release of IL-1β and cell death resulting from incubation with pH 8 $A\beta_{42}$ fibrils. However, no significant difference was identified between the level of IL-1β released from wildtype THP-1 cells compared to that from ASCDef cells in response to Aβ fibrils, or between the number of ASC specks that formed in response to different Aβ fibrils preparations (Figure 4.20). As speck formation was observed, these results indicate that whilst the NLRP3 inflammasome could be playing a role in cell death and activation, no differential effect was identified. Assays allowing a more precise read-out of NLRP3 inflammasome activation may be required to confirm these conclusions, as speck formation is not a sensitive measure of the extent of activation, it simply reports whether the inflammasome is activated or not.

The effect that different Aβ fibril preparations have on the capability of triggering an adaptive immune response was also investigated in this work. It was found that CD80 expression was increased in response to all Aβ fibrils tested. This is similar to a recent study in which it was shown that $A\beta_{42}$ oligomers increased the expression of both CD80 and CD86 co-stimulatory molecules, however the effects of fibrillar forms of the peptide were not tested in this work (Gericke et al., 2020). *De novo* $A\beta_{40}$ fibrils were found to induce a significantly greater increase in expression compared to 2A $A\beta_{40}$ and pH 2 $A\beta_{42}$ fibrils when mean fluorescence was measured (Figure 4.25). This could be a result of the heterogenous nature of the *de novo* fibril preparations; the samples consist of a range of different fibril structures with the potential to have an effect. Unlike CD80, the increase in MHC class II expression measured was minimal, and only significant over the effects of buffer for the $A\beta_{40}$ fibrils (Figure 4.26). Whilst α-synuclein fibrils have been shown to induce MHC class II expression in microglia, and MHC class II has been consistently found to be upregulated in AD brains, the effect of Aβ fibrils is not extensively researched (Harms et al., 2017; Hopperton et al., 2017; Van der Perren et al., 2020). It could therefore be that the concentration of Aβ fibril used in these experiments was not sufficient to induce MHC class II expression, in comparison to that of a plaque within an AD brain.

The *in vitro* nature of this work does come with some limitations; as the Aβ fibrils were incubated with cells for up to 72 h, it is possible that within this time the fibrils may have undergone some disaggregation or structural changes, which could contribute to the effects the fibrils had on cells that were outlined in this chapter. Further to this, as the cells are cultured at pH 7.4, it could be postulated that the $A\beta_{42}$ fibrils that were formed at pH 2 would be more likely to undergo these changes, when subjected to such a change in pH. To check for this, pH 2 $A\beta_{42}$ fibrils were incubated in cell culture media alone for 72 h before analysis using EM. Whilst this confirmed that the pH 2 fibrils did remain fibrillar within this time, this method is not sensitive enough to rule out any changes to fibril structure.

Whilst the concentration of Aβ in the CSF is used in AD diagnosis, this is a measure of soluble Aβ species and does not represent the concentration of aggregated Aβ that is present in an AD plaque. A study in which the frontal cortical grey matter from human Alzheimer's disease and control subjects was fractionated based on different pools of Aβ species estimated that an AD brain had a total of 6.5 mg of Aβ, compared to 1.7 mg in control brains (Roberts et al., 2017). 48% of the Aβ was located in a membrane pool, and 45% was extracted using formic acid, which dissolves fibrillar deposits. The concentration of Aβ in both of these fractions was estimated to be low micromolar (Roberts et al., 2017). This is consistent with the concentrations of Aβ used in the

experiments in this work, and with the range of Aβ concentrations commonly used in the literature (Yates et al., 2000; Petkova et al., 2005; Walsh et al., 2009; Pan et al., 2011).

In summary, the data presented in this chapter demonstrates the consequences that differences in Aβ fibril preparations can have on their effects on immune cells. Differences in both toxicity and immune cell activation were identified, which would govern the impact of the fibrils within an AD brain. Further work is required to identify the mechanisms of toxicity and activation.

5 Differences in the cell association, uptake and degradation of distinct Aβ fibril preparations by immune cells

5.1 Introduction

In addition to the activation of microglial and monocytic cells by Aβ fibrils, there is also evidence that these cells can contribute to the uptake and degradation of the fibrils (discussed in Section 1.4.5). A number of genes identified to be associated with an increased risk of LOAD have been found to be involved in this clearance (Table 1.5), highlighting the importance of this process in disease. Microglia can clear fibrils either via internalisation of the fibrils and subsequent degradation within lysosomes or via the release of amyloid-degrading enzymes (Rogers et al., 2002). Lysosomal enzymes cathepsin B and TPP-1 have been shown to cleave Aβ fibrils, aiding in the breakdown of Aβ fibrils once internalised (Mueller-Steiner et al., 2006; Solé-Domènech et al., 2018). However, it is not known how polymorphism affects the uptake and degradation of Aβ fibrils.

There is evidence to suggest that differences in amyloid structure could convey differences in the extent to which the structures interact with cells. For example, a study in which the properties of two structurally distinct misfolded protein oligomers of the model protein HypF-N (Type A and Type B) are compared has been previously discussed in this thesis in the context of immune cell activation (Section 4.1) (Mannini et al., 2019). Although not fibrillar, these species both have a β-sheet core structure and bind to ThT, but the structures differ in the solvent exposure of hydrophobic residues and overall flexibility. Type B oligomers were found to have a higher ability to bind to microglial membranes than the Type A oligomers, as shown by confocal microscopy of N13 microglial cells incubated with fluorescently labelled HypF-N oligomers (Mannini et al., 2019). In addition, differential interactomes were identified for the two oligomer structures using proteomics, with Type B oligomers found to have a higher affinity for membrane receptors than Type A oligomers (Mannini et al., 2019). This was proposed to be a result of more hydrophilic surfaces and more dynamic structure of the Type B oligomer and was suggested to result in more immune signaling, thus explaining increased release of pro-inflammatory cytokines at lower concentration ranges than the Type A oligomers. In addition, it was found that 31.2% of Type A oligomers were internalised by microglial cells, compared to less than 3% of Type B oligomers (Mannini et al., 2019). This provides evidence that differences in the structures of amyloid species can also affect the extent of uptake by cells.

In addition to this, the previously discussed α-synuclein polymorphs 'ribbons' and 'fibrils' (Section 4.1) were found to have differences in their interaction with cell membranes. When the binding of Alexa-Fluor 488 labelled α-synuclein polymorphs to SH-SY5Y cells was assessed using flow cytometry, it was found that the 'fibril' polymorph of α-synuclein fibrils bind to cells with higher affinity compared to the 'ribbon' polymorph (Bousset et al., 2013). As both polymorphs were found to have similar affinities for complex lipid mixtures extracted from brain, this greater binding of the fibril polymorph was proposed to be due to the increased binding to proteins or receptors within the cell membrane (Bousset et al., 2013). Furthermore, it was found that the toxicity of the 'fibril' polymorph was a consequence of this membrane binding and the permeabilization of membrane lipid bilayers (Pieri et al., 2012).

Further to differences in cell interaction and internalisation, there is evidence to suggest differences in the degradation of different amyloid polymorphs. For example, when compared to *in vitro* formed fibrils it was found that $A\beta_{40}$ fibrils extracted from the vasculature of AD brains are more resistant to proteinase K proteolysis, suggesting that differences in the molecular structure of fibrils could result in them being more or less susceptible to degradation (Kollmer et al., 2019). This could be a reflection of structural differences between the fibrils, as a result of different growth conditions and co-factors present in fibrillation. Similarly, it has been found that different 'strains' of α-synuclein fibrils with different structures derived from PD and MSA were more resistant to proteinase K degradation than those from DLB (Van der Perren et al., 2020). This again provides evidence that the structure of amyloid fibrils can convey differences in their degradation. We hypothesise that differences in Aβ fibril structure could result in differences in the accessibility of cleavage sites to proteases and thus the proteolytic breakdown of the fibrils.

This thesis chapter aims to investigate whether Aβ fibril preparations differ in the level of their initial association with microglial cells. The capability of microglia to internalise different Aβ fibrils preparations and sort these to lysosomes is also investigated. The extent of degradation of the Aβ fibril preparations is assessed by tracking internalised fibrils over time, and by incubating Aβ fibril preparations with lysosomal fractions isolated from microglial cells.

5.2 The production of fluorescently labelled Aβ fibril preparations

In order to investigate the uptake and degradation of different Aβ fibril polymorphs by microglial cells, fibrils that can be visualised using confocal microscopy and flow cytometry were required. To produce fibrils that can be tracked by confocal imaging, $A\beta_{40}$ and $A\beta_{42}$ monomers were labelled with ATTO-594 dye and these monomers were used

in fibril assembly reactions. Amine labelling was used to achieve this labelling; $A\beta_{40}$ and $A\beta_{42}$ monomers were reacted with 4x molar excess of ATTO-594 NHS ester (Figure 5.1).

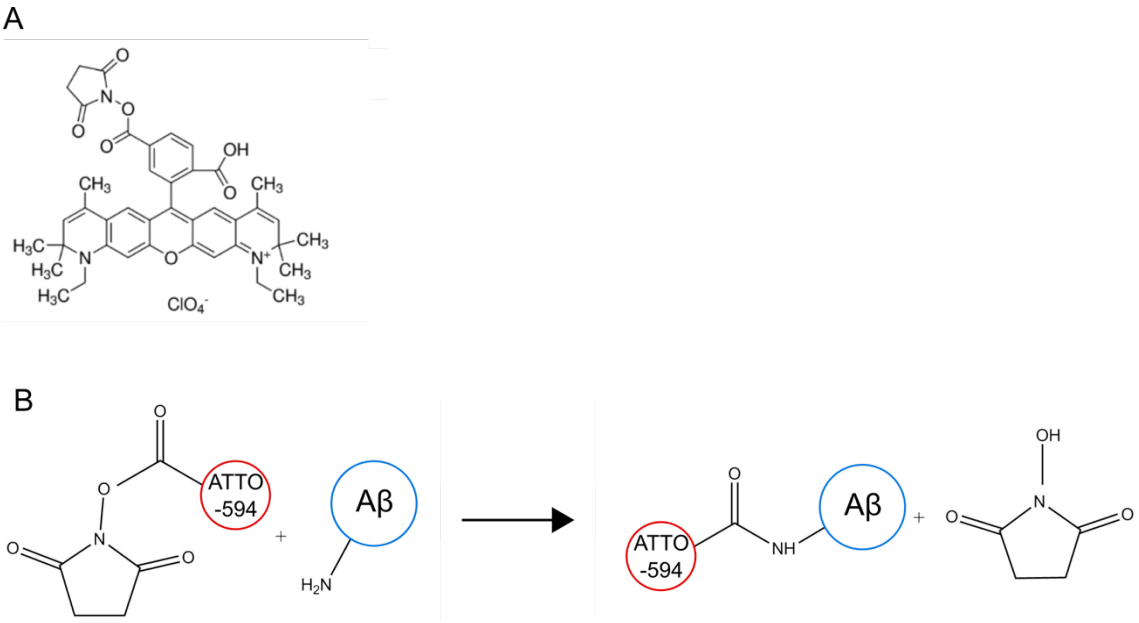

Figure 5.1. Structure of ATTO-594 dye and NHS-ester conjugation reaction with Aβ
(A) Molecular structure of ATTO-594 NHS-ester dye. (B) Outline of NHS-ester conjugation of ATTO-594 onto Aβ monomer via reaction with amines.

The reactions containing Aβ monomer and ATTO-594 were then quenched and purified by SEC using a Superdex 75 analytical column 10/300 (Section 2.3.7). For both reactions, two clearly fluorescent bands were visible on the SEC column, corresponding to ATTO-594 labelled Aβ monomer and excess ATTO-594 dye (Figure 5.2A). A more dilute sample of the $A\beta_{42}$ labelling reaction was loaded onto the SEC column in order to prevent aggregation, therefore resulting in lower absorbances (Figure 5.2C). The first fluorescent band on the column eluted at the expected volume for the mass of Aβ monomer (~12 min) (Figure 5.2B/C). This first peak was therefore collected and these samples were visibly blue in colour (Figure 5.2D). Collected samples corresponding to eluted $A\beta_{40}$ and $A\beta_{42}$ peaks (Figure 5.2B/C) were analysed using SDS-PAGE (Figure 5.2E). This revealed a single band in both $A\beta_{40}$ and $A\beta_{42}$ samples, which were of the expected sizes of $A\beta_{40}$ and $A\beta_{42}$ monomers, as compared to unlabelled control samples (Figure 5.2E). The fainter band seen for the $A\beta_{42}$ sample compared to $A\beta_{40}$ is reflective of the lower concentration of $A\beta_{42}$ that was used in the labelling reaction in order to prevent aggregation. The gel was then excited at 601 nm, this revealed that 594 nm fluorescence corresponds to the $A\beta_{40}$ and $A\beta_{42}$ bands (Figure 5.2F), further confirming that these collected samples have been labelled with ATTO-594 dye.

$A\beta_{40}$ and $A\beta_{42}$ monomer labelled with ATTO-594 was freeze-dried and resuspended for use in the formation of Aβ fibrils. 2A, 3Q and *de novo* $A\beta_{40}$ fibril polymorphs and pH 2 and pH 8 $A\beta_{42}$ fibrils populations were produced under the conditions previously used

(Section 2.5) but using labelled monomer and unlabelled monomer in a 1:100 ratio, respectively.

To demonstrate that the labelled monomer had been incorporated into fibrils, fibril samples were centrifuged to pellet insoluble material as previously described (Section 2.6.2). This resulted in a pellet for all fibril preparations that was visibly blue, and a clear supernatant (Figure 5.3A). This indicates that the ATTO-594 labelled Aβ monomer has been incorporated into insoluble aggregates. To assess these aggregates further and confirm amyloid fibril formation, the fibril preparations were imaged using EM (Figure 5.3B). This confirms that the fluorescent pelleted material seen in Figure 5.3A is fibrillar for all fibril preparations.

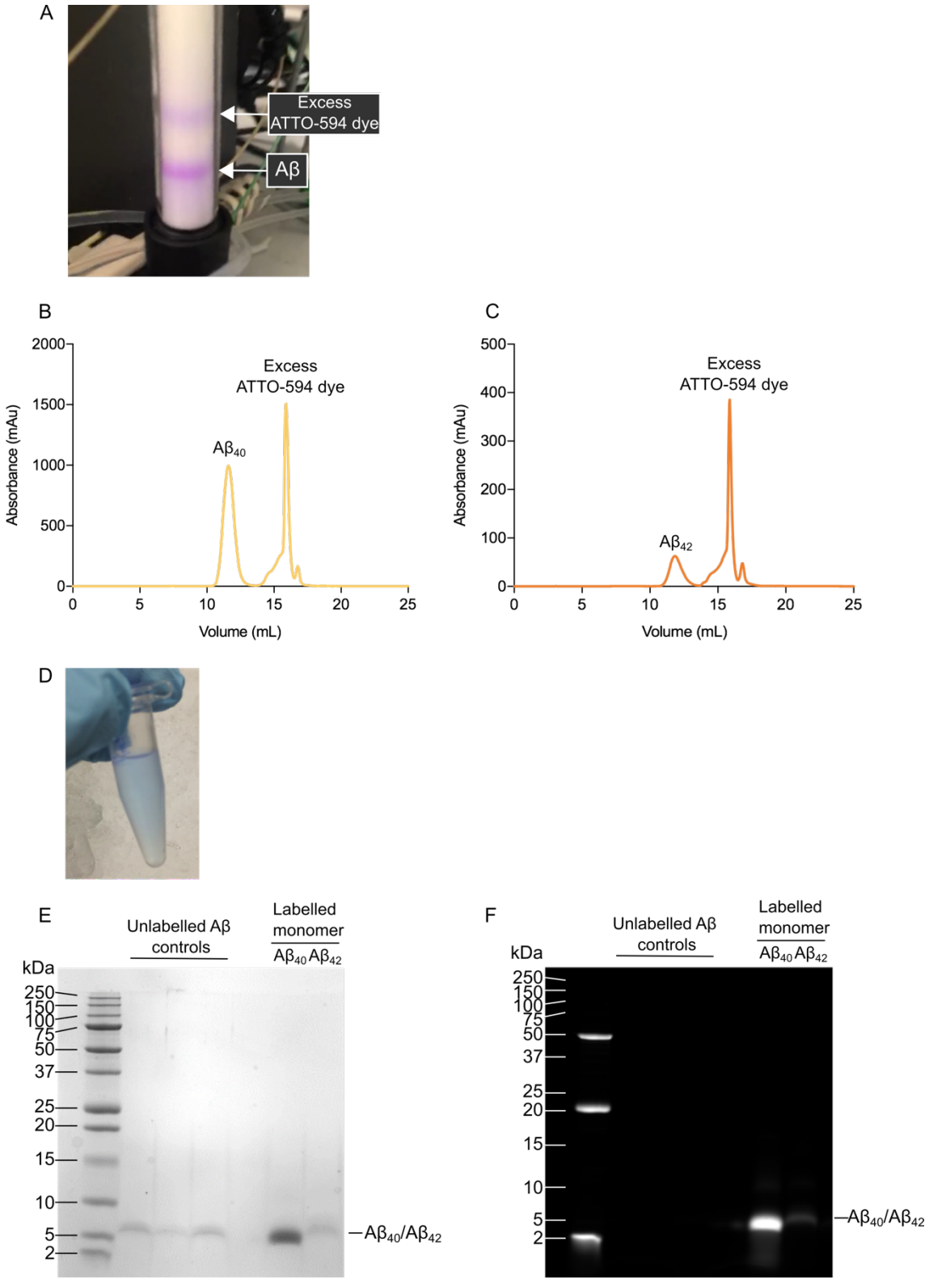

Figure 5.2. Labelling of Aβ monomers with ATTO-594 NHS ester dye
(A) $A\beta_{40}$ and $A\beta_{42}$ monomers were reacted with 4X molar excess of ATTO-594 NHS ester overnight at 4 °C then purified by SEC using a Superdex 75 analytical column 10/300. This results in two visibly fluorescent bands on the column corresponding to labelled Aβ monomer and free excess ATTO-594 dye. (B and C) SEC traces of $A\beta_{40}$ and $A\beta_{42}$ labelling mixtures. (D) Example of Aβ peak collected from the SEC column showing blue colouration indicating ATTO-594 labelling of Aβ peptide. (E) SDS-PAGE of unlabelled Aβ monomer and samples taken from $A\beta_{40}$ and $A\beta_{42}$ peaks shown in B/C shown to correspond to the mass of Aβ. (F) Fluorescent imaging of the gel using a G-Box imaging system (Syngene). The location of 594 fluorescence corresponds to the location of $A\beta_{40}$ and $A\beta_{42}$ monomer collected from peaks in B/C.

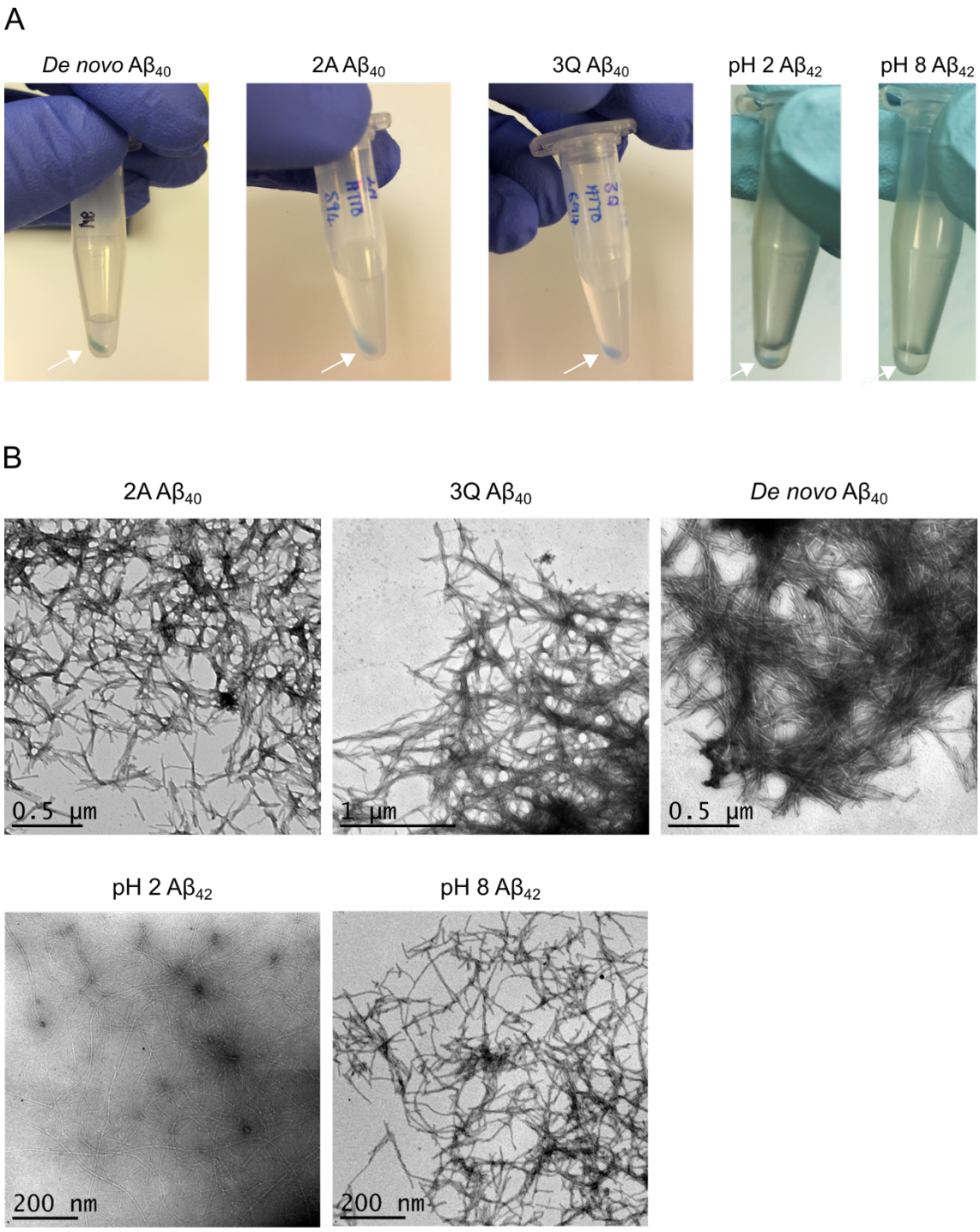

Figure 5.3. ATTO-594 labelled Aβ fibril preparations pellets and EM images
(A) Fibril preparations containing 1% ATTO-594 labelled Aβ monomer were centrifuged at 16,873 xg for 40 min to pellet insoluble material. ATTO-594 labelled peptide (blue) can be seen to be localised to this insoluble pellet fraction for all fibril samples. (B) 1% ATTO-594 labelled 2A, 3Q and *de novo* $A\beta_{40}$ and pH 2 and pH 8 $A\beta_{42}$ fibril preparations were imaged by negative stain EM on a JEOL 1400 microscope. Images are representative.

To assess the effect of 1% ATTO-594 labelled Aβ monomer on fibrillation kinetics, the formation of *de novo* fibrils using this percentage of labelled monomer was monitored using ThT (Figure 5.4A). This revealed comparable growth kinetics to *de novo* fibrils formed from 100% unlabelled $A\beta_{40}$ monomer (Figure 3.9), indicating that the 1% ATTO-594 labelled Aβ monomer is not altering fibril growth. To further assess the effects of ATTO-594 labelled monomer on fibrillation, fibril yields were also performed on the fibrils formed from 1% ATTO-594 Aβ monomers (Figure 5.4B). This showed that the majority of Aβ peptide in all five Aβ fibril preparations was in the insoluble fraction, and values were comparable to those for unlabelled fibrils (Figure 3.10, 3.13, 3.16).

In summary, $A\beta_{40}$ and $A\beta_{42}$ monomers were labelled with ATTO-594 NHS ester using amine labelling. These peptides were shown to be fluorescent and then were used in fibril reactions to form fluorescently labelled 2A, 3Q and *de novo* $A\beta_{40}$ fibril preparations and pH 2 and pH 8 $A\beta_{42}$ fibril preparations. Fibril reactions were carried out as described in Section 2.5 but using 1% ATTO-594 labelled monomer with 99% unlabelled monomer. The resulting aggregates were shown to be fluorescent and fibrillar, with the expected growth kinetics and fibril yields. These fluorescently labelled fibrils were then used in imaging and flow cytometry experiments.

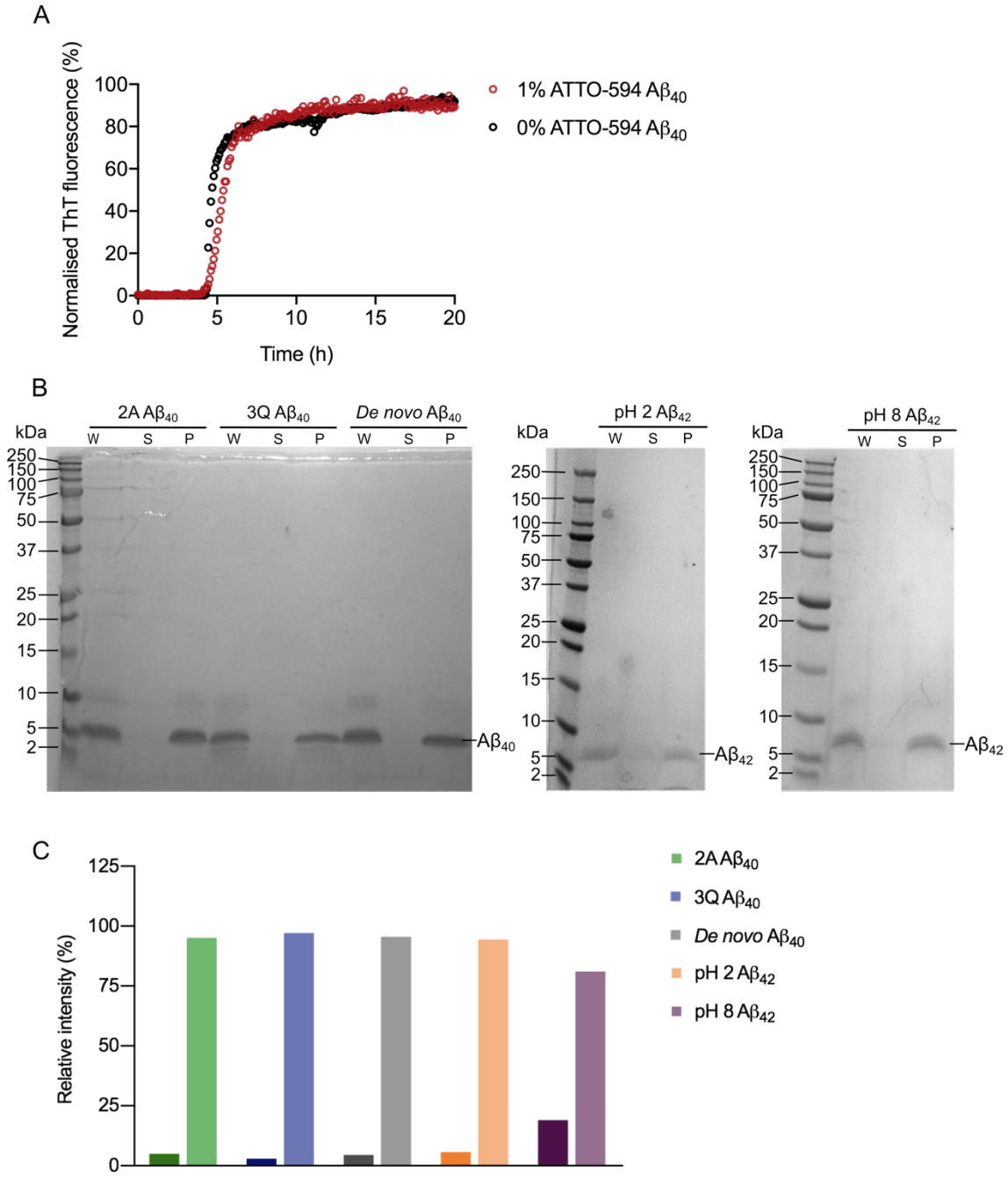

Figure 5.4. ThT kinetics and fibril yields of ATTO-594 labelled Aβ fibril preparations
(A) Fibril growth kinetics monitored by ThT of unlabelled $A\beta_{40}$ monomer mixed with 1% ATTO-594 labelled $A\beta_{40}$ monomer at a final concentration of 100 µM, incubated at 37 °C with orbital shaking. The fibril growth kinetics of 100% unlabelled $A\beta_{40}$ monomer is shown in comparison. (B) Samples of 1% ATTO-594 labelled fibril preparations were centrifuged at 16,873 xg for 40 min, the supernatant subsequently removed and the pellet resuspended in fresh fibril buffer. Equal volumes of the whole sample before centrifugation (W), the supernatant fraction after centrifugation (S) and the resuspended pellet fraction (P) were analysed using SDS-PAGE on a 15% Tris-Tricine gel. (C) Densitometry was carried out in order to quantify $A\beta_{40}$ levels in each fraction.

5.3 Analysis of the association, uptake and degradation of Aβ fibril preparations by BV-2 microglia

Following the production and characterisation of 1% ATTO-594 labelled fibril preparations, the interaction, uptake and breakdown of these fibrils by BV-2 microglial cells was monitored using a combination of confocal microscopy and flow cytometry. For these experiments, BV-2 microglial cells were incubated with 1 μM (monomer-equivalent concentration) of the fluorescently labelled fibril preparations for a 4 h pulse. The cell media was then removed, the cells washed to remove non-cell-associated fibrils and replaced with fresh cell media. Live-cell confocal microscopy and flow cytometry were performed on samples immediately after this pulse incubation (0 h chase timepoint), and then up to 72 h after this pulse incubation, in the absence of additional peptide. Confocal microscopy was used in order to determine the cellular localisation of fluorescently labelled fibrils, and the use of the cell stain LysoTracker Green allowed observation of any colocalisation of fibrils with acidic lysosomal compartments. Flow cytometry was used in parallel to imaging, to quantify cell-associated fluorescence using larger populations of cells. An outline of this experimental approach is shown in Figure 5.5.

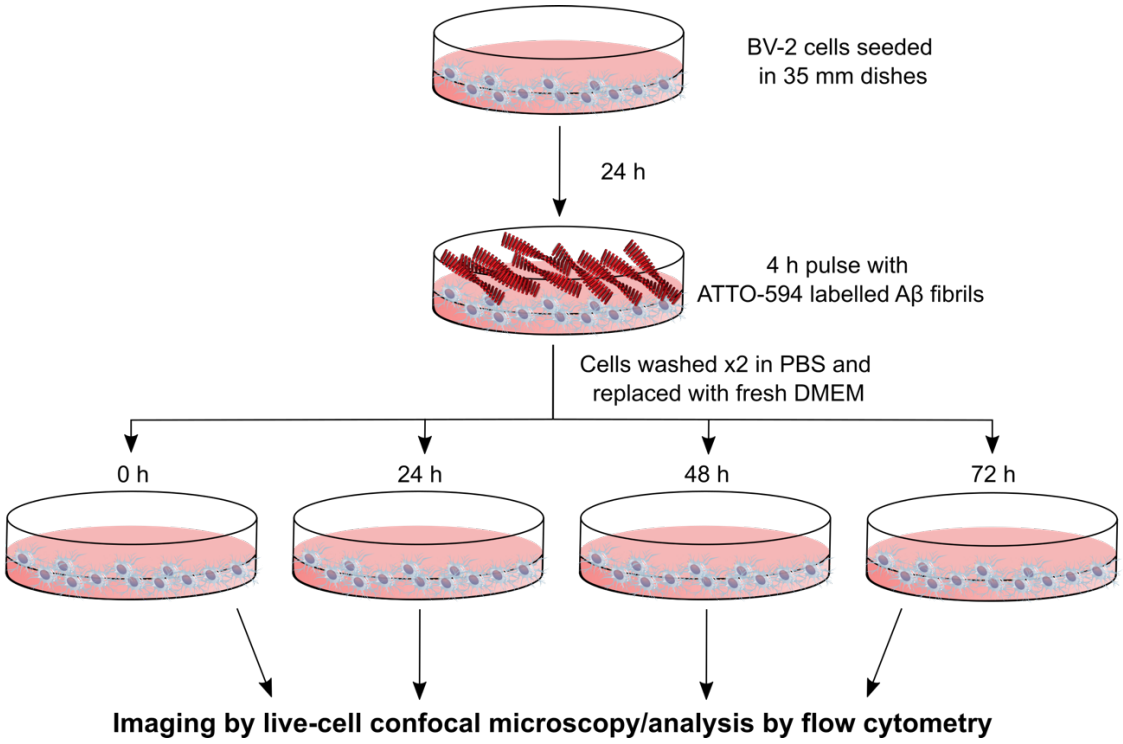

Figure 5.5. Outline of the experimental approach used to assess the association, uptake and degradation of Aβ fibrils by BV-2 microglial cells
Following the production of Aβ fibril preparations incorporating 1% ATTO-594 labelled Aβ monomer, experiments were performed to assess the relationship between these fibrils and BV-2 microglial cells. Aβ fibrils were incubated with BV-2 cells at a final monomer-equivalent concentration of 1 μM for 4 h ('pulse' incubation). Cells were then washed and replaced with fresh media. Chase experiments in which cells were either imaged using live-cell confocal microscopy or analysed using flow cytometry were performed at 0, 24, 48 or 72 h. This was to determine the fate of the Aβ fibrils that were incubated with cells over time, in terms of their cellular localisation and the extent of cell-associated fluorescence.

5.3.1 Analysis of BV-2 microglial cells after 4 h pulse with Aβ fibril preparations

Confocal microscopy revealed after a 4 h pulse that 2A, 3Q and *de novo* $A\beta_{40}$ fibrils were associated with the cell surface of BV-2 cells, as shown by red fluorescence surrounding cells (Figure 5.6A). No evidence of internalisation of the Aβ fibrils or colocalisation with LysoTracker Green was observed at this timepoint. Results from flow cytometry were consistent with observations from confocal imaging, with cell-associated fluorescence increased compared to untreated cells to the same extent for all three $A\beta_{40}$ fibril polymorphs (Figure 5.6B). However, a differential level of $A\beta_{42}$ fibril association was observed, with less evidence of pH 2 $A\beta_{42}$ fibril association with BV-2 cells when compared to pH 8 $A\beta_{42}$ fibrils. This was demonstrated by live-cell confocal imaging in which limited cell-associated red fluorescence was observed for cells incubated with pH 2 $A\beta_{42}$ fibrils, whereas fluorescently labelled pH 8 $A\beta_{42}$ fibrils can be seen to surround BV-2 cells, indicative of association with cell surfaces membranes (Figure 5.7A). These observations were consolidated by flow cytometry, in which the cell-associated fluorescence was lower for cells incubated with pH 2 $A\beta_{42}$ fibrils compared to those incubated with pH 8 $A\beta_{42}$ fibrils (Figure 5.7B). Taken together these results suggest that pH 2 $A\beta_{42}$ fibrils interact less with BV-2 microglial cells than pH 8 $A\beta_{42}$ fibrils.

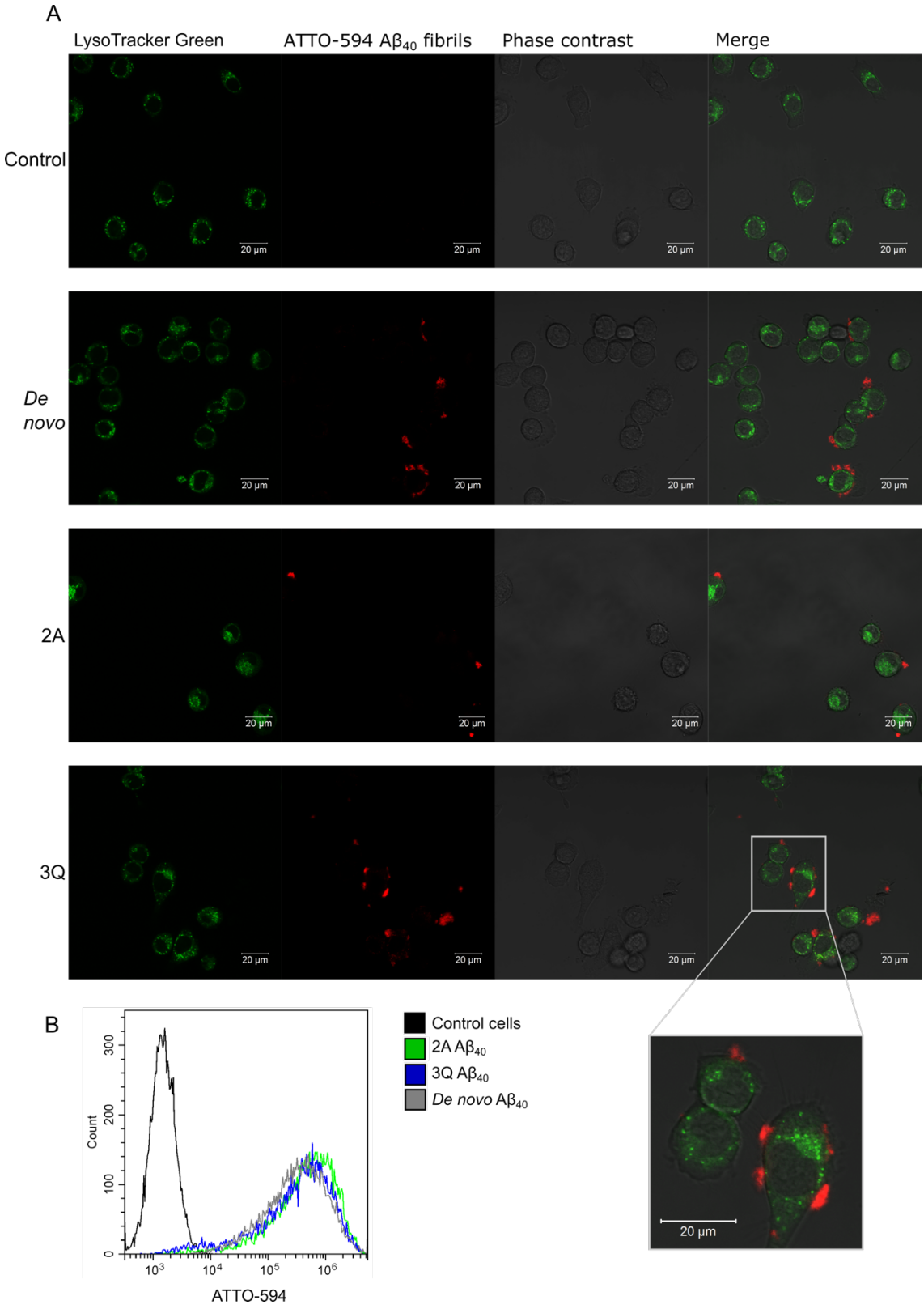

Figure 5.6. Analysis of BV-2 cells after pulse incubation with ATTO-594 labelled Aβ40 fibrils (A) BV-2 cells were incubated with 1 μM (monomer-equivalent concentration) of 1% ATTO-labelled 2A, 3Q and *de novo* Aβ40 fibrils for 4 h before cells were washed x2 in PBS and replaced with fresh imaging media. Cells were stained with LysoTracker Green and imaged by live-cell confocal imaging using a Zeiss LSM700 confocal microscope to show cell-associated fluorescence. Scale bar = 20 μm (B) BV-2 cells were incubated under the same conditions as in A, before cell-associated fluorescence was measured using flow cytometry. Representative traces are shown, 10,000 cells were measured per replicate (n=3). Control cells were incubated in the absence of Aβ fibrils.

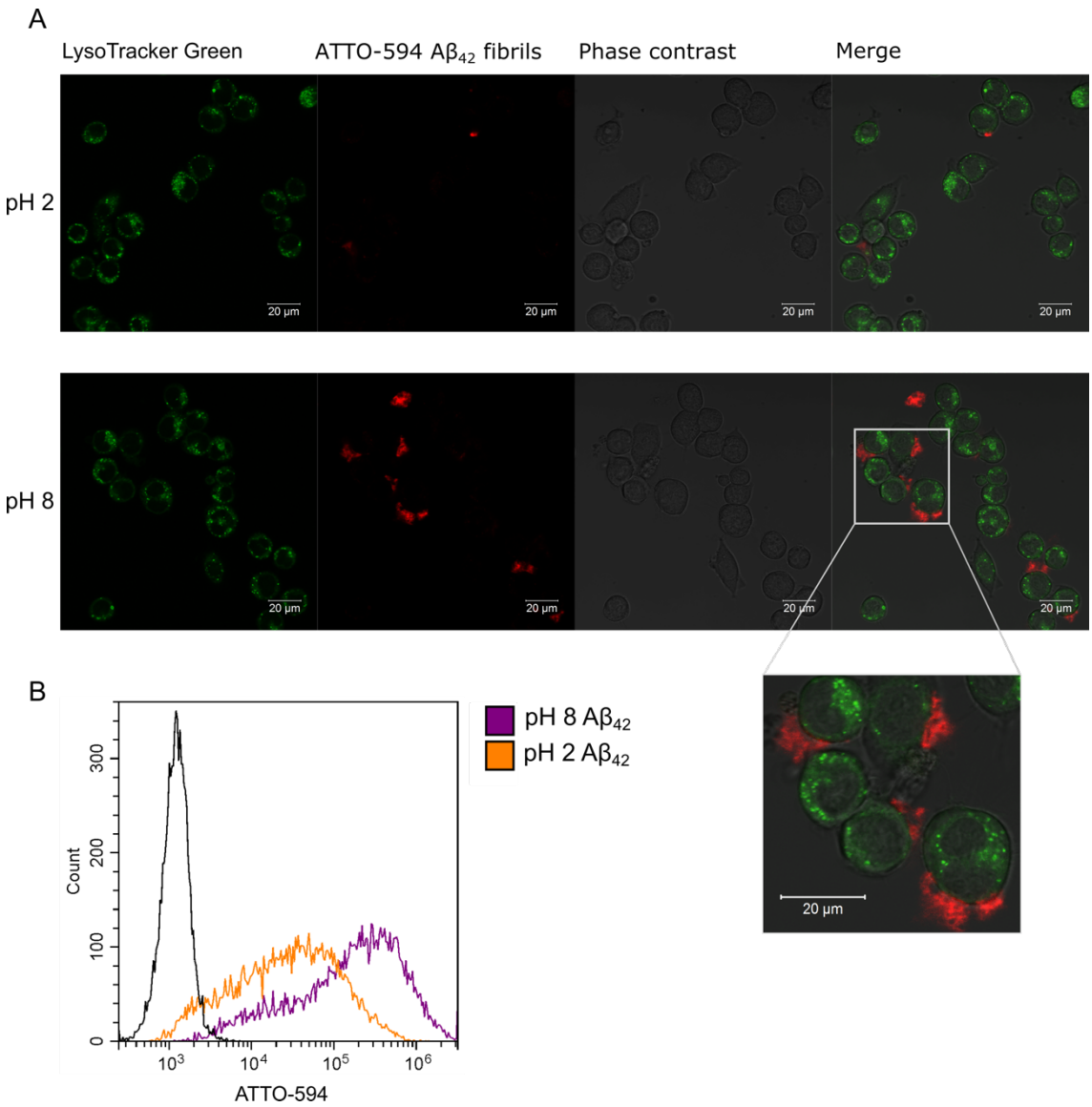

Figure 5.7. Analysis of BV-2 cells after pulse incubation with ATTO-594 labelled Aβ42 fibrils (A) BV-2 cells were incubated with 1 µM (monomer-equivalent concentration) of 1% ATTO-labelled pH 2 or pH 8 $A\beta_{42}$ fibrils for 4 h before cells were washed x2 in PBS and replaced with fresh imaging media. Cells were stained with LysoTracker Green and imaged by live-cell confocal imaging using a Zeiss LSM700 confocal microscope to identify localisation of Aβ fibrils. Scale bar = 20 µm (B) BV-2 cells were incubated under the same conditions as (A) before cell-associated fluorescence was measured using flow cytometry. Representative traces are shown, 10,000 cells were measured per replicate (n=3). Control cells were incubated in the absence of Aβ fibrils.

5.3.2 Analysis of BV-2 microglial cells 24 h after pulse with Aβ fibril preparations

Having demonstrated that after a 4 h pulse incubation ATTO-594 labelled Aβ fibrils are associated with the surfaces of BV-2 microglial cells with no evidence of internalisation, cells were analysed at later time points to track the uptake of the fibrils. When live-cell confocal microscopy was performed on samples 24 h after the 4 h pulse incubation with ATTO-594 labelled fibrils, it was found that the majority of red fluorescence corresponding to the ATTO-594 labelled fibrils was intracellular, indicative of cellular uptake. There was some Aβ fibril remaining on the cell surface, but this was minimal. This was observed for all $A\beta_{40}$ and $A\beta_{42}$ fibril polymorphs, indicating that these BV-2 microglial cells are capable of internalising Aβ fibrils within 24 h (Figure 5.8/Figure 5.9). Once internalised, colocalisation is observed between Aβ fibrils and Lysotracker Green, indicating that the fibrils are being trafficked after internalisation into the acidic compartments of the endolysosomal pathway (shown by arrows in Figure 5.8 and Figure 5.9).

Flow cytometry showed that after a 24 h chase cell-associated fluorescence had decreased. This indicates that some of the fibrillar material had been degraded during this time or had become detached from the cells. For $A\beta_{40}$ fibrils, cells incubated with 2A fibrils had a greater level of cell-associated fluorescence at this timepoint compared to 3Q and *de novo* fibril preparations (Figure 5.8B). Profiles are similar for both $A\beta_{42}$ fibril preparations, with both showing a downward shift in cell-associated fluorescence. However, a larger population of cells with cell-associated fluorescence that overlaps with that of control cells, which were incubated in the absence of ATTO-594 labelled Aβ fibrils, can be seen for cells incubated with pH 2 $A\beta_{42}$ fibrils compared to pH 8 fibrils at this timepoint (Figure 5.9B).

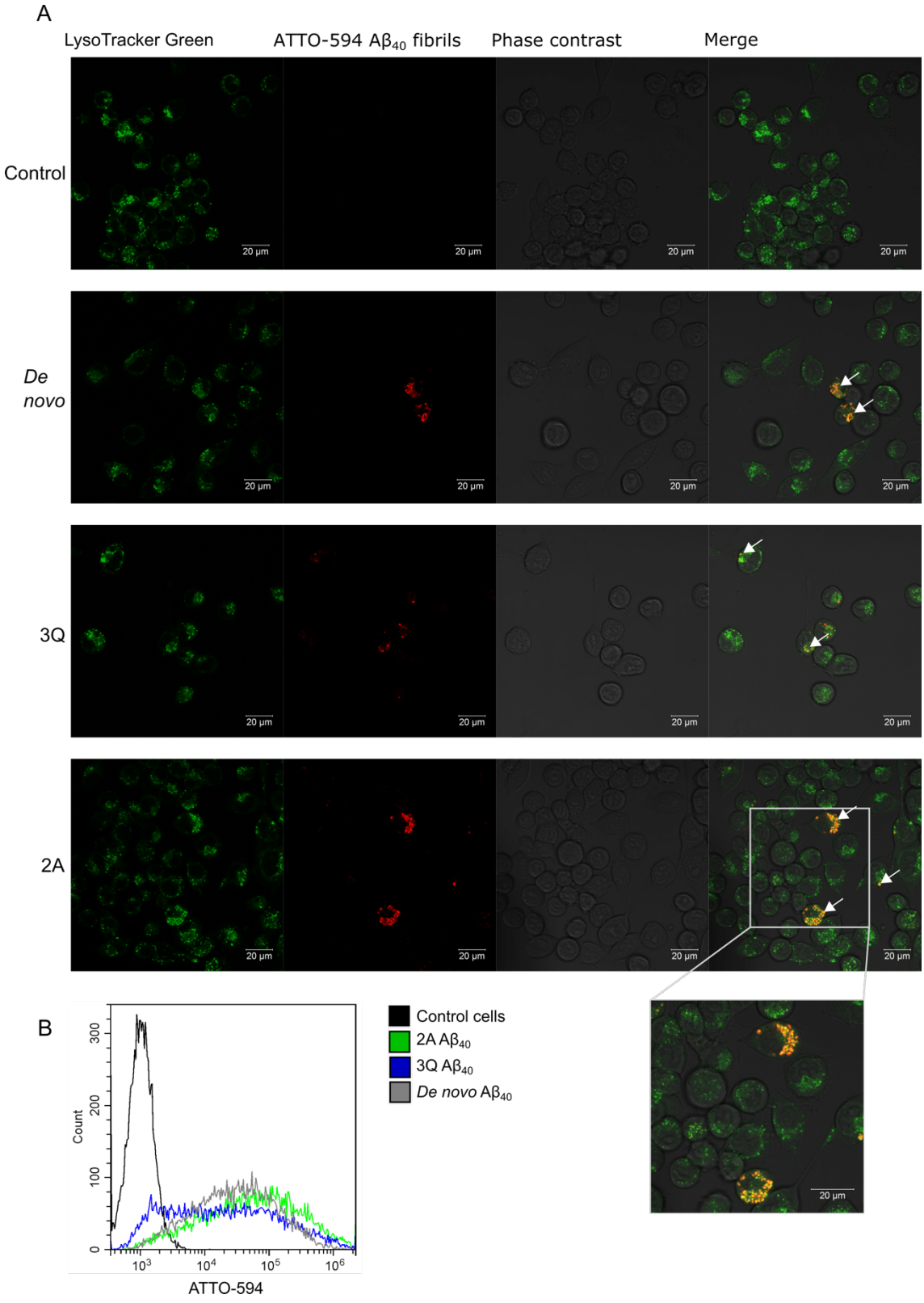

Figure 5.8. Analysis of BV-2 cells 24 h after pulse incubation with ATTO-594 labelled Aβ$_{40}$ fibrils

(A) BV-2 cells were incubated with 1 µM (monomer-equivalent concentration) of 1% ATTO-labelled 2A, 3Q and *de novo* Aβ$_{40}$ fibrils for 4 h before cells were washed x2 in PBS, replaced with fresh cell media and incubated for a further 24 h. Cells were then stained with LysoTracker green and imaged by live-cell confocal imaging using a Zeiss LSM700 confocal microscope to identify localisation of Aβ fibrils. Yellow areas indicate colocalization of Aβ fibrils with lysosomes, as highlighted by arrows. Scale bar = 20 µm (B) BV-2 cells were incubated under the same conditions as (A) before cell-associated fluorescence was measured using flow cytometry. Representative traces are shown, 10,000 cells were measured per replicate (n=3). Control cells were incubated in the absence of Aβ fibrils.

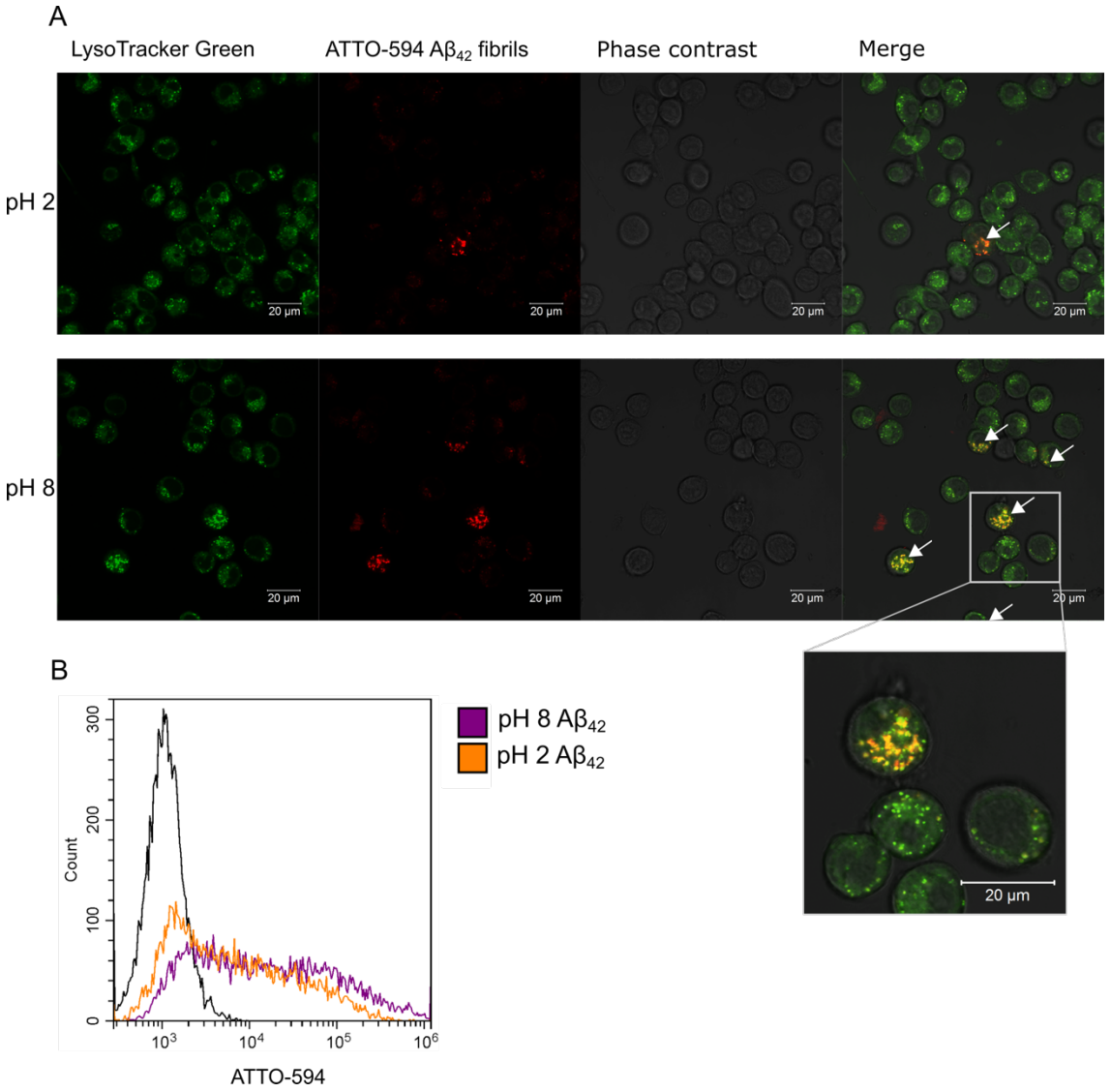

Figure 5.9. Analysis of BV-2 cells 24 h after pulse incubation with ATTO-594 labelled Aβ$_{42}$ fibrils

(A) BV-2 cells were incubated with 1 µM (monomer-equivalent concentration) of 1% ATTO-labelled pH 2 and pH 8 Aβ$_{42}$ fibrils for 4 h before cells were washed x2 in PBS, replaced with fresh cell media and incubated for a further 24 h. Cells were then stained with LysoTracker Green and imaged by live-cell confocal imaging using a Zeiss LSM700 confocal microscope to identify localisation of Aβ fibrils. Yellow areas indicate colocalization of Aβ fibrils with lysosomes, as highlighted by arrows. Scale bar = 20 µm (B) BV-2 cells were incubated under the same conditions as (A) before cell-associated fluorescence was measured using flow cytometry. Representative traces are shown, 10,000 cells were measured per replicate (n=3). Control cells were incubated in the absence of Aβ fibrils.

5.3.3 Analysis of BV-2 microglial cells 48 h and 72 h after pulse with Aβ fibril preparations

The same confocal and flow cytometry experiments were carried out at later timepoints to assess the location and extent of ATTO-594 labelled Aβ fibrils. Since confocal imaging experiments at 24 h demonstrated that nearly all fluorescently labelled Aβ material was located intracellularly, a decrease in cell-associated fluorescence over time would indicate that the fibrils are being degraded within the cells.

Confocal imaging experiments were carried out 72 h after the initial 4 h pulse incubation of BV-2 cells with ATTO-594 labelled fibrils. It was visibly observed that there was less evidence of red fluorescence remaining at this timepoint for all Aβ fibril preparations, indicating degradation of the fibrils by BV-2 cells. However, it was observed that there was more red fluorescence remaining inside BV-2 cells that were incubated with 2A $A\beta_{40}$ fibrils compared to those incubated with 3Q or *de novo* $A\beta_{40}$ fibrils (Figure 5.10A). This suggests that the 2A fibrils could be more resistant to degradation than the other $A\beta_{40}$ fibril preparations. This was supported by flow cytometry experiments which were carried out 48 h after the pulse incubation of BV-2 cells with fluorescent fibrils. These flow cytometry experiments showed a clear and consistent shift towards higher cell-associated fluorescence in the trace of BV-2 cells that were incubated with 2A fibrils compared to the other $A\beta_{40}$ fibril preparations (Figure 5.10B).

No differences were identified in the level of the two $A\beta_{42}$ fibril polymorphs remaining at this timepoint (Figure 5.11A). This was supported by flow cytometry experiments at 48 h, in which pH 2 and pH 8 $A\beta_{42}$ traces can be seen to be very similar at this timepoint, suggesting a similar level of fibril remaining and therefore no identifiable differences in the extent of degradation between these fibrils (Figure 5.11B).

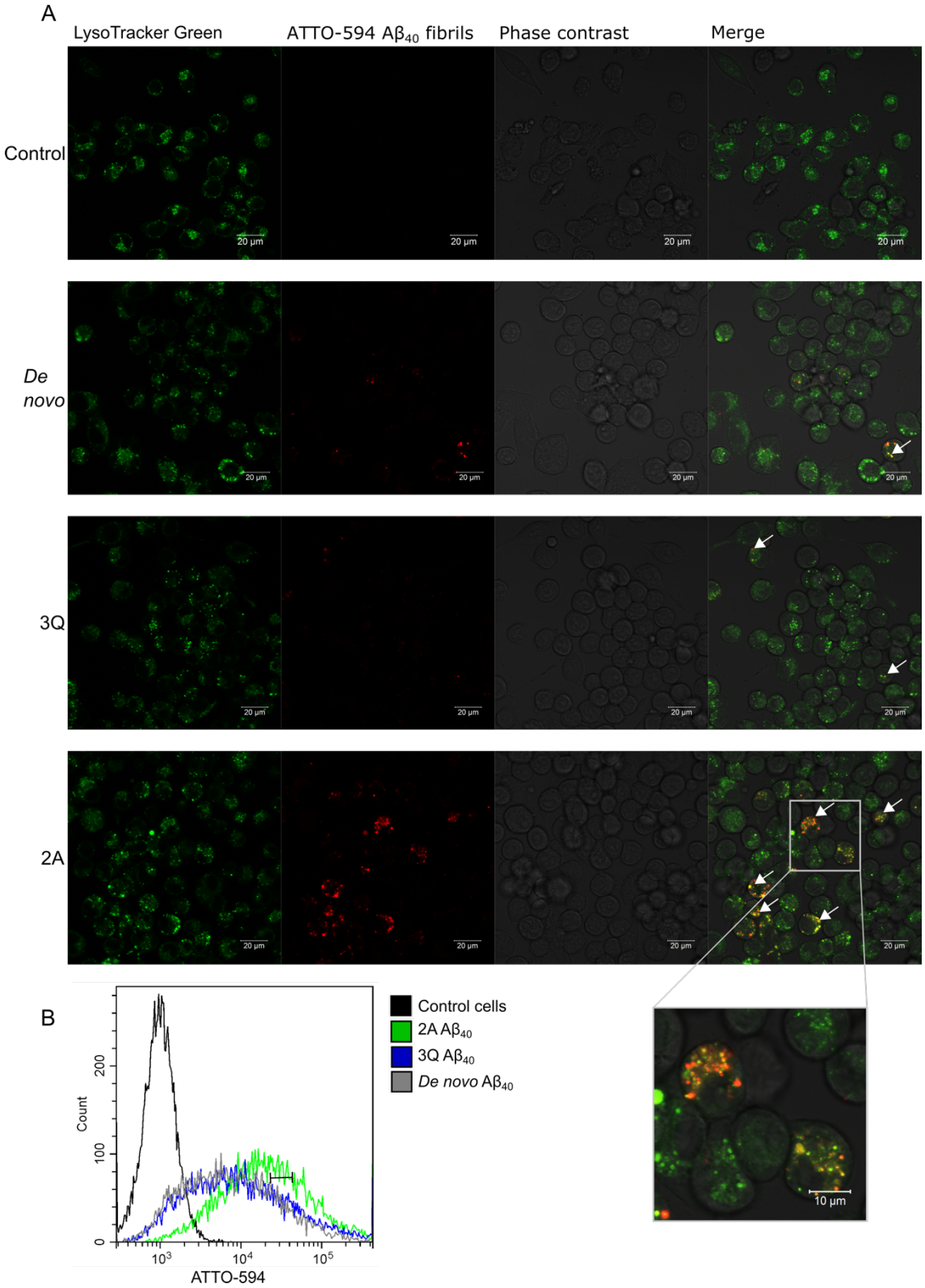

Figure 5.10. Analysis of BV-2 cells at 48 h and 72 h timepoints after pulse incubation with ATTO-594 labelled Aβ40 fibrils

(A) BV-2 cells were incubated with 1 µM (monomer-equivalent concentration) of 1% ATTO-labelled 2A, 3Q and *de novo* $A\beta_{40}$ fibrils for 4 h before cells were washed x2 in PBS, replaced with fresh cell media and incubated for a further 72 h. Cells were then stained with LysoTracker green and imaged by live-cell confocal imaging using a Zeiss LSM700 confocal microscope to identify localisation of Aβ fibrils. Yellow areas indicate colocalization of Aβ fibrils with lysosomes, as highlighted by arrows. Scale bar = 20 µm (B) BV-2 cells were treated as in (A) but incubated for 48 h before cell-associated fluorescence was measured using flow cytometry. Representative traces are shown, 10,000 cells were measured per replicate (n=3). Control cells were incubated in the absence of Aβ fibrils.

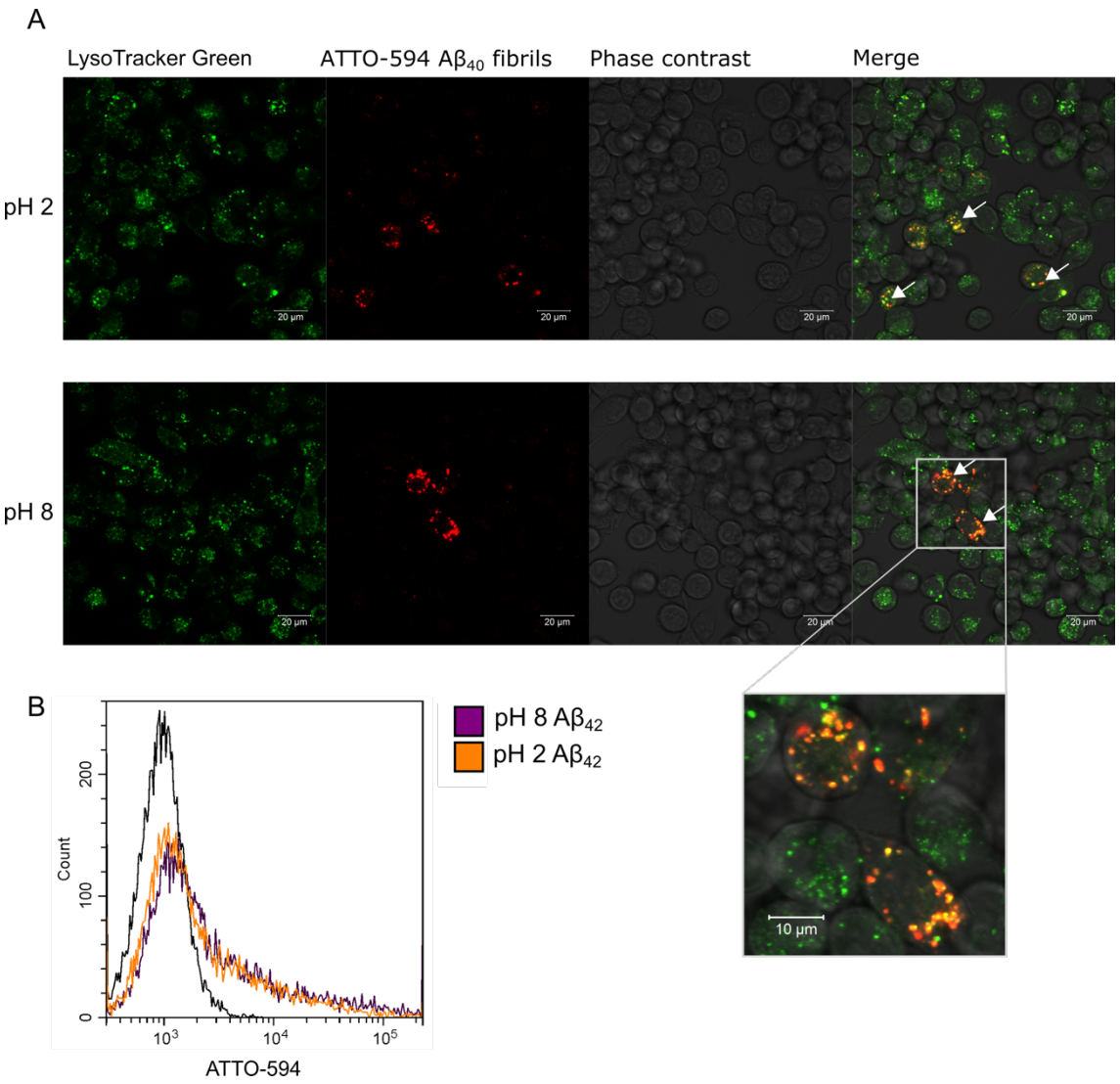

Figure 5.11. Analysis of BV-2 cells at 48 h and 72 h timepoints after pulse incubation with ATTO-594 labelled Aβ$_{42}$ fibrils
(A) BV-2 cells were incubated with 1 µM (monomer-equivalent concentration) of 1% ATTO-labelled pH 2 and pH 8 Aβ$_{42}$ fibrils for 4 h before cells were washed x2 in PBS, replaced with fresh cell media and incubated for a further 72 h. Cells were then stained with LysoTracker green and imaged by live-cell confocal imaging using a Zeiss LSM700 confocal microscope to identify localisation of Aβ fibrils. Yellow areas indicate colocalization of Aβ fibrils with lysosomes, as highlighted by arrows. Scale bar = 20 µm (B) BV-2 cells were treated as in (A) but incubated for 48 h before cell-associated fluorescence was measured using flow cytometry. Representative traces are shown, 10,000 cells were measured per replicate (n=3). Control cells were incubated with fibrillation buffer in the absence of Aβ fibrils

In summary, a number of interesting observations were made about the biological properties of different Aβ fibrils in their interactions with microglial cells. Firstly, it was shown that pH 8 Aβ$_{42}$ fibrils associate more with BV-2 cells than pH 2 Aβ$_{42}$ fibrils after a 4 h pulse incubation. It was then shown that BV-2 microglial cells are efficient at internalising all of the different Aβ fibril preparations, with the majority of fluorescent fibrillar material found to be intracellular and colocalising with lysosomes 24 h after incubation. Differences in the extent of degradation once internalised were then identified between Aβ$_{40}$ fibril preparations, with more 2A fibril found to be remaining after 48 h and 72 h compared to other Aβ$_{40}$ fibril preparations. Flow cytometry overlays showing the

level of cell-associated fluorescence of BV-2 cells incubated with each of the different Aβ fibril preparations at 0 h, 24 h and 48 h are shown in Figure 5.12.

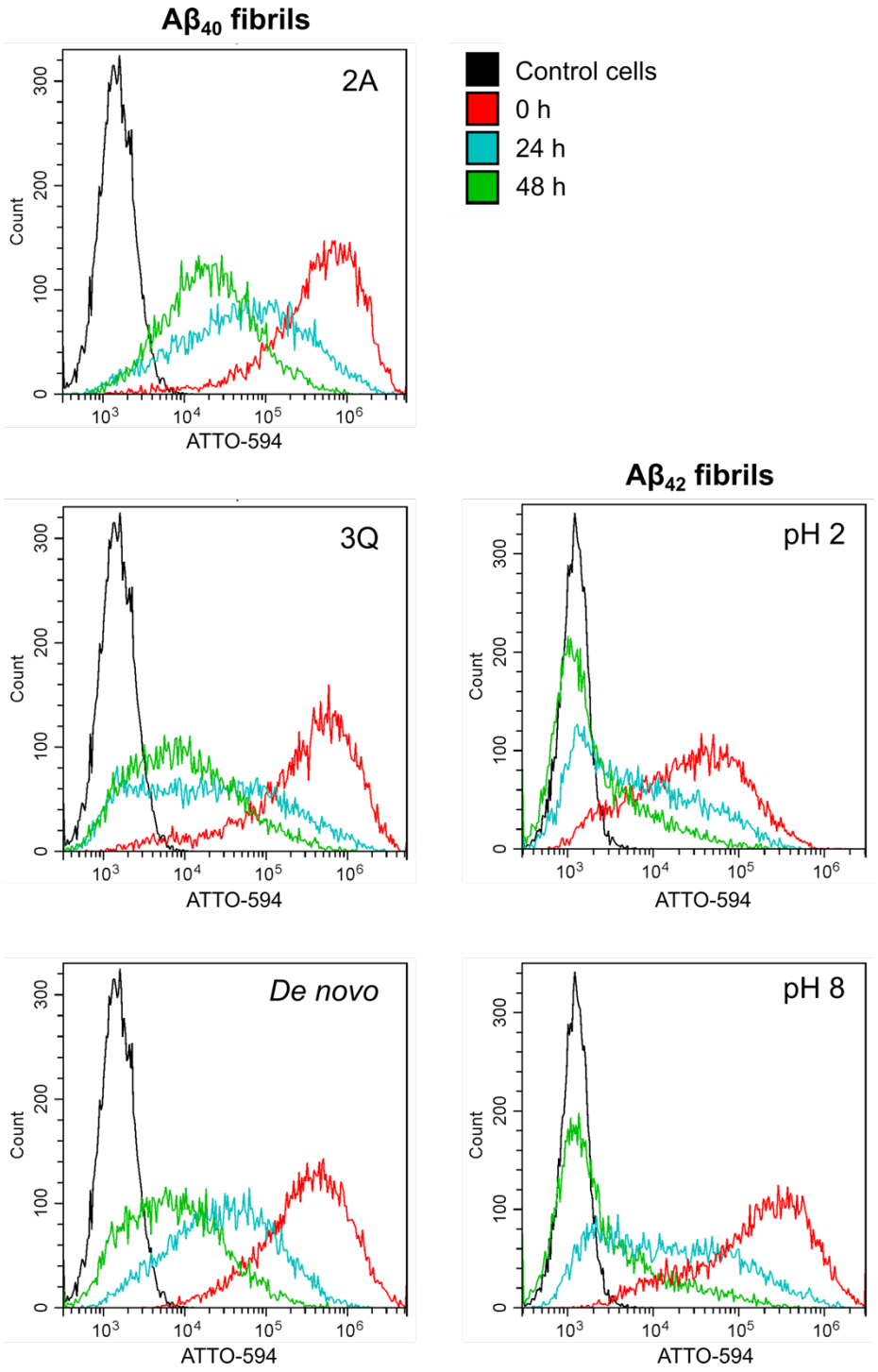

Figure 5.12. Flow cytometry overlays of BV-2 cell-associated fluorescence over time after pulse incubation with ATTO-594 labelled Aβ fibrils
BV-2 cells were incubated with 1 μM (monomer-equivalent concentration) of 1% ATTO-labelled Aβ fibrils for 4 h before cells were washed x2 in PBS and replaced with fresh cell media. Cell-associated fluorescence was measured using flow cytometry at 0 h (red), 24 h (blue), and 48 h (green) after this pulse incubation. Representative traces are shown, 10,000 cells were measured per replicate (n=3). Control cells were incubated with fibrillation buffer in the absence of Aβ fibrils

5.4 Lysosomal degradation of Aβ fibril preparations

Confocal microscopy revealed that all of the different Aβ fibril preparations tested were internalised by BV-2 microglial cells efficiently within 24 h, and flow cytometry showed that the level of fluorescently labelled fibril associated with cells decreased over time. These experiments indicated that 2A $A\beta_{40}$ fibrils remained in BV-2 cells for longer following a pulse incubation than other $A\beta_{40}$ fibril preparations, suggesting that these fibrils could be more resistant to degradation. These data point towards lysosomal degradation of the fibrils, and therefore this process was explored further.

For these experiments, lysosomes from BV-2 cells were isolated by subcellular fractionation (Section 2.11.1). For this, fractionation of BV-2 cell homogenates was performed by ultracentrifugation using a Percoll gradient (Morten et al., 2007). Fractions were then collected and analysed for alkaline phosphatase activity and α-N-acetylgalactosaminidase (NAGA) activity, as markers of membrane compartments and lysosomes respectively (Figure 5.13). Fractions shown to be most enriched for NAGA (16-19) were pooled and ultracentrifuged to remove Percoll and to pellet the lysosomes (Figure 5.13). The lysosomal fractions were stored at -80 until use. Prior to use, lysosomal fractions were subjected to 3 freeze-thaw cycles to disrupt membranes and thus release the hydrolases.

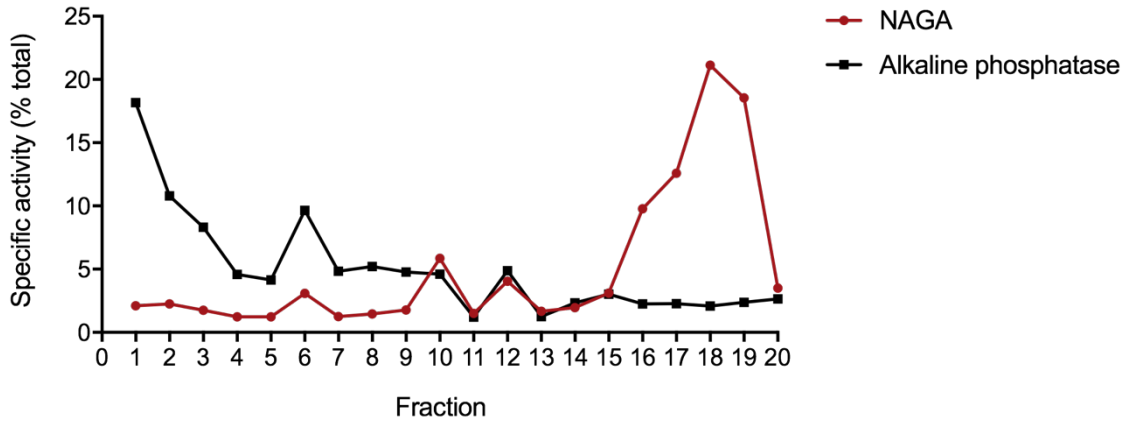

Figure 5.13. Alkaline phosphatase and NAGA activities of BV-2 cell fractions
Lysosome isolation and enrichment was performed by homogenising BV-2 cells using a ball bearing homogeniser with 10 µm clearance. This homogenate was centrifuged and the supernatant containing the post-nucleur fraction was ultracentrifuged on a 27% Percoll gradient to fractionate. 20 fractions were collected from this gradient (1 top, 20 bottom) and were analysed for alkaline phosphatase and NAGA activity as markers of plasma membrane and lysosomes respectively. Fractions 16-19 were retained based on these assays and a further ultracentrifugation step performed to further concentrate the lysosome samples and remove Percoll.

The proteolytic activity of lysosomes was first tested using $A\beta_{40}$ monomer. For this, $A\beta_{40}$ monomer was resuspended in ammonium acetate (pH 4.5) and incubated with a concentration series of isolated lysosomes for 4 h at 37 °C before samples were analysed by SDS-PAGE (Figure 5.14). Concentrations of lysosomes are given as a measure of NAGA activity units, as measured using the NAGA assay (Section 2.11.2.1). This allowed the enzymatic activity of the lysosomal fractions to be normalised between different lysosome batches and experimental repeats. These initial experiments revealed the digestion of $A\beta_{40}$ peptide by the lysosome samples, with the peptide almost entirely degraded at the highest concentration tested (1 NAGA unit), and at least two clear bands observed on the gel at lower concentrations of lysosome (0.125 NAGA units). This showed that lysosomal fractions from BV-2 cells contain proteases that can degrade the Aβ peptide sequence.

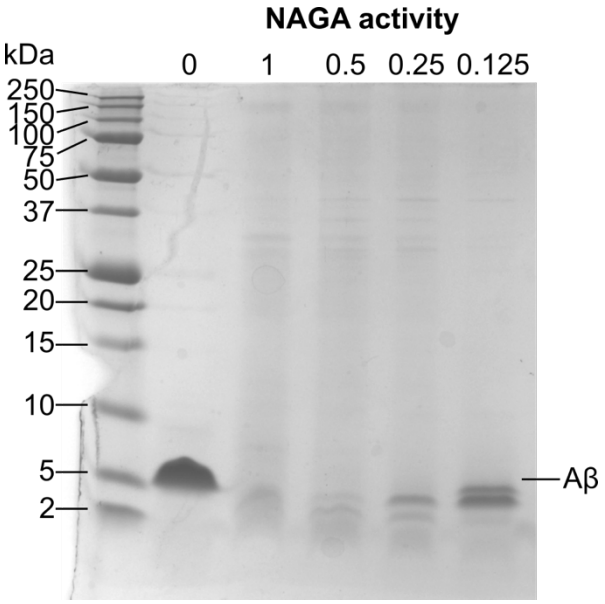

Figure 5.14. *In vitro* degradation of $A\beta_{40}$ monomer by BV-2 cell lysosomes
200 μM monomeric Aβ peptide was incubated in ammonium acetate (pH 4.5) for 4 h at 37 °C with increasing concentrations of lysosomes isolated from BV-2 cells. NAGA activity of lysosome samples was determined using the NAGA assay (Section 2.11.2.1). Samples were analysed by SDS-PAGE using a 13% Tris-Tricine gel.

As confocal microscopy and flow cytometry experiments suggested differences in the degradation of $A\beta_{40}$ fibril preparations, with more 2A fibril shown to be remaining after 48 h compared to 3Q and *de novo* fibrils, lysosomal degradation experiments focused on $A\beta_{40}$ fibrils. In initial experiments, 200 μM monomer-equivalent concentrations of 2A, 3Q and *de novo* fibrils were incubated with increasing concentrations of isolated lysosomes from BV-2 cells, for 4 h, 24 h or 48 h, in order to assess degradation over time and identify an appropriate concentration of lysosome to use (Figure 5.15).

From these experiments it was shown that BV-2 lysosomal enzymes are capable of digesting all three $A\beta_{40}$ fibril preparations tested. This was indicated by SDS-PAGE gels of samples in which a reduction in the main band corresponding to full-length $A\beta_{40}$ peptide is seen, along with the appearance of lower bands corresponding to digestion products (Figure 5.15). Aβ fibrils exhibited increased resistance to proteolysis compared to the soluble form of the peptide, which is consistent with previously published data (Qiu et al., 1998; Farris et al., 2003; Leissring et al., 2003; Morten et al., 2007; Liao and Van Nostrand, 2010).

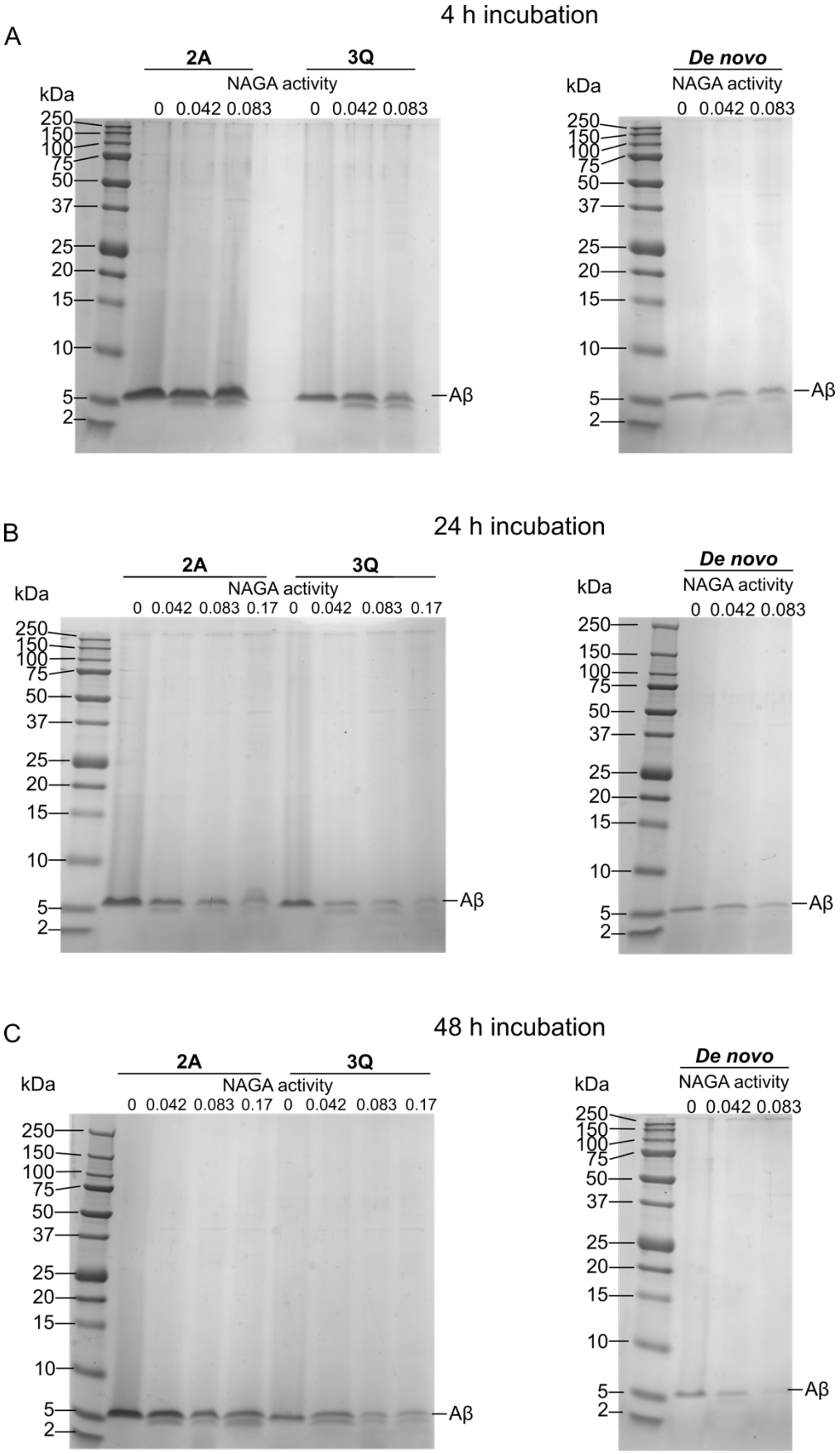

Figure 5.15. *In vitro* degradation of Aβ$_{40}$ fibril preparations by BV-2 cell lysosomes
200 µM monomer-equivalent concentration of 2A, 3Q and *de novo* Aβ fibril preparations were incubated for 4 h, 24 h or 48 h with increasing concentrations of lysosomes isolated from BV-2 cell homogenates. NAGA activity of lysosome samples was determined using the NAGA assay (Section 2.11.2.1) and used as a measure of lysosome concentration. Resulting samples were analysed by SDS-PAGE using 13 % Tris-Tricine gels.

Based on these experiments, 0.083 NAGA units in a reaction volume of 60 µL and 200 µM Aβ fibrils were taken to be the most appropriate conditions, and the digestions were repeated using three different batches of 2A, 3Q and *de novo* $A\beta_{40}$ fibrils and lysosomes under these conditions. Densitometry was then performed on the resulting SDS-PAGE gels to assess the reduction in intensity of the band corresponding to full-length $A\beta_{40}$ in samples of digested 2A, 3Q and *de novo* $A\beta_{40}$ fibrils to identify any differences between them (Figure 5.16). Results of this showed that 2A fibrils were consistently degraded to a lesser extent by lysosomes than 3Q and *de novo* fibrils, consistent with previous confocal microscopy and flow cytometry experiments (Figure 5.16). This difference was significant between 2A and 3Q fibrils after 4 h incubation with lysosomes and between 2A and *de novo* fibrils after 48 h incubation with lysosomes (Figure 5.16).

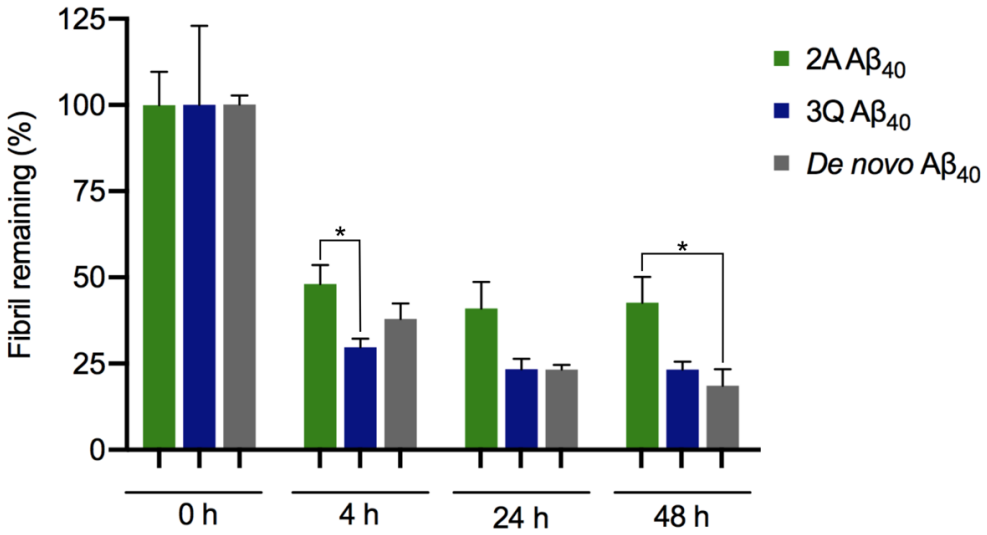

Figure 5.16. Quantification of *in vitro* lysosomal degradation of $A\beta_{40}$ fibril preparations
2A, 3Q and *de novo* $A\beta_{40}$ fibril preparations were incubated with lysosomes isolated from BV-2 cells with a final NAGA activity of 0.083. Samples were taken after 0h, 4h, 24h and 48h before analysis using SDS-PAGE. Densitometry was performed on gels to measure the intensity of the $A\beta_{40}$ peptide band at the 4 timepoints and the reduction in the intensity compared to the 0h timepoint was calculated. Error bars represent mean ± SEM. Tukey's multiple comparison test, *, $p \geq 0.05$ (n=3)

In summary, lysosomes were isolated from BV-2 microglial cells and the proteases present in these lysosomal fractions were shown to cleave monomeric $A\beta_{40}$ peptide, resulting in the formation of digestion products visible by SDS-PAGE (Figure 5.14). Further to this, 2A, 3Q and *de novo* $A\beta_{40}$ fibril preparations were all shown to be cleaved by lysosomal enzymes. When these decreases were quantified by densitometry it was found that 2A fibrils consistently have the most full-length peptide remaining after incubation with lysosomes compared to the other $A\beta_{40}$ fibril preparations (Figure 5.16). This finding is consistent with results from flow cytometry and confocal microscopy experiments and suggests 2A fibrils are more resistant to digestion than 3Q and *de novo* fibrils.

5.5 Discussion

In this chapter the association, uptake and degradation of different Aβ fibril preparations by BV-2 microglial cells was analysed. Using confocal microscopy, it was possible to track fluorescent fibrils over time from their initial interactions of fibrils with the cell surface, through to their uptake into lysosomes and their degradation. This microscopy analysis was complemented by flow cytometry experiments which enabled quantification of cell-associated fluorescence of 1000s of individual cells.

It was first demonstrated that pH 8 $A\beta_{42}$ fibrils associate with the surface of BV-2 microglial cells to a greater extent than pH 2 $A\beta_{42}$ fibrils after a 4 h incubation. The specific structural feature(s) of the pH 8 $A\beta_{42}$ fibrils that is responsible for this increased interaction with cells has not yet been identified. However, differences in the N-termini of these structures could play a role. In the pH 8 $A\beta_{42}$ fibril structure residues 1-14 are described to be dynamic, whereas in the pH 2 $A\beta_{42}$ fibril structure the N-terminus is ordered and part of the cross-β 'core' of the fibril (Figure 1.7) (Colvin et al., 2016; Gremer et al., 2017). These dynamic N-termini protruding from the inner core of pH 8 $A\beta_{42}$ fibrils could interact with cell membranes, and the absence of these regions in pH 2 $A\beta_{42}$ fibrils could explain their reduced cell association (Ulamec et al., 2020). To test this, these N-terminal regions could be proteolytically cleaved from pH 8 $A\beta_{42}$ fibrils and their ability to interact with cells and cause the cellular responses studied.

This preferential interaction of pH 8 $A\beta_{42}$ fibrils with microglial cell membranes could have a number of consequences. Increased association could result from an increased interaction with receptors on the cell surface of microglial cells. This could trigger inflammatory pathways resulting in greater release of pro-inflammatory mediators. This aligns with the results presented in Chapter 4, in which it was found that pH 8 $A\beta_{42}$ fibrils elicit a greater release of pro-inflammatory cytokines IL-6, TNF-α and IL-1β from immune cells compared to pH 2 $A\beta_{42}$ fibrils. Conversely, perturbation of cell membranes is one mechanism by which amyloid fibrils can have toxic effects on cells, again supported by the results from experiments in Chapter 4 of this thesis in which it was shown that pH 8 $A\beta_{42}$ fibrils are more toxic towards BV-2 microglial cells and other immune cells compared to pH 2 $A\beta_{42}$ fibrils (Martins et al., 2008; Bäuerlein et al., 2017; Han et al., 2017).

In the context of an AD brain, an increased interaction with microglial cells could result in the death of microglial cells, reducing their capability to clear Aβ. However, despite initial differences in cell association, both pH 2 and pH 8 $A\beta_{42}$ fibrils were taken up and degraded. Other factors could play a role in determining whether fibrils are cleared by microglia, including ageing and mutations associated with AD. Microglial phenotypes

previously discussed that are associated with disease (Section 1.4.5.3) or mutations in microglia associated with increased risk of AD could alter the ability of these cells to clear Aβ fibrils (Krasemann et al., 2017; Deczkowska et al., 2018; Frigerio et al., 2019; Marschallinger et al., 2020). This could also be the case with ageing and could therefore resulting in an accumulation of fibrils that are more difficult to degrade than others (Hickman et al., 2008; Krabbe et al., 2013). The effects of these factors on the capability of microglia to clear the different Aβ fibril preparations used in this thesis could be investigated in future work.

Once internalised, live-cell confocal imaging revealed that the fluorescently labelled Aβ fibrils colocalise with LysoTracker Green, a lysosome stain. This indicates that the fibrils are being trafficked via the endocytic pathway to lysosomes, a cellular compartment which is involved in breakdown of cellular and extracellular material (Hu et al., 2015). No differences were identified between $A\beta_{42}$ fibrils in their breakdown by BV-2 cells when assessed using live-cell confocal imaging and flow cytometry. However, more 2A $A\beta_{40}$ fibril remained within BV-2 cells 48 h and 72 h after incubation with the fibrils, compared to 3Q and *de novo* $A\beta_{40}$ fibril preparations. This suggests that BV-2 cells degrade these fibrils to a lesser extent than the other $A\beta_{40}$ fibril preparations. This could be due to increased resistance of 2A fibrils to proteolytic cleavage or could alternatively be due to the 2A fibrils interfering with intracellular processes, thus reducing their clearance capabilities. For example, amyloid fibrils formed from β_2-microglobulin (β_2m) have been shown to alter the trafficking of lysosomal membrane proteins and reduce degradation of a model substrate for lysosomal proteases, thus indicating perturbation of the endolysosomal pathway by fibrils (Jakhria et al., 2014). This interference with lysosome function would have a knock-on effect on the breakdown of the fibrils themselves. *In vivo*, an Aβ fibril polymorph that is more resistant to degradation than others is likely to become a dominant fibril structure within the brain, as it cannot be cleared. This is supported by a recent study which found that *ex vivo* Aβ fibrils extracted from disease tissue are more resistant to proteolysis than those formed *in vitro*, suggesting that fibrils present in AD were selected in the brain due to their ability to escape this clearance (Schönfelder et al., 2021).

The degradation of Aβ fibrils was also studied in cell-free experiments using lysosomal fractions from BV-2 cells. These results confirmed that lysosomal enzymes are capable of cleaving the fibrils, resulting in the formation of proteolytic products (Figure 5.15). Further to this, the level of cleavage was lowest for 2A $A\beta_{40}$ fibrils compared to other $A\beta_{40}$ fibril polymorphs, consistent with previous results. These results suggest that an intrinsic property of 2A fibrils endows them with increased resistance to proteolysis. One possibility is that the 2A structure is more resistant than that of the other fibrils studied in

this work to cleavage by lysosomal proteases. The known cleavage sites of lysosomal enzymes cathepsin B and TPP-1 have been mapped onto the 2A and 3Q $A\beta_{40}$ fibril structures to visualise differences (Figure 5.17) (Mueller-Steiner et al., 2006; Solé-Domènech et al., 2018). With the most obvious difference between these fibril structures being the 2-fold symmetry of the 2A structure and the 3-fold symmetry of the 3Q structure, it could be that these differences in arrangement of the fibril subunits make the structures more or less accessible to proteases and thus make them more or less resistant to degradation. Unfortunately, for the fibrils studied herein, it was not possible to identify the cleavage sites for lysosomal proteases in this work due to time constraints. However, future studies could identify the cleavage products produced from incubation of the different fibril preparations with lysosomal fractions, thus allowing mapping of cleavage sites to determine whether the 2A fibril structure obscures specific protease cleavage sites. In addition, the contribution of specific lysosomal proteases could be investigated by the incubation of fibrils with individual purified enzymes *in vitro*.

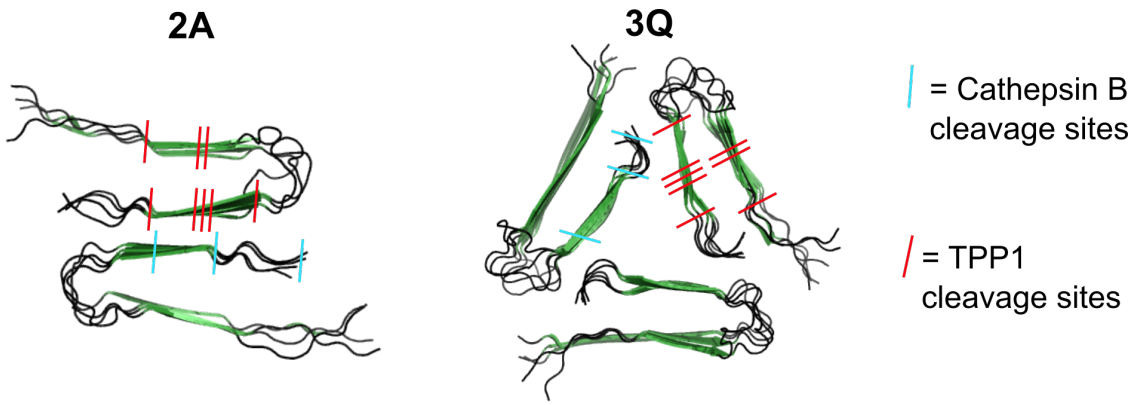

Figure 5.17. Cleavage sites of two lysosomal proteases mapped onto 2A and 3Q $A\beta_{40}$ fibril structures
The cleavage sites of Cathepsin B and TPP-1, two lysosomal enzymes known to cleave Aβ fibrils, mapped onto 2A and 3Q $A\beta_{40}$ fibril structures.

An alternative explanation for the differences in the susceptibility of the fibrils to degradation in lysosomes and by lysosomal proteases could be the stability of the fibrils at acidic pH. It has been previously demonstrated using β_2m as a model system, that the stability of amyloid fibrils can be altered by changed in pH, with acidification resulting in the disassembly of fibrils and increased release of oligomeric species (Tipping et al., 2015a). However, whilst the effect of pH on the stability of the Aβ fibrils studied herein has not been explored, differences in the stability of 2A and 3Q fibrils at pH 7.4 have been reported. It was found that 2A fibrils are more stable compared to 3Q fibrils at 24 °C, however no differences were identified at 37 °C, the temperature that was used in the current work (Qiang et al., 2013). Nonetheless, this does suggest that it would be worthwhile exploring whether at pH 4.5 and pH 7.4, when compared to 2A, that 3Q fibrils

more readily depolymerise into non-fibrillar species that have enhanced sensitivity to proteolysis.

In summary, results in this chapter have demonstrated that Aβ fibril preparations differ in the extent to which they associate with cell membranes of BV-2 microglial cells, which may have a number of functional consequences. In addition, it was shown that BV-2 microglial cells are able to internalise these Aβ fibrils, but that there are differences in the extent of fibril degradation of the fibril preparations by microglia and lysosomal proteases. This suggests that fibril polymorphism will result in differences in the ability of microglia to clear Aβ fibrils in AD. Future studies should therefore explore whether *ex vivo* fibrils from AD also exhibit differences in their uptake and breakdown by microglia and lysosomal proteases.

6 Concluding remarks and future perspectives

Structural studies of amyloid fibrils have revealed the phenomenon of fibril polymorphism, in which peptides within fibrils can have distinct molecular structures (Gallardo et al., 2020). This has been shown to be a feature of Aβ fibrils, which form the cores of plaques in AD brains. *In vitro*, these differences in fibril structure can result from differences in growth conditions and co-factors, whilst *in vivo* differences in fibril structure have been associated with differences in the clinical presentation of disease (Lu et al., 2013; Qiang et al., 2013). This thesis provides evidence that fibril polymorphism will affect the biological properties of Aβ fibrils in relation to the response of microglia.

Differences in biological properties were demonstrated in this work between Aβ fibrils formed from peptides with different sequences, but also importantly between fibrils formed from the same peptide sequence. For example, $A\beta_{40}$ E22Δ fibrils were shown to be toxic towards microglial and macrophage cells, whereas wild-type $A\beta_{40}$ fibrils were shown not to affect cell viability. This could be a reflection of the distinctive fibril structure that is formed from peptide harbouring this mutation (Schütz et al., 2015). Furthermore, fibrils formed at pH 8 from $A\beta_{42}$ monomer were shown to be toxic towards microglial, macrophage and monocytic cells, whereas those formed from the same $A\beta_{42}$ peptide at pH 2 had no effects on the viability of these cells. Further differences between these two $A\beta_{42}$ fibril preparations were identified in this work, with the pH 8 fibrils also found to elicit a greater release of pro-inflammatory cytokines from microglial and monocytic cells than pH 2 fibrils. In addition, it was found that the pH 8 fibrils showed a higher level of association with BV-2 microglial cells than the pH 2 fibrils. This implicates differences in the structures of the fibrils formed under these different conditions in the effects that they have on microglial and monocytic cells.

Based on these observations, a model for the cellular responses to the two $A\beta_{42}$ fibril preparations can be produced (Figure 6.1). An increased initial level of cell association of the pH 8 $A\beta_{42}$ fibrils is likely to be key in this model in explaining the increased toxicity and inflammatory response elicited by these fibrils. Increased interaction with cell surfaces could be indicative of increased receptor binding, which may lead to amplified receptor activation and cell signalling that results in the triggering of an immune response and the release of inflammatory mediators. These enhanced interactions with cell surfaces could also help to explain the toxicity of the pH 8 $A\beta_{42}$ fibrils, with previous studies of amyloid fibrils reporting disruption to cell membranes as a mechanism of fibril toxicity (Martins et al., 2008; Pieri et al., 2012; Bousset et al., 2013; Goodchild et al., 2014). Future experiments could be performed in order to further explore the mechanisms of toxicity and activation of an inflammatory response by the fibrils.

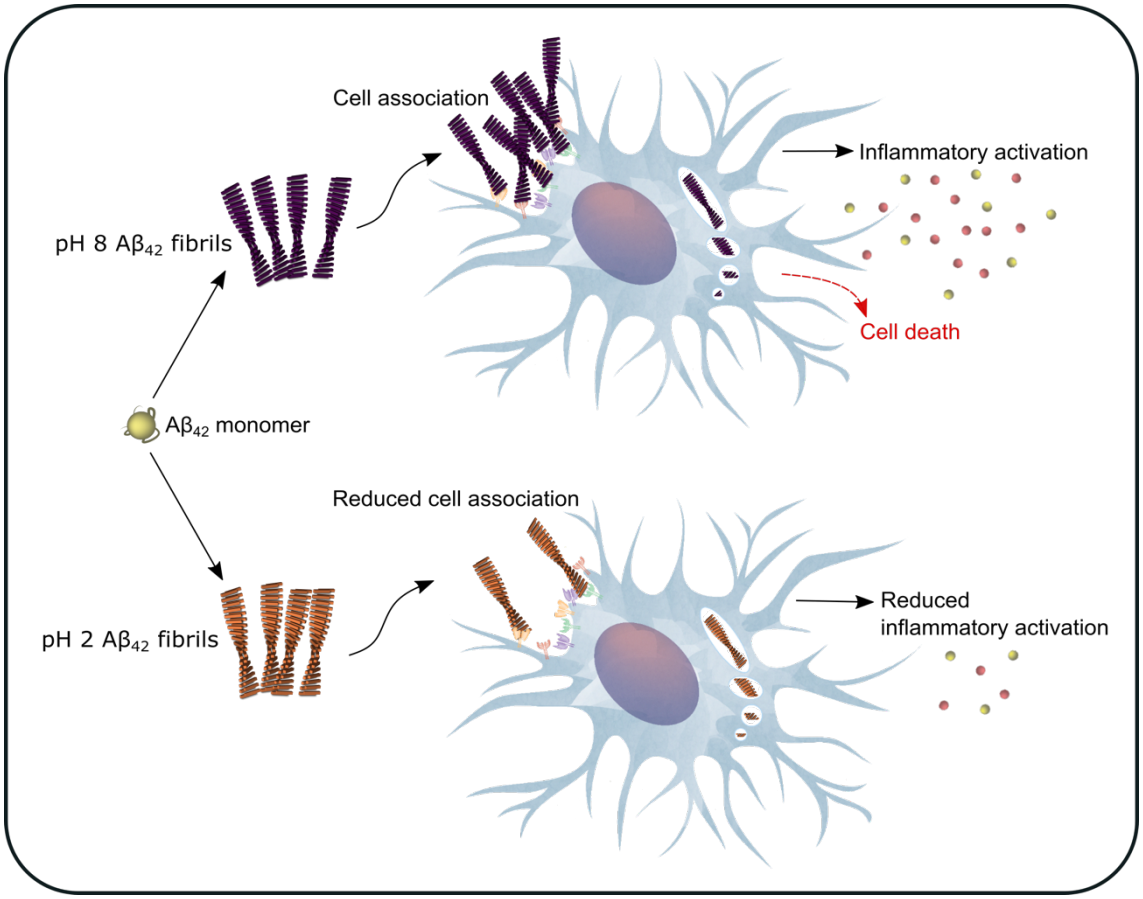

Figure 6.1. Model of differences identified between Aβ$_{42}$ fibril preparations
In this work, two populations of amyloid fibrils were formed from the same starting Aβ$_{42}$ peptide using different fibrillation conditions based on previous structural studies, one formed at pH 8 and the other formed at pH 2. The fibrils formed at pH 8 were shown to associate more with microglial cells than pH 2 fibrils during the same incubation. We hypothesise that this increased cell association results in the increased activation of cell surface receptors of these immune cells that are involved in triggering an inflammatory response. This would explain the increased release of pro-inflammatory mediators measured, TNF-α, IL-6 and IL-1β. Further to this, incubation with pH 8 Aβ$_{42}$ fibrils was shown to result in a decrease in cell viability, whereas incubation with the pH 2 fibrils did not have this effect. The mechanism of this toxicity requires further investigation but could also result from this difference in cell membrane interaction.

The Aβ$_{40}$ fibril preparations tested (2A, 3Q and *de novo*) were found to have a consistently reduced impact on microglial and monocytic cells compared to the Aβ$_{42}$ fibrils discussed, with minimal effects on cell viability and the release of pro-inflammatory cytokines. In addition to these differences between fibrils of different sequences, differences were also identified between the different Aβ$_{40}$ fibril preparations, in their degradation (Figure 6.2). It was determined that the BV-2 cells used in these experiments were capable and efficient at internalising all Aβ fibril preparations under the conditions tested. However, once internalised it was observed that 2A Aβ$_{40}$ fibrils remained inside the cells for a prolonged length of time compared to the other Aβ$_{40}$ fibril preparations. Experiments using isolated lysosomes also suggested that there could be differences in the rates of lysosomal digestion between the fibrils. Different arrangements of peptides

within a fibril could dictate the accessibility of cleavage sites to proteases, making some fibril structures more resistant to enzymatic degradation than others.

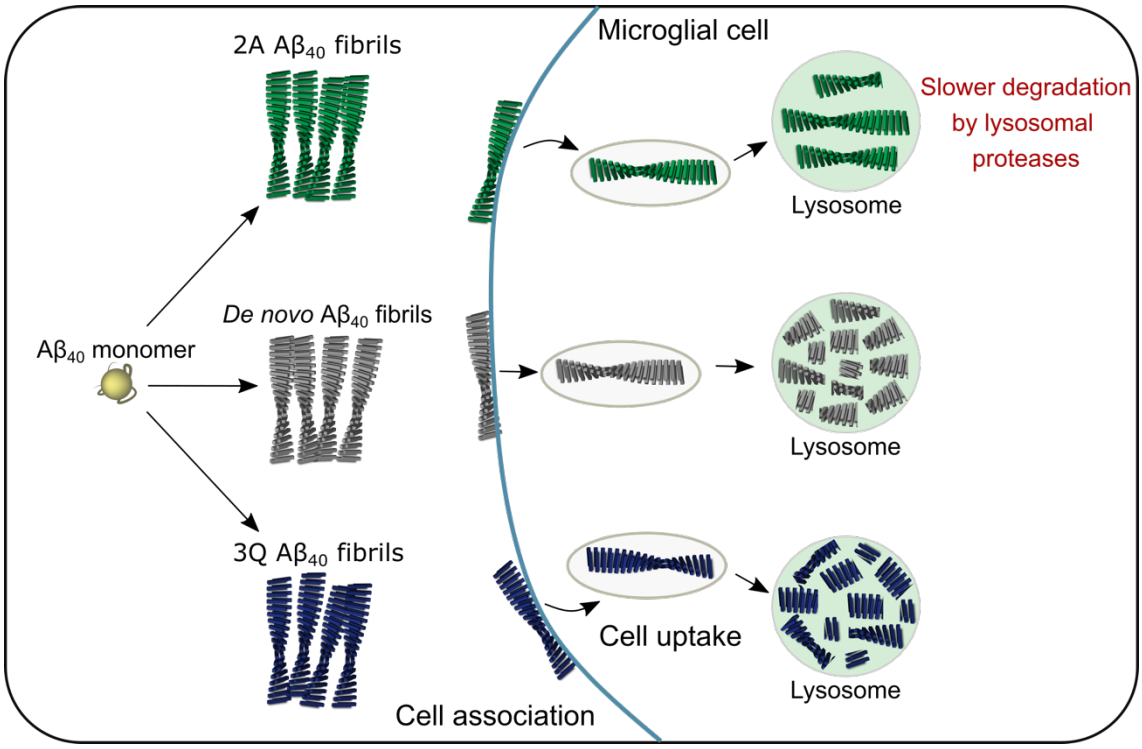

Figure 6.2. Model of differences identified between Aβ40 fibril preparations
Seeding reactions were performed using 2A and 3Q fibril seeds and Aβ40 monomer to produce populations of 2A and 3Q fibrils with previously described structures. Aβ40 was also incubated alone at 37 °C with shaking to produce a population of 'de novo' Aβ40 fibrils for comparison. Differences between these fibril preparations were not identified in terms of their toxicity or ability to trigger release of inflammatory cytokines. All three Aβ40 fibril preparations were found to interact with BV-2 cells and were internalised by these cells where they were shown to colocalise with lysosomes. However, evidence suggests that once internalised, the 2A fibrils are degraded to a lesser extent than the 3Q and de novo Aβ40 fibril preparations, suggesting a higher resistance to digestion by lysosomal proteases.

The properties of the six different Aβ fibril populations tested, identified from experiments performed in this thesis, are summarised in Table 6.1.

Fibril preparation	Toxicity	Cytokine release	Cell surface binding	Cellular uptake	Degradation
2A Aβ40	-	+	+	+	+
3Q Aβ40	-	+	+	+	++
De novo Aβ40	-	+	+	+	++
Aβ40 E22Δ	++	n/a	n/a	n/a	n/a
pH 2 Aβ42	-	++	+	+	++
pH 8 Aβ42	++	+++	++	+	++

Table 6.1. Summary of the effects of the Aβ fibril preparations tested in this thesis

One limitation of this work is that all experiments were carried out *in vitro*. Based on the results described here from cellular experiments identifying differences between Aβ fibril preparations, further insight into the effects of these different structures could also be gained by *in vivo* experiments using mouse models. Previous work has involved injecting Aβ material into the brains of AD model mice and assessing the propagation and pathology that results (Meyer-Luehmann et al., 2006). Carrying out similar studies using the defined populations of Aβ fibrils produced and tested in this work could provide more in-depth information on their toxicity, ability to trigger neuroinflammation and their clearance within a more complex multicellular environment.

In addition, these experiments were performed using *in vitro* formed Aβ fibrils. Whilst there is no evidence to suggest that these specific fibril structures exist within AD brains, fibril polymorphism has been identified *in vivo* and these results provide evidence for the biological differences that fibril polymorphs in the brain could possess (Lu et al., 2013; Rasmussen et al., 2017; Kollmer et al., 2019; Ghosh et al., 2021). The differences identified in this work *in vitro* would have significant implications within a brain environment. As the processes studied in this work are all interlinked, predicting consequences in a brain environment is complex. For example, decreases in the viability of immune cells resulting from certain fibril structures could also impact the ability of these cells to clear the Aβ, thus worsening pathology.

Foremost, the work in this thesis has shown differences in the toxicity of different Aβ fibril preparations. While this has been previously demonstrated for α-synuclein fibrils, the comparative toxicity of different Aβ fibril populations has not previously been studied in detail (Bousset et al., 2013). In addition to *in vitro* structures, different Aβ fibril structures have been identified *in vivo,* and the results from this thesis suggest that the presence of a certain fibril polymorph over another in the brain could have different consequences on the surrounding cells. This could mean that some fibrils are more detrimental and others more inert, possibly affecting the severity and clinical presentation of AD. This is supported by a study in which a different predominant Aβ fibril structure was identified in two AD patients with distinct clinical presentations (Lu et al., 2013). Furthermore, a higher level of Aβ fibril polymorphism was identified in patients with rapidly progressing AD compared to other subtypes, which could be indicative of the presence of a more toxic or detrimental fibril structure within these polymorphs (Lu et al., 2013; Qiang et al., 2017). This theory could help to explain why there is no clear correlation between Aβ load in the brain and clinical severity of disease, as different populations of Aβ fibrils can have differing effects within the brain environment. Consequences of the death of immune cells in the brain in response to toxic Aβ fibril structures could be the reduced clearance

of Aβ resulting in increased Aβ load, and also reduced clearance of degenerating neurons.

The toxicity of the fibrils observed in this work could be direct, or indirect by driving inflammation and the production of cytokines. Differences were identified in this research in the release of pro-inflammatory cytokines from monocytic and microglial cells in response to different Aβ fibril preparations. The cytokines that were measured (TNF-α, IL-6 and IL-1β) have been shown to be elevated in AD, contributing to the neuroinflammation observed and having neurotoxic effects (Ekdahl et al., 2003; Cumiskey et al., 2007; Harry et al., 2008; Mishra et al., 2012) (discussed in Section 1.4.4). Therefore, an increased release of these inflammatory mediators in response to a certain fibril polymorph over another in a brain environment would have more damaging effects on neurons, thus resulting in worsened neurodegeneration.

Finally, possible differences identified between the degradation of different fibril structures would have consequences *in vivo*, with fibril structures that are more resistant to degradation likely to become the dominant fibril structure in the brain. Structures that are not cleared as quickly as others by microglial cells in the brain are likely to accumulate, resulting in increased Aβ load. It was recently shown for more than twenty different amyloid fibril samples, including Aβ fibrils, that fibrils extracted from disease tissue are more proteolytically stable than those formed *in vitro* (Schönfelder et al., 2021). These findings support the 'proteolytic selection hypothesis', which suggests that amyloid fibrils that are found in disease were selected within the body due to their ability to escape mechanisms of endogenous proteolytic clearance (Bansal et al., 2021). These experiments were performed using proteinase K and pronase E rather than endogenous lysosomal enzymes, and differences in protease resistance was suggested to result from differences in fibril structure and the presence of cofactors in *ex vivo* fibrils (Schönfelder et al., 2021).

Clearly, more work is required to bridge the gap between *in vitro* Aβ structures and the consequences of fibril polymorphism *in vivo.* For this, the use of *ex vivo* Aβ fibrils could be paramount. A number of studies have now successfully extracted Aβ fibrils from the brain tissue of AD patients post-mortem, and structures of these fibrils resolved (Lu et al., 2013; Kollmer et al., 2019; Ghosh et al., 2021). The study of the biological effects of these fibrils *in vitro* such as those performed in this study could be very informative, especially when combined with clinical and structural information.

Critically, differences between Aβ fibrils *in vivo* could also have implications on diagnosis and treatment. If the structure of a more toxic or pathological Aβ fibril is identified, probing for these structures or structural features could be significant in the diagnosis and also

prognosis of disease, perhaps helping to identify the best treatment. ^{11}C-Pittsburgh compound B is a radioactive analog of the amyloid binding dye used in this work, ThT, and is used as a PET tracer to assess Aβ pathology and aid in AD diagnosis (Klunk et al., 2004). There is therefore potential for the development of further amyloid imaging agents with improved specificity for identified structural features of pathogenic amyloid fibrils, thus providing information not just on overall Aβ load but on the implications of the amyloid that is present.

In summary, this work has provided evidence for the functional consequences for Aβ fibril polymorphism. With Aβ and immune processes both heavily implicated in AD, the results presented herein suggest the interplay between fibril structure and the inflammatory response could be a key factor in neurodegeneration in AD.

References

Aguzzi, A., and Polymenidou, M. (2004). Mammalian Prion Biology: One Century of Evolving Concepts. *Cell* 116, 313–327. doi:10.1016/S0092-8674(03)01031-6.

Ajami, B., Bennett, J. L., Krieger, C., Tetzlaff, W., and Rossi, F. M. V. (2007). Local self-renewal can sustain CNS microglia maintenance and function throughout adult life. *Nat. Neurosci.* 10, 1538–1543. doi:10.1038/nn2014.

Albert, M. S., DeKosky, S. T., Dickson, D., Dubois, B., Feldman, H. H., Fox, N. C., et al. (2011). The diagnosis of mild cognitive impairment due to Alzheimer's disease: Recommendations from the National Institute on Aging-Alzheimer's Association workgroups on diagnostic guidelines for Alzheimer's disease. *Alzheimer's Dement.* 7, 270–279. doi:10.1016/j.jalz.2011.03.008.

Arosio, P., Knowles, T. P. J., and Linse, S. (2015). On the lag phase in amyloid fibril formation. *Phys. Chem. Chem. Phys.* 17, 7606. doi:10.1039/C4CP05563B.

ASC KO & KD THP-1 Cells | Inflammasome test monocytes | InvivoGen Available at: https://www.invivogen.com/thp1-ko-kd-asc#citations [Accessed August 16, 2021].

Bacterial Endotoxins/Pyrogens | FDA Available at: https://www.fda.gov/inspections-compliance-enforcement-and-criminal-investigations/inspection-technical-guides/bacterial-endotoxinspyrogens [Accessed September 2, 2021].

Bal-Price, A., and Brown, G. C. (2001). Inflammatory Neurodegeneration Mediated by Nitric Oxide from Activated Glia-Inhibiting Neuronal Respiration, Causing Glutamate Release and Excitotoxicity. *J. Neurosci.* 21, 6480–6491. doi:10.1523/JNEUROSCI.21-17-06480.2001.

Bamberger, M. E., Harris, M. E., McDonald, D. R., Husemann, J., and Landreth, G. E. (2003). A cell surface receptor complex for fibrillar β-amyloid mediates microglial activation. *J. Neurosci.* 23, 2665–2674. doi:10.1523/JNEUROSCI.23-07-02665.2003.

Bansal, A., Schmidt, M., Rennegarbe, M., Haupt, C., Liberta, F., Stecher, S., et al. (2021). AA amyloid fibrils from diseased tissue are structurally different from in vitro formed SAA fibrils. *Nat. Commun. 2021 121* 12, 1–9. doi:10.1038/s41467-021-21129-z.

Bauer, J., Strauss, S., Schreiter-Gasser, U., Ganter, U., Schlegel, P., Witt, I., et al. (1991). Interleukin-6 and α-2-macroglobulin indicate an acute-phase state in

Alzheimer's disease cortices. *FEBS Lett.* 285, 111–114. doi:10.1016/0014-5793(91)80737-N.

Bäuerlein, F. J. B., Saha, I., Mishra, A., Kalemanov, M., Martínez-Sánchez, A., Klein, R., et al. (2017). In Situ Architecture and Cellular Interactions of PolyQ Inclusions. *Cell* 171, 179-187.e10. doi:10.1016/J.CELL.2017.08.009.

Bauernfeind, F. G., Horvath, G., Stutz, A., Alnemri, E. S., MacDonald, K., Speert, D., et al. (2009). Cutting Edge: NF-κB Activating Pattern Recognition and Cytokine Receptors License NLRP3 Inflammasome Activation by Regulating NLRP3 Expression. *J. Immunol.* 183, 787–791. doi:10.4049/jimmunol.0901363.

Bedient, L., Pokharel, S. M., Chiok, K. R., Mohanty, I., Beach, S. S., Miura, T. A., et al. (2020). Lytic Cell Death Mechanisms in Human Respiratory Syncytial Virus-Infected Macrophages: Roles of Pyroptosis and Necroptosis. *Viruses 2020, Vol. 12, Page 932* 12, 932. doi:10.3390/V12090932.

Benitez, B. A., Jin, S. C., Guerreiro, R., Graham, R., Lord, J., Harold, D., et al. (2014). Missense variant in TREML2 protects against Alzheimer's disease. *Neurobiol. Aging* 35, 1510.e19-1510.e26. doi:10.1016/j.neurobiolaging.2013.12.010.

Bessen, R. A., Kocisko, D. A., Raymond, G. J., Nandan, S., Lansbury, P. T., and Caughey, B. (1995). Non-genetic propagation of strain-specific properties of scrapie prion protein. *Nat. 1995 3756533* 375, 698–700. doi:10.1038/375698a0.

Biancalana, M., and Koide, S. (2010). Molecular Mechanism of Thioflavin-T Binding to Amyloid Fibrils. *Biochim. Biophys. Acta* 1804, 1405. doi:10.1016/J.BBAPAP.2010.04.001.

Blasi, E., Barluzzi, R., Bocchini, V., Mazzolla, R., and Bistoni, F. (1990). Immortalization of murine microglial cells by a v-raf / v-myc carrying retrovirus. *J. Neuroimmunol.* 27, 229–237. doi:10.1016/0165-5728(90)90073-V.

Botos, I., Segal, D. M., and Davies, D. R. (2011). The structural biology of Toll-like receptors. *Structure* 19, 447–459. doi:10.1016/j.str.2011.02.004.

Bousset, L., Pieri, L., Ruiz-Arlandis, G., Gath, J., Jensen, P. H., Habenstein, B., et al. (2013). Structural and functional characterization of two alpha-synuclein strains. *Nat. Commun.* 4, 1–13. doi:10.1038/ncomms3575.

Braak, H., and Braak, E. (1991). Neuropathological stageing of Alzheimer-related changes. *Acta Neuropathol.* 82, 239–259. doi:10.1007/BF00308809.

Braak, H., Sastre, M., and Del Tredici, K. (2007). Development of α-synuclein immunoreactive astrocytes in the forebrain parallels stages of intraneuronal pathology in sporadic Parkinson's disease. *Acta Neuropathol.* 114, 231–241. doi:10.1007/s00401-007-0244-3.

Bradt, B. M., Kolb, W. P., and Cooper, N. R. (1998). Complement-dependent proinflammatory properties of the Alzheimer's disease β-peptide. *J. Exp. Med.* 188, 431–438. doi:10.1084/jem.188.3.431.

Brown, M. R., Radford, S. E., and Hewitt, E. W. (2020). Modulation of β-Amyloid Fibril Formation in Alzheimer's Disease by Microglia and Infection. *Front. Mol. Neurosci.* 0, 228. doi:10.3389/FNMOL.2020.609073.

Bunce, S. J., Wang, Y., Stewart, K. L., Ashcroft, A. E., Radford, S. E., Hall, C. K., et al. (2019). Molecular insights into the surface-catalyzed secondary nucleation of amyloid-β40 (Aβ40) by the peptide fragment Aβ16–22. *Sci. Adv.* 5, 8216. doi:10.1126/SCIADV.AAV8216.

Castellano, J. M., Kim, J., Stewart, F. R., Jiang, H., DeMattos, R. B., Patterson, B. W., et al. (2011). Human apoE isoforms differentially regulate brain amyloid-β peptide clearance. *Sci. Transl. Med.* 3. doi:10.1126/scitranslmed.3002156.

Cattaneo, A., Cattane, N., Galluzzi, S., Provasi, S., Lopizzo, N., Festari, C., et al. (2017). Association of brain amyloidosis with pro-inflammatory gut bacterial taxa and peripheral inflammation markers in cognitively impaired elderly. *Neurobiol. Aging* 49, 60–68. doi:10.1016/j.neurobiolaging.2016.08.019.

Chakrabarty, P., Li, A., Ladd, T. B., Strickland, M. R., Koller, E. J., Burgess, J. D., et al. (2018). TLR5 decoy receptor as a novel anti-amyloid therapeutic for Alzheimer's disease. *J. Exp. Med.* 215, 2247–2264. doi:10.1084/jem.20180484.

Charidimou, A., Boulouis, G., Gurol, M. E., Ayata, C., Bacskai, B. J., Frosch, M. P., et al. (2017). Emerging concepts in sporadic cerebral amyloid angiopathy. *Brain* 140, 1829–1850. doi:10.1093/brain/awx047.

Chen, G., Xu, T., Yan, Y., Zhou, Y., Jiang, Y., Melcher, K., et al. (2017). Amyloid beta: structure, biology and structure-based therapeutic development. *Acta Pharmacol. Sin.* 38, 1205–1235. doi:10.1038/APS.2017.28.

Chételat, G., La Joie, R., Villain, N., Perrotin, A., De La Sayette, V., Eustache, F., et al. (2013). Amyloid imaging in cognitively normal individuals, at-risk populations and preclinical Alzheimer's disease. *NeuroImage Clin.* 2, 356–365.

doi:10.1016/j.nicl.2013.02.006.

Chih Jin, S., Benitez, B. A., Karch, C. M., Cooper, B., Skorupa, T., Carrell, D., et al. (2014). Coding variants in TREM2 increase risk for Alzheimer's disease. doi:10.1093/hmg/ddu277.

Christie, R. H., Freeman, M., and Hyman, B. T. (1996). Expression of the macrophage scavenger receptor, a multifunctional lipoprotein receptor, in microglia associated with senile plaques in Alzheimer's disease. *Am. J. Pathol.* 148, 399–403. Available at: /pmc/articles/PMC1861668/?report=abstract [Accessed September 9, 2020].

Codolo, G., Plotegher, N., Pozzobon, T., Brucale, M., Tessari, I., Bubacco, L., et al. (2013). Triggering of Inflammasome by Aggregated α–Synuclein, an Inflammatory Response in Synucleinopathies. *PLoS One* 8, e55375. doi:10.1371/journal.pone.0055375.

Cohen, S. I. A., Arosio, P., Presto, J., Kurudenkandy, F. R., Biverstål, H., Dolfe, L., et al. (2015). A molecular chaperone breaks the catalytic cycle that generates toxic Aβ oligomers. *Nat. Struct. Mol. Biol.* 22, 207–213. doi:10.1038/NSMB.2971.

Colvin, M. T., Silvers, R., Frohm, B., Su, Y., Linse, S., and Griffin, R. G. (2015). High Resolution Structural Characterization of Aβ42 Amyloid Fibrils by Magic Angle Spinning NMR. *J. Am. Chem. Soc.* 137, 7509–7518. doi:10.1021/jacs.5b03997.

Colvin, M. T., Silvers, R., Ni, Q. Z., Can, T. V., Sergeyev, I., Rosay, M., et al. (2016). Atomic Resolution Structure of Monomorphic Aβ42 Amyloid Fibrils. *J. Am. Chem. Soc.* 138, 9663–9674. doi:10.1021/jacs.6b05129.

Coraci, I. S., Husemann, J., Berman, J. W., Hulette, C., Dufour, J. H., Campanella, G. K., et al. (2002). CD36, a class B scavenger receptor, is expressed on microglia in Alzheimer's disease brains and can mediate production of reactive oxygen species in response to β-amyloid fibrils. *Am. J. Pathol.* 160, 101–112. doi:10.1016/S0002-9440(10)64354-4.

Corder, E. H., Saunders, A. M., Strittmatter, W. J., Schmechel, D. E., Gaskell, P. C., Small, G. W., et al. (1993). Gene dose of apolipoprotein E type 4 allele and the risk of Alzheimer's disease in late onset families. *Science (80-.).* 261, 921–923. doi:10.1126/science.8346443.

Cumiskey, D., Curran, B. P., Herron, C. E., and O'Connor, J. J. (2007). A role for inflammatory mediators in the IL-18 mediated attenuation of LTP in the rat dentate gyrus. *Neuropharmacology* 52, 1616–1623.

doi:10.1016/j.neuropharm.2007.03.006.

Cummings, J. L. (2000). Cognitive and behavioral heterogeneity in Alzheimer's disease: seeking the neurobiological basis. *Neurobiol. Aging* 21, 845–861. doi:10.1016/S0197-4580(00)00183-4.

Czirr, E., Castello, N. A., Mosher, K. I., Castellano, J. M., Hinkson, I. V., Lucin, K. M., et al. (2017). Microglial complement receptor 3 regulates brain Aβ levels through secreted proteolytic activity. *J. Exp. Med.* 214, 1081–1092. doi:10.1084/jem.20162011.

Davalos, D., Grutzendler, J., Yang, G., Kim, J. V., Zuo, Y., Jung, S., et al. (2005). ATP mediates rapid microglial response to local brain injury in vivo. *Nat. Neurosci.* 8, 752–758. doi:10.1038/nn1472.

Davidson, H. W., West, M. A., and Watts, C. (1990). Endocytosis, intracellular trafficking, and processing of membrane IgG and monovalent antigen/membrane IgG complexes in B lymphocytes. *J. Immunol.* 144, 4101–9. Available at: http://www.ncbi.nlm.nih.gov/pubmed/2187925 [Accessed July 23, 2021].

de Rojas, I., Moreno-Grau, S., Tesi, N., Grenier-Boley, B., Andrade, V., Jansen, I., et al. (2020). Common variants in Alzheimer's disease: Novel association of six genetic variants with AD and risk stratification by polygenic risk scores. *medRxiv*, 19012021. doi:10.1101/19012021.

Dear, A., Georg Meisl, Anđela Šarić, Michaels, T. C. T., Magnus Kjaergaard, Sara Linse, et al. (2020). Identification of on- and off-pathway oligomers in amyloid fibril formation. *Chem. Sci.* 11, 6236–6247. doi:10.1039/C9SC06501F.

Deaths registered in England and Wales - Office for National Statistics Available at: https://www.ons.gov.uk/peoplepopulationandcommunity/birthsdeathsandmarriages/deaths/datasets/deathsregisteredinenglandandwalesseriesdrreferencetables [Accessed April 21, 2020].

Deb, S., Zhang, J. W., and Gottschall, P. E. (2003). β-amyloid induces the production of active, matrix-degrading proteases in cultured rat astrocytes. *Brain Res.* 970, 205–213. doi:10.1016/S0006-8993(03)02344-8.

Deczkowska, A., Keren-Shaul, H., Weiner, A., Colonna, M., Schwartz, M., and Amit, I. (2018). Disease-Associated Microglia: A Universal Immune Sensor of Neurodegeneration. *Cell* 173, 1073–1081. doi:10.1016/j.cell.2018.05.003.

Deczkowska, A., Weiner, A., and Amit, I. (2020). The Physiology, Pathology, and Potential Therapeutic Applications of the TREM2 Signaling Pathway. *Cell* 181, 1207–1217. doi:10.1016/J.CELL.2020.05.003.

Dominy, S. S., Lynch, C., Ermini, F., Benedyk, M., Marczyk, A., Konradi, A., et al. (2019). Porphyromonas gingivalis in Alzheimer's disease brains: Evidence for disease causation and treatment with small-molecule inhibitors. *Sci. Adv.* 5, eaau3333. doi:10.1126/sciadv.aau3333.

Doody, R. S., Stevens, J. C., Beck, C., Dubinsky, R. M., Kaye, J. A., Gwyther, L., et al. (2001). Practice parameter: Management of dementia (an evidence-based review). *Neurology* 56, 1154–1166. doi:10.1212/WNL.56.9.1154.

Drost, N., Houtman, J., Cseresnyés, Z., Niesner, R., Rinnenthal, J.-L., Miller, K. R., et al. (2020). The Amyloid-beta rich CNS environment alters myeloid cell functionality independent of their origin. *Sci. Rep.* 10, 7152. doi:10.1038/s41598-020-63989-3.

Duce, Tsatsanis, A., Cater, M., James, S., Robb, E., Wikhe, K., et al. (2010). Iron-export ferroxidase activity of β-amyloid precursor protein is inhibited by zinc in Alzheimer's disease. *Cell* 142, 857–867. doi:10.1016/J.CELL.2010.08.014.

Eanes, E. D., and Glenner, G. G. (1968). X-ray diffraction studies on amyloid filaments. *J. Histochem. Cytochem.* 16, 673–677. doi:10.1177/16.11.673.

Ekdahl, C. T., Claasen, J. H., Bonde, S., Kokaia, Z., and Lindvall, O. (2003). Inflammation is detrimental for neurogenesis in adult brain. *Proc. Natl. Acad. Sci. U. S. A.* 100, 13632–13637. doi:10.1073/pnas.2234031100.

El Khoury, J. B., Moore, K. J., Means, T. K., Leung, J., Terada, K., Toft, M., et al. (2003). CD36 mediates the innate host response to β-amyloid. *J. Exp. Med.* 197, 1657–1666. doi:10.1084/jem.20021546.

Epstein, E. A., and Chapman, M. R. (2008). Polymerizing the fibre between bacteria and host cells: The biogenesis of functional amyloid fibres. *Cell. Microbiol.* 10, 1413–1420. doi:10.1111/j.1462-5822.2008.01148.x.

Esparza, T. J., Zhao, H., Cirrito, J. R., Cairns, N. J., Bateman, R. J., Holtzman, D. M., et al. (2013). Amyloid-beta Oligomerization in Alzheimer Dementia vs. High Pathology Controls. *Ann. Neurol.* 73, 104. doi:10.1002/ANA.23748.

Falcon, B., Zhang, W., Murzin, A. G., Murshudov, G., Garringer, H. J., Vidal, R., et al. (2018a). Structures of filaments from Pick's disease reveal a novel tau protein fold.

Nature 561, 137–140. doi:10.1038/s41586-018-0454-y.

Falcon, B., Zhang, W., Schweighauser, M., Murzin, A. G., Vidal, R., Garringer, H. J., et al. (2018b). Tau filaments from multiple cases of sporadic and inherited Alzheimer's disease adopt a common fold. *Acta Neuropathol.* 136, 699–708. doi:10.1007/s00401-018-1914-z.

Falcon, B., Zivanov, J., Zhang, W., Murzin, A. G., Garringer, H. J., Vidal, R., et al. (2019). Novel tau filament fold in chronic traumatic encephalopathy encloses hydrophobic molecules. *Nature* 568, 420–423. doi:10.1038/s41586-019-1026-5.

Farris, W., Mansourian, S., Chang, Y., Lindsley, L., Eckman, E. A., Frosch, M. P., et al. (2003). Insulin-degrading enzyme regulates the levels of insulin, amyloid β-protein, and the β-amyloid precursor protein intracellular domain in vivo. *Proc. Natl. Acad. Sci. U. S. A.* 100, 4162–4167. doi:10.1073/pnas.0230450100.

Fassbender, K., Walter, S., Kühl, S., Landmann, R., Ishii, K., Bertsch, T., et al. (2004). The LPS receptor (CD14) links innate immunity with Alzheimer's disease. *FASEB J.* 18, 203–205. doi:10.1096/fj.03-0364fje.

Fitzpatrick, A. W. P., Falcon, B., He, S., Murzin, A. G., Murshudov, G., Garringer, H. J., et al. (2017). Cryo-EM structures of tau filaments from Alzheimer's disease. *Nature* 547, 185–190. doi:10.1038/nature23002.

Franchi, L., Eigenbrod, T., and Núñez, G. (2009). Cutting Edge: TNF-α Mediates Sensitization to ATP and Silica via the NLRP3 Inflammasome in the Absence of Microbial Stimulation. *J. Immunol.* 183, 792–796. doi:10.4049/jimmunol.0900173.

Franklin, B. S., Bossaller, L., De Nardo, D., Ratter, J. M., Stutz, A., Engels, G., et al. (2014). The adaptor ASC has extracellular and "prionoid" activities that propagate inflammation. *Nat. Immunol.* 15, 727–737. doi:10.1038/ni.2913.

Frautschy, S. A., Yang, F., Irrizarry, M., Hyman, B., Saido, T. C., Hsiao, K., et al. (1998). Microglial response to amyloid plaques in APPsw transgenic mice. *Am. J. Pathol.* 152, 307–317.

Frigerio, C. S., Wolfs, L., Fattorelli, N., Perry, V. H., Fiers, M., and De Strooper, B. (2019). The Major Risk Factors for Alzheimer's Disease: Age, Sex, and Genes Modulate the Microglia Response to Aβ Plaques. *Cell Rep.* 27, 1293–1306. doi:10.1016/j.celrep.2019.03.099.

Friker, L. L., Scheiblich, H., Hochheiser, I. V, Brinkschulte, R., Riedel, D., Latz, E., et al.

(2020). β-Amyloid Clustering around ASC Fibrils Boosts Its Toxicity in Microglia. *Cell Rep.* 30, 3743-3754.e6. doi:10.1016/j.celrep.2020.02.025.

Gallardo, R., Ranson, N. A., and Radford, S. E. (2020). Amyloid structures: much more than just a cross-β fold. *Curr. Opin. Struct. Biol.* 60, 7–16. doi:10.1016/J.SBI.2019.09.001.

Gate, D., Saligrama, N., Leventhal, O., Yang, A. C., Unger, M. S., Middeldorp, J., et al. (2020). Clonally expanded CD8 T cells patrol the cerebrospinal fluid in Alzheimer's disease. *Nat. 2020 5777790* 577, 399–404. doi:10.1038/s41586-019-1895-7.

Gath, J., Bousset, L., Habenstein, B., Melki, R., Meier, B. H., and Böckmann, A. (2014). Yet another polymorph of α-synuclein: solid-state sequential assignments. *Biomol. NMR Assign.* 8, 395–404. doi:10.1007/s12104-013-9526-y.

Gatz, M., Reynolds, C. A., Fratiglioni, L., Johansson, B., Mortimer, J. A., Berg, S., et al. (2006). Role of genes and environments for explaining Alzheimer disease. *Arch. Gen. Psychiatry* 63, 168–174. doi:10.1001/archpsyc.63.2.168.

Gericke, C., Mallone, A., Engelhardt, B., Nitsch, R. M., and Ferretti, M. T. (2020). Oligomeric Forms of Human Amyloid-Beta(1–42) Inhibit Antigen Presentation. *Front. Immunol.* 11. doi:10.3389/fimmu.2020.01029.

Ghosh, U., Thurber, K. R., Yau, W.-M., and Tycko, R. (2021). Molecular structure of a prevalent amyloid-β fibril polymorph from Alzheimer's disease brain tissue. *Proc. Natl. Acad. Sci.* 118. doi:10.1073/PNAS.2023089118.

Ginhoux, F., Greter, M., Leboeuf, M., Nandi, S., See, P., Gokhan, S., et al. (2010). Fate mapping analysis reveals that adult microglia derive from primitive macrophages. *Science (80-.).* 330, 841–845. doi:10.1126/science.1194637.

Goedert, M., Jakes, R., and Spillantini, M. G. (2017). The Synucleinopathies: Twenty Years On. *J. Parkinsons. Dis.* 7, S51. doi:10.3233/JPD-179005.

Gomez-Nicola, D., and Boche, D. (2015). Post-mortem analysis of neuroinflammatory changes in human Alzheimer's disease. *Alzheimers. Res. Ther.* 7. doi:10.1186/S13195-015-0126-1.

Goodchild, S. C., Sheynis, T., Thompson, R., Tipping, K. W., Xue, W.-F., Ranson, N. A., et al. (2014). β2-Microglobulin Amyloid Fibril-Induced Membrane Disruption Is Enhanced by Endosomal Lipids and Acidic pH. *PLoS One* 9, e104492. doi:10.1371/JOURNAL.PONE.0104492.

Gordon, B. A., Blazey, T. M., Su, Y., Hari-Raj, A., Dincer, A., Flores, S., et al. (2018). Spatial patterns of neuroimaging biomarker change in individuals from families with autosomal dominant Alzheimer's disease: a longitudinal study. *Lancet Neurol.* 17, 241–250. doi:10.1016/S1474-4422(18)30028-0.

Götz, J., Chen, F., Van Dorpe, J., and Nitsch, R. M. (2001). Formation of neurofibrillary tangles in P301L tau transgenic mice induced by Aβ42 fibrils. *Science (80-.).* 293, 1491–1495. doi:10.1126/science.1062097.

Grabowski, T. J., Cho, H. S., Vonsattel, J. P. G., Rebeck, G. W., and Greenberg, S. M. (2001). Novel amyloid precursor protein mutation in an Iowa family with dementia and severe cerebral amyloid angiopathy. *Ann. Neurol.* 49, 697–705. doi:10.1002/ANA.1009.

Gremer, L., Schölzel, D., Schenk, C., Reinartz, E., Labahn, J., Ravelli, R. B. G., et al. (2017). Fibril structure of amyloid-beta(1-42) by cryo – electron microscopy. *Science (80-.).* 358, 116–119. doi:10.1042/BJ20081572.

Griciuc, A., Patel, S., Federico, A. N., Choi, S. H., Innes, B. J., Oram, M. K., et al. (2019). TREM2 Acts Downstream of CD33 in Modulating Microglial Pathology in Alzheimer's Disease. *Neuron* 103, 820-835.e7. doi:10.1016/j.neuron.2019.06.010.

Griffin, W. S. T., Stanley, L. C., Ling, C., White, L., MacLeod, V., Perrot, L. J., et al. (1989). Brain interleukin 1 and S-100 immunoreactivity are elevated in Down syndrome and Alzheimer disease. *Proc. Natl. Acad. Sci. U. S. A.* 86, 7611–7615. doi:10.1073/pnas.86.19.7611.

Grozdanov, V., Bousset, L., Hoffmeister, M., Bliederhaeuser, C., Meier, C., Madiona, K., et al. (2019). Increased Immune Activation by Pathologic α-Synuclein in Parkinson's Disease. *Ann. Neurol.* 86, 593–606. doi:10.1002/ana.25557.

Guerrero-Ferreira, R., Taylor, N. M. I., Arteni, A. A., Kumari, P., Mona, D., Ringler, P., et al. (2019). Two new polymorphic structures of human full-length alpha-synuclein fibrils solved by cryo-electron microscopy. *Elife* 8. doi:10.7554/eLife.48907.

Guerrero-Ferreira, R., Taylor, N. M. I., Mona, D., Ringler, P., Lauer, M. E., Riek, R., et al. (2018). Cryo-EM structure of alpha-synuclein fibrils. *Elife* 7. doi:10.7554/eLife.36402.

Gustot, A., Gallea, J. I., Sarroukh, R., Celej, M. S., Ruysschaert, J. M., and Raussens, V. (2015). Amyloid fibrils are the molecular trigger of inflammation in Parkinson's disease. *Biochem. J.* 471, 323–333. doi:10.1042/BJ20150617.

Guzova, J. A., Primiano, M. J., Jiao, A., Stock, J., Lee, C., Winkler, A. R., et al. (2019). Optimized protocols for studying the NLRP3 inflammasome and assessment of potential targets of CP-453,773 in undifferentiated THP1 cells. *J. Immunol. Methods* 467, 19–28. doi:10.1016/J.JIM.2019.02.002.

Haeberlein, S. B., Hehn, C. von, Tian, Y., Chalkias, S., Muralidharan, K. K., Chen, T., et al. (2020). Emerge and Engage topline results: Phase 3 studies of aducanumab in early Alzheimer's disease. *Alzheimer's Dement.* 16, e047259. doi:10.1002/ALZ.047259.

Halle, A., Hornung, V., Petzold, G. C., Stewart, C. R., Monks, B. G., Reinheckel, T., et al. (2008). The NALP3 inflammasome is involved in the innate immune response to amyloid-β. *Nat. Immunol.* 9, 857–865. doi:10.1038/ni.1636.

Hamilton, R. (2000). Lewy bodies in Alzheimer's disease: a neuropathological review of 145 cases using alpha-synuclein immunohistochemistry. *Brain Pathol.* 10, 378–384. doi:10.1111/J.1750-3639.2000.TB00269.X.

Han, S., Kollmer, M., Markx, D., Claus, S., Walther, P., and Fändrich, M. (2017). Amyloid plaque structure and cell surface interactions of β-amyloid fibrils revealed by electron tomography. *Sci. Reports 2017 71* 7, 1–8. doi:10.1038/srep43577.

Hanseeuw, B. J., Betensky, R. A., Jacobs, H. I. L., Schultz, A. P., Sepulcre, J., Becker, J. A., et al. (2019). Association of Amyloid and Tau with Cognition in Preclinical Alzheimer Disease: A Longitudinal Study. *JAMA Neurol.* 76, 915–924. doi:10.1001/jamaneurol.2019.1424.

Hansson, O., Seibyl, J., Stomrud, E., Zetterberg, H., Trojanowski, J. Q., Bittner, T., et al. (2018). CSF biomarkers of Alzheimer's disease concord with amyloid-β PET and predict clinical progression: A study of fully automated immunoassays in BioFINDER and ADNI cohorts. *Alzheimer's Dement.* 14, 1470–1481. doi:10.1016/j.jalz.2018.01.010.

Hansson, O., Zetterberg, H., Buchhave, P., Andreasson, U., Londos, E., Minthon, L., et al. (2007). Prediction of Alzheimer's disease using the CSF Aβ42/Aβ40 ratio in patients with mild cognitive impairment. *Dement. Geriatr. Cogn. Disord.* 23, 316–320. doi:10.1159/000100926.

Hardy, J. A., and Selkoe, D. J. (2002). The amyloid hypothesis of Alzheimer's disease: progress and problems on the road to therapeutics. *Science* 297, 353–356. doi:10.1126/SCIENCE.1072994.

Harms, A. S., Delic, V., Thome, A. D., Bryant, N., Liu, Z., Chandra, S., et al. (2017). α-Synuclein fibrils recruit peripheral immune cells in the rat brain prior to neurodegeneration. *Acta Neuropathol. Commun.* 5, 85. doi:10.1186/s40478-017-0494-9.

Harold, D., Abraham, R., Hollingworth, P., Sims, R., Gerrish, A., Hamshere, M. L., et al. (2009). Genome-wide association study identifies variants at CLU and PICALM associated with Alzheimer's disease. *Nat. Genet.* 41, 1088–1093. doi:10.1038/ng.440.

Harry, G. J., d'Hellencourt, C. L., McPherson, C. A., Funk, J. A., Aoyama, M., and Wine, R. N. (2008). Tumor necrosis factor p55 and p75 receptors are involved in chemical-induced apoptosis of dentate granule neurons. *J. Neurochem.* 106, 281–298. doi:10.1111/J.1471-4159.2008.05382.X.

Hartley, D. M., Walsh, D. M., Ye, C. P., Diehl, T., Vasquez, S., Vassilev, P. M., et al. (1999). Protofibrillar Intermediates of Amyloid β-Protein Induce Acute Electrophysiological Changes and Progressive Neurotoxicity in Cortical Neurons. *J. Neurosci.* 19, 8876–8884. doi:10.1523/JNEUROSCI.19-20-08876.1999.

Heise, H., Hoyer, W., Becker, S., Andronesi, O. C., Riedel, D., and Baldus, M. (2005). Molecular-level secondary structure, polymorphism, and dynamics of full-length α-synuclein fibrils studied by solid-state NMR. *Proc. Natl. Acad. Sci. U. S. A.* 102, 15871–15876. doi:10.1073/pnas.0506109102.

Heneka, M. T. (2017). Inflammasome activation and innate immunity in Alzheimer's disease. *Brain Pathol.* 27, 220–222. doi:10.1111/bpa.12483.

Heneka, M. T., Carson, M. J., Khoury, J. El, Landreth, G. E., Brosseron, F., Feinstein, D. L., et al. (2015a). Neuroinflammation in Alzheimer's disease. *Lancet Neurol.* 14, 388–405. doi:10.1016/S1474-4422(15)70016-5.

Heneka, M. T., Golenbock, D. T., and Latz, E. (2015b). Innate immunity in Alzheimer's disease. *Nat. Immunol.* 16, 229–236. doi:10.1038/ni.3102.

Heneka, M. T., Kummer, M. P., Stutz, A., Delekate, A., Schwartz, S., Vieira-Saecker, A., et al. (2013). NLRP3 is activated in Alzheimer's disease and contributes to pathology in APP/PS1 mice. *Nature* 493, 674–678. doi:10.1038/nature11729.

Herrup, K. (2015). The case for rejecting the amyloid cascade hypothesis. *Nat. Neurosci.* 18, 794–799. doi:10.1038/nn.4017.

Hickman, S. E., Allison, E. K., and El Khoury, J. (2008). Microglial dysfunction and defective β-amyloid clearance pathways in aging alzheimer's disease mice. *J. Neurosci.* 28, 8354–8360. doi:10.1523/JNEUROSCI.0616-08.2008.

Hollingworth, P., Harold, D., Sims, R., Gerrish, A., Lambert, J. C., Carrasquillo, M. M., et al. (2011). Common variants at ABCA7, MS4A6A/MS4A4E, EPHA1, CD33 and CD2AP are associated with Alzheimer's disease. *Nat. Genet.* 43, 429–436. doi:10.1038/ng.803.

Honig, L. S., Vellas, B., Woodward, M., Boada, M., Bullock, R., Borrie, M., et al. (2018). Trial of Solanezumab for Mild Dementia Due to Alzheimer's Disease. *N. Engl. J. Med.* 378, 321–330. doi:10.1056/nejmoa1705971.

Hopperton, K. E., Mohammad, D., Trépanier, M. O., Giuliano, V., and Bazinet, R. P. (2017). Markers of microglia in post-mortem brain samples from patients with Alzheimer's disease: a systematic review. *Mol. Psychiatry 2018 232* 23, 177–198. doi:10.1038/mp.2017.246.

Hu, Y.-B., Dammer, E. B., Ren, R.-J., and Wang, G. (2015). The endosomal-lysosomal system: from acidification and cargo sorting to neurodegeneration. *Transl. Neurodegener. 2015 41* 4, 1–10. doi:10.1186/S40035-015-0041-1.

Hu, Z.-W., Vugmeyster, L., Au, D. F., Ostrovsky, D., Sun, Y., and Qiang, W. (2019). Molecular structure of an N-terminal phosphorylated β-amyloid fibril. *Proc. Natl. Acad. Sci.* 116, 11253–11258. doi:10.1073/PNAS.1818530116.

Hu, Z. W., Ma, M. R., Chen, Y. X., Zhao, Y. F., Qiang, W., and Li, Y. M. (2017). Phosphorylation at ser8 as an intrinsic regulatory switch to regulate the morphologies and structures of alzheimer's 40-residue β-Amyloid (Aβ40) fibrils. *J. Biol. Chem.* 292, 2611–2623. doi:10.1074/jbc.M116.757179.

Huang, L.-K., Chao, S.-P., and Hu, C.-J. (2020). Clinical trials of new drugs for Alzheimer disease. *J. Biomed. Sci.* 27. doi:10.1186/S12929-019-0609-7.

Hurtley, S. M. (2009). Astrocytes in Alzheimer's. *Sci. Signal.* 2. doi:10.1126/scisignal.260ec82.

Husemann, J., Loike, J. D., Kodama, T., and Silverstein, S. C. (2001). Scavenger receptor class B type I (SR-BI) mediates adhesion of neonatal murine microglia to fibrillar beta-amyloid. *J. Neuroimmunol.* 114, 142–50. doi:10.1016/s0165-5728(01)00239-9.

Huynh, T. P. V., Davis, A. A., Ulrich, J. D., and Holtzman, D. M. (2017). Apolipoprotein E and Alzheimer's disease: The influence of apolipoprotein E on amyloid-β and other amyloidogenic proteins. *J. Lipid Res.* 58, 824–836. doi:10.1194/jlr.R075481.

Hyman, B. T., Phelps, C. H., Beach, T. G., Bigio, E. H., Cairns, N. J., Carrillo, M. C., et al. (2012). National Institute on Aging-Alzheimer's Association guidelines for the neuropathologic assessment of Alzheimer's disease. *Alzheimer's Dement.* 8, 1–13. doi:10.1016/j.jalz.2011.10.007.

Iadanza, M. G., Jackson, M. P., Hewitt, E. W., Ranson, N. A., and Radford, S. E. (2018). A new era for understanding amyloid structures and disease. *Nat. Rev. Mol. Cell Biol.* 19, 755–773. doi:10.1038/s41580-018-0060-8.

Ismail, R., Parbo, P., Madsen, L. S., Hansen, A. K., Hansen, K. V., Schaldemose, J. L., et al. (2020). The relationships between neuroinflammation, beta-amyloid and tau deposition in Alzheimer's disease: a longitudinal PET study. *J. Neuroinflammation* 17, 151. doi:10.1186/s12974-020-01820-6.

Itagaki, S., McGeer, P. L., Akiyama, H., Zhu, S., and Selkoe, D. (1989). Relationship of microglia and astrocytes to amyloid deposits of Alzheimer disease. *J. Neuroimmunol.* 24, 173–182. doi:10.1016/0165-5728(89)90115-X.

Italiani, P., Puxeddu, I., Napoletano, S., Scala, E., Melillo, D., Manocchio, S., et al. (2018). Circulating levels of IL-1 family cytokines and receptors in Alzheimer's disease: new markers of disease progression? *J. Neuroinflammation 2018 151* 15, 1–12. doi:10.1186/S12974-018-1376-1.

Iwatsubo, T., Odaka, A., Suzuki, N., Mizusawa, H., Nukina, N., and Ihara, Y. (1994). Visualization of Aβ42(43) and Aβ40 in senile plaques with end-specific Aβ monoclonals: Evidence that an initially deposited species is Aβ42(43). *Neuron* 13, 45–53. doi:10.1016/0896-6273(94)90458-8.

Jack, C. R., Albert, M. S., Knopman, D. S., McKhann, G. M., Sperling, R. A., Carrillo, M. C., et al. (2011). Introduction to the recommendations from the National Institute on Aging-Alzheimer's Association workgroups on diagnostic guidelines for Alzheimer's disease. *Alzheimer's Dement.* 7, 257–262. doi:10.1016/j.jalz.2011.03.004.

Jack, C. R., Petersen, R. C., Xu, Y., O'Brien, P. C., Smith, G. E., Ivnik, R. J., et al. (1998). Rate of medial temporal lobe atrophy in typical aging and Alzheimer's disease. *Neurology* 51, 993–9. Available at: http://www.ncbi.nlm.nih.gov/pubmed/9781519 [Accessed February 13, 2018].

Jagust, W. J., and Landau, S. M. (2021). Temporal Dynamics of β-Amyloid Accumulation in Aging and Alzheimer Disease. *Neurology* 96, e1347–e1357. doi:10.1212/WNL.0000000000011524.

Jakhria, T., Hellewell, A. L., Porter, M. Y., Jackson, M. P., Tipping, K. W., Xue, W. F., et al. (2014). ??2-microglobulin amyloid fibrils are nanoparticles that disrupt lysosomal membrane protein trafficking and inhibit protein degradation by lysosomes. *J. Biol. Chem.* doi:10.1074/jbc.M114.586222.

Jansen, I. E., Savage, J. E., Watanabe, K., Bryois, J., Williams, D. M., Steinberg, S., et al. (2019). Genome-wide meta-analysis identifies new loci and functional pathways influencing Alzheimer's disease risk. *Nat. Genet.* 51, 404–413. doi:10.1038/s41588-018-0311-9.

Jarrett, J., Berger, E., and Lansbury, P. (1993). The carboxy terminus of the beta amyloid protein is critical for the seeding of amyloid formation: implications for the pathogenesis of Alzheimer's disease. *Biochemistry* 32, 4693–4697. doi:10.1021/BI00069A001.

Jarrett, J. T., Berger, E. P., and Peter T. Lansbury, J. (2002). The carboxy terminus of the .beta. amyloid protein is critical for the seeding of amyloid formation: Implications for the pathogenesis of Alzheimer's disease. *Biochemistry* 32, 4693–4697. doi:10.1021/BI00069A001.

Jiang, H., Burdick, D., Glabe, C. G., Cotman, C. W., and Tenner, A. J. (1994). beta-Amyloid activates complement by binding to a specific region of the collagen-like domain of the C1q A chain. *J. Immunol.* 152, 5050–9. Available at: http://www.jimmunol.org/content/152/10/5050 [Accessed August 13, 2020].

Jin, J. J., Kim, H. D., Maxwell, J. A., Li, L., and Fukuchi, K. I. (2008). Toll-like receptor 4-dependent upregulation of cytokines in a transgenic mouse model of Alzheimer's disease. *J. Neuroinflammation* 5, 23. doi:10.1186/1742-2094-5-23.

Jonsson, T., Atwal, J. K., Steinberg, S., Snaedal, J., Jonsson, P. V., Bjornsson, S., et al. (2012). A mutation in APP protects against Alzheimer's disease and age-related cognitive decline. *Nature* 488, 96. doi:10.1038/nature11283.

Jonsson, T., Stefansson, H., Steinberg, S., Jonsdottir, I., Jonsson, P. V., Snaedal, J., et al. (2013). Variant of *TREM2* Associated with the Risk of Alzheimer's Disease. *N. Engl. J. Med.* 368, 107–116. doi:10.1056/NEJMoa1211103.

Jucker, M., and Walker, L. C. (2013). Self-propagation of pathogenic protein aggregates

in neurodegenerative diseases. *Nature* 501, 45–51. doi:10.1038/nature12481.

Kakuda, N., Miyasaka, T., Iwasaki, N., Nirasawa, T., Wada-Kakuda, S., Takahashi-Fujigasaki, J., et al. (2017). Distinct deposition of amyloid-β species in brains with Alzheimer's disease pathology visualized with MALDI imaging mass spectrometry. *Acta Neuropathol. Commun. 2017 51* 5, 1–8. doi:10.1186/S40478-017-0477-X.

Karch, C. M., Cruchaga, C., and Goate, A. M. (2014). Alzheimer's disease genetics: From the bench to the clinic. *Neuron* 83, 11–26. doi:10.1016/j.neuron.2014.05.041.

Kawasaki, T., and Kawai, T. (2014). Toll-like receptor signaling pathways. *Front. Immunol.* 5, 461. doi:10.3389/fimmu.2014.00461.

Kayed, R., and Lasagna-Reeves, C. A. (2013). Molecular Mechanisms of Amyloid Oligomers Toxicity. *J. Alzheimer's Dis.* 33, 67–78. doi:10.3233/JAD-2012-129001.

Keren-Shaul, H., Spinrad, A., Weiner, A., Matcovitch-Natan, O., Dvir-Szternfeld, R., Ulland, T. K., et al. (2017). A Unique Microglia Type Associated with Restricting Development of Alzheimer's Disease. *Cell* 169, 1276-1290.e17. doi:10.1016/j.cell.2017.05.018.

Kim, J.-H., Sohn, H.-J., Yoo, J.-K., Kang, H., Seong, G.-S., Chwae, Y.-J., et al. (2016). NLRP3 Inflammasome Activation in THP-1 Target Cells Triggered by Pathogenic Naegleria fowleri. *Infect. Immun.* 84, 2422. doi:10.1128/IAI.00275-16.

Kleinberger, G., Yamanishi, Y., Suárez-Calvet, M., Czirr, E., Lohmann, E., Cuyvers, E., et al. (2014). TREM2 mutations implicated in neurodegeneration impair cell surface transport and phagocytosis. *Sci. Transl. Med.* 6. doi:10.1126/scitranslmed.3009093.

Klingstedt, T., Shirani, H., Åslund, K. O. A., Cairns, N. J., Sigurdson, C. J., Goedert, M., et al. (2013). The Structural Basis for Optimal Performance of Oligothiophene-Based Fluorescent Amyloid Ligands: Conformational Flexibility is Essential for Spectral Assignment of a Diversity of Protein Aggregates. *Chem. – A Eur. J.* 19, 10179–10192. doi:10.1002/CHEM.201301463.

Klunk, W. E., Engler, H., Nordberg, A., Wang, Y., Blomqvist, G., Holt, D. P., et al. (2004). Imaging Brain Amyloid in Alzheimer's Disease with Pittsburgh Compound-B. *Ann. Neurol.* 55, 306–319. doi:10.1002/ana.20009.

Knezevic, D., and Mizrahi, R. (2018). Molecular imaging of neuroinflammation in Alzheimer's disease and mild cognitive impairment. *Prog. Neuro-*

Psychopharmacology Biol. Psychiatry 80, 123–131. doi:10.1016/J.PNPBP.2017.05.007.

Knopman, D. S., Amieva, H., Petersen, R. C., Chételat, G., Holtzman, D. M., Hyman, B. T., et al. (2021). Alzheimer disease. *Nat. Rev. Dis. Prim.* 7, 33. doi:10.1038/s41572-021-00269-y.

Knopman, D. S., Parisi, J. E., Salviati, A., Floriach-Robert, M., Boeve, B. F., Ivnik, R. J., et al. (2003). Neuropathology of Cognitively Normal Elderly. *J. Neuropathol. Exp. Neurol.* 62, 1087–1095. doi:10.1093/jnen/62.11.1087.

Knowles, T. P. J., Vendruscolo, M., and Dobson, C. M. (2014). The amyloid state and its association with protein misfolding diseases. *Nat. Rev. Mol. Cell Biol.* 15, 384–396. doi:10.1038/nrm3810.

Koch, K. M. (1992). Dialysis-related amyloidosis. *Kidney Int.* 41, 1416–1429. doi:10.1038/ki.1992.207.

Koenigsknecht, J., and Landreth, G. (2004). Microglial phagocytosis of fibrillar β-amyloid through a β1 integrin-dependent mechanism. *J. Neurosci.* 24, 9838–9846. doi:10.1523/JNEUROSCI.2557-04.2004.

Koffie, R. M., Meyer-Luehmann, M., Hashimoto, T., Adams, K. W., Mielke, M. L., Garcia-Alloza, M., et al. (2009). Oligomeric amyloid β associates with postsynaptic densities and correlates with excitatory synapse loss near senile plaques. *Proc. Natl. Acad. Sci.* 106, 4012–4017. doi:10.1073/PNAS.0811698106.

Kollmer, M., Close, W., Funk, L., Rasmussen, J., Bsoul, A., Schierhorn, A., et al. (2019). Cryo-EM structure and polymorphism of Aβ amyloid fibrils purified from Alzheimer's brain tissue. *Nat. Commun.* 10, 1–8. doi:10.1038/s41467-019-12683-8.

Korbel, J. O., Tirosh-Wagner, T., Urban, A. E., Chen, X. N., Kasowski, M., Dai, L., et al. (2009). The genetic architecture of Down syndrome phenotypes revealed by high-resolution analysis of human segmental trisomies. *Proc. Natl. Acad. Sci. U. S. A.* 106, 12031–12036. doi:10.1073/pnas.0813248106.

Krabbe, G., Halle, A., Matyash, V., Rinnenthal, J. L., Eom, G. D., Bernhardt, U., et al. (2013). Functional Impairment of Microglia Coincides with Beta-Amyloid Deposition in Mice with Alzheimer-Like Pathology. *PLoS One* 8, e60921. doi:10.1371/journal.pone.0060921.

Krasemann, S., Madore, C., Cialic, R., Baufeld, C., Calcagno, N., El Fatimy, R., et al.

(2017). The TREM2-APOE Pathway Drives the Transcriptional Phenotype of Dysfunctional Microglia in Neurodegenerative Diseases. *Immunity* 47, 566-581.e9. doi:10.1016/j.immuni.2017.08.008.

Kreisl, W. C., Lyoo, C. H., McGwier, M., Snow, J., Jenko, K. J., Kimura, N., et al. (2013). In vivo radioligand binding to translocator protein correlates with severity of Alzheimer's disease. *Brain* 136, 2228–2238. doi:10.1093/BRAIN/AWT145.

Kumar, D. K. V., Choi, H. S., Washicosky, K. J., Eimer, W. A., Tucker, S., Ghofrani, J., et al. (2016). Amyloid-β peptide protects against microbial infection in mouse and worm models of Alzheimer's disease. *Sci. Transl. Med.* 8, 340ra72-340ra72. doi:10.1126/scitranslmed.aaf1059.

Kumar, S., Wirths, O., Theil, S., Gerth, J., Bayer, T., and Walter, J. (2013). Early intraneuronal accumulation and increased aggregation of phosphorylated Abeta in a mouse model of Alzheimer's disease. *Acta Neuropathol.* 125, 699–709. doi:10.1007/S00401-013-1107-8.

Kummer, M., and Heneka, M. (2014). Truncated and modified amyloid-beta species. *Alzheimers. Res. Ther.* 6. doi:10.1186/ALZRT258.

LaDu, M. J., Falduto, M. T., Manelli, A. M., Reardon, C. A., Getz, G. S., and Frail, D. E. (1994). Isoform-specific binding of apolipoprotein E to beta-amyloid. *J. Biol. Chem.* 269, 23403–23406.

Lam, B., Masellis, M., Freedman, M., Stuss, D. T., and Black, S. E. (2013). Clinical, imaging, and pathological heterogeneity of the Alzheimer's disease syndrome. *Alzheimer's Res. Ther.* 5, 1. doi:10.1186/alzrt155.

Lambert, J. C., Heath, S., Even, G., Campion, D., Sleegers, K., Hiltunen, M., et al. (2009). Genome-wide association study identifies variants at CLU and CR1 associated with Alzheimer's disease. *Nat. Genet.* 41, 1094–1099. doi:10.1038/ng.439.

Lambert, J. C., Ibrahim-Verbaas, C. A., Harold, D., Naj, A. C., Sims, R., Bellenguez, C., et al. (2013). Meta-analysis of 74,046 individuals identifies 11 new susceptibility loci for Alzheimer's disease. *Nat. Genet.* 45, 1452–1458. doi:10.1038/ng.2802.

Lambert, M., Barlow, A., … B. C.-P. of the, and 1998, undefined (1998). Diffusible, nonfibrillar ligands derived from Aβ1–42 are potent central nervous system neurotoxins. *Natl. Acad Sci.* 95, 6448–6453. Available at: https://www.pnas.org/content/95/11/6448.short [Accessed September 18, 2021].

Langer, F., Eisele, Y. S., Fritschi, S. K., Staufenbiel, M., Walker, L. C., and Jucker, M. (2011). Soluble Aβ Seeds Are Potent Inducers of Cerebral β-Amyloid Deposition. *J. Neurosci.* 31, 14488–14495. doi:10.1523/JNEUROSCI.3088-11.2011.

Lee, S.-H., Meilandt, W. J., Xie, L., Gandham, V. D., Ngu, H., Barck, K. H., et al. (2021). Trem2 restrains the enhancement of tau accumulation and neurodegeneration by β-amyloid pathology. *Neuron* 109, 1283-1301.e6. doi:10.1016/j.neuron.2021.02.010.

Leissring, M. A., Farris, W., Chang, A. Y., Walsh, D. M., Wu, X., Sun, X., et al. (2003). Enhanced proteolysis of β-amyloid in APP transgenic mice prevents plaque formation, secondary pathology, and premature death. *Neuron* 40, 1087–1093. doi:10.1016/S0896-6273(03)00787-6.

Leng, F., and Edison, P. (2021). Neuroinflammation and microglial activation in Alzheimer disease: where do we go from here? *Nat. Rev. Neurol.* 17, 157–172. doi:10.1038/s41582-020-00435-y.

Letiembre, M., Liu, Y., Walter, S., Hao, W., Pfander, T., Wrede, A., et al. (2009). Screening of innate immune receptors in neurodegenerative diseases: A similar pattern. *Neurobiol. Aging* 30, 759–768. doi:10.1016/j.neurobiolaging.2007.08.018.

Li, B., Ge, P., Murray, K. A., Sheth, P., Zhang, M., Nair, G., et al. (2018a). Cryo-EM of full-length α-synuclein reveals fibril polymorphs with a common structural kernel. *Nat. Commun.* 9, 1–10. doi:10.1038/s41467-018-05971-2.

Li, D., and Wu, M. (2021). Pattern recognition receptors in health and diseases. *Signal Transduct. Target. Ther. 2021 61* 6, 1–24. doi:10.1038/s41392-021-00687-0.

Li, Y., Zhao, C., Luo, F., Liu, Z., Gui, X., Luo, Z., et al. (2018b). Amyloid fibril structure of α-synuclein determined by cryo-electron microscopy. *Cell Res.* 28, 897–903. doi:10.1038/s41422-018-0075-x.

Liao, M. C., and Van Nostrand, W. E. (2010). Degradation of soluble and fibrillar amyloid β-protein by matrix metalloproteinase (MT1-MMP) in vitro. *Biochemistry* 49, 1127–1136. doi:10.1021/bi901994d.

Liddelow, S. A., Guttenplan, K. A., Clarke, L. E., Bennett, F. C., Bohlen, C. J., Schirmer, L., et al. (2017). Neurotoxic reactive astrocytes are induced by activated microglia. *Nature* 541, 481–487. doi:10.1038/nature21029.

Liu, C. C., Zhao, N., Fu, Y., Wang, N., Linares, C., Tsai, C. W., et al. (2017a). ApoE4

Accelerates Early Seeding of Amyloid Pathology. *Neuron* 96, 1024-1032.e3. doi:10.1016/j.neuron.2017.11.013.

Liu, J. Z., Erlich, Y., and Pickrell, J. K. (2017b). Case-control association mapping by proxy using family history of disease. *Nat. Genet.* 49, 325–331. doi:10.1038/ng.3766.

Liu, Y., Walter, S., Stagi, M., Cherny, D., Letiembre, M., Schulz-Schaeffer, W., et al. (2005). LPS receptor (CD14): a receptor for phagocytosis of Alzheimer's amyloid peptide. *Brain* 128, 1778–1789. doi:10.1093/brain/awh531.

Lu, A., Magupalli, V. G., Ruan, J., Yin, Q., Atianand, M. K., Vos, M. R., et al. (2014). Unified polymerization mechanism for the assembly of asc-dependent inflammasomes. *Cell* 156, 1193–1206. doi:10.1016/j.cell.2014.02.008.

Lu, J. X., Qiang, W., Yau, W. M., Schwieters, C. D., Meredith, S. C., and Tycko, R. (2013). Molecular structure of β-amyloid fibrils in alzheimer's disease brain tissue. *Cell* 154, 1257. doi:10.1016/j.cell.2013.08.035.

Madine, J. (2019). Cofactor-mediated amyloidogenesis. *Biosci. Rep.* 39. doi:10.1042/BSR20190327.

Madine, J., Pandya, M. J., Hicks, M. R., Rodger, A., Yates, E. A., Radford, S. E., et al. (2012). Site-specific identification of an Aβ fibril-heparin interaction site by using solid-state NMR spectroscopy. *Angew. Chemie - Int. Ed.* doi:10.1002/anie.201204459.

Majumdar, A., Chung, H., Dolios, G., Wang, R., Asamoah, N., Lobel, P., et al. (2008). Degradation of fibrillar forms of Alzheimer's amyloid β-peptide by macrophages. *Neurobiol. Aging* 29, 707–715. doi:10.1016/j.neurobiolaging.2006.12.001.

Makin, S. (2018). The amyloid hypothesis on trial. *Nature* 559, S4–S7. doi:10.1038/d41586-018-05719-4.

Mannini, B., Vecchi, G., Labrador-Garrido, A., Fabre, B., Fani, G., Franco, J. M., et al. (2019). Differential Interactome and Innate Immune Response Activation of Two Structurally Distinct Misfolded Protein Oligomers. *ACS Chem. Neurosci.* 10, 3464–3478. doi:10.1021/acschemneuro.9b00088.

Mariathasan, S., Weiss, D. S., Newton, K., McBride, J., O'Rourke, K., Roose-Girma, M., et al. (2006). Cryopyrin activates the inflammasome in response to toxins and ATP. *Nature* 440, 228–232. doi:10.1038/nature04515.

Marioni, R. E., Harris, S. E., Zhang, Q., McRae, A. F., Hagenaars, S. P., Hill, W. D., et al. (2018). GWAS on family history of Alzheimer's disease. *Transl. Psychiatry* 8, 99. doi:10.1038/s41398-018-0150-6.

Marschallinger, J., Iram, T., Zardeneta, M., Lee, S. E., Lehallier, B., Haney, M. S., et al. (2020). Lipid-droplet-accumulating microglia represent a dysfunctional and proinflammatory state in the aging brain. *Nat. Neurosci.* 23, 194–208. doi:10.1038/s41593-019-0566-1.

Martinon, F., Pétrilli, V., Mayor, A., Tardivel, A., and Tschopp, J. (2006). Gout-associated uric acid crystals activate the NALP3 inflammasome. *Nature* 440, 237–241. doi:10.1038/nature04516.

Martins, I. C., Kuperstein, I., Wilkinson, H., Maes, E., Vanbrabant, M., Jonckheere, W., et al. (2008). Lipids revert inert Aβ amyloid fibrils to neurotoxic protofibrils that affect learning in mice. *EMBO J.* 27, 224. doi:10.1038/SJ.EMBOJ.7601953.

Masters, C. L., Bateman, R., Blennow, K., Rowe, C. C., Sperling, R. A., and Cummings, J. L. (2015). Alzheimer's disease. *Nat. Rev. Dis. Prim. 2015 11* 1, 1–18. doi:10.1038/nrdp.2015.56.

Masters, C. L., Simms, G., Weinman, N. A., Multhaup, G., McDonald, B. L., and Beyreuther, K. (1985). Amyloid plaque core protein in Alzheimer disease and Down syndrome. *Proc. Natl. Acad. Sci. U. S. A.* 82, 4245–4249. doi:10.1073/pnas.82.12.4245.

Masumoto, J., Taniguchi, S., Ayukawa, K., Sarvotham, H., Kishino, T., Niikawa, N., et al. (1999). ASC, a novel 22-kDa protein, aggregates during apoptosis of human promyelocytic leukemia HL-60 cells. *J. Biol. Chem.* 274, 33835–33838. doi:10.1074/jbc.274.48.33835.

Mawuenyega, K. G., Sigurdson, W., Ovod, V., Munsell, L., Kasten, T., Morris, J. C., et al. (2010). Decreased clearance of CNS β-amyloid in Alzheimer's disease. *Science (80-.).* 330, 1774. doi:10.1126/science.1197623.

McKhann, G. M., Knopman, D. S., Chertkow, H., Hyman, B. T., Jack, C. R., Kawas, C. H., et al. (2011). The diagnosis of dementia due to Alzheimer's disease: Recommendations from the National Institute on Aging-Alzheimer's Association workgroups on diagnostic guidelines for Alzheimer's disease. *Alzheimer's Dement.* 7, 263–269. doi:10.1016/j.jalz.2011.03.005.

McLean, C. A., Cherny, R. A., Fraser, F. W., Fuller, S. J., Smith, M. J., Beyreuther, K.,

et al. (1999). Soluble pool of Aβ amyloid as a determinant of severity of neurodegeneration in Alzheimer's disease. *Ann. Neurol.* 46, 860–866. doi:10.1002/1531-8249(199912)46:6<860::AID-ANA8>3.0.CO;2-M.

McManus, R. M., and Heneka, M. T. (2017). Role of neuroinflammation in neurodegeneration: New insights. *Alzheimer's Res. Ther.* 9, 14. doi:10.1186/s13195-017-0241-2.

Mehto, S., Jena, K. K., Nath, P., Chauhan, S., Kolapalli, S. P., Das, S. K., et al. (2019). The Crohn's Disease Risk Factor IRGM Limits NLRP3 Inflammasome Activation by Impeding Its Assembly and by Mediating Its Selective Autophagy. *Mol. Cell* 73, 429-445.e7. doi:10.1016/J.MOLCEL.2018.11.018.

Meyer-Luehmann, M., Coomaraswamy, J., Bolmont, T., Kaeser, S., Schaefer, C., Kilger, E., et al. (2006). Exogenous Induction of Cerebral ß-Amyloidogenesis Is Governed by Agent and Host. *Science (80-.).* 313, 1781–1784. doi:10.1126/SCIENCE.1131864.

Meyer-Luehmann, M., Spires-Jones, T. L., Prada, C., Garcia-Alloza, M., De Calignon, A., Rozkalne, A., et al. (2008). Rapid appearance and local toxicity of amyloid-β plaques in a mouse model of Alzheimer's disease. *Nature* 451, 720–724. doi:10.1038/nature06616.

Mezyk-Kopeć, R., Bzowska, M., Stalińska, K., Chełmicki, T., Podkalicki, M., Jucha, J., et al. (2009). Identification of ADAM10 as a major TNF sheddase in ADAM17-deficient fibroblasts. *Cytokine* 46, 309–315. doi:10.1016/j.cyto.2009.03.002.

Milanesi, L., Sheynis, T., Xue, W.-F., Orlova, E. V., Hellewell, A. L., Jelinek, R., et al. (2012). Direct three-dimensional visualization of membrane disruption by amyloid fibrils. *Proc. Natl. Acad. Sci.* 109, 20455–20460. doi:10.1073/PNAS.1206325109.

Mishra, A., Kim, H. J., Shin, A. H., and Thayer, S. A. (2012). Synapse loss induced by interleukin-1β requires pre-and post-synaptic mechanisms. *J. Neuroimmune Pharmacol.* 7, 571–578. doi:10.1007/s11481-012-9342-7.

Mittelbronn, M., Dietz, K., Schluesener, H. J., and Meyermann, R. (2001). Local distribution of microglia in the normal adult human central nervous system differs by up to one order of magnitude. *Acta Neuropathol.* 101, 249–255. doi:10.1007/s004010000284.

Monsonego, A., Zota, V., Karni, A., Krieger, J. I., Bar-Or, A., Bitan, G., et al. (2003). Increased T cell reactivity to amyloid β protein in older humans and patients with

Alzheimer disease. *J. Clin. Invest.* 112, 415–422. doi:10.1172/JCI18104.

Moore, K. J., El Khoury, J., Medeiros, L. A., Terada, K., Geula, C., Luster, A. D., et al. (2002). A CD36-initiated signaling cascade mediates inflammatory effects of β-amyloid. *J. Biol. Chem.* 277, 47373–47379. doi:10.1074/jbc.M208788200.

Morales, R., Moreno-Gonzalez, I., and Soto, C. (2013). Cross-Seeding of Misfolded Proteins: Implications for Etiology and Pathogenesis of Protein Misfolding Diseases. *PLoS Pathog.* 9. doi:10.1371/journal.ppat.1003537.

Moreno-Gonzalez, I., Edwards, G., Salvadores, N., Shahnawaz, M., Diaz-Espinoza, R., and Soto, C. (2017). Molecular interaction between type 2 diabetes and Alzheimer's disease through cross-seeding of protein misfolding. *Mol. Psychiatry* 22, 1327–1334. doi:10.1038/mp.2016.230.

Morten, I. J., Gosal, W. S., Radford, S. E., and Hewitt, E. W. (2007). Investigation into the role of macrophages in the formation and degradation of β2-microglobulin amyloid fibrils. *J. Biol. Chem.* 282, 29691–29700. doi:10.1074/jbc.M705004200.

Mueller-Steiner, S., Zhou, Y., Arai, H., Roberson, E. D., Sun, B., Chen, J., et al. (2006). Antiamyloidogenic and Neuroprotective Functions of Cathepsin B: Implications for Alzheimer's Disease. *Neuron* 51, 703–714. doi:10.1016/j.neuron.2006.07.027.

Murphy, M. P., LeVine, H., and III (2010). Alzheimer's Disease and the β-Amyloid Peptide. *J. Alzheimers. Dis.* 19, 311. doi:10.3233/JAD-2010-1221.

Nagele, R. G., D'Andrea, M. R., Lee, H., Venkataraman, V., and Wang, H. Y. (2003). Astrocytes accumulate Aβ42 and give rise to astrocytic amyloid plaques in Alzheimer disease brains. *Brain Res.* 971, 197–209. doi:10.1016/S0006-8993(03)02361-8.

Naj, A. C., Jun, G., Beecham, G. W., Wang, L. S., Vardarajan, B. N., Buros, J., et al. (2011). Common variants at MS4A4/MS4A6E, CD2AP, CD33 and EPHA1 are associated with late-onset Alzheimer's disease. *Nat. Genet.* 43, 436–443. doi:10.1038/ng.801.

Nakamura, A., Kaneko, N., Villemagne, V. L., Kato, T., Doecke, J., Doré, V., et al. (2018). High performance plasma amyloid-β biomarkers for Alzheimer's disease. *Nature* 554, 249–254. doi:10.1038/nature25456.

Nathan, C., and Cunningham-Bussel, A. (2013). Beyond oxidative stress: an immunologist's guide to reactive oxygen species. *Nat. Rev. Immunol. 2013 135* 13,

349–361. doi:10.1038/nri3423.

Nelson, P. T., Alafuzoff, I., Bigio, E. H., Bouras, C., Braak, H., Cairns, N. J., et al. (2012). Correlation of alzheimer disease neuropathologic changes with cognitive status: A review of the literature. *J. Neuropathol. Exp. Neurol.* 71, 362–381. doi:10.1097/NEN.0b013e31825018f7.

Nilsson, Andreas Åslund, Ina Berg, Sofie Nyström, Peter Konradsson, Anna Herland, et al. (2007). Imaging Distinct Conformational States of Amyloid-β Fibrils in Alzheimer's Disease Using Novel Luminescent Probes. *ACS Chem. Biol.* 2, 553–560. doi:10.1021/CB700116U.

Nimmerjahn, A., Kirchhoff, F., and Helmchen, F. (2005). Neuroscience: Resting microglial cells are highly dynamic surveillants of brain parenchyma in vivo. *Science (80-.).* 308, 1314–1318. doi:10.1126/science.1110647.

Ojala, J., Alafuzoff, I., Herukka, S. K., van Groen, T., Tanila, H., and Pirttilä, T. (2009). Expression of interleukin-18 is increased in the brains of Alzheimer's disease patients. *Neurobiol. Aging* 30, 198–209. doi:10.1016/j.neurobiolaging.2007.06.006.

Olson, M. I., and Shaw, C.-M. (1969). Presenile dementia and Alzheimer's disease in mongolism. *Brain* 92, 147–156. doi:10.1093/brain/92.1.147.

Olzscha, H., Schermann, S. M., Woerner, A. C., Pinkert, S., Hecht, M. H., Tartaglia, G. G., et al. (2011). Amyloid-like Aggregates Sequester Numerous Metastable Proteins with Essential Cellular Functions. *Cell* 144, 67–78. doi:10.1016/J.CELL.2010.11.050.

Ono, K., Takahashi, R., Ikeda, T., Mizuguchi, M., Hamaguchi, T., and Yamada, M. (2014). Exogenous amyloidogenic proteins function as seeds in amyloid β-protein aggregation. *Biochim. Biophys. Acta - Mol. Basis Dis.* 1842, 646–653. doi:10.1016/j.bbadis.2014.01.002.

Ostrowitzki, S., Lasser, R. A., Dorflinger, E., Scheltens, P., Barkhof, F., Nikolcheva, T., et al. (2017). A phase III randomized trial of gantenerumab in prodromal Alzheimer's disease. *Alzheimer's Res. Ther. 2017 91* 9, 1–15. doi:10.1186/S13195-017-0318-Y.

Ovchinnikova, O. Y., Finder, V. H., Vodopivec, I., Nitsch, R. M., and Glockshuber, R. (2011). The Osaka FAD mutation E22Δ leads to the formation of a previously unknown type of amyloid β fibrils and modulates Aβ neurotoxicity. *J. Mol. Biol.* 408, 780–791. doi:10.1016/j.jmb.2011.02.049.

Pallitto, M. M., and Murphy, R. M. (2001). A Mathematical Model of the Kinetics of β-Amyloid Fibril Growth from the Denatured State. *Biophys. J.* 81, 1805–1822. doi:10.1016/S0006-3495(01)75831-6.

Palmqvist, S., Janelidze, S., Stomrud, E., Zetterberg, H., Karl, J., Zink, K., et al. (2019). Performance of Fully Automated Plasma Assays as Screening Tests for Alzheimer Disease-Related β-Amyloid Status. *JAMA Neurol.* 76, 1060–1069. doi:10.1001/jamaneurol.2019.1632.

Palpagama, T. H., Waldvogel, H. J., Faull, R. L. M., and Kwakowsky, A. (2019). The Role of Microglia and Astrocytes in Huntington's Disease. *Front. Mol. Neurosci.* 12. doi:10.3389/fnmol.2019.00258.

Pan, X. D., Zhu, Y. G., Lin, N., Zhang, J., Ye, Q. Y., Huang, H. P., et al. (2011). Microglial phagocytosis induced by fibrillar β-amyloid is attenuated by oligomeric β-amyloid: implications for Alzheimer's disease. *Mol. Neurodegener. 2011 61* 6, 1–18. doi:10.1186/1750-1326-6-45.

Panza, F., Lozupone, M., Logroscino, G., and Imbimbo, B. P. (2019). A critical appraisal of amyloid-β-targeting therapies for Alzheimer disease. *Nat. Rev. Neurol. 2018 152* 15, 73–88. doi:10.1038/s41582-018-0116-6.

Paravastu, A. K., Leapman, R. D., Yau, W. M., and Tycko, R. (2008). Molecular structural basis for polymorphism in Alzheimer's β-amyloid fibrils. *Proc. Natl. Acad. Sci. U. S. A.* 105, 18349–18354. doi:10.1073/pnas.0806270105.

Paravastu, A. K., Qahwash, I., Leapman, R. D., Meredith, S. C., and Tycko, R. (2009). Seeded growth of β-amyloid fibrils from Alzheimer's brain-derived fibrils produces a distinct fibril structure. *Proc. Natl. Acad. Sci. U. S. A.* 106, 7443–7448. doi:10.1073/pnas.0812033106.

Paresce, D. M., Ghosh, R. N., and Maxfield, F. R. (1996). Microglial cells internalize aggregates of the Alzheimer's disease amyloid β-protein via a scavenger receptor. *Neuron* 17, 553–565. doi:10.1016/S0896-6273(00)80187-7.

Park, S.-H., Kukushkin, Y., Gupta, R., Chen, T., Konagai, A., Hipp, M. S., et al. (2013). PolyQ Proteins Interfere with Nuclear Degradation of Cytosolic Proteins by Sequestering the Sis1p Chaperone. *Cell* 154, 134–145. doi:10.1016/J.CELL.2013.06.003.

Pastore, A., Raimondi, F., Rajendran, L., and Temussi, P. A. (2020). Why does the Aβ peptide of Alzheimer share structural similarity with antimicrobial peptides?

Commun. Biol. 3, 1–7. doi:10.1038/s42003-020-0865-9.

Patel, N. S., Paris, D., Mathura, V., Quadros, A. N., Crawford, F. C., and Mullan, M. J. (2005). Inflammatory cytokine levels correlate with amyloid load in transgenic mouse models of Alzheimer's disease. *J. Neuroinflammation* 2. doi:10.1186/1742-2094-2-9.

Peng, C., Gathagan, R. J., Covell, D. J., Medellin, C., Stieber, A., Robinson, J. L., et al. (2018). Cellular milieu imparts distinct pathological α-synuclein strains in α-synucleinopathies. *Nature* 557, 558–563. doi:10.1038/s41586-018-0104-4.

Perez-Nievas, B. G., and Serrano-Pozo, A. (2018). Deciphering the astrocyte reaction in Alzheimer's disease. *Front. Aging Neurosci.* 10, 114. doi:10.3389/fnagi.2018.00114.

Petkova, A. T., Ishii, Y., Balbach, J. J., Antzutkin, O. N., Leapman, R. D., Delaglio, F., et al. (2002). A structural model for Alzheimer's β-amyloid fibrils based on experimental constraints from solid state NMR. *Proc. Natl. Acad. Sci. U. S. A.* 99, 16742–16747. doi:10.1073/pnas.262663499.

Petkova, A. T., Leapman, R. D., Guo, Z., Yau, W. M., Mattson, M. P., and Tycko, R. (2005). Self-propagating, molecular-level polymorphism in Alzheimer's β-amyloid fibrils. *Science (80-.).* 307, 262–265. doi:10.1126/science.1105850.

Petkova, A. T., Yau, W. M., and Tycko, R. (2006). Experimental constraints on quaternary structure in Alzheimer's β-amyloid fibrils. *Biochemistry* 45, 498–512. doi:10.1021/bi051952q.

Pieri, L., Madiona, K., Bousset, L., and Melki, R. (2012). Fibrillar α-Synuclein and Huntingtin Exon 1 Assemblies Are Toxic to the Cells. *Biophys. J.* 102, 2894–2905. doi:10.1016/J.BPJ.2012.04.050.

Poole, S., Singhrao, S. K., Kesavalu, L., Curtis, M. A., and Crean, S. J. (2013). Determining the presence of periodontopathic virulence factors in short-term postmortem Alzheimer's disease brain tissue. *J. Alzheimer's Dis.* 36, 665–677. doi:10.3233/JAD-121918.

Portelius, E., Bogdanovic, N., Gustavsson, M. K., Volkmann, I., Brinkmalm, G., Zetterberg, H., et al. (2010). Mass spectrometric characterization of brain amyloid beta isoform signatures in familial and sporadic Alzheimer's disease. *Acta Neuropathol.* 120, 185. doi:10.1007/S00401-010-0690-1.

Price, J. L., McKeel, D. W., Buckles, V. D., Roe, C. M., Xiong, C., Grundman, M., et al. (2009). Neuropathology of nondemented aging: Presumptive evidence for preclinical Alzheimer disease. *Neurobiol. Aging* 30, 1026–1036. doi:10.1016/j.neurobiolaging.2009.04.002.

Priller, C., Bauer, T., Mitteregger, G., Krebs, B., Kretzschmar, H. A., and Herms, J. (2006). Synapse Formation and Function Is Modulated by the Amyloid Precursor Protein. *J. Neurosci.* 26, 7212–7221. doi:10.1523/JNEUROSCI.1450-06.2006.

Qiang, W., Kelley, K., and Tycko, R. (2013). Polymorph-specific kinetics and thermodynamics of β-amyloid fibril growth. *J. Am. Chem. Soc.* 135, 6860–6871. doi:10.1021/ja311963f.

Qiang, W., Yau, W.-M., Luo, Y., Mattson, M. P., and Tycko, R. (2012). Antiparallel β-sheet architecture in Iowa-mutant β-amyloid fibrils. *Proc. Natl. Acad. Sci.* 109, 4443–4448. doi:10.1073/PNAS.1111305109.

Qiang, W., Yau, W. M., Lu, J. X., Collinge, J., and Tycko, R. (2017). Structural variation in amyloid-β fibrils from Alzheimer's disease clinical subtypes. *Nature* 541, 217–221. doi:10.1038/nature20814.

Qiu, W. Q., Walsh, D. M., Ye, Z., Vekrellis, K., Zhang, J., Podlisny, M. B., et al. (1998). Insulin-degrading enzyme regulates extracellular levels of amyloid β- protein by degradation. *J. Biol. Chem.* 273, 32730–32738. doi:10.1074/jbc.273.49.32730.

Rasmussen, J., Mahler, J., Beschorner, N., Kaeser, S. A., Häsler, L. M., Baumann, F., et al. (2017). Amyloid polymorphisms constitute distinct clouds of conformational variants in different etiological subtypes of Alzheimer's disease. *Proc. Natl. Acad. Sci. U. S. A.* 114, 13018–13023. doi:10.1073/pnas.1713215114.

Reed-Geaghan, E. G., Savage, J. C., Hise, A. G., and Landreth, G. E. (2009). CD14 and toll-like receptors 2 and 4 are required for fibrillar Aβ-stimulated microglial activation. *J. Neurosci.* 29, 11982–11992. doi:10.1523/JNEUROSCI.3158-09.2009.

Reisberg, B., Doody, R., Stöffler, A., Schmitt, F., Ferris, S., and Möbius, H. J. (2003). Memantine in Moderate-to-Severe Alzheimer's Disease. *N. Engl. J. Med.* 348, 1333–1341. doi:10.1056/nejmoa013128.

Rice, H. C., De Malmazet, D., Schreurs, A., Frere, S., Van Molle, I., Volkov, A. N., et al. (2019). Secreted amyloid-b precursor protein functions as a GABA B R1a ligand to modulate synaptic transmission. *Science (80-.).* 363. doi:10.1126/science.aao4827.

Rijal Upadhaya, A., Kosterin, I., Kumar, S., von Arnim, C. A. F., Yamaguchi, H., Fändrich, M., et al. (2014). Biochemical stages of amyloid-β peptide aggregation and accumulation in the human brain and their association with symptomatic and pathologically preclinical Alzheimer's disease. *Brain* 137, 887–903. doi:10.1093/BRAIN/AWT362.

Roberts, B. R., Lind, M., Wagen, A. Z., Rembach, A., Frugier, T., Li, Q. X., et al. (2017). Biochemically-defined pools of amyloid-β in sporadic Alzheimer's disease: correlation with amyloid PET. *Brain* 140, 1486–1498. doi:10.1093/BRAIN/AWX057.

Rogaev, E. I., Sherrington, R., Rogaeva, E. A., Levesque, G., Ikeda, M., Liang, Y., et al. (1995). Familial Alzheimer's disease in kindreds with missense mutations in a gene on chromosome 1 related to the Alzheimer's disease type 3 gene. *Nature* 376, 775–778. doi:10.1038/376775a0.

Rogers, J., Cooper, N. R., Webster, S., Schultz, J., McGeer, P. L., Styren, S. D., et al. (1992). Complement activation by β-amyloid in Alzheimer disease. *Proc. Natl. Acad. Sci. U. S. A.* 89, 10016–10020. doi:10.1073/pnas.89.21.10016.

Rogers, J., Strohmeyer, R., Kovelowski, C. J., and Li, R. (2002). Microglia and inflammatory mechanisms in the clearance of amyloid β peptide. *Glia* 40, 260–269. doi:10.1002/glia.10153.

Rovelet-Lecrux, A., Hannequin, D., Raux, G., Le Meur, N., Laquerrière, A., Vital, A., et al. (2006). APP locus duplication causes autosomal dominant early-onset Alzheimer disease with cerebral amyloid angiopathy. *Nat. Genet.* 38, 24–26. doi:10.1038/ng1718.

Rubenstein, E., Hartley, S., and Bishop, L. (2020). Epidemiology of Dementia and Alzheimer Disease in Individuals with Down Syndrome. *JAMA Neurol.* 77, 262–264. doi:10.1001/jamaneurol.2019.3666.

Safar, J., Wille, H., Itri, V., Groth, D., Serban, H., Torchia, M., et al. (1998). Eight prion strains have PrPSc molecules with different conformations. *Nat. Med. 1998 410* 4, 1157–1165. doi:10.1038/2654.

Salloway, S., Honigberg, L. A., Cho, W., Ward, M., Friesenhahn, M., Brunstein, F., et al. (2018). Amyloid positron emission tomography and cerebrospinal fluid results from a crenezumab anti-amyloid-beta antibody double-blind, placebo-controlled, randomized phase II study in mild-to-moderate Alzheimer's disease (BLAZE). *Alzheimer's Res. Ther. 2018 101* 10, 1–13. doi:10.1186/S13195-018-0424-5.

Sarlus, H., and Heneka, M. T. (2017). Microglia in Alzheimer's disease. *J. Clin. Invest.* 127, 3240–3249. doi:10.1172/JCI90606.

Satpute-Krishnan, P., DeGiorgis, J. A., Conley, M. P., Jang, M., and Bearer, E. L. (2006). A peptide zipcode sufficient for anterograde transport within amyloid precursor protein. *Proc. Natl. Acad. Sci.* 103, 16532–16537. doi:10.1073/PNAS.0607527103.

Schönfelder, J., Pfeiffer, P. B., Pradhan, T., Bijzet, J., Hazenberg, B. P. C., Schönland, S. O., et al. (2021). Protease resistance of ex vivo amyloid fibrils implies the proteolytic selection of disease-associated fibril morphologies. *Amyloid*. doi:10.1080/13506129.2021.1960501.

Schütz, A. K., Vagt, T., Huber, M., Ovchinnikova, O. Y., Cadalbert, R., Wall, J., et al. (2015). Atomic-Resolution Three-Dimensional Structure of Amyloid β Fibrils Bearing the Osaka Mutation. *Angew. Chemie Int. Ed.* 54, 331–335. doi:10.1002/anie.201408598.

Selkoe, D. J. (1998). The cell biology β-amyloid precursor protein and presenilin in Alzheimer's disease. *Trends Cell Biol.* 8, 447–453. doi:10.1016/S0962-8924(98)01363-4.

Selkoe, D. J., and Hardy, J. (2016). The amyloid hypothesis of Alzheimer's disease at 25 years. *EMBO Mol. Med.* 8, 595–608. doi:10.15252/emmm.201606210.

Sengupta, U., Nilson, A. N., and Kayed, R. (2016). The Role of Amyloid-β Oligomers in Toxicity, Propagation, and Immunotherapy. *EBioMedicine* 6, 42. doi:10.1016/J.EBIOM.2016.03.035.

Serra-Batiste, M., Ninot-Pedrosa, M., Bayoumi, M., Gairí, M., Maglia, G., and Carulla, N. (2016). Aβ42 assembles into specific β-barrel pore-forming oligomers in membrane-mimicking environments. *Proc. Natl. Acad. Sci. U. S. A.* 113, 10866–10871. doi:10.1073/pnas.1605104113.

Serrano-Pozo, A., Frosch, M. P., Masliah, E., and Hyman, B. T. (2011). Neuropathological alterations in Alzheimer disease. *Cold Spring Harb. Perspect. Med.* 1. doi:10.1101/cshperspect.a006189.

Sevigny, J., Chiao, P., Bussière, T., Weinreb, P. H., Williams, L., Maier, M., et al. (2016). The antibody aducanumab reduces Aβ plaques in Alzheimer's disease. *Nat. 2016 5377618* 537, 50–56. doi:10.1038/nature19323.

Sheedy, F. J., Grebe, A., Rayner, K. J., Kalantari, P., Ramkhelawon, B., Carpenter, S.

B., et al. (2013). CD36 coordinates NLRP3 inflammasome activation by facilitating intracellular nucleation of soluble ligands into particulate ligands in sterile inflammation. *Nat. Immunol.* 14, 812–820. doi:10.1038/ni.2639.

Shi, J., Zhao, Y., Wang, K., Shi, X., Wang, Y., Huang, H., et al. (2015). Cleavage of GSDMD by inflammatory caspases determines pyroptotic cell death. *Nature* 526, 660–665. doi:10.1038/nature15514.

Shi, Q., Chowdhury, S., Ma, R., Le, K. X., Hong, S., Caldarone, B. J., et al. (2017). Complement C3 deficiency protects against neurodegeneration in aged plaque-rich APP/PS1 mice. *Sci. Transl. Med.* 9. doi:10.1126/scitranslmed.aaf6295.

Shoji, M., Golde, T. E., Ghiso, J., Cheung, T. T., Estus, S., Shaffer, L. M., et al. (1992). Production of the Alzheimer amyloid β protein by normal proteolytic processing. *Science (80-.).* 258, 126–129. doi:10.1126/SCIENCE.1439760.

Silvers, R., Colvin, M. T., Frederick, K. K., Jacavone, A. C., Lindquist, S., Linse, S., et al. (2017). Aggregation and Fibril Structure of AβM01-42 and Aβ1-42. *Biochemistry* 56, 4850–4859. doi:10.1021/acs.biochem.7b00729.

Simard, A. R., Soulet, D., Gowing, G., Julien, J. P., and Rivest, S. (2006). Bone marrow-derived microglia play a critical role in restricting senile plaque formation in Alzheimer's disease. *Neuron* 49, 489–502. doi:10.1016/j.neuron.2006.01.022.

Sims, R., Hill, M., and Williams, J. (2020). The multiplex model of the genetics of Alzheimer's disease. *Nat. Neurosci.* 23, 311–322. doi:10.1038/s41593-020-0599-5.

Sims, R., Van Der Lee, S. J., Naj, A. C., Bellenguez, C., Badarinarayan, N., Jakobsdottir, J., et al. (2017). Rare coding variants in PLCG2, ABI3, and TREM2 implicate microglial-mediated innate immunity in Alzheimer's disease. *Nat. Genet.* 49, 1373–1384. doi:10.1038/ng.3916.

Sleegers, K., Brouwers, N., Gijselinck, I., Theuns, J., Goossens, D., Wauters, J., et al. (2006). APP duplication is sufficient to cause early onset Alzheimer's dementia with cerebral amyloid angiopathy. *Brain* 129, 2977–2983. doi:10.1093/brain/awl203.

Smith-Garvin, J. E., Koretzky, G. A., and Jordan, M. S. (2009). T cell activation. *Annu. Rev. Immunol.* 27, 591–619. doi:10.1146/annurev.immunol.021908.132706.

Solé-Domènech, S., Rojas, A. V, Maisuradze, G. G., Scheraga, H. A., Lobel, P., and Maxfield, F. R. (2018). Lysosomal enzyme tripeptidyl peptidase 1 destabilizes fibrillar Aβ by multiple endoproteolytic cleavages within the β-sheet domain. *Proc.*

Natl. Acad. Sci. U. S. A. 115, 1493–1498. doi:10.1073/pnas.1719808115.

Song, M., Jin, J. J., Lim, J. E., Kou, J., Pattanayak, A., Rehman, J. A., et al. (2011). TLR4 mutation reduces microglial activation, increases Aβ deposits and exacerbates cognitive deficits in a mouse model of Alzheimer's disease. *J. Neuroinflammation* 8, 92. doi:10.1186/1742-2094-8-92.

Soscia, S. J., Kirby, J. E., Washicosky, K. J., Tucker, S. M., Ingelsson, M., Hyman, B., et al. (2010). The Alzheimer's disease-associated amyloid β-protein is an antimicrobial peptide. *PLoS One* 5. doi:10.1371/journal.pone.0009505.

Sousa, J., Cá, B., Maceiras, A. R., Simões-Costa, L., Fonseca, K. L., Fernandes, A. I., et al. (2020). Mycobacterium tuberculosis associated with severe tuberculosis evades cytosolic surveillance systems and modulates IL-1β production. *Nat. Commun. 2020 111* 11, 1–14. doi:10.1038/s41467-020-15832-6.

Sperling, R. A., Aisen, P. S., Beckett, L. A., Bennett, D. A., Craft, S., Fagan, A. M., et al. (2011). Toward defining the preclinical stages of Alzheimer's disease: Recommendations from the National Institute on Aging-Alzheimer's Association workgroups on diagnostic guidelines for Alzheimer's disease. *Alzheimer's Dement.* 7, 280–292. doi:10.1016/j.jalz.2011.03.003.

Spitzer, P., Condic, M., Herrmann, M., Oberstein, T. J., Scharin-Mehlmann, M., Gilbert, D. F., et al. (2016). Amyloidogenic amyloid-β-peptide variants induce microbial agglutination and exert antimicrobial activity. *Sci. Rep.* 6, 1–11. doi:10.1038/srep32228.

Stewart, C. R., Stuart, L. M., Wilkinson, K., Van Gils, J. M., Deng, J., Halle, A., et al. (2010). CD36 ligands promote sterile inflammation through assembly of a Toll-like receptor 4 and 6 heterodimer. *Nat. Immunol.* 11, 155–161. doi:10.1038/ni.1836.

Stewart, K. L., Hughes, E., Yates, E. A., Akien, G. R., Huang, T. Y., Lima, M. A., et al. (2016). Atomic Details of the Interactions of Glycosaminoglycans with Amyloid-β Fibrils. *J. Am. Chem. Soc.* doi:10.1021/jacs.6b02816.

Stewart, K. L., Hughes, E., Yates, E. A., Middleton, D. A., and Radford, S. E. (2017). Molecular Origins of the Compatibility between Glycosaminoglycans and Aβ40 Amyloid Fibrils. *J. Mol. Biol.* 429, 2449. doi:10.1016/J.JMB.2017.07.003.

Stöhr, J., Condello, C., Watts, J. C., Bloch, L., Oehler, A., Nick, M., et al. (2014). Distinct synthetic Aβ prion strains producing different amyloid deposits in bigenic mice. *Proc. Natl. Acad. Sci.* 111, 10329–10334. doi:10.1073/PNAS.1408968111.

Stöhr, J., Watts, J. C., Mensinger, Z. L., Oehler, A., Grillo, S. K., DeArmond, S. J., et al. (2012). Purified and synthetic Alzheimer's amyloid beta (Aβ) prions. *Proc. Natl. Acad. Sci.* 109, 11025–11030. doi:10.1073/PNAS.1206555109.

Strohäker, T., Jung, B. C., Liou, S. H., Fernandez, C. O., Riedel, D., Becker, S., et al. (2019). Structural heterogeneity of α-synuclein fibrils amplified from patient brain extracts. *Nat. Commun.* 10, 1–12. doi:10.1038/s41467-019-13564-w.

Sulzer, D., Alcalay, R. N., Garretti, F., Cote, L., Kanter, E., Agin-Liebes, J., et al. (2017). T cells from patients with Parkinson's disease recognize α-synuclein peptides. *Nature* 546, 656–661. doi:10.1038/nature22815.

Sunde, M., Serpell, L. C., Bartlam, M., Fraser, P. E., Pepys, M. B., and Blake, C. C. F. (1997). Common core structure of amyloid fibrils by synchrotron X-ray diffraction. *J. Mol. Biol.* 273, 729–739. doi:10.1006/JMBI.1997.1348.

Svadlakova, T., Hubatka, F., Knotigova, P. T., Kulich, P., Masek, J., Kotoucek, J., et al. (2020). Proinflammatory effect of carbon-based nanomaterials: In vitro study on stimulation of inflammasome NLRP3 via destabilisation of lysosomes. *Nanomaterials* 10, 418. doi:10.3390/nano10030418.

Swanson, K. V., Deng, M., and Ting, J. P. Y. (2019). The NLRP3 inflammasome: molecular activation and regulation to therapeutics. *Nat. Rev. Immunol.* 19, 477–489. doi:10.1038/s41577-019-0165-0.

Tahara, K., Kim, H.-D., Jin, J.-J., Maxwell, J. A., Li, L., and Fukuchi, K.-I. (2006). Role of toll-like receptor signalling in Ab uptake and clearance. *Brain* 129, 3006–3019. doi:10.1093/brain/awl249.

Tanaka, T., Narazaki, M., and Kishimoto, T. (2014). Il-6 in inflammation, Immunity, And disease. *Cold Spring Harb. Perspect. Biol.* 6, 16295–16296. doi:10.1101/cshperspect.a016295.

Telling, G. C., Parchi, P., DeArmond, S. J., Cortelli, P., Montagna, P., Gabizon, R., et al. (1996). Evidence for the conformation of the pathologic isoform of the prion protein enciphering and propagating prion diversity. *Science (80-.).* 274, 2079–2082. doi:10.1126/science.274.5295.2079.

Thal, D. R., Rüb, U., Orantes, M., and Braak, H. (2002). Phases of Aβ-deposition in the human brain and its relevance for the development of AD. *Neurology* 58, 1791–1800. doi:10.1212/WNL.58.12.1791.

Thambisetty, M., An, Y., Nalls, M., Sojkova, J., Swaminathan, S., Zhou, Y., et al. (2013). Effect of complement CR1 on brain amyloid burden during aging and its modification by APOE genotype. *Biol. Psychiatry* 73, 422–428. doi:10.1016/j.biopsych.2012.08.015.

Tipping, K. W., Karamanos, T. K., Jakhria, T., Iadanza, M. G., Goodchild, S. C., Tuma, R., et al. (2015a). pH-induced molecular shedding drives the formation of amyloid fibril-derived oligomers. *Proc. Natl. Acad. Sci.* doi:10.1073/pnas.1423174112.

Tipping, K. W., van Oosten-Hawle, P., Hewitt, E. W., and Radford, S. E. (2015b). Amyloid Fibres: Inert End-Stage Aggregates or Key Players in Disease? *Trends Biochem. Sci.* 40, 719–727. doi:10.1016/j.tibs.2015.10.002.

Tö, M., Michaels, T. C. T., Sanagavarapu, K., Yang, X., Meisl, G., Cohen, S. I. A., et al. (2018). Secondary nucleation in amyloid formation. *Chem. Commun* 54, 8667. doi:10.1039/c8cc02204f.

Togo, T., Akiyama, H., Iseki, E., Kondo, H., Ikeda, K., Kato, M., et al. (2002). Occurrence of T cells in the brain of Alzheimer's disease and other neurological diseases. *J. Neuroimmunol.* 124, 83–92. doi:10.1016/S0165-5728(01)00496-9.

Tomiyama, T., Nagata, T., Shimada, H., Teraoka, R., Fukushima, A., Kanemitsu, H., et al. (2008). A new amyloid β variant favoring oligomerization in Alzheimer's-type dementia. *Ann. Neurol.* 63, 377–387. doi:10.1002/ana.21321.

Toyama, B. H., Kelly, M. J. S., Gross, J. D., and Weissman, J. S. (2007). The structural basis of yeast prion strain variants. *Nat. 2007 4497159* 449, 233–237. doi:10.1038/nature06108.

Tuttle, M. D., Comellas, G., Nieuwkoop, A. J., Covell, D. J., Berthold, D. A., Kloepper, K. D., et al. (2016). Solid-state NMR structure of a pathogenic fibril of full-length human α-synuclein. *Nat. Struct. Mol. Biol.* 23, 409–415. doi:10.1038/nsmb.3194.

Tycko, R. (2014). Physical and structural basis for polymorphism in amyloid fibrils. *Protein Sci.* 23, 1528–1539. doi:10.1002/pro.2544.

Tycko, R. (2015). Amyloid Polymorphism: Structural Basis and Neurobiological Relevance. *Neuron*. doi:10.1016/j.neuron.2015.03.017.

Tycko, R., Sciarretta, K. L., Orgel, J. P. R. O., and Meredith, S. C. (2009). Evidence for novel β-sheet structures in Iowa mutant β-amyloid fibrils. *Biochemistry* 48, 6072–6084. doi:10.1021/bi9002666.

Ulamec, S. M., Brockwell, D. J., and Radford, S. E. (2020). Looking Beyond the Core: The Role of Flanking Regions in the Aggregation of Amyloidogenic Peptides and Proteins. *Front. Neurosci.* 14, 1216. doi:10.3389/fnins.2020.611285.

Ulrich, J. D., Ulland, T. K., Mahan, T. E., Nyström, S., Peter Nilsson, K., Song, W. M., et al. (2018). ApoE facilitates the microglial response to amyloid plaque pathology. *J. Exp. Med.* 215, 1047–1058. doi:10.1084/jem.20171265.

Vafadari, B., Salamian, A., and Kaczmarek, L. (2016). MMP-9 in translation: from molecule to brain physiology, pathology, and therapy. *J. Neurochem.* 139, 91–114. doi:10.1111/jnc.13415.

Valle-Delgado, J. J., Alfonso-Prieto, M., Groot, N. S., Ventura, S., Samitier, J., Rovira, C., et al. (2010). Modulation of Aβ 42 fibrillogenesis by glycosaminoglycan structure . *FASEB J.* 24, 4250–4261. doi:10.1096/FJ.09-153551.

van der Kant, R., Goldstein, L. S. B., and Ossenkoppele, R. (2019). Amyloid-β-independent regulators of tau pathology in Alzheimer disease. *Nat. Rev. Neurosci. 2019 211* 21, 21–35. doi:10.1038/s41583-019-0240-3.

van der Lee, S. J., Wolters, F. J., Ikram, M. K., Hofman, A., Ikram, M. A., Amin, N., et al. (2018). The effect of APOE and other common genetic variants on the onset of Alzheimer's disease and dementia: a community-based cohort study. *Lancet Neurol.* 17, 434–444. doi:10.1016/S1474-4422(18)30053-X.

Van der Perren, A., Gelders, G., Fenyi, A., Bousset, L., Brito, F., Peelaerts, W., et al. (2020). The structural differences between patient-derived α-synuclein strains dictate characteristics of Parkinson's disease, multiple system atrophy and dementia with Lewy bodies. *Acta Neuropathol.* 139, 977–1000. doi:10.1007/s00401-020-02157-3.

Venegas, C., Kumar, S., Franklin, B. S., Dierkes, T., Brinkschulte, R., Tejera, D., et al. (2017). Microglia-derived ASC specks crossseed amyloid-β in Alzheimer's disease. *Nature* 552, 355–361. doi:10.1038/nature25158.

Villemagne, V. L., Doré, V., Burnham, S. C., Masters, C. L., and Rowe, C. C. (2018). Imaging tau and amyloid-? proteinopathies in Alzheimer disease and other conditions. *Nat. Rev. Neurol.* 14, 225–236. doi:10.1038/nrneurol.2018.9.

Vogt, N. M., Kerby, R. L., Dill-McFarland, K. A., Harding, S. J., Merluzzi, A. P., Johnson, S. C., et al. (2017). Gut microbiome alterations in Alzheimer's disease. *Sci. Rep.* 7, 1–11. doi:10.1038/s41598-017-13601-y.

Vom Berg, J., Prokop, S., Miller, K. R., Obst, J., Kälin, R. E., Lopategui-Cabezas, I., et al. (2012). Inhibition of IL-12/IL-23 signaling reduces Alzheimer's diseasea-like pathology and cognitive decline. *Nat. Med.* 18, 1812–1819. doi:10.1038/nm.2965.

Walsh, D. M., Klyubin, I., Fadeeva, J. V., Cullen, W. K., Anwyl, R., Wolfe, M. S., et al. (2002). Naturally secreted oligomers of amyloid β protein potently inhibit hippocampal long-term potentiation in vivo. *Nat. 2002 4166880* 416, 535–539. doi:10.1038/416535a.

Walsh, D. M., Thulin, E., Minogue, A. M., Gustavsson, N., Pang, E., Teplow, D. B., et al. (2009). A facile method for expression and purification of the Alzheimer's disease-associated amyloid β-peptide. *FEBS J.* 276, 1266–1281. doi:10.1111/j.1742-4658.2008.06862.x.

Wälti, M. A., Ravotti, F., Arai, H., Glabe, C. G., Wall, J. S., Böckmann, A., et al. (2016). Atomic-resolution structure of a disease-relevant Aβ(1-42) amyloid fibril. *Proc. Natl. Acad. Sci. U. S. A.* 113, E4976–E4984. doi:10.1073/pnas.1600749113.

Wang, R., Sweeney, D., Gandy, S. E., and Sisodia, S. S. (1996). The profile of soluble amyloid β protein in cultured cell media. Detection and quantification of amyloid β protein and variants by immunoprecipitation-mass spectrometry. *J. Biol. Chem.* 271, 31894–31902. doi:10.1074/jbc.271.50.31894.

Webers, A., Heneka, M. T., and Gleeson, P. A. (2020). The role of innate immune responses and neuroinflammation in amyloid accumulation and progression of Alzheimer's disease. *Immunol. Cell Biol.* 98, 28–41. doi:10.1111/imcb.12301.

Webster, S., Bradt, B., Rogers, J., and Cooper, N. (1997). Aggregation state-dependent activation of the classical complement pathway by the amyloid β peptide. *J. Neurochem.* 69, 388–398. doi:10.1046/j.1471-4159.1997.69010388.x.

Westermark, P., Andersson, A., and Westermark, G. T. (2011). Islet amyloid polypeptide, islet amyloid, and diabetes mellitus. *Physiol. Rev.* 91, 795–826. doi:10.1152/physrev.00042.2009.

Wilkinson, K., and El Khoury, J. (2012). Microglial scavenger receptors and their roles in the pathogenesis of Alzheimer's disease. *Int. J. Alzheimers. Dis.* doi:10.1155/2012/489456.

Wiltfang, J., Esselmann, H., Bibl, M., Hüll, M., Hampel, H., Kessler, H., et al. (2007). Amyloid β peptide ratio 42/40 but not Aβ42 correlates with phospho-Tau in patients with low- and high-CSF Aβ40 load. *J. Neurochem.* 101, 1053–1059.

doi:10.1111/j.1471-4159.2006.04404.x.

Wiseman, F. K., Al-Janabi, T., Hardy, J., Karmiloff-Smith, A., Nizetic, D., Tybulewicz, V. L. J., et al. (2015). A genetic cause of Alzheimer disease: Mechanistic insights from Down syndrome. *Nat. Rev. Neurosci.* 16, 564–574. doi:10.1038/nrn3983.

Wittenberg, R., Hu, B., Jagger, C., Kingston, A., Knapp, M., Comas-Herrera, A., et al. (2020). Projections of care for older people with dementia in England: 2015 to 2040. *Age Ageing* 49, 264–269. doi:10.1093/ageing/afz154.

Wyss-Coray, T., Loike, J. D., Brionne, T. C., Lu, E., Anankov, R., Yan, F., et al. (2003). Adult mouse astrocytes degrade amyloid-β in vitro and in situ. *Nat. Med.* 9, 453–457. doi:10.1038/nm838.

Xia, Q., Yang, X. Y., Shi, J. Bin, Liu, Z. J., Peng, Y. H., Wang, W. J., et al. (2021). The Protective A673T Mutation of Amyloid Precursor Protein (APP) in Alzheimer's Disease. *Mol. Neurobiol.* doi:10.1007/s12035-021-02385-y.

Xiao, Y., Ma, B., McElheny, D., Parthasarathy, S., Long, F., Hoshi, M., et al. (2015). Aβ(1-42) fibril structure illuminates self-recognition and replication of amyloid in Alzheimer's disease. *Nat. Struct. Mol. Biol.* 22, 499–505. doi:10.1038/nsmb.2991.

Xu, G., Fromholt, S. E., Chakrabarty, P., Zhu, F., Liu, X., Pace, M. C., et al. (2020). Diversity in Aβ deposit morphology and secondary proteome insolubility across models of Alzheimer-type amyloidosis. *Acta Neuropathol. Commun.* 8. doi:10.1186/s40478-020-00911-y.

Xue, W. F., Hellewell, A. L., Gosal, W. S., Homans, S. W., Hewitt, E. W., and Radford, S. E. (2009). Fibril fragmentation enhances amyloid cytotoxicity. *J. Biol. Chem.* 284, 34272–34282. doi:10.1074/jbc.M109.049809.

Yamada, T., Sasaki, H., Furuya, H., Miyata, T., Goto, I., and Sakaki, Y. (1987). Complementary DNA for the mouse homolog of the human amyloid beta protein precursor. *Biochem. Biophys. Res. Commun.* 149, 665–671. doi:10.1016/0006-291X(87)90419-0.

Yan, P., Hu, X., Song, H., Yin, K., Bateman, R. J., Cirrito, J. R., et al. (2006). Matrix metalloproteinase-9 degrades amyloid-β fibrils in vitro and compact plaques in situ. *J. Biol. Chem.* 281, 24566–24574. doi:10.1074/jbc.M602440200.

Yates, S. L., Burgess, L. H., Kocsis-Angle, J., Antal, J. M., Dority, M. D., Embury, P. B., et al. (2000). Amyloid β and amylin fibrils induce increases in proinflammatory

cytokine and chemokine production by THP-1 cells and murine microglia. *J. Neurochem.* 74, 1017–1025. doi:10.1046/j.1471-4159.2000.0741017.x.

Yin, K. J., Cirrito, J. R., Yan, P., Hu, X., Xiao, Q., Pan, X., et al. (2006). Matrix metalloproteinases expressed by astrocytes mediate extracellular amyloid-β peptide catabolism. *J. Neurosci.* 26, 10939–10948. doi:10.1523/JNEUROSCI.2085-06.2006.

Yoo, S., Zhang, S., Kreutzer, A. G., and Nowick, J. S. (2018). An Efficient Method for the Expression and Purification of Aβ(M1-42). *Biochemistry* 57, 3861–3866. doi:10.1021/acs.biochem.8b00393.

Zhang, B., Gaiteri, C., Bodea, L. G., Wang, Z., McElwee, J., Podtelezhnikov, A. A., et al. (2013). Integrated systems approach identifies genetic nodes and networks in late-onset Alzheimer's disease. *Cell* 153, 707–720. doi:10.1016/j.cell.2013.03.030.

Zigman, W. B., and Lott, I. T. (2007). Alzheimers disease in down syndrome: Neurobiology and risk. *Ment. Retard. Dev. Disabil. Res. Rev.* 13, 237–246. doi:10.1002/mrdd.20163.